

ISSN 1573-160X

Vol. 31, Iss. 4

July – August

2024



Physical Oceanography

<http://physical-oceanography.ru/>



ISSN 1573-160X

Vol. 31, no. 4. 2024

July – August

Founded in January 1987

Publication frequency:

6 issues per year

Physical Oceanography

Scientific and theoretical journal

FOUNDER AND PUBLISHER:

Federal State Budget Scientific Institution

Federal Research Centre

“Marine Hydrophysical Institute of RAS”

Peer reviewed scientific journal.

The Journal publishes original research results, review articles (at the editorial board's request) and brief reports on the following sections of hydrophysics:

- thermohydrodynamics of the ocean and atmosphere;
- analysis of observational results and methods of calculation of ocean hydrophysical fields;
- experimental and expeditionary studies;
- satellite hydrophysics;
- mathematical modelling of marine systems;
- automation of scientific research of the seas and oceans.

Objectives

- familiarisation of the world and Russian scientific community with the results of theoretical, experimental and expeditionary studies of the World Ocean;
- exchange of scientific information, experience, research and observation data with specialists from different regions of the country and abroad;
- increase of publication activity of national authors, rating of scientific organisations of Russia and level of national publications in the world scientific community according to their citation data;
- theoretical and practical assistance to scientists in preparing articles for printing that meet modern requirements of publication and scientific ethics;
- strengthening the popularity and authority of the publication, increasing the number of regular subscribers

The Journal is indexed in:

Google Scholar
Web of Science (ESCI)
Scopus
EBSCO Publishing

journal@mhi-ras.ru

<http://physical-oceanography.ru/>

Founder, Publisher and Editorial Office address:

2, Kapitanskaya St., Sevastopol, 299011

Russia

Phone, fax: + 7 (8692) 54-02-23

EDITORIAL BOARD

- Sergey K. Kononov** – Editor-in-Chief, Director of FSBSI FRC MHI, corresponding member of RAS, Dr.Sci. (Geogr.), ORCID ID: 0000-0002-5200-8448, secretary@mhi-ras.ru (Sevastopol, Russia)
- Vladimir N. Belokopytov** – Deputy Editor-in-Chief, Head of Department of FSBSI FRC MHI, Dr.Sci. (Geogr.), ORCID ID: 0000-0003-4699-9588 (Sevastopol, Russia)
- Aleksandr I. Kubryakov** – Deputy Editor-in-Chief, Chief Scientist Researcher of FSBSI FRC MHI, Dr.Sci. (Phys.-Math.), ORCID ID: 0000-0003-1899-9230, ResearcherID: F-8959-2014, (Sevastopol, Russia)
- Igor K. Ivashchenko** – Executive Editor, Senior Scientist of FSBSI FRC MHI, Ph.D. (Econ.), (Sevastopol, Russia)
- Yuri V. Artamonov** – Head Scientist Researcher of FSBSI FRC MHI, Dr.Sci. (Geogr.), ResearcherID: AAC-6651-2020 (Sevastopol, Russia)
- Sergey V. Berdnikov** – Director of FRC SSC of RAS, Dr.Sci. (Geogr.), ORCID ID: 0000-0002-3095-5532 (Rostov-on-Don, Russia)
- Valery G. Bondur** – Scientific Supervisor of ISR "AEROCOSMOS", academician of RAS, Dr.Sci. (Techn.), ORCID ID: 0000-0002-2049-6176 (Moscow, Russia)
- Demuri I. Demetrasvili** – Head of the sector of mathematical modeling of geophysical processes of sea and atmosphere, the Nodia Institute of Geophysics of the Javakishvili Tbilisi State University, Dr.Sci. (Phys.-Math.), ORCID ID: 0000-0002-4789-4852 (Tbilisi, Georgia)
- Sergey A. Dobrolyubov** – Dean of Faculty of Geography of MSU, academician of RAS, Dr.Sci. (Geogr.), prof., ResearcherID: A-9688-2012 (Moscow, Russia)
- Grigory I. Dolgikh** – Director of POI FEB of RAS, Dr.Sci. (Phys.-Math.), academician of RAS, prof., ORCID ID: 0000-0002-2806-3834 (Vladivostok, Russia)
- Vladimir A. Dulov** – Head of Laboratory of FSBSI FRC MHI, Dr.Sci. (Phys.-Math.), prof., ORCID ID: 0000-0002-0038-7255, (Sevastopol, Russia)
- Vladimir V. Efimov** – Head of Department of FSBSI FRC MHI, Dr.Sci. (Phys.-Math.), prof., ResearcherID: P-2063-2017, (Sevastopol, Russia)
- Vladimir V. Fomin** – Head of Department of FSBSI FRC MHI, Dr.Sci. (Phys.-Math.), ORCID ID: 0000-0002-9070-4460, (Sevastopol, Russia)
- Isaac Gertman** – Head of the Physical Oceanography Department of Israel Oceanographic & Limnological Research, Head of IOLR data center ISRAMAR, Ph.D. (Geogr.), ORCID ID: 0000-0002-6953-6722 (Haifa, Israel)
- Dmitry G. Gryazin** – Head of Department, Chief Metrologist of SRC of the "Concern CSRI Elektropribor" JSC, Dr.Sci. (Techn.), prof. of Mechatronics of ITMO University, Scopus AuthorID: 25638150600, (Saint Petersburg, Russia)
- Rashit A. Ibraev** – Chief Scientist Researcher of INM of RAS, corresponding member of RAS, Dr.Sci. (Phys.-Math.), ORCID ID: 0000-0002-9099-4541 (Moscow, Russia)
- Vasilii V. Knysh** – Head Scientist Researcher of FSBSI FRC MHI, Dr.Sci. (Phys.-Math.), prof., ResearcherID: B-3603-2018 (Sevastopol, Russia)
- Gennady K. Korotaev** – Scientific Supervisor of FSBSI FRC MHI, corresponding member of RAS, Dr.Sci. (Phys.-Math.), prof., ResearcherID: K-3408-2017 (Sevastopol, Russia)
- Vladimir N. Kudryavtsev** – Executive Director of Satellite Oceanography Laboratory of RSHU, Dr.Sci. (Phys.-Math.), prof., ResearcherID: G-1502-2014 (Saint Petersburg)
- Michael E. G. Lee** – Head of Department of FSBSI FRC MHI, Dr.Sci. (Phys.-Math.), prof., ORCID ID: 0000-0002-2292-1877 (Sevastopol, Russia)
- Gennady G. Matishov** – Deputy President of RAS, Deputy academician-Secretary of the Department of Earth Sciences of Supervisor of RAS – Head of the Oceanology, Atmospheric Physics and Geography Section, Scientific Supervisor of SSC of RAS, Supervisor of MMBI KSC of RAS, academician of RAS, Dr.Sci. (Geogr.), prof., ORCID ID: 0000-0003-4430-5220 (Rostov-on-Don, Russia)
- Nikolay A. Rimski-Korsakov** – Deputy Director (Marine Engineering) of FSBSI P.P. Shirshov IO of RAS, Dr.Sci. (Techn.), ResearcherID: K-8378-2017 (Moscow, Russia)
- Angelo Rubino** – Professor of Ca' Foscari University, Ph.D. (Phys. Oceanogr.), ORCID ID: 0000-0003-3857-4811 (Venice, Italy)
- Anatoly S. Samodurov** – Head of Department of FSBSI FRC MHI, Dr.Sci. (Phys.-Math.), ResearcherID: V-8642-2017 (Sevastopol, Russia)
- Georgy I. Shapiro** – Head of Plymouth Ocean Forecasting Centre of the University of Plymouth, Dr.Sci. (Phys.-Math.), prof. in Phys. Oceanogr., (Plymouth, Great Britain)
- Naum B. Shapiro** – Head Scientist Researcher of FSBSI FRC MHI, Dr.Sci. (Phys.-Math.), ResearcherID: A-8585-2017 (Sevastopol, Russia)
- Mikhail V. Shokurov** – Head Scientist Researcher of FSBSI FRC MHI, Dr.Sci. (Phys.-Math.), ORCID ID: 0000-0003-1595-8281 (Sevastopol, Russia)
- Elena F. Vasechkina** – Deputy Director of FSBSI FRC MHI, Chief Research Associate of FSBSI FRC MHI, Dr.Sci. (Geogr.), ORCID ID: 0000-0001-7007-9496 (Sevastopol, Russia)
- Elizaveta V. Zabolotskikh** – Head Scientist Researcher of RSHU, Dr.Sci. (Phys.-Math.), Scopus Author ID: 6506482460 (Saint Petersburg, Russian)
- Vladimir B. Zalesny** – Head Scientific Researcher of INM of RAS, Dr.Sci. (Phys.-Math.), prof., ORCID ID: 0000-0003-3829-3374 (Moscow, Russia)
- Andrey G. Zatsepin** – Chief of Laboratory of FSBSI P.P. Shirshov IO of RAS, Chief Research Associate of FSBSI P.P. Shirshov IO of RAS, Dr.Sci. (Phys.-Math.), ORCID ID: 0000-0002-5527-5234 (Moscow, Russia)
- George Zodiatis** – Senior Researcher of Laboratory of Coastal and Marine Research of the Institute of Applied and Computational Mathematics, for Research and Technology Foundation – Hellas, Ph.D. (Oceanol.), ResearcherID: J-3032-2013 (Heraklion, Crete, Greece)

CONTENTS

Vol. 31, no 4. 2024

July – August, 2024

THERMOHYDRODYNAMICS OF THE OCEAN AND THE ATMOSPHERE

- Shokurov M. V., Kraevskaya N. Yu.** Sea breeze circulation: Theory and two-dimensional simulation (Review) 447

ANALYSIS OF OBSERVATIONS AND METHODS OF CALCULATING HYDROPHYSICAL FIELDS IN THE OCEAN

- Artamonov Yu. V., Skripaleva E. A., Nikolsky N. V.** Climatic structure and intra-annual variability of temperature fronts on the ocean surface in the Patagonian shelf region 467
- Goryachkin Yu. N., Lazorenko D. I., Fomin V V.** Dynamics of accumulative coast under the influence of transverse hydraulic structure 486
- Churilova T. Ya., Efimova T. V., Moiseeva N. A., Skorokhod E. Yu., Kalmykova D. V., Sutorikhin I. A., Kirillov V. V.** Comparison of bio-optical properties of optically complex waters with different trophic status 507

EXPERIMENTAL AND FIELD RESEARCH

- Malinovsky V. V., Korinenko A. E.** Investigation of the wind wave breaking shapes using the sea surface video records 527

AUTOMATION OF RESEARCH OF SEAS AND OCEANS

- Gryazin D. G., Gleb K. A.** An advanced electric power generator for offshore autonomous stations 539
- Zhuk E. V., Markova N. V.** Geoinformation system for *Argo* floats drift assessment: The Black Sea case 562

SATELLITE HYDROPHYSICS

- Cheshm Siyahi V., Zabolotskikh E. V., V. N. Kudryavtsev V. N.** Evaluating and Adjusting ERA5 Wind Speed for Extratropical Cyclones and Polar Lows Using AMSR-2 Observations 580



All the materials of the journal are available under Creative Commons Attribution-NonCommercial 4.0 International (CC BY-NC 4.0)

Review article

Sea Breeze Circulation: Theory and Two-Dimensional Simulation (Review)

M. V. Shokurov, N. Yu. Kraevskaya ✉

Marine Hydrophysical Institute of RAS, Sevastopol, Russian Federation

✉ kraevskaja_n@mhi-ras.ru

Abstract

Purpose. Sea breeze circulation is a common mesoscale phenomenon near the coasts of water bodies. However, at the moment, a number of the published review papers on this topic remain small. Therefore, the purpose of the work is to complement the existing reviews on sea breezes by generalizing the available knowledge on the influence of air heating intensity near the land surface, atmosphere stratification, synoptic background wind and the Coriolis force upon the sea breeze circulation.

Methods and Results. An overview of the results of studies involving the theoretical research methods, namely linear theory and two-dimensional numerical simulation, is presented. At first, the sea breeze circulation is considered within the framework of linear theory. Further, a technical description of two-dimensional models and the breeze features obtained applying these models are presented. The published works having been reviewed made it possible to consider the influence of four main factors (heat flux, atmosphere stratification, background synoptic wind and the Coriolis force) upon the breeze circulation.

Conclusions. Within the framework of linear theory, the breeze circulation represents an internal inertial-gravity wave with a diurnal period. Depending on the uniformity of vertical profile of the background synoptic wind, its influence on the linear sea breeze circulation leads to the asymmetry of circulation relative to the coast and to limitation of the breeze height. In a nonlinear regime, the important feature of breeze circulation obtained by applying numerical simulation consists in formation of a gravity current propagating over the surface. The nonlinear regime implies a fairly clear dependence of the velocity of gravity current front propagation on its height. The main manifestation of the background wind influence upon the gravity current is the change in its height that results in formation of a stationary or rapidly spreading current. Due to the Coriolis force influence, both within the framework of linear theory and in the nonlinear regime, an along-coastal velocity component is formed that leads to a decrease of the velocity component perpendicular to the coastline.

Keywords: sea breeze circulation, linear theory, numerical simulation, internal gravity waves

Acknowledgment: The investigation was carried out within the framework of the theme of state assignment of FSBSI FRC MHI FNNN-2024-0014.

For citation: Shokurov, M.V. and Kraevskaya, N.Yu., 2024. Sea Breeze Circulation: Theory and Two-Dimensional Simulation (Review). *Physical Oceanography*, 31(4), pp. 447-466.

© 2024, M. V. Shokurov, N. Yu. Kraevskaya

© 2024, Physical Oceanography

Introduction

Sea breeze circulation is a common mesoscale phenomenon near the coasts of water bodies. Sea breeze occurs under effect of a pressure gradient due to different heating of the air near the land surface and the water body surface.

Sea breeze develops in the lower layer of the atmosphere and affects boundary layer structures [1, 2] and the atmosphere above it [3, 4] as well as the formation of

cumulus convection [5–7] and interacts with processes of various scales in the atmosphere and ocean [8–11]. Being formed in coastal regions, sea breeze affects the weather and climate of these areas. In addition, the relevance of sea breeze research is determined by its effect on pollution transport [12–14], especially in urbanized industrially developed coastal regions. The structure of sea breeze circulation (Fig. 1) includes gravity current, front, gravity current head, region of strong turbulent mixing behind the head, returned current, thermal internal boundary layer (TIBL) [15].

Sea breeze gravity current is a flow of cold sea air onto the land. The boundary between cold and warm air on the land (a sea breeze front) is usually characterized by large gradients of temperature, pressure and humidity. Directly behind the breeze front, the raised gravity current head is located which is formed due to the convergence of cold and warm air masses located above the water body and land, respectively. The head height is several times greater than the current main body one. Behind the head, a region of strong turbulent mixing is formed due to the instability of the Kelvin – Helmholtz waves which arise at the boundary between two layers of air with different densities and velocities. A returned current is directed in the opposite direction above the sea breeze gravity current. A thermal internal boundary layer is formed inside the body of the cold gravity current. It occurs when cold air moves onto the land and is gradually warmed by the land surface.

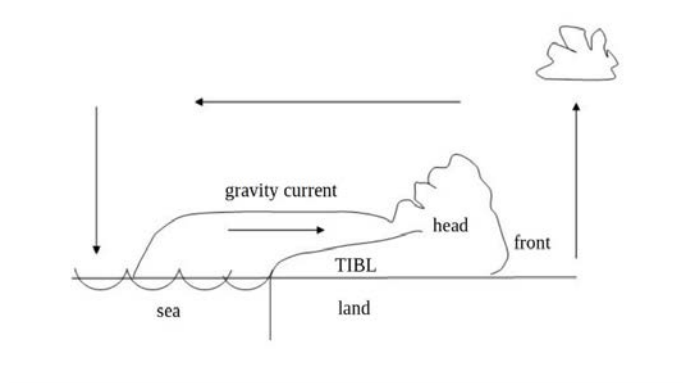


Fig. 1. Structure of breeze circulation (TIBL – thermal internal boundary layer)

The sea breeze development is influenced by a large number of factors [16]. The main factor determining the sea breeze occurrence is the heat flux at the land surface [17, 18], under effect of which a pressure difference over the land and sea surfaces is formed.

Other major factors affecting sea breezes include background synoptic wind [19–21], Earth’s rotation [22, 23] and atmospheric stratification [24–26] which is different over the sea and the land and varies with the diurnal cycle. Secondary factors affecting sea breeze circulation include surface friction ¹ [27], turbulent mixing [19, 28, 29], topography (height and slope) [30, 31], coastline shape [32, 10],

¹ Malone, T.F., ed., 1951. *Compendium of Meteorology*. Boston, Massachusetts: American Meteorological Society, 1334 p.

basin [33, 34] and land scale [35–37] as well as air humidity [5, 38]. Although most of these factors affect sea breezes after they have formed, some can affect the balance of forces and support or prevent their development.

The history of sea breeze circulation research spans over a century. A fairly detailed description of the early stages is given in monograph ² and reviews [39, 40, 15]. Various methods are applied to study sea breezes: theory, numerical simulation, experiments and *in situ* observations. Among the theoretical methods for studying sea breezes, the following are distinguished: linear theory [22, 41, 42], nonlinear theory for some exact solutions [43, 44] and similarity theory [25, 26, 45, 46].

Numerical simulation studies can be divided into two categories. The first category includes idealized two-dimensional models with simplified representation of physical processes [17, 18, 28, 47, 48]. The second category covers numerical simulation of sea breezes in specific geographic regions using three-dimensional mesoscale atmospheric models with high spatial resolution and detailed representation of physical processes [49–56]. The stages of development and comparison of two-dimensional and three-dimensional models are presented in works ³ [16].

Both laboratory ⁴ [57] and *in situ* [51, 58] experiments have been carried out. The behavior of gravity currents depending on the parameters of environment [59–61] is mainly studied in laboratory experiments. The largest number of works are devoted to *in situ* observations which include contact [50, 54, 62, 63] and remote observations from satellites in different spectral ranges [34, 64, 65] as well as meteorological radar data, to mention but a few.

This work is purposed at presenting the main results of the impact of surface heat flux, background wind, stratification and the Coriolis force on sea breeze circulation using analytical theory and ideal two-dimensional simulation.

Linear theory of sea breeze circulation

Sea breeze studies in the 19th century and in the first half of the 20th century were more qualitative. By the 1950s, the observations had revealed that sea breeze had the form of a circulation cell changing its direction during the day. Sea breeze is formed due to different heat capacity of the land and sea which results in a temperature gradient formation at the land-sea interface. This leads to the formation of a pressure gradient and, as a result, sea breeze circulation. Sea breeze is observed in calm weather or with a weak background wind. The nighttime sea breeze is less intense than the daytime one.

² Simpson, J.E., 1994. *Sea Breeze and Local Winds*. Cambridge: Cambridge University Press, 234 p.

³ Clark, I.W., 1986. *A Three-Dimensional Numerical Model of the Sea Breeze for the Plymouth Region: Thesis*. Devon, England: University of Plymouth, 259 p. <https://doi.org/10.24382/1380>

⁴ Simpson, J.E., 1997. *Gravity Currents in the Environment and the Laboratory*. Cambridge, United Kingdom: Cambridge University Press, 244 p.

Experimental dependences of wind speed on temperature, distribution of meteorological parameters, breeze horizontal and vertical sizes, their dependence on season and latitude in individual geographic regions were obtained. For example, it is found that the daytime sea breeze extends to a distance of up to 50 km in middle latitudes and up to 150 km in the tropics. The nighttime sea breeze penetrates shorter distances than the daytime one.

The background wind can both strengthen and weaken the breeze or prevent its development. When the headwind is calm, the breeze manifests itself as a cold front. When the breeze develops, air moves at a right angle to the coastline, the breeze direction changes due to the Coriolis force ¹.

Based on observational data, the authors of the first theoretical works considered the following questions: what forces should be taken into consideration for the correct description of the sea breeze, how to obtain the difference in time between its maximum intensity and temperature corresponding to observations ¹?

The first work that provided a quantitative description of sea breeze circulation was devoted to the linear theory [22]. Assuming that locally, at a coastline point near the surface, the acceleration is determined by the pressure gradient created by the temperature contrast between the sea and land, the Coriolis force and linear Rayleigh friction, a correct elliptical shape of the velocity hodograph was obtained. The clockwise velocity vector rotation was also established. However, no spatial distribution of all three components of velocity, temperature and pressure was obtained since complete equations of hydrodynamics were not solved. It is demonstrated that the circulation source of breeze circulation cell is temperature (buoyancy) contrast between land and sea. It should be noted that application of linear friction made it possible to obtain a phase shift in the model between heating and the sea breeze circulation intensity close to observations.

At the same time, in [66], the author examines the atmosphere reaction to a given temperature distribution which was a periodic function of time and an exponentially decaying function of height. Theoretical result describing the dependence of the maximum wind speed on height in the daytime sea breeze agreed quite well with the experimental data at the equator. In the middle latitudes, the velocity dependence on height in both daytime and nighttime sea breezes is similar to that observed in the tropics. The difference is that velocity vector changes its direction during the day due to the Coriolis force.

In work ¹, a linear solution for a horizontally periodic heat source was obtained, which provided the application of the Fourier transform. At the 45th parallel, this solution described the observed circulation quite completely. It was found that the height of both daytime and nighttime sea breezes was 400 m and increased with rising friction. The Coriolis force effect is manifested in the occurrence of an alongshore velocity component which is shifted in time by approximately 12 hours relative to the component normal to the shore. The maximum temperature difference at the land-sea boundary and the maximum sea breeze intensity differ in time by 4.7 hours. Consideration of friction and the Coriolis force reduces this shift. The height occupied by the returned current is 4–5 times greater than one of the current near

the surface. The maximum velocity in the returned current is approximately 4 times lower than in the surface current. The upper boundary of sea breeze circulation increases with rising friction and decreases with the increasing Coriolis force.

An important study examining the background wind effect on breezes is [67]. It examines the response of a homogeneous stratified flow to a heat source (island) of finite horizontal size on the surface. Waves are formed in the atmosphere on the leeward side of the island, their horizontal wavelength depends on the island dimensions.

Work [47] demonstrates that the motion can be divided into two parts – the rotational part and the large-scale wave potential motion. The wave motion occupies a large horizontal scale of ~5000 km and transfers mass from land to sea with small velocity values of ~1 km/h.

In [68] the formation of breeze circulation forerunner is considered in a stably stratified atmosphere in the form of internal gravity waves generated near the coastline at the moment of heating activation and propagating quite quickly from the coast towards the sea and towards the land.

A certain stage was [24]. Due to consideration of turbulent viscosity and thermal conductivity, a sixth order equation for stream function was obtained, so it had to be solved numerically. It was found that large values of velocity gradients near the coast arose due to the absence of temperature advection. The returned current directed from the coast towards the sea is two times weaker than one directed towards the coast. Affected by the Coriolis force, the wind velocity vector rotates clockwise at all heights. The distance over which the sea breeze propagates increases with rising atmospheric stratification. The background wind from the coast makes the maximum of the coast-perpendicular velocity shift towards the sea and its value decreases with an increase in the background wind. A sharp front is formed at the coast at small values of the background wind speed.

In [69], thermal convection in a stratified fluid is studied using the Boussinesq approximation and constant values of viscosity and thermal conductivity. Convection is caused by heating or cooling of the lower surface. At an infinitely small amplitude of heating, temperature field is controlled by a single parameter proportional to the vertical temperature gradient, heated surface size, thermal expansion coefficient, gravitational acceleration and is inversely proportional to viscosity and thermal conductivity.

Work [70] notes that the rotation rate of wind velocity vector during a sea breeze varies within a day. A two-dimensional linear model was applied for the study. The specified velocity is determined by three terms: the Coriolis parameter, the vector product of horizontal mesoscale pressure gradient by the sea breeze velocity and the vector product of horizontal synoptic pressure gradient by the sea breeze velocity.

In [25], the reaction of a stratified atmosphere to periodic heating was considered with the application of linearized equations in the Boussinesq approximation with regard to viscosity and thermal conductivity. The solution structure can be characterized by a single parameter which is proportional to

the heating frequency, the horizontal dimension of the heated surface and inversely proportional to the buoyancy frequency and viscosity coefficient. After perturbation of the basic state, three regimes can be observed: a thermal wave propagating upward (in which no air movement is observed), convection (in which the temperature perturbation is accompanied by air movement in the form of circulation, without vertical propagation) and an internal wave propagating downward.

A significant theoretical achievement in the linear theory of sea breezes became [41]. Unlike [24], viscosity and thermal conductivity were absent there and spatial distribution of heating was specified explicitly. This lowered the equation order for the stream function to the second one and significantly simplified the solution analysis. It was indicated that sea breeze circulation could be considered as an internal inertial-gravity wave of diurnal period generated on the surface by a buoyancy source. Qualitative difference is emphasized between the middle latitudes where this wave is captured near the surface and the tropics where it is radiated upward from the coastline. In the tropics, there is a time shift of 12 hours between circulation and heating. In the middle latitudes, under effect of the Coriolis force, this is not observed. The dissipation inclusion in the form of Rayleigh friction reduces the differences in the breeze structure in the tropics and middle latitudes. The effect of buoyancy and Coriolis force on the sea breeze circulation intensity was analyzed using Bjerknes circulation theorem. It is indicated that the circulation is predominantly affected by the Coriolis force, rather than the buoyancy force.

In [42], the horizontal scale of a sea breeze circulation cell is considered under the linear theory taking into account turbulent mixing with constant viscosity and thermal conductivity coefficients. The resulting horizontal scale of a sea breeze cell is a function of latitude and is proportional to the ratio of buoyancy frequency to the diurnal frequency and the vertical scale determined by thermal conductivity. The function describing the dependence on latitude takes a constant value for latitudes less than 30 degrees and decreases on drawing near the poles. In addition, it was found that the velocity component perpendicular to the shore decreased with distance from it as the Coriolis parameter increases.

In [27], based on the ideas from [41], it is shown that rotation and friction affect the sea breeze intensity, but they are not important at the initial stage of development. The authors analyzed transient processes at the initial stage of sea breeze development in the morning hours with sudden and gradual heating activation. Complete diurnal cycle was also analyzed. The characteristic sea breeze time scale is a combination of the inertial period and the attenuation time due to friction. For the time exceeding this scale, the distance over which the sea breeze propagates is limited by the Rossby radius of deformation with regard to friction. At the equator, friction is the limiting parameter for the intensity and propagation range.

A series of studies devoted to the effect of a uniform background synoptic wind on sea breeze circulation within the framework of the linear theory was resumed with the appearance of [71] which did not take into account the Coriolis force effect, i.e. considered the sea breeze at the equator. The main physical result is that the sets of

internal gravity waves emitted from the surface from the coastline are subject to a Doppler shift, which manifests itself in the asymmetry of the waves relative to the coastline and wave dispersion on the leeward side. In addition to this effect, another additional feature arises – a set of stationary internal waves above the coastline similar to internal gravity waves arising when a stratified uniform wind flows around mountainous terrain. The solution corresponding to the stationary set becomes predominant with an increase in the background wind speed.

Further, in [7, 72], the Coriolis force effect was already taken into account, i.e. the problem of synoptic wind effect on the sea breeze in the middle latitudes was considered. It is shown that here, as well as at the equator, a set of stationary internal waves arises.

The wind profile is rarely vertically uniform in real synoptic situations. As a rule, a vertical wind speed shift takes place. In [73], the effect of thermal wind directed along the coastline on the sea breeze was considered. It is indicated that the sea breeze circulation cell becomes asymmetrical relative to the coastline leaning towards the sea.

It is known that the presence of a vertical velocity shift in a stratified fluid leads to the formation of critical levels at certain heights where the frequency of the internal inertial-gravity wave becomes zero considering the Doppler shift [74–77]. The problem of the effect of shore-perpendicular background wind shift on the sea breeze circulation at the equator has been considered relatively recently [48]. The main result is that critical layers are formed at certain heights absorbing internal waves and thus limiting the height of the sea breeze circulation ray propagating along the flow.

Recent paper [78] reveals that in the tropics, the sea breeze inertial-gravity wave of the diurnal period passes two critical levels and the attenuation region located between them. In the middle latitudes, the sea breeze inertial-gravity wave in the atmosphere without background wind attenuates with height. Therefore, the critical level effect will be observed under the following condition: the critical level height is less than the sea breeze circulation height. Based on a comparison of vertical flux of angular momentum at different latitudes, it is found that its greatest attenuation at the critical level occurs at the 15th degree, the least one – at the 45th.

Two-dimensional numerical models of sea breeze circulation

Application of linear models has significantly expanded the understanding of sea breeze circulation at a qualitative level. However, linear theory cannot provide a description of areas in the structure of sea breeze circulation with intense vertical and horizontal movements.

The first nonlinear numerical models of sea breeze circulation appeared with the advent of the first computers [19, 28, 47, 79]. With a straight coast, the problem of sea breeze circulation is essentially two-dimensional – all components of the velocity, temperature and pressure distribution do not depend on the coordinate directed along the coast. Thus, the formulation of the problem consists of solving hydrodynamics equations taking into account the Coriolis force in a vertical plane

perpendicular to the coastline. In terms of calculations, two-dimensional models use significantly fewer computer resources than three-dimensional ones.

The first stages included the solution of the motion equations of incompressible fluid in the Boussinesq and hydrostatic approximations due to the lack of computing resources. The need to use the hydrostatic approximation and the limits of its applicability were assessed in detail in later works: in [80], the size of the heating source for which the hydrostatic approximation would be valid was discussed; the results of [81] revealed that for intense sea breezes, the non-hydrostatic approximation yielded a weaker sea breeze compared to the calculation using the hydrostatic approximation. For weak sea breezes, the differences between two approximations are small.

Over time, as the power of computers increased, approximations were gradually abandoned. In particular, a non-hydrostatic system of motion equations was applied for the simulation of sea breeze gravity currents taking into account compressibility in the so-called inelastic form and complete consideration of compressibility took place.

Initially, the breeze structure was considered in its simplest formulation without taking into account external factors. Then the influence of individual factors and their various combinations was added to the consideration. The task was to determine at what combination of factors certain features of sea breeze circulation can arise.

Below is an overview of two-dimensional numerical models of sea breeze circulation. First, the features of the numerical models are considered and then the main physical results obtained with their help are discussed.

One of the earliest works on numerical simulation [47] considered a two-dimensional numerical model of a sea breeze in a vertical plane perpendicular to the coastline. The velocity field was decomposed into divergent and rotational components. The rotational component was determined from a numerical solution of the vorticity equation by the finite-difference method.

In the next paper [79], a numerical model of the sea breeze was constructed using the hydrostatic approximation. The turbulent viscosity and thermal conductivity coefficients were functions of height. The temperature above the land surface with a diurnal variation was specified as the boundary conditions on the surface. The temperature above the sea surface did not change. The vorticity equation and the heat transfer equation were solved numerically.

In [28, 19], a numerical model in primitive equations was used. For turbulent viscosity and thermal conductivity, parameterizations were used to describe the atmospheric boundary layer. In [19], the influence of synoptic wind on sea breeze circulation was studied.

The ready-made models and their modifications were successfully used in a number of subsequent works: for example, a model was constructed in [82] based on the model from [28, 19]; a two-dimensional mesoscale model from [83] was used in [84].

In [17], a system of equations taking into account the Coriolis force and ignoring viscosity and friction as well as the hydrostatic approximation was used for the calculation. An arbitrary heat flux was specified as the boundary conditions on the surface.

In the nonlinear part of [24], a system of equations in the Boussinesq approximation was used taking into account rotation, viscosity and thermal conductivity. Atmospheric stratification was also taken into account. A boundary condition for the surface temperature was used to create initial disturbance.

Paper [29] is devoted to studying the differences between daytime and nighttime breezes, so special attention was paid to the turbulence parameterization in the day and night atmospheric boundary layer over land.

In [1, 23], a two-dimensional version of a three-dimensional model [85] developed for describing atmospheric processes of various scales was used to study the sea breeze. Horizontal viscosity was described by harmonic and biharmonic operators. A boundary layer, in which the coefficients of vertical viscosity and thermal conductivity were functions of the local Richardson number, was especially distinguished.

In [86], a hydrostatic model [17] was used. The heat flux was specified on the surface and varied linearly with the height in the boundary layer. This height was determined by the buoyancy value on the surface.

In [87], the equations are written taking into account the geostrophic constant wind in the hydrostatic approximation. Prognostic equations for potential temperature, specific humidity and turbulent kinetic energy were used. The potential temperature profile for the standard atmosphere (3.3 K/km) was used to initialize the model; the relative humidity was 40% and remained constant vertically. The sea surface temperature did not change and the soil temperature and humidity were calculated using the energy budget.

In the non-hydrostatic model in [88], the equations are written taking into account the Earth's rotation and turbulent mixing. The potential temperature on the sea surface was assumed to be constant and the temperature on the land surface varied with time proportionally to the sine.

In the theoretical part of [21], a two-dimensional version of the three-dimensional model was used. The model included primitive equations in the approximations of hydrostatics and incompressibility. Separation by spatial scales into mesoscale and synoptic processes was implemented. The short-wave and long-wave radiation transfer equations were solved, the energy budget on the surface was calculated, a multilayer soil model was included and a level 2.5 scheme was used to parameterize turbulence.

In [4], a two-dimensional hydrostatic model was used. The pressure was divided into two parts – a large-scale part and a part created by differential heating. The vertical component of the velocity was calculated from the continuity equation. A non-local diffusion scheme was used to parameterize the turbulent heat flux, and a local scheme with calculation of the turbulent viscosity coefficient was used to describe the turbulent momentum fluxes.

In [63], a two-dimensional model was used for a real geographic region since the coastline on the west coast of the Netherlands is almost straight. Real wind and temperature profiles obtained from observations were used to set the initial state of the atmosphere in the simulation.

In [26, 89], a mesoscale model of topographic vorticity was used. The predictive variables of the model include potential temperature, turbulent kinetic energy, and two horizontal components of vorticity. A dry (unsaturated) atmosphere was considered, a constant geostrophic wind was specified and the soil was described by a separate model. Filtering of high-frequency processes was carried out using a scheme with numerical viscosity. Non-hydrostatic and inelastic approximations were used and a closure scheme of order 1.5 was used to describe turbulent mixing.

Recently, two-dimensional idealized versions of full three-dimensional models with descriptions of all physical processes have been increasingly used. For example, a two-dimensional version of the mesoscale atmospheric model [90] was used in [18] for studying sea breeze gravity currents and in [7, 48] devoted to the linear theory taking into account the background wind.

Summarizing the review of two-dimensional numerical models of sea breeze circulation, note that the differences in the models consisted both in the approximations of the hydrodynamic equations used and in the methods of physical processes parameterization including turbulence in the boundary layer, radiation transfer, microphysics of clouds and precipitation and processes in the soil.

Now let us move on to the consideration of the main physical results obtained using two-dimensional numerical models of breeze circulation.

Work [47] resulted in a sea breeze gravity current near the surface which corresponded to the rotational part of the solution. The vorticity is formed in the area of the horizontal temperature gradient, which occupies ~100 km. The maximum vorticity is located in the area of the maximum horizontal temperature gradient near the coast. The velocity in the sea breeze gravity current is 2.8 m/s, which corresponds to the actually observed sea breeze.

In [79], the time-dependence of the sea breeze structure was described. The time, distance and height, the maximum values of velocity were observed at, were determined. Presence of a returned current, temperature gradient transfer and, as a consequence, the maximum velocity onto the land were noted. The obtained structure was compared with the observational data. The maximum values of velocity in the model were lower than the observed ones which could be associated with the background wind that existed during the observations and was not taken into account in the model.

Works [28, 19] consider the breeze circulation structure at different values of velocity, background wind direction and stratification profiles. It is noted that the most intense breeze is observed in cases without background wind, with wind from the coast and wind parallel to the coast with a low-pressure area over the sea. The background wind affects the propagation of the breeze onto the land: with wind from the coast, the breeze spreads less inland compared to the case without wind. In

all experiments, a decrease in temperature over the sea far from the coast is observed.

In [82], the first numerical simulation of the full diurnal cycle of sea breeze circulation was carried out, both daytime and nighttime breezes were considered. During the development of the daytime breeze, a current front was observed, near which an intensive vertical movement (~ 0.1 m/s) took place at a height of 600–850 m. A clockwise turn of the wind was observed during the day. A nighttime breeze was obtained – the spread of cold air from the land leading to the rise of warm air over the sea. A temperature inversion was observed over the land at night.

Important paper [17] shows that the velocity of the sea breeze gravity current front depends only on the total amount of heat supplied to the convective boundary layer over land and does not depend on the heat profile shape in the heated layer. In fact, the front velocity is determined by the integral height-wise buoyancy deficit at the head of the gravity current which is consistent with the general theory of gravity currents. It is also shown that the Coriolis force leads to a decrease in the velocity of front propagation and an increase in the alongshore velocity component.

According to [24], the total heat flux determines the kinetic energy of the sea breeze circulation cell. The cell asymmetry is also shown, namely: the upper return branch of the circulation is thicker than the lower one and the velocities in the return branch are lower than near the surface.

The most important result was the explanation of the causes of the asymmetry between the daytime and nighttime breezes [29]. Even with the same absolute values of heat fluxes on the surface during the day and night, the asymmetry between the daytime and nighttime breezes is due to the difference in stratification and the intensity of turbulent mixing over land.

Study [23] demonstrates the dependence of sea breeze circulation on latitude emphasizing the influence of the Coriolis force. In particular, at the equator, the daytime breeze (directed from the sea onto the land) is observed throughout the day, while at other latitudes a nighttime breeze is also formed. The breeze of maximum intensity is observed at different times of the day depending on the latitude – the closer to the equator, the later the maximum of the nighttime breeze is reached.

An important question addressed in [86] is what fraction of the potential energy generated by daytime heating is converted into kinetic energy of sea breeze circulation. As convective mixing increases, less potential energy can be available for convective scale and the potential energy available for breeze circulation increases.

In [84], the dependence of breeze circulation over a small lake on synoptic wind speed and water temperature is considered. The effect of water temperature is not important for narrow, elongated water bodies with a weak synoptic wind since the cooling of the stably stratified surface layer is insignificant compared to the air heating above the land surface. However, the apparent heat flux from the water surface increases with a strong synoptic wind, thus leading to sea breeze intensification. A sufficiently strong synoptic wind carries the entire breeze cell downstream.

The influence of background wind on breeze is studied in [87]. Particle trajectories are used as a diagnostic tool which can be used to draw conclusions about the sea breeze intensity. The sea breeze is most intense at a headwind speed of 5 m/s which coincides with the sea breeze propagation velocity while the circulation remains stationary relative to the shore. A stronger wind carries away the circulation towards the sea.

In [88], the breeze dependence on two dimensionless parameters characterizing the nonlinearity and hydrostaticity degree is considered. When using the linear model, the results coincide with the results of the linear theory: the maximum breeze velocity is observed near the shore and the breeze is almost symmetrical relative to it. When using the nonlinear model, a breeze front takes place, the maximum breeze is observed over land, the maximum horizontal velocity increases proportionally to the square of the nonlinearity parameter. The difference between the hydrostatic and non-hydrostatic cases is small in most experiments. Sea breeze circulation and vertical air lift are more intense in the non-hydrostatic case compared to the hydrostatic one.

Work [21] shows that if sea breeze and background wind directions coincide, the breeze is a weak disturbance for the background flow. At moderate values of the background headwind, the breeze is most intense. At even greater values of this wind, the breeze cell is carried away towards the sea and becomes weaker than in the case without background wind.

The vertical structure of the sea breeze on the coast of the Netherlands was considered in [4]. Three cases with a sea breeze were analyzed. The mass flux in the returned branch of the current depends on the large-scale flux and on the potential temperature gradients in the boundary layer and above the inversion. In this case, it is greater than in the lower branch when the vertical gradient of the potential temperature above the boundary layer is greater than the initial vertical gradient of the potential temperature above the inversion.

In [63] motivated by observations of the deep inland penetration of sea breezes in the Netherlands (up to 100 km from the coast), the most important factors influencing the penetration of sea breezes onto the land are identified based on the results of numerical simulation: the background counter synoptic wind and the heat flux on the surface. The values of these quantities determine the temporal and spatial scales of the sea breeze propagation onto the land.

In [26], the results of two-dimensional numerical simulation were used to verify the similarity theory previously constructed on the basis of *in situ* measurements [91]. The analysis showed that the sea breeze velocity depended only on the total heat flux on the surface and its height depended on the atmosphere stratification.

In [89], based on the results of two-dimensional numerical simulation, the similarity theory from [26] was generalized and a dimensionless index that characterizes the sea breeze propagation onto the land in the presence of a headwind in the atmosphere was introduced. The analysis showed that, depending on the background wind speed, two regimes were observed: the sea breeze propagation onto the land and its velocity decrease without such propagation.

Paper [18] is devoted to the study of the influence of stratification and the effect of different types of heating on the gravity current. If the full amount of heat enters the region at the initial moment of time, the gravity current reaches quickly the regime with a constant propagation velocity which is determined by the density gradient at the current front and the current height. The dependence of the front propagation velocity on the total amount of heat turns out to be valid for a wide range of atmospheric stability values. If a more realistic heating depending on time is considered, then a density and vorticity gradient is formed inside the cold current which leads to intensification of the internal circulation, weakening of the density gradient at the front and, as a result, to its slowdown.

To summarize the review of physical results obtained using two-dimensional nonlinear models, it can be concluded that the structure and dynamics of the sea breeze have been described and interpreted using these models which is confirmed by numerous observations.

Conclusions

The paper examines the principal features of sea breeze circulation obtained using linear theory and two-dimensional numerical simulation. Of the variety of factors affecting sea breeze circulation, only a few are considered. They are heating intensity, atmospheric stratification, synoptic wind and the Coriolis force

Sea breeze circulation can be considered under the linear theory as an internal inertial-gravity wave of the diurnal period radiated from the surface as a result of daytime heating and nighttime cooling of the atmospheric boundary layer over the land. The Coriolis force effect leads to the identification of two sea breeze circulation regimes. The circulation has the form of a wave propagating upward and from the coast in the latitude range from the equator to the 30th degree and it has the form of a cell limited in height and horizontally in the latitude range from the 30th degree to the pole.

When taking into account the uniform background wind at all latitudes, the breeze wave becomes asymmetrical relative to the coastline and a set of stationary high-frequency internal waves appears above the coastline. The presence of a background wind shift leads to the formation of critical levels that limit the height of sea breeze circulation.

Linear theory is applicable only for small values of heating amplitude as a nonlinear phenomenon, gravity current, is formed in the breeze structure when the amplitude increases. Two-dimensional simulation is used for theoretical description of sea breeze in nonlinear mode. It is shown that the presence of uniform background wind leads to a change in the height of the gravity current head which affects its propagation velocity.

Wind with shift changes the height of the current head and leads to the formation of an intense vertical elevation in front of the front when the angle of the gravity current front to the horizontal changes. Both uniform wind and wind with shift can prevent the current propagation and, conversely, increase its velocity.

Taking into account the nonlinearity, the Coriolis force effect leads to a decrease in the front propagation velocity and an increase in the alongshore velocity component.

The present paper summarizes the available results obtained using several theoretical research methods that describe the influence of selected environmental factors on the dynamics of sea breeze circulation formation and development, while this summary cannot provide a complete description of the phenomenon.

The reviewed works demonstrate consistent development of the breeze circulation theory, however, recent studies devoted, for example, to the linear theory, show that still there are some unresolved issues.

REFERENCES

- 1 Anthes, R.A., 1978. *The Height of the Planetary Boundary Layer and the Production of Circulation in a Sea Breeze Model. Journal of the Atmospheric Sciences*, 35(7), pp. 1231-1239. [https://doi.org/10.1175/1520-0469\(1978\)035<1231:THOTPB>2.0.CO;2](https://doi.org/10.1175/1520-0469(1978)035<1231:THOTPB>2.0.CO;2)
- 2 Feliks, Y., 1994. An Analytical Model of the Diurnal Oscillation of the Inversion Base Due to the Sea Breeze. *Journal of the Atmospheric Sciences*, 51(7), pp. 991-998. [https://doi.org/10.1175/1520-0469\(1994\)051<0991:AAMOTD>2.0.CO;2](https://doi.org/10.1175/1520-0469(1994)051<0991:AAMOTD>2.0.CO;2)
- 3 Jin, Y., Koch, S.E., Lin, Y.-L., Ralph, F.M. and Chen, C., 1996. Numerical Simulations of an Observed Gravity Current and Gravity Waves in an Environment Characterized by Complex Stratification and Shear. *Journal of the Atmospheric Sciences*, 53(23), pp. 3570-3588. [https://doi.org/10.1175/1520-0469\(1996\)053<3570:NSOAG>2.0.CO;2](https://doi.org/10.1175/1520-0469(1996)053<3570:NSOAG>2.0.CO;2)
- 4 Tijn, A.B.C., Holtslag, A.A.M. and van Delden, A.J., 1999. Observations and Modeling of the Sea Breeze with the Return Current. *Monthly Weather Review*, 127(5), pp. 625-640. [https://doi.org/10.1175/1520-0493\(1999\)127<0625:OAMOTS>2.0.CO;2](https://doi.org/10.1175/1520-0493(1999)127<0625:OAMOTS>2.0.CO;2)
- 5 Yan, H. and Anthes, R.A., 1988. The Effect of Variations in Surface Moisture on Mesoscale Circulation. *Monthly Weather Review*, 116(1), pp. 192-208. [https://doi.org/10.1175/1520-0493\(1988\)116<0192:TEOVIS>2.0.CO;2](https://doi.org/10.1175/1520-0493(1988)116<0192:TEOVIS>2.0.CO;2)
- 6 Bryan, G.H. and Rotunno, R., 2014. The Optimal State for Gravity Currents in Shear. *Journal of the Atmospheric Sciences*, 71(1), pp. 448-468. <https://doi.org/10.1175/JAS-D-13-0156.1>
- 7 Du, Y. and Rotunno, R., 2018. Diurnal Cycle of Rainfall and Winds near the South Coast of China. *Journal of the Atmospheric Sciences*, 75(6), pp. 2065-2082. <https://doi.org/10.1175/JAS-D-17-0397.1>
- 8 Franchito, S.H., Rao, V.B., Stech, J.L. and Lorenzetti, J.A., 1998. The Effect of Coastal Upwelling on the Sea-Breeze Circulation at Cabo Frio, Brazil: A Numerical Experiment. *Annales Geophysicae*, 16, pp. 866-881. <https://doi.org/10.1007/s00585-998-0866-3>
- 9 Dailey, P.S. and Fovell, R.G., 1999. Numerical Simulation of the Interaction between the Sea-Breeze Front and Horizontal Convective Rolls. Part I: Offshore Ambient Flow. *Monthly Weather Review*, 127(5), pp. 858-878. [https://doi.org/10.1175/1520-0493\(1999\)127<0858:NSOTIB>2.0.CO;2](https://doi.org/10.1175/1520-0493(1999)127<0858:NSOTIB>2.0.CO;2)
- 10 Gilliam, R.C., Raman, S. and Niyogi, D.D.S., 2004. Observational and Numerical Study on the Influence of Large-Scale Flow Direction and Coastline Shape on Sea-Breeze Evolution. *Boundary-Layer Meteorology*, 111, pp. 275-300. <https://doi.org/10.1023/B:BOUN.0000016494.99539.5a>
- 11 Chen, X., Zhang, F. and Zhao, K., 2016. Diurnal Variations of the Land-Sea Breeze and Its Related Precipitation over South China. *Journal of the Atmospheric Sciences*, 73(12), pp. 4793-4815. <https://doi.org/10.1175/JAS-D-16-0106.1>
- 12 Clappier, A., Martilli, A., Grossi, P., Thunis, P., Pasi, F., Krueger, B.C., Calpini, B., Graziani, G. and van den Bergh, H., 2000. Effect of Sea Breeze on Air Pollution in the Greater Athens

- Area. Part I: Numerical Simulations and Field Observations. *Journal of Applied Meteorology and Climatology*, 39(4), pp. 546-562. [https://doi.org/10.1175/1520-0450\(2000\)039<0546:EOSBOA>2.0.CO;2](https://doi.org/10.1175/1520-0450(2000)039<0546:EOSBOA>2.0.CO;2)
- 13 Bastin, S., Drobinski, P., Dabas, A., Delville, P., Reitebuch, O. and Werner, C., 2005. Impact of the Rhône and Durance Valleys on Sea-Breeze Circulation in the Marseille Area. *Atmospheric Research*, 74(1-4), pp. 303-328. <https://doi.org/10.1016/j.atmosres.2004.04.014>
 - 14 Soler, M.R., Arasa, R., Merino, M., Olid, M. and Ortega, S., 2011. Modelling Local Sea-Breeze Flow and Associated Dispersion Patterns over a Coastal Area in North-East Spain: A Case Study. *Boundary-Layer Meteorology*, 140, pp. 37-56. <https://doi.org/10.1007/s10546-011-9599-z>
 - 15 Miller, S.T.K., Keim, B.D., Talbot, R.W. and Mao, H., 2003. Sea Breeze: Structure, Forecasting, and Impacts. *Reviews of Geophysics*, 41(3), 1011. <https://doi.org/10.1029/2003RG000124>
 - 16 Crosman, E.T. and Horel, J.D., 2010. Sea and Lake Breezes: A Review of Numerical Studies. *Boundary-Layer Meteorology*, 137, pp. 1-29. <https://doi.org/10.1007/s10546-010-9517-9>
 - 17 Pearson, R.A., 1973. Properties of the Sea Breeze Front as Shown by a Numerical Model. *Journal of Atmospheric Sciences*, 30(6), pp. 1050-1060. [https://doi.org/10.1175/1520-0469\(1973\)030<1050:POTSBF>2.0.CO;2](https://doi.org/10.1175/1520-0469(1973)030<1050:POTSBF>2.0.CO;2)
 - 18 Robinson, F.J., Patterson, M.D. and Sherwood, S.C., 2013. A Numerical Modeling Study of the Propagation of Idealized Sea-Breeze Density Currents. *Journal of the Atmospheric Sciences*, 70(2), pp. 653-668. <https://doi.org/10.1175/JAS-D-12-0113.1>
 - 19 Estoque, M.A., 1962. The Sea Breeze as a Function of the Prevailing Synoptic Situation. *Journal of Atmospheric Sciences*, 19(3), pp. 244-250. [https://doi.org/10.1175/1520-0469\(1962\)019<0244:TSBAAF>2.0.CO;2](https://doi.org/10.1175/1520-0469(1962)019<0244:TSBAAF>2.0.CO;2)
 - 20 Liu, C. and Moncrieff, M.W., 1996. A Numerical Study of the Effects of Ambient Flow and Shear on Density Currents. *Monthly Weather Review*, 124(10), pp. 2282-2303. [https://doi.org/10.1175/1520-0493\(1996\)124<2282:ANSOTE>2.0.CO;2](https://doi.org/10.1175/1520-0493(1996)124<2282:ANSOTE>2.0.CO;2)
 - 21 Arritt, R.W., 1993. Effects of the Large-Scale Flow on Characteristic Features of the Sea Breeze. *Journal of Applied Meteorology and Climatology*, 32(1), pp. 116-125. [https://doi.org/10.1175/1520-0450\(1993\)032<0116:EOTLSF>2.0.CO;2](https://doi.org/10.1175/1520-0450(1993)032<0116:EOTLSF>2.0.CO;2)
 - 22 Haurwitz, B., 1947. Comments on the Sea-Breeze Circulation. *Journal of Atmospheric Sciences*, 4(1), pp. 1-8. [https://doi.org/10.1175/1520-0469\(1947\)004<0001:COTSBC>2.0.CO;2](https://doi.org/10.1175/1520-0469(1947)004<0001:COTSBC>2.0.CO;2)
 - 23 Yan, H. and Anthes, R.A., 1987. The Effect of Latitude on the Sea Breeze. *Monthly Weather Review*, 115(5), pp. 936-956. [https://doi.org/10.1175/1520-0493\(1987\)115<0936:TEOLOT>2.0.CO;2](https://doi.org/10.1175/1520-0493(1987)115<0936:TEOLOT>2.0.CO;2)
 - 24 Walsh, J.E., 1974. Sea Breeze Theory and Applications. *Journal of Atmospheric Sciences*, 31(8), pp. 2012-2026. [https://doi.org/10.1175/1520-0469\(1974\)031<2012:SBTAA>2.0.CO;2](https://doi.org/10.1175/1520-0469(1974)031<2012:SBTAA>2.0.CO;2)
 - 25 Kimura, R. and Eguchi, T., 1978. On Dynamical Processes of Sea- and Land-Breeze Circulation. *Journal of the Meteorological Society of Japan. Ser. II*, 56(2), pp. 67-85. https://doi.org/10.2151/jmsj1965.56.2_67
 - 26 Porson, A., Steyn, D.G. and Schayes, G., 2007. Sea-Breeze Scaling from Numerical Model Simulations, Part I: Pure Sea Breezes. *Boundary-Layer Meteorology*, 122, pp. 17-29. <https://doi.org/10.1007/s10546-006-9090-4>
 - 27 Dalu, G.A. and Pielke, R.A., 1989. An Analytical Study of the Sea Breeze. *Journal of the Atmospheric Sciences*, 46(12), pp. 1815-1825. [https://doi.org/10.1175/1520-0469\(1989\)046<1815:AASOTS>2.0.CO;2](https://doi.org/10.1175/1520-0469(1989)046<1815:AASOTS>2.0.CO;2)

- 28 Estoque, M.A., 1961. A Theoretical Investigation of the Sea Breeze. *Quarterly Journal of the Royal Meteorological Society*, 87(372), pp. 136-146. <https://doi.org/10.1002/qj.49708737203>
- 29 Mak, M.K. and Walsh, J.E., 1976. On the Relative Intensities of Sea and Land Breezes. *Journal of the Atmospheric Sciences*, 33(2), pp. 242-251. [https://doi.org/10.1175/1520-0469\(1976\)033<0242:OTRIOS>2.0.CO;2](https://doi.org/10.1175/1520-0469(1976)033<0242:OTRIOS>2.0.CO;2)
- 30 Mahrer, Y. and Pielke, R.A., 1977. The Effects of Topography on Sea and Land Breezes in a Two-Dimensional Numerical Model. *Monthly Weather Review*, 105(9), pp. 1151-1162. [https://doi.org/10.1175/1520-0493\(1977\)105<1151:TEOTOS>2.0.CO;2](https://doi.org/10.1175/1520-0493(1977)105<1151:TEOTOS>2.0.CO;2)
- 31 Kikuchi, Y., Arakawa, S., Kimur, F., Sharasaki, K. and Nagano Y., 1981. Numerical Study on the Effects of Mountains on the Land and Sea Breeze Circulation in the Kanto District. *Journal of the Meteorological Society of Japan. Ser. II*, 59(5), pp. 723-738. https://doi.org/10.2151/jmsj1965.59.5_723
- 32 McPherson, R.D., 1970. A Numerical Study of the Effect of a Coastal Irregularity on the Sea Breeze. *Journal of Applied Meteorology and Climatology*, 9(5), pp. 767-777. [https://doi.org/10.1175/1520-0450\(1970\)009<0767:ANSOTE>2.0.CO;2](https://doi.org/10.1175/1520-0450(1970)009<0767:ANSOTE>2.0.CO;2)
- 33 Neumann, J. and Mahrer, Y., 1975. A Theoretical Study of the Lake and Land Breezes of Circular Lakes. *Monthly Weather Review*, 103(6), pp. 474-485. [https://doi.org/10.1175/1520-0493\(1975\)103<0474:ATSOTL>2.0.CO;2](https://doi.org/10.1175/1520-0493(1975)103<0474:ATSOTL>2.0.CO;2)
- 34 Gille, S.T. and Llewellyn Smith, S.G., 2014. When Land Breezes Collide: Converging Diurnal Winds over Small Bodies of Water. *Quarterly Journal of the Royal Meteorological Society*, 140(685), pp. 2573-2581. <https://doi.org/10.1002/qj.2322>
- 35 Neumann, J. and Mahrer, Y., 1974. A Theoretical Study of the Sea and Land Breezes of Circular Islands. *Journal of the Atmospheric Sciences*, 31(8), pp. 2027-2039. [https://doi.org/10.1175/1520-0469\(1974\)031<2027:ATSOTS>2.0.CO;2](https://doi.org/10.1175/1520-0469(1974)031<2027:ATSOTS>2.0.CO;2)
- 36 Xian, Z. and Pielke, R.A., 1991. The Effects of Width of Landmasses on the Development of Sea Breezes. *Journal of Applied Meteorology*, 30(9), pp. 1280-1304. [https://doi.org/10.1175/1520-0450\(1991\)030<1280:TEOWOL>2.0.CO;2](https://doi.org/10.1175/1520-0450(1991)030<1280:TEOWOL>2.0.CO;2)
- 37 Drobinski, P. and Dubos, T., 2009. Linear Breeze Scaling: From Large-Scale Land/Sea Breezes to Mesoscale Inland Breezes. *Quarterly Journal of the Royal Meteorological Society*, 135(644), pp. 1766-1775. <https://doi.org/10.1002/qj.496>
- 38 Baker, R.D., Lynn, B.H., Boone, A., Tao, W.-K. and Simpson, J., 2001. The Influence of Soil Moisture, Coastline Curvature, and Land-Breeze Circulations on Sea-Breeze-Initiated Precipitation. *Journal of Hydrometeorology*, 2(2), pp. 193-211. [https://doi.org/10.1175/1525-7541\(2001\)002<0193:TIOSMC>2.0.CO;2](https://doi.org/10.1175/1525-7541(2001)002<0193:TIOSMC>2.0.CO;2)
- 39 Avissar, R. Moran, M.D., Wu, G., Meroney, R.N. and Pielke, R.A., 1990. Operating Ranges of Mesoscale Numerical Models and Meteorological Wind Tunnels for the Simulation of Sea and Land Breezes. *Boundary-Layer Meteorology*, 50(1), pp. 227-275. <https://doi.org/10.1007/BF00120526>
- 40 Abbs, D.J. and Physick, W.L., 1992. Sea-Breeze Observations and Modelling: A Review. *Australian Meteorological Magazine*, 41, pp. 7-19.
- 41 Rotunno, R., 1983. On the Linear Theory of the Land and Sea Breeze. *Journal of the Atmospheric Sciences*, 40(8), pp. 1999-2009. [https://doi.org/10.1175/1520-0469\(1983\)040<1999:OTLTOT>2.0.CO;2](https://doi.org/10.1175/1520-0469(1983)040<1999:OTLTOT>2.0.CO;2)
- 42 Niino, H., 1987. The Linear Theory of Land and Sea Breeze Circulation. *Journal of the Meteorological Society of Japan. Ser. II*, 65(6), pp. 901-921. https://doi.org/10.2151/jmsj1965.65.6_901
- 43 Benjamin, T.B., 1968. Gravity Currents and Related Phenomena. *Journal of Fluid Mechanics*, 31(2), pp. 209-248. <https://doi.org/10.1017/S0022112068000133>

- 44 Xu, Q., 1992. Density Currents in Shear Flows – A Two-Fluid Model. *Journal of the Atmospheric Sciences*, 49(6), pp. 511-524. [https://doi.org/10.1175/1520-0469\(1992\)049<0511:DCISFA>2.0.CO;2](https://doi.org/10.1175/1520-0469(1992)049<0511:DCISFA>2.0.CO;2)
- 45 Biggs, W.G. and Graves, M.E., 1962. A Lake Breeze Index. *Journal of Applied Meteorology and Climatology*, 1(4), pp. 474-480. [https://doi.org/10.1175/1520-0450\(1962\)001<0474:ALBI>2.0.CO;2](https://doi.org/10.1175/1520-0450(1962)001<0474:ALBI>2.0.CO;2)
- 46 Antonelli, M. and Rotunno, R., 2007. Large-Eddy Simulation of the Onset of the Sea Breeze. *Journal of the Atmospheric Sciences*, 64(12), pp. 4445-4457. <https://doi.org/10.1175/2007JAS2261.1>
- 47 Pearce, R.P., 1955. The Calculation of a Sea-Breeze Circulation in Terms of the Differential Heating across the Coastline. *Quarterly Journal of the Royal Meteorological Society*, 81(349), pp. 351-381. <https://doi.org/10.1002/qj.49708134906>
- 48 Du, Y., Rotunno, R. and Zhang, F., 2019. Impact of Vertical Wind Shear on Gravity Wave Propagation in the Land-Sea-Breeze Circulation at the Equator. *Journal of the Atmospheric Sciences*, 76(10), pp. 3247-3265. <https://doi.org/10.1175/JAS-D-19-0069.1>
- 49 Pielke, R.A., 1974. A Three-Dimensional Numerical Model of the Sea Breezes over South Florida. *Monthly Weather Review*, 102(2), pp. 115-139. [https://doi.org/10.1175/1520-0493\(1974\)102<0115:ATDNMO>2.0.CO;2](https://doi.org/10.1175/1520-0493(1974)102<0115:ATDNMO>2.0.CO;2)
- 50 Steyn, D.G. and McKendry, I.G., 1988. Quantitative and Qualitative Evaluation of a Three-Dimensional Mesoscale Numerical Model Simulation of a Sea Breeze in Complex Terrain. *Monthly Weather Review*, 116(10), pp. 1914-1926. [https://doi.org/10.1175/1520-0493\(1988\)116<1914:QAQEOA>2.0.CO;2](https://doi.org/10.1175/1520-0493(1988)116<1914:QAQEOA>2.0.CO;2)
- 51 Yimin, M. and Lyons, T.J., 2000. Numerical Simulation of a Sea Breeze under Dominant Synoptic Conditions at Perth. *Meteorology and Atmospheric Physics*, 73, pp. 89-103. <https://doi.org/10.1007/s007030050067>
- 52 Zhu, M. and Atkinson, B.W., 2004. Observed and Modelled Climatology of the Land-Sea Breeze Circulation over the Persian Gulf. *International Journal of Climatology*, 24(7), pp. 883-905. <https://doi.org/10.1002/joc.1045>
- 53 Zhang, Y., Chen, Y.-L., Schroeder, T.A. and Kodama, K., 2005. Numerical Simulations of Sea-Breeze Circulations over Northwest Hawaii. *Weather and Forecasting*, 20(6), pp. 827-846. <https://doi.org/10.1175/WAF859.1>
- 54 Challa, V.S., Indracanti, J., Rabarison, M.K., Patrick, C., Baham, J.M., Young, J., Hughes, R., Hardy, M.G., Swanier, S.J. [et al.], 2009. A Simulation Study of Mesoscale Coastal Circulations in Mississippi Gulf Coast. *Atmospheric Research*, 91(1), pp. 9-25. <https://doi.org/10.1016/j.atmosres.2008.05.004>
- 55 Efimov, V.V. and Barabanov, V.S., 2011. Development of the Summer Breeze Circulation in the West Part of the Black Sea. *Physical Oceanography*, 20(5), pp. 335-346. <https://doi.org/10.1007/s11110-011-9089-3>
- 56 Arrillaga, J.A., Yagüe, C., Sastre, M. and Román-Cascón, C., 2016. A Characterization of Sea-Breeze Events in the Eastern Cantabrian Coast (Spain) from Observational Data and WRF Simulations. *Atmospheric Research*, 181, pp. 265-280. <https://doi.org/10.1016/j.atmosres.2016.06.021>
- 57 Mitsumoto, S., Ueda, H. and Ozoe, H., 1983. A Laboratory Experiment on the Dynamics of the Land and Sea Breeze. *Journal of the Atmospheric Sciences*, 40(5), pp. 1228-1240. [https://doi.org/10.1175/1520-0469\(1983\)040<1228:ALEOTD>2.0.CO;2](https://doi.org/10.1175/1520-0469(1983)040<1228:ALEOTD>2.0.CO;2)
- 58 Intrieri, J.M., Little, C.G., Shaw, W.J., Banta, R.M., Durkee, P.A. and Hardesty, R.M., 1990. The Land/Sea Breeze Experiment (LASBEX). *Bulletin of the American Meteorological Society*, 71(5), pp. 656-664. <https://doi.org/10.1175/1520-0477-71.5.656>

- 59 Simpson, J.E. and Britter, R.E., 1980. A Laboratory Model of an Atmospheric Mesofront. *Quarterly Journal of the Royal Meteorological Society*, 106(449), pp. 485-500. <https://doi.org/10.1002/qj.49710644907>
- 60 Rottman, J.W. and Simpson, J.E., 1983. Gravity Currents Produced by Instantaneous Releases of a Heavy Fluid in a Rectangular Channel. *Journal of Fluid Mechanics*, 135, pp. 95-110. <https://doi.org/10.1017/S0022112083002979>
- 61 Shin, J.O., Dalziel, S.B. and Linden, P.F., 2004. Gravity Currents Produced by Lock Exchange. *Journal of Fluid Mechanics*, 521, pp. 1-34. <https://doi.org/10.1017/S002211200400165X>
- 62 Fisher, E.L., 1960. An Observational Study of the Sea Breeze. *Journal of the Atmospheric Sciences*, 17(6), pp. 645-660. [https://doi.org/10.1175/1520-0469\(1960\)017<0645:AOSOTS>2.0.CO;2](https://doi.org/10.1175/1520-0469(1960)017<0645:AOSOTS>2.0.CO;2)
- 63 Tijm, A.B.C., Van Delden, A.J. and Holtslag, A.A.M., 1999. The Inland Penetration of Sea Breezes. *Contributions to Atmospheric Physics*, 72(4), pp. 317-328.
- 64 Wakimoto, R.M. and Atkins, N.T., 1994. Observations of the Sea-Breeze Front during CaPE. Part I: Single-Doppler, Satellite, and Cloud Photogrammetry Analysis. *Monthly Weather Review*, 122(6), pp. 1092-1114. [https://doi.org/10.1175/1520-0493\(1994\)122<1092:OOTSBF>2.0.CO;2](https://doi.org/10.1175/1520-0493(1994)122<1092:OOTSBF>2.0.CO;2)
- 65 Anjos, M. and Lopes, A., 2019. Sea Breeze Front Identification on the Northeastern Coast of Brazil and Its Implications for Meteorological Conditions in the Sergipe Region. *Theoretical and Applied Climatology*, 137, pp. 2151-2165. <https://doi.org/10.1007/s00704-018-2732-x>
- 66 Schmidt, F.H., 1947. An Elementary Theory of the Land- and Sea-Breeze Circulation. *Journal of the Atmospheric Sciences*, 4(1), pp. 9-20. [https://doi.org/10.1175/1520-0469\(1947\)004<0009:AETOTL>2.0.CO;2](https://doi.org/10.1175/1520-0469(1947)004<0009:AETOTL>2.0.CO;2)
- 67 Malkus, J.S. and Stern, M.E., 1953. The Flow of a Stable Atmosphere over a Heated Island, Part 1. *Journal of the Atmospheric Sciences*, 10(1), pp. 30-41. [https://doi.org/10.1175/1520-0469\(1953\)010<0030:TFOASA>2.0.CO;2](https://doi.org/10.1175/1520-0469(1953)010<0030:TFOASA>2.0.CO;2)
- 68 Geisler, J.E. and Bretherton, F.P., 1969. The Sea-Breeze Forerunner. *Journal of the Atmospheric Sciences*, 26(1), pp. 82-95. [https://doi.org/10.1175/1520-0469\(1969\)026<0082:TSBF>2.0.CO;2](https://doi.org/10.1175/1520-0469(1969)026<0082:TSBF>2.0.CO;2)
- 69 Kimura, R., 1975. Dynamics of Steady Convections over Heat and Cool Islands. *Journal of the Meteorological Society of Japan. Ser. II*, 53(6), pp. 440-457. https://doi.org/10.2151/jmsj1965.53.6_440
- 70 Neumann, J., 1977. On the Rotation Rate of the Direction of Sea and Land Breezes. *Journal of the Atmospheric Sciences*, 34(12), pp. 1913-1917. [https://doi.org/10.1175/1520-0469\(1977\)034<1913:OTRROT>2.0.CO;2](https://doi.org/10.1175/1520-0469(1977)034<1913:OTRROT>2.0.CO;2)
- 71 Qian, T., Epifanio, C.C. and Zhang, F., 2009. Linear Theory Calculations for the Sea Breeze in a Background Wind: The Equatorial Case. *Journal of the Atmospheric Sciences*, 66(6), pp. 1749-1763. <https://doi.org/10.1175/2008JAS2851.1>
- 72 Jiang, Q., 2012. On Offshore Propagating Diurnal Waves. *Journal of the Atmospheric Sciences*, 69(5), pp. 1562-1581. <https://doi.org/10.1175/JAS-D-11-0220.1>
- 73 Drobinski, P., Rotunno, R. and Dubos, T., 2011. Linear Theory of the Sea Breeze in a Thermal Wind. *Quarterly Journal of the Royal Meteorological Society*, 137(659), pp. 1602-1609. <https://doi.org/10.1002/qj.847>
- 74 Miles, J.W., 1961. On the Stability of Heterogeneous Shear Flows. *Journal of Fluid Mechanics*, 10(4), pp. 496-508. <https://doi.org/10.1017/S0022112061000305>
- 75 Booker, J.R. and Bretherton, F.P., 1967. The Critical Layer for Internal Gravity Waves in a Shear Flow. *Journal of Fluid Mechanics*, 27(3), pp. 513-539. <https://doi.org/10.1017/S0022112067000515>

- 76 Jones, W.L., 1967. Propagation of Internal Gravity Waves in Fluids with Shear Flow and Rotation. *Journal of Fluid Mechanics*, 30(3), pp. 439-448. <https://doi.org/10.1017/S0022112067001521>
- 77 Grimshaw, R., 1975. Internal Gravity Waves: Critical Layer Absorption in a Rotating Fluid. *Journal of Fluid Mechanics*, 70(2), pp. 287-304. <https://doi.org/10.1017/S0022112075002030>
- 78 Shokurov, M.V. and Kraevskaya, N.Yu., 2022. Critical Levels of the Sea Breeze Circulation within the Framework of Linear Theory. *Physical Oceanography*, 29(6), pp. 602-618. <https://doi.org/10.22449/1573-160X-2022-6-602-618>
- 79 Fisher, E.L., 1961. A Theoretical Study of the Sea Breeze. *Journal of the Atmospheric Sciences*, 18(2), pp. 216-233. [https://doi.org/10.1175/1520-0469\(1961\)018<0216:ATSOTS>2.0.CO;2](https://doi.org/10.1175/1520-0469(1961)018<0216:ATSOTS>2.0.CO;2)
- 80 Martin, C.L. and Pielke, R.A., 1983. The Adequacy of the Hydrostatic Assumption in Sea Breeze Modeling over Flat Terrain. *Journal of the Atmospheric Sciences*, 40(6), pp. 1472-1481. [https://doi.org/10.1175/1520-0469\(1983\)040<1472:TAOTHA>2.0.CO;2](https://doi.org/10.1175/1520-0469(1983)040<1472:TAOTHA>2.0.CO;2)
- 81 Yang, X., 1991. A Study of Nonhydrostatic Effects in Idealized Sea Breeze Systems. *Boundary-Layer Meteorology*, 54, pp. 183-208. <https://doi.org/10.1007/BF00119419>
- 82 Neumann, J. and Mahrer, Y., 1971. A Theoretical Study of the Land and Sea Breeze Circulation. *Journal of the Atmospheric Sciences*, 28(4), pp. 532-542. [https://doi.org/10.1175/1520-0469\(1971\)028<0532:ATSOTL>2.0.CO;2](https://doi.org/10.1175/1520-0469(1971)028<0532:ATSOTL>2.0.CO;2)
- 83 Pielke, R.A., 1974. A Comparison of Three-Dimensional and Two-Dimensional Numerical Predictions of Sea Breezes. *Journal of the Atmospheric Sciences*, 31(6), pp. 1577-1585. [https://doi.org/10.1175/1520-0469\(1974\)031<1577:ACOTDA>2.0.CO;2](https://doi.org/10.1175/1520-0469(1974)031<1577:ACOTDA>2.0.CO;2)
- 84 Segal, M. and Pielke, R.A., 1985. The Effect of Water Temperature and Synoptic Winds on the Development of Surface Flows over Narrow, Elongated Water Bodies. *Journal of Geophysical Research: Oceans*, 90(C3), pp. 4907-4910. <https://doi.org/10.1029/JC090iC03p04907>
- 85 Anthes, R.A. and Warner, T.T., 1978. Development of Hydrodynamic Models Suitable for Air Pollution and Other Mesometeorological Studies. *Monthly Weather Review*, 106(8), pp. 1045-1078. [https://doi.org/10.1175/1520-0493\(1978\)106<1045:DOHMSF>2.0.CO;2](https://doi.org/10.1175/1520-0493(1978)106<1045:DOHMSF>2.0.CO;2)
- 86 Richiardone, R. and Pearson, R.A., 1983. Inland Convection and Energy Transfers in a Sea Breeze Model. *Quarterly Journal of the Royal Meteorological Society*, 109(460), pp. 325-338. <https://doi.org/10.1002/qj.49710946006>
- 87 Bechtold, P., Pinty, J.-P. and Mascart, F., 1991. A Numerical Investigation of the Influence of Large-Scale Winds on Sea-Breeze- and Inland-Breeze-Type Circulations. *Journal of Applied Meteorology and Climatology*, 30(9), pp. 1268-1279. [https://doi.org/10.1175/1520-0450\(1991\)030<1268:ANIOTI>2.0.CO;2](https://doi.org/10.1175/1520-0450(1991)030<1268:ANIOTI>2.0.CO;2)
- 88 Ookouchi, Y., 1992. On the Parameter Dependence of Two-Dimensional Sea-Breeze Models. *Journal of the Meteorological Society of Japan. Ser. II*, 70(2), pp. 689-701. https://doi.org/10.2151/jmsj1965.70.2_689
- 89 Porson, A., Steyn, D.G. and Schayes, G.S., 2007. Formulation of an Index for Sea Breezes in Opposing Winds. *Journal of Applied Meteorology and Climatology*, 46(8), pp. 1257-1263. <https://doi.org/10.1175/JAM2525.1>
- 90 Skamarock, W.C. and Klemp, J.B., 2008. A Time-Split Nonhydrostatic Atmospheric Model for Weather Research and Forecasting Applications. *Journal of Computational Physics*, 227(7), pp. 3465-3485. <https://doi.org/10.1016/j.jcp.2007.01.037>
- 91 Steyn, D.G., 2003. Scaling the Vertical Structure of Sea Breezes Revisited. *Boundary-Layer Meteorology*, 107, pp. 177-188. <https://doi.org/10.1023/A:1021568117280>

Submitted 25.10.2023; approved after review 13.05.2024;
accepted for publication 16.05.2024.

About the authors:

Mikhail V. Shokurov, Leading Research Associate, Marine Hydrophysical Institute of RAS (2 Kapitanskaya Str., Sevastopol, 299011, Russian Federation), DSc. (Phys.-Math.), **ORCID ID: 0000-0003-1595-8281**, **ResearcherID: V-7160-2017**, shokurov.m@gmail.com

Natalia Yu. Kraevskaya, Junior Research Associate, Marine Hydrophysical Institute of RAS (2 Kapitanskaya Str., Sevastopol, 299011, Russian Federation), **ORCID ID: 0000-0002-9031-2985**, **ResearcherID: ABA-1822-2020**, krayevskaja_n@mhi-ras.ru

Contribution of the co-authors:

Mikhail V. Shokurov – general scientific supervision of the study, formulation of the study goal and objectives, discussion of the work, editing of the manuscript

Natalia Yu. Kraevskaya – discussion of the work, editing of the manuscript

The authors have read and approved the final manuscript.

The authors declare that they have no conflict of interest.

Climatic Structure and Intra-Annual Variability of Temperature Fronts on the Ocean Surface in the Patagonian Shelf Region

Yu. V. Artamonov ✉, E. A. Skripaleva, N. V. Nikolsky

Marine Hydrophysical Institute of RAS, Sevastopol, Russian Federation

✉ artam-ant@yandex.ru

Abstract

Purpose. The aim of the study is to analyze the features of mean long-term structure and intra-annual variability of the characteristics of temperature fronts on the ocean surface in the Patagonian shelf region.

Methods and Results. Mean daily values of the ocean surface temperature from the NOAA OI SST data and the geostrophic velocity components on the surface at the nodes of a 0.25° regular grid from the CMEMS reanalysis for 1993–2020 were used. It is shown that at the western periphery of a large-scale cyclonic meander formed by the currents in the Patagonian shelf region (south of 45°S), three branches of the Subantarctic Front are traced; they correspond to the West Falkland Current and to two jets of the East Falkland Current. North of 45°S, where one Falkland Current jet is observed, one branch of the Subantarctic Front is identified. On the eastern periphery of the meander, the front corresponding to the common stream of the Brazil Current and the Falkland Return Current is revealed. Besides, south of 40°S, a separate branch of the Subantarctic Front corresponding to one more recirculation of the Falkland Current is observed. It is shown that at the meander western periphery, the branches of the Subantarctic Front are most intensified in February – March, at its eastern periphery – in March – April, and at the meander northern peak (in the zone of the Brazil – Falkland Confluence) – in April – May and November.

Conclusions. It is found that on the western periphery of the cyclonic meander, south of 45°S, the main branch of the Subantarctic Front approximately follows the 900–1000 m isobaths, north of 45°S – the 150–170 m isobaths, and closer to the Brazil – Falkland Confluence – the 50–60 m isobaths. At the meander eastern periphery, north of 40°S, the main branch of the front is very close to the 800–1000 m isobaths, south of 40°S – to the 1000–2500 m isobaths. It has been established that the differences between the seasonal cycles of intensity of the Subantarctic Front branches are related to the dissimilar warming and cooling rates of surface waters separated by these branches.

Keywords: Patagonian shelf, large-scale cyclonic meander, bottom topography, Subantarctic Front, Falkland Current, Brazil Current, seasonal variability, horizontal temperature gradient

Acknowledgements: The study was carried out within the framework of a theme of state assignment of FSBSI FRC MHI FNNN-2024-0014 “Fundamental studies of interaction processes in the sea – air system which form variability of marine environment physical state at different spatial and temporal scales”.

For citation: Artamonov, Yu.V., Skripaleva, E.A. and Nikolsky, N.V., 2024. Climatic Structure and Intra-Annual Variability of Temperature Fronts on the Ocean Surface in the Patagonian Shelf Region. *Physical Oceanography*, 31(4), pp. 467-485.

© 2024, Yu. V. Artamonov, E. A. Skripaleva, N. V. Nikolsky

© 2024, Physical Oceanography

Introduction

It is known that the flow of the Northern Branch of the Antarctic Circumpolar Current (NB ACC) when exiting the Drake Passage turns along an anticyclonic



trajectory in the area of the Birdwood Bank and penetrates to the north ¹ in the form of several jets [1–11]. These jets go around the Falkland Islands in the form of the Western (WFC) and Eastern (EFC) Falkland Currents and pass over the Patagonian Shelf and the continental slope. North of 45°S, the WBC and EBC practically merge forming the common Falkland (Malvinas) Current (FC). Part of the FC flow in the area of 38–40°S turns to the south forming a large-scale cyclonic meander over the Patagonian Shelf and the continental slope. The other part of the FC flow goes north and meets the Brazil Current (BC) forming a confluence zone of these currents at approximately 36–38°S. At approximately 45°S, the eastern periphery of the cyclonic meander (Falkland Return Current, FRC) turns east and then follows the northern boundary of the Falkland Plateau as NB ACC ¹ [1, 3–6, 11–17]. The northward transport of cold subantarctic waters by the Falkland Current leads to the formation of intense hydrological fronts in the Patagonian shelf region and continental slope which are zones of increased bioproductivity according to [14, 15, 18–20]. High commercial importance of the Patagonian shelf waters has led to increased interest in the variability of the frontal structure in this area. Most studies [1, 3, 4, 6, 8, 12, 14–17, 21, 22] focus on the analysis of the structure of currents or dynamic fronts. It is shown that FC is characterized by a multi-jet structure, with two most intense jets being distinguished – coastal and seaward. Their cores (velocity maxima) are located on relatively flat sections of the shelf slope where the bottom depth is approximately 150–200 and 1400–1500 m, respectively [15, 17].

Some studies have shown that there is a connection between the FC jets and the fronts in the sea surface temperature (SST) field. The maxima (in absolute value) of its negative zonal gradients coincide with the maximum meridional current velocities [14, 15]. However, studies that analyze the structural features and variability of temperature fronts in the Patagonian shelf region are relatively few in number, and the temperature fronts associated with the FC jet system have different names: the Patagonian shelf front [14], the Falkland or Malvinas front [15] and the Subantarctic Front (SAF) [2, 7, 23]. In the present paper, we will adhere to one terminology and call all temperature fronts associated with the FC jets SAF branches. Some inconsistencies in the structure and position of the SAF branches are observed in the studies of different authors based on different data. Thus, in [23], based on the World Ocean Atlas–1994 hydrological array, it is shown that the SAF position in the temperature field along the Patagonian continental slope is stable throughout the year and repeats the configuration of the 500–700 m isobaths. In [14], based on satellite SST data from the NOAA/NASA *Pathfinder* array, several temperature fronts are identified separating shelf waters from the colder waters transported by the FC, with the most intense front located near the 200 m isobath. In [15], based on contact measurements and MODIS Aqua satellite images, it is concluded that the most intense temperature SAF passes along the 1400 m isobath.

It should also be noted that the intra-annual variability of the SAF characteristics has been poorly studied: relatively short data time series analyzed insufficiently to obtain statistically reliable climate norms or front variability considered in individual sections which does not allow estimating its features along the entire length of

¹ Sarukhanyan, E.I. and Smirnov, N.P., 1986. *Water Masses and Circulation of the Southern Ocean*. Leningrad: Gidrometeoizdat, 288 p. (in Russian).



the front [7, 14]. Currently, it has become possible to use long-term data series of ocean reanalyses and arrays obtained by optimal interpolation of contact and satellite measurements with high spatio-temporal resolution to study the structure and variability of fronts. The aim of this work is to refine mean long-term spatial structure of fronts in the SST field and the climatic seasonal variability of their characteristics in the Patagonian shelf region based on the NOAA OI SST array data for 1993–2020.

Materials and methods

The paper examines the southwest Atlantic region located above the Patagonian shelf and the continental slope between the Falkland Islands and 35°S, bounded on the west by 50°W (Fig. 1, *a*). The bottom topography scheme is constructed using data from the General Bathymetric Chart of the Oceans (GEBCO) available at: http://www.gebco.net/data_and_products/gridded_bathymetry_data/ with a spatial resolution of 15 arc seconds.

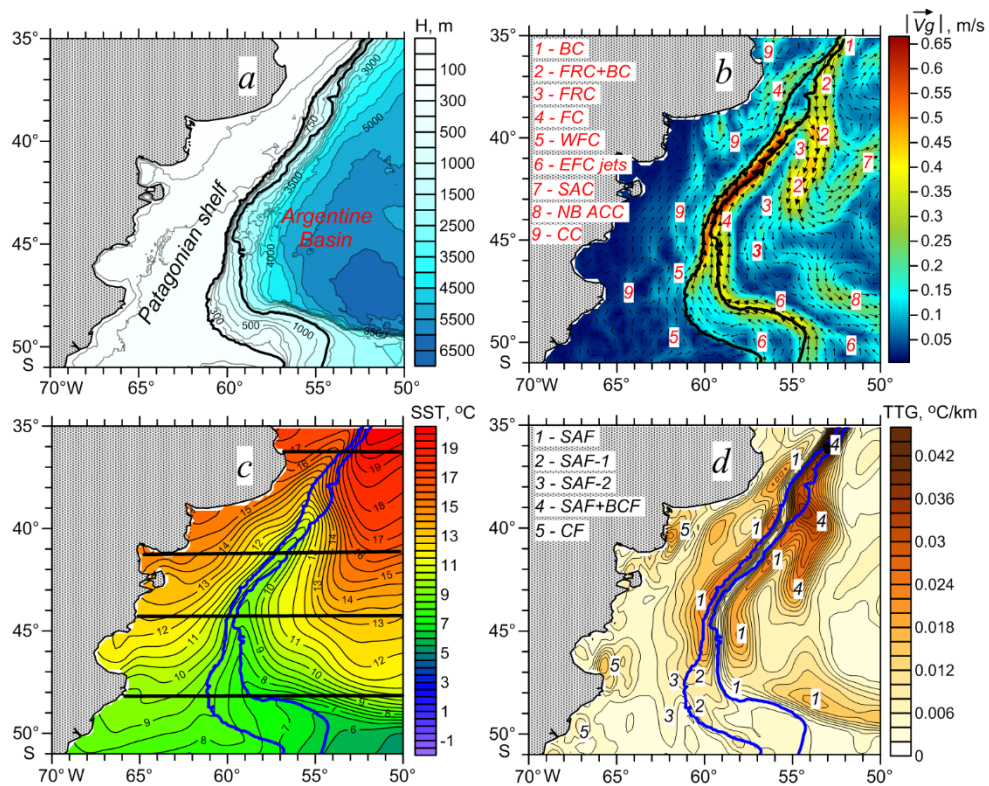


Fig. 1. Scheme of the bottom relief in the study area (*a*), spatial distribution of the mean long-term values of velocity module $|\vec{V}_g|$ and the geostrophic current vectors (*b*), temperature (SST) (*c*) and total temperature gradient (TTG) (*d*) on the sea surface. Bold lines indicate locations of the 200 m and 1400 m isobaths. Horizontal lines show the parallels for which the climatic mean annual and monthly distributions of ZTG and the meridional velocity component V_g are presented. Abbreviation decoding: BC – Brazil Current, FC – Falkland Current, FRC – Falkland Return Current, WFC – West Falkland Current, EFC – East Falkland Current, SAC – South Atlantic Current, NB ACC – Northern Branch of the Antarctic Circumpolar Current, CC – coastal currents, SAF – Subantarctic Front, BCF – Brazil Current Front, CF – coastal fronts

Structure and variability of temperature fronts were studied using the *NOAA Optimum Interpolation Sea Surface Temperature (OI SST)* data available at: <https://www.ncei.noaa.gov/data/sea-surface-temperature-optimum-interpolation/v2.1/access/avhrr/> which contains mean daily SST values at the regular grid nodes with a step of 0.25° for 1993–2020 obtained by the method of optimal interpolation of satellite and contact measurement data [24]. The formation of temperature fronts on the surface is associated with water circulation (with advection of cold and warm waters by oppositely directed currents). Therefore, to interpret the spatial structure features of fronts in the SST field, the mean long-term structure of currents obtained based on the *Copernicus Marine Environment Monitoring Service (CMEMS)* reanalysis (http://marine.copernicus.eu/?option=com_csw&view=details&product_id=SEAL_EVEL_GLO_PHY_L4_REP_OBSERVATIONS_008_047) was analyzed. The reanalysis data represent mean daily values of geostrophic velocity components on the surface at the regular grid nodes with a step of 0.25° for 1993–2020. It should be noted that the reanalyses included in *CMEMS* are in good agreement with *in situ* measurements in the Patagonian shelf region [17]. In [22], high consistency of geostrophic velocities on the surface with actual velocity measurements is also noted.

The geostrophic velocities from the array used in the present paper were compared with the total velocities, including the wind drift component, according to the *ECMWF ORAS5* and *GLORYS2V4* reanalyses included in *CMEMS*. It was found that the positions of the main maxima of the geostrophic and total velocities practically coincided. Minor differences in the velocity values between the total and geostrophic currents are insignificant for solving our problem since we consider the mean long-term structure of currents and the position of flows only for interpreting the spatial structure of temperature fronts.

The same grid step of the initial data arrays and the coincidence of the coordinates of its nodes permits to compare the position of the cores of geostrophic currents and temperature fronts correctly and the time period of the 28-year data is sufficient to obtain statistically reliable mean SST and geostrophic velocity characteristics ².

Based on the initial mean daily SST values and the geostrophic velocity components, their climatic mean monthly and long-term values were calculated at each grid node and then used to calculate meridional, zonal and full horizontal SST gradients, velocity module $|\vec{V}_g|$ and current vectors direction.

In the region under consideration, temperature fronts and currents have mainly a quasi-meridional orientation, therefore, when identifying fronts in the SST field, the criterion of the maximum (in absolute value) of the zonal temperature gradient (ZTG) was used, and when identifying the current core, the criterion of the maximum of the meridional component of the geostrophic velocity V_g was used. A positive or negative value of the ZTG shows an increase or decrease in temperature in the direction from west to east. The front intensity is understood as

² Monin, A.S., 1999. *Hydrodynamics of the Atmosphere, Ocean and Earth's Interior*. Saint Petersburg: Gidrometeoizdat, 524 p. (in Russian).

the value of the maximum of the gradient corresponding to the front. The position of temperature fronts and current cores was determined on the ZTG and V_g samples along parallels with a step of 0.25° at latitude.

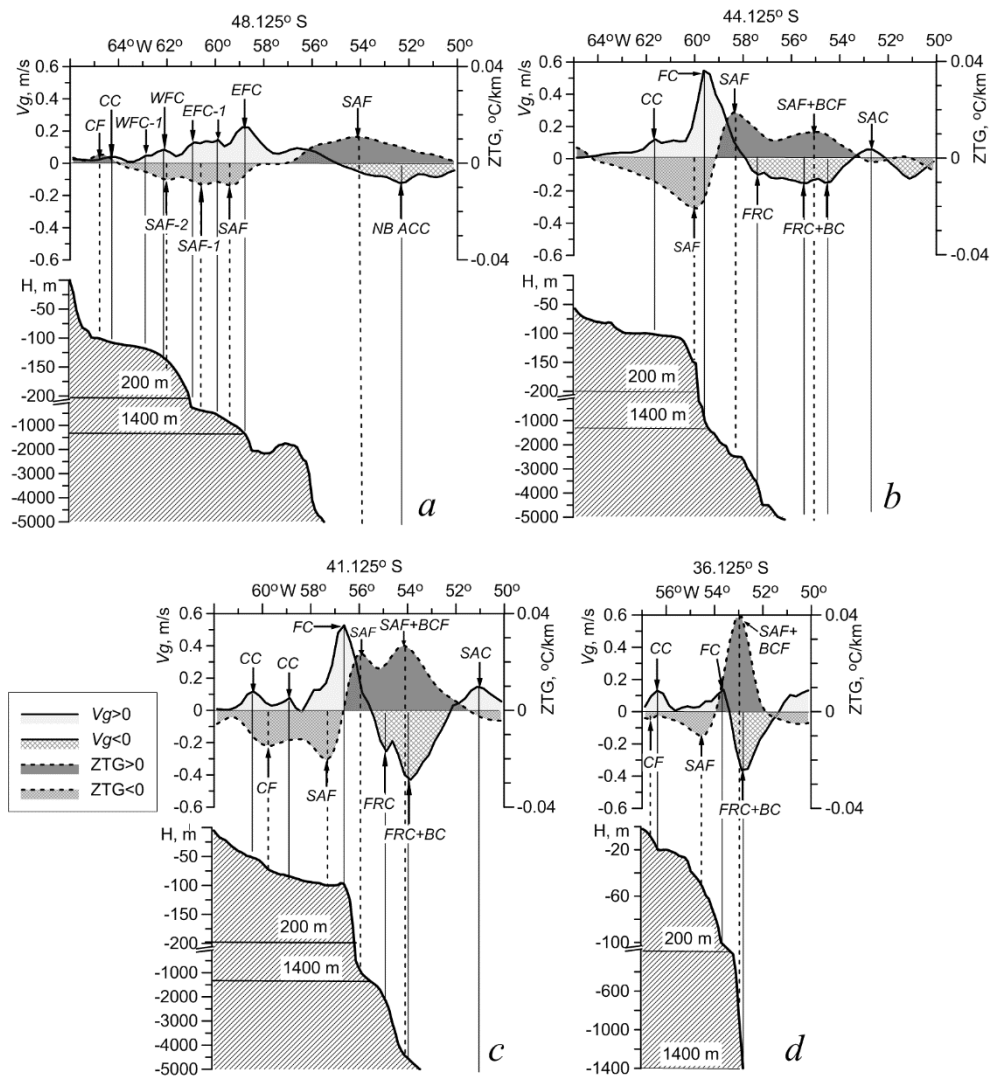


Fig. 2. Distributions of mean long-term values of ZTG (dashed curves) and V_g (solid curves) along 48.125°S (*a*), 44.125°S (*b*), 41.125°S (*c*) and 36.125°S (*d*) against the background of bottom profile (shaded). Positions of temperature fronts are shown by dashed lines, and those of current jets – by solid ones

Research results

Spatial distributions of the mean annual values of geostrophic velocity module and vectors (Fig. 1, *b*) show that the position of the current jets in the Patagonian shelf region is largely determined by the bottom topography features (Fig. 1, *a*). Note that coastal currents are traced over the shallowest part of the shelf with depths $< 50\text{--}100$ m and they are not associated with the large-scale cyclonic

PHYSICAL OCEANOGRAPHY VOL. 31 ISS. 4 (2024) 471

meander formed by the Falkland Current (Figs. 1, *b*; 2). In the southern part of the study area (south of 45°S), where the shelf widens and relatively flat areas of the continental slope (terraces) are observed (Fig. 1, *a*), the West and East Falkland Currents are characterized by a multi-jet structure. Over the shelf with depths of 100–150 m, two weak West Falkland Current (WFC and WFC-1) jets can be observed. Seaward, between the 200 and 500 m isobaths, a wide flow corresponding to a relatively weak jet of the East Falkland Current (EFC-1) is observed. The most intense EFC jet passes over the continental slope approximately along the 1400 m isobath (Figs. 1, *b*; 2, *a*). The position of the main EFC jet in the mean long-term field of geostrophic velocity is in good agreement with the data of actual measurements carried out in this region in different years [15, 21]. Another weak EFC jet passes in the southern part of the Argentine Basin, approximately along the 2400–2500 m isobaths (Fig. 1, *b*).

North of 45°S, where the 200 and 1400 m isobaths are located close to each other (Fig. 1, *a*), the WFC and EFC jets merge forming one intense FC flow which represents the western periphery of the cyclonic meander (Figs. 1, *b*; 2, *b*).

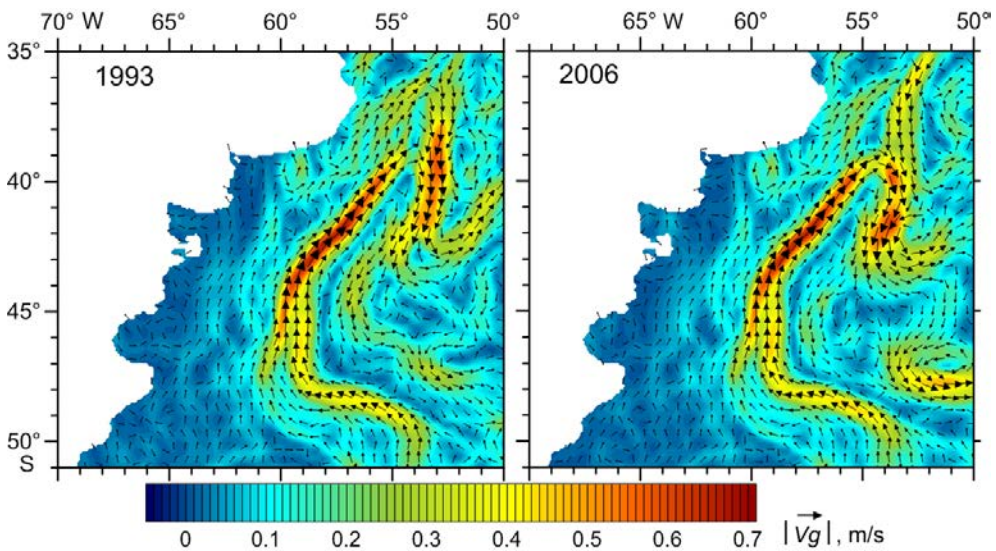


Fig. 3. Spatial distributions of the mean annual values of velocity module $|\vec{v}_g|$ and vectors of geostrophic currents for different years

In the northern part of the meander, two FC recirculation zones were identified due to the bottom topography influence. It clarifies earlier studies that identified only one FC recirculation zone [1, 3–6, 11–17]. The first zone is located at approximately 40°S, north of which a terrace between the 200 and 1400 m isobaths is observed (Fig. 1, *a*). Here, part of the FC flow turns south in the form of a FRC which passes over the continental slope approximately along the 2000–3500 m isobaths (Figs. 1, *b*; 2, *b*; 2, *c*). South of 47°S, the FRC turns east and follows the northern boundary of the Falkland Plateau as the NB ACC (Figs. 1, *b*; 2, *a*). Another part of the FC flow continues to follow north along the western edge of the terrace above the 100–200 m isobaths; it meets the Brazil Current at 35–36°S

and forms the second recirculation zone. Confluence of the BC and the FRC forms an intense common flow (FRC+BC) which follows south over the continental slope seaward of the 1400 m isobath to approximately 39°S (Figs. 1, *b*; 2, *d*). Further south, in the region of 40–41°S, part of the FRC+BC flow turns to the east and passes over the deep-water part of the Argentine Basin approximately above the 5500 m isobath. The main part of the FRC+BC flow continues to follow to the south above the 4500 m isobath (Figs. 1, *b*; 2, *c*) and between 43° and 44.5°S turns to the northeast along an anticyclonic trajectory and then follows in an easterly direction in the form of the South Atlantic Current (SAC) (Figs. 1, *b*; 2, *b*, 2, *c*).

Main circulation features revealed in the mean long-term field of geostrophic velocity are clearly seen in the distributions of current vectors and velocity module for each year (Fig. 3). Despite the interannual variability of flow intensity, the position of the main WFC, EFC, FC jets, the FRC+BC flow and two FC recirculations (in the region of 40°S and between 35° and 36°S) controlled by the bottom topography features is maintained throughout each year.

Multidirectional geostrophic flows lead to the formation of well-defined tongues of cold and warm waters in the SST field (Fig. 1, *c*), at the boundaries of which zones of increased total horizontal temperature gradients (TTG) or frontal zones (Fig. 1, *d*) are formed. According to [8, 19, 20], jets of intense currents are barriers that impede horizontal water exchange and separate water masses with different transformation degrees.

Let us present the main features of the mean long-term structure of temperature fronts formed on the peripheries of a large-scale cyclonic meander. It should be noted that over the shallow part of the shelf with depths of < 100 m, relatively weak extremes of SST gradients of different signs associated with the advection of shelf waters by coastal currents and called conventionally coastal fronts are observed (Figs. 1, *d*; 2). Since the CF branches do not belong to the system of large-scale cyclonic meander fronts, they are not discussed in this paper.

On the southwestern periphery of the meander south of 45°S, three fronts are identified as the SAF branches. The eastern branch (the SAF itself), most intense of them, passes approximately 0.5° west of the main EFC jet above the 900–1000 m isobaths. The weaker central branch (SAF-1) is located within the EFC-1 flow above the 300–400 m isobaths. The western branch (SAF-2) coincides practically with the WFC jet and is observed above the 130–150 m isobaths (Fig. 2, *a*). North of 45°S, where the western periphery of the meander is formed by a single FC flow, the SAF is also represented by a single branch. Here, the front is located approximately 0.25° west of the FC flow above the 150–170 m isobaths (Fig. 2, *b*). In the northwestern part of the meander, the SAF passes above the 100 m isobath, while its position shift to the west relative to the FC core position increases gradually and at the 41°S latitude reaches 0.5° (Fig. 2, *c*). Closer to the Brazil – Falkland Confluence, the SAF is located above depths of 50–60 m, noticeably weakens and shifts to the west relative to the FC by almost 1° (Fig. 2, *d*). On the north-eastern periphery of the cyclonic meander formed by the common FRC+BC flow, an intense

front is observed in the SST field. It is formed as a result of the convergence of the Subantarctic Front and the Brazil Current Front (SAF+BCF). This front passes over the 800–1000 m isobaths and coincides practically in position with the core of RB FC+BC (Fig. 2, *d*). Up to approximately 39–40°S, the SAF+BCF separates the cold waters transported by the FC and the warm waters transported by the FRC+BC flow. On the eastern periphery of the meander south of 40°S, a wide zone of high ZTG values is observed. Within this zone, to the west of the main ZTG maximum corresponding to the SAF+BCF, another ZTG maximum is distinguished corresponding to another SAF branch (Fig. 2, *c*). Formation of two temperature fronts in this section of the meander is associated with two southerly flows (the FRC and the general FRC+BC flow). Here, the SAF separates the coldest waters transported by FC from the south from warmer waters coming from the north with the FRC and the SAF+BCF, in turn, separates the latter from even warmer waters transported by the FRC+BC. The SAF+BCF branch coincides practically in position with the FRC+BC core and the SAF is shifted to the west of the FRC jet by almost 1° (Fig. 2, *c*). These two fronts (SAF and SAF+BCF) persist up to approximately 45°S, with the SAF being observed over the continental slope along the 1000–2500 m isobaths and gradually strengthening in the southern direction while the SAF+BCF passes over depths greater than 4000 m and, conversely, weakens gradually (Figs. 2, *b*; 2, *c*). It should be noted that the identification of two SAF branches on the eastern periphery of the meander between 40° and 45°S clarifies the earlier results of [14] which noted the existence of one seaward temperature front south of 40°S characterized by weak positive SST gradients.

In general, the performed analysis of the relationship between the position of the SAF branches and the bottom topography features showed that, in contrast to previously obtained results [14, 15, 23], the main SAF branch passes over different isobaths in different water area parts: in the southwestern part – over the 900–1000 m isobaths, north of 45°S – over the 150–170 m isobaths, at the top of the cyclonic meander – over the 50–60 m isobaths, on the eastern periphery of the meander up to approximately 40°S – above the 800–1000 m isobaths and to the south – above the 1000–2500 m isobaths.

It should be noted that, in general, on the large-scale meander peripheries, the temperature fronts on the surface either coincide in position with the cores of geostrophic currents or are located to the west, while the maximum shift does not exceed 1° at longitude and is noted on the eastern periphery of the meander.

South of 47–48°S, where the FRC+BC flow turns east and follows the northern boundary of the Falkland Plateau as NB ACC, the mean annual SST field exhibits one main ZTG extreme corresponding to the SAF (Fig. 2, *a*).

Analysis of the mean monthly SST distributions showed that, despite the high seasonal variability, well-defined tongues of cold and warm waters are observed throughout the year (Fig. 4), as a result of which the main features of the mean annual frontal structure are observed during all months (Fig. 5).

Distributions of the climatic mean monthly zonal SST gradients showed that the SAF branches influenced by bottom topography, especially on the western

periphery of the meander, have a stable position, with their intra-annual shifts at longitude not exceeding 1° (Figs. 5, 6). At the same time, the intra-annual changes in the intensity of the SAF branches differ significantly in various parts of the water area. Thus, their values do not exceed $0.012^\circ\text{C}/\text{km}$ in the south (Fig. 6, *a*), increase to $0.016\text{--}0.02^\circ\text{C}/\text{km}$ north of 45°S (Figs. 6, *b*; 6, *c*), decrease again at the top of the meander and are $0.006^\circ\text{C}/\text{km}$ at $35\text{--}36^\circ\text{S}$ (Fig. 6, *d*). The values of seasonal changes in the SAF+BCF intensity decrease in the southerly direction from $0.04\text{--}0.05^\circ\text{C}/\text{km}$ at $35\text{--}36^\circ\text{S}$ to $0.012^\circ\text{C}/\text{km}$ at 44°S (Figs. 6, *b*–*d*).

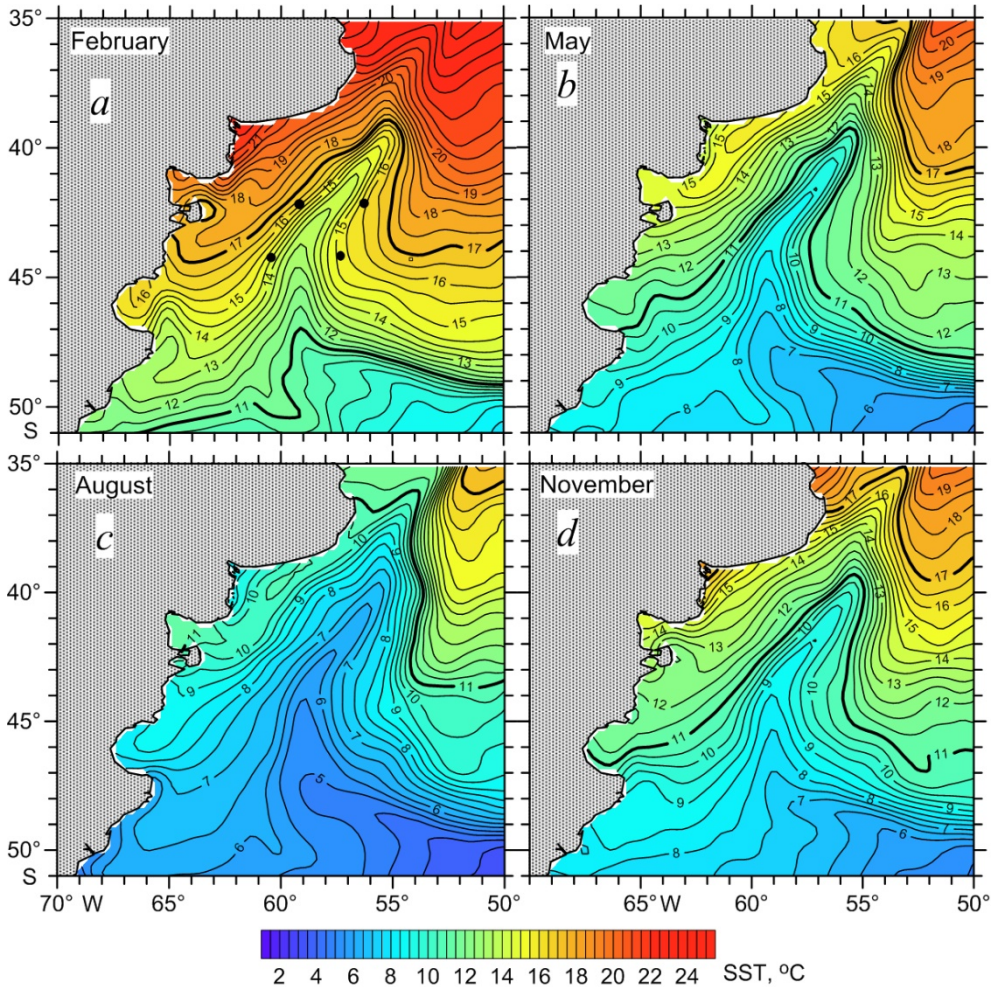


Fig. 4. Distributions of the climatic mean monthly SST values in February (*a*), May (*b*), August (*c*) and November (*d*). Bold lines denote the 11°C and 17°C isotherms

Differences in the periods of maximum intensification of fronts in different areas of the western (Fig. 7, *a*) and eastern (Fig. 7, *b*) peripheries of the large-scale meander are also noted.

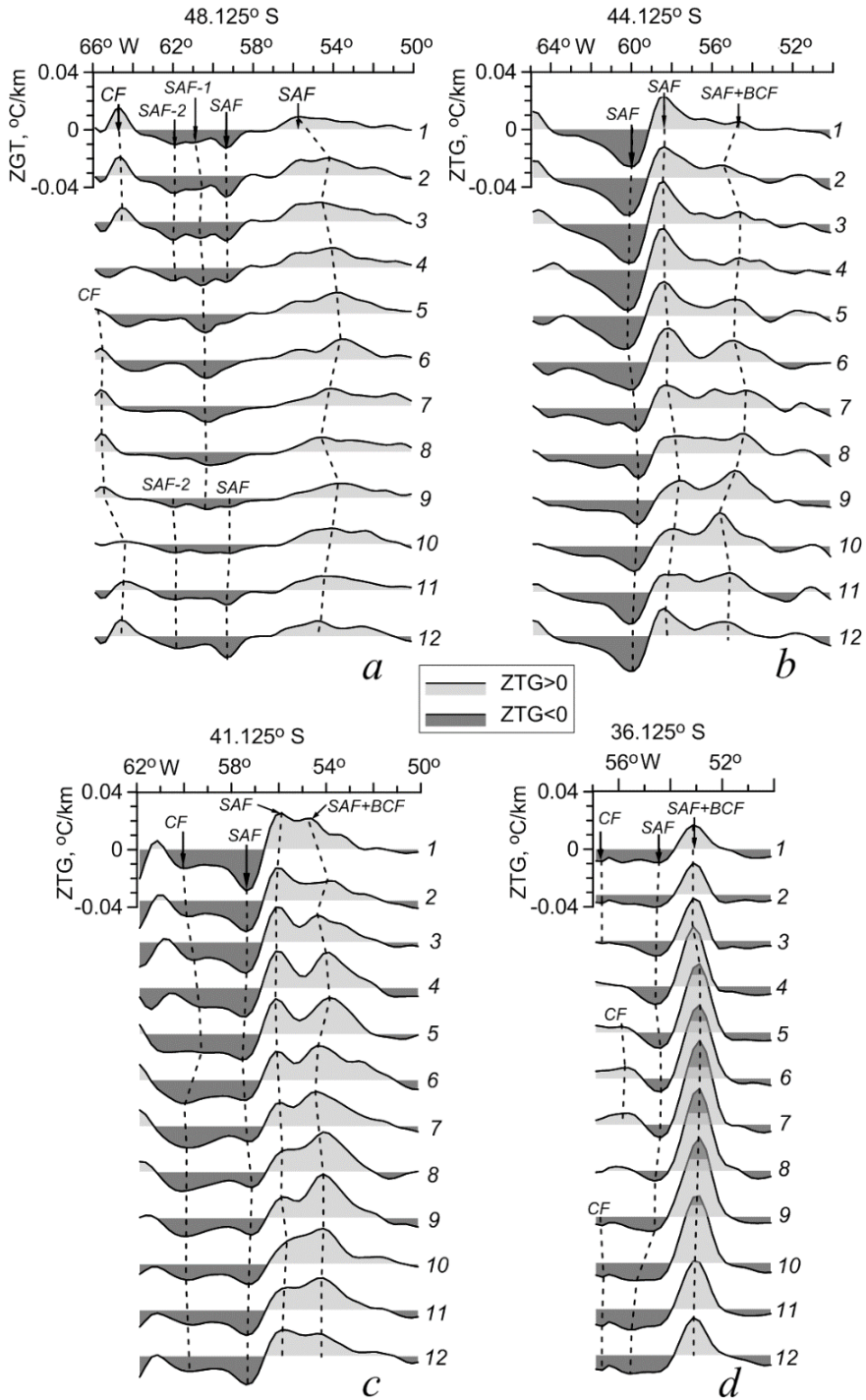


Fig. 5. Distributions of the climatic mean monthly ZTG values along 48.125°S (a), 44.125°S (b), 41.125°S (c) and 36.125°S (d). Positions of temperature fronts are shown by dashed lines, numerals by the curves are months

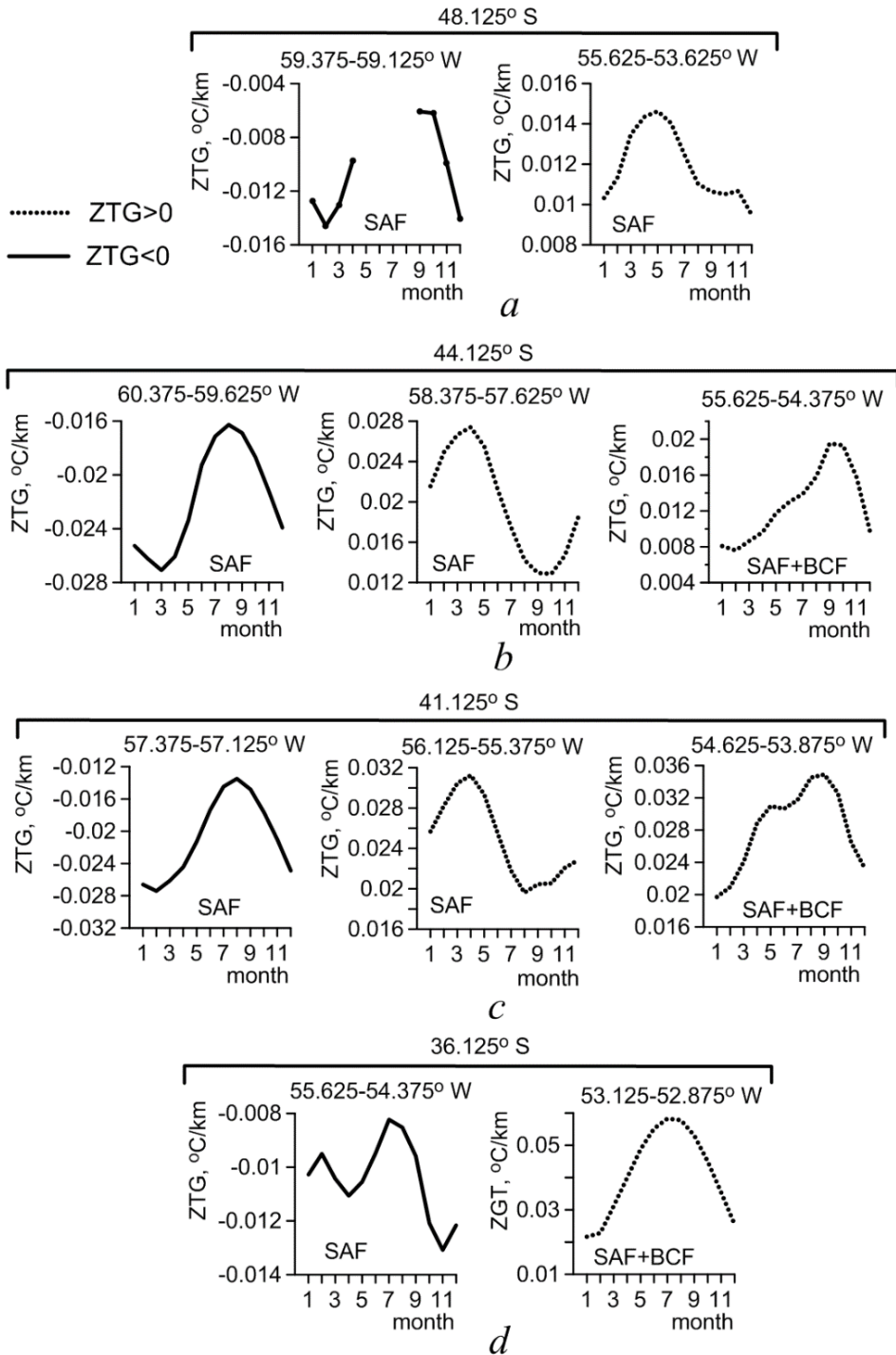


Fig. 6. Graphs of climatic seasonal cycle of SAF and SAF+BCF intensity and range of their longitudinal displacement during a year (shown on the graphs) on 48.125°S (a), 44.125°S (b), 41.125°S (c) and 36.125°S (d)

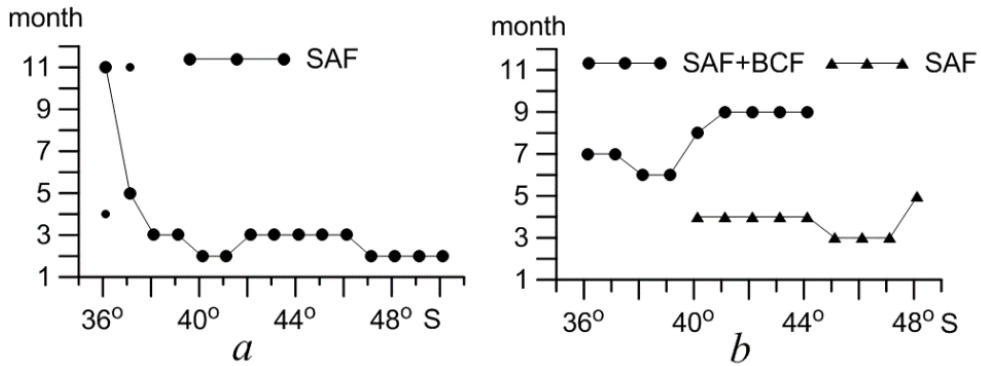


Fig. 7. Month of maximum intensification of SAF and SAF+BCF at the western (*a*) and eastern (*b*) peripheries of a cyclonic meander. Dots in fragment *a* show the onset of the second, weaker, maximum of SAF intensity

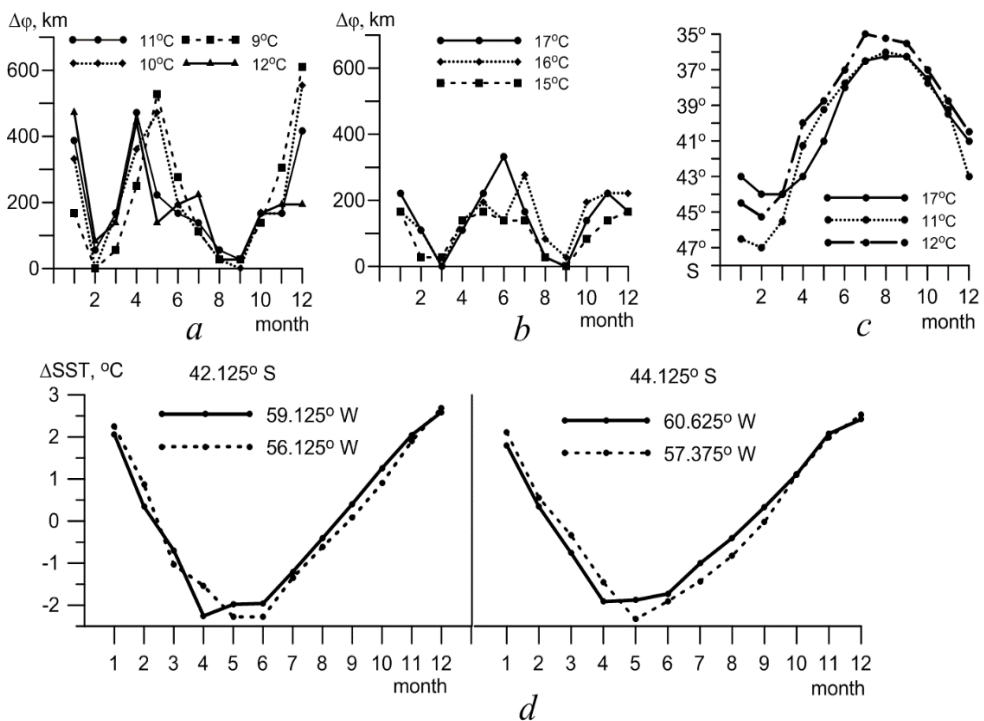


Fig. 8. Displacement (at latitude) speed (km/month) of various isotherms in the tongues of cold (*a*) and warm (*b*) waters; extreme northern position of the 11 °C and 12 °C isotherms in the cold water tongue and extreme southern position of the 17 °C isotherm in the warm water tongue for each month (*c*); Δ SST intra-annual cycle in certain grid knots (shown by points in Fig. 4, *a*) at the western (solid curves) and eastern (dotted curves) meander peripheries (*d*)

Seasonal variability features of front intensity in the SST field are associated with differences in the rate of intra-annual shifts of isotherms in the tongues of cold and warm waters (Fig. 4) caused by the combined influence of advection and seasonal warming/cooling of surface waters separated by fronts.

The paper estimates the latitude shifts during the year of the 9–12°C and 15–17°C isotherms, typical for cold and warm water tongues, respectively. For this purpose, the difference in kilometers ($\Delta\varphi$) between the extreme northern and extreme southern positions of these isotherms in cold and warm water tongues, respectively, in January relative to December, in February relative to January, etc. was calculated (Figs. 8, *a*; 8, *b*).

Intra-annual variations of $\Delta\varphi$ show that during the periods of maximum warming (February – March) and cooling (August – September) of surface waters³ these isotherms change their latitudinal position slightly. In April – May, when intensive cooling of waters takes place, the 9–12 °C isotherms shift northwards almost 450–500 km. With warming up of surface waters in October – February, they shift southwards. The maximum shifts reflecting the greatest rate of warming for the 9–11 °C isotherms are observed in December with $\Delta\varphi$ values reaching 400–600 km; for the 12 °C isotherm – in January with $\Delta\varphi$ values of ~ 500 km (Fig. 8, *a*). It is worth noting that the intra-annual variations of $\Delta\varphi$ for the 15–17 °C isotherms in the warm water tongue are similar to the variations of $\Delta\varphi$ for the 9–12 °C isotherms, but their values decrease and do not exceed 200–300 km (Fig. 8, *b*). In general, during the year, the shifts of the northern boundary of the cold water tongue according to the 11 °C and 12 °C isotherms and the southern boundary of the warm water tongue according to the 17 °C isotherm from the extreme southern to the extreme northern position reach 11°, 12°, and 8° latitudes, respectively (Fig. 8, *c*).

Note the following features analyzing the relationship between the seasonal variability of the SAF branches intensity and the isotherms shift in the cold and warm water tongues. On the southwestern periphery of the meander, the western (SAF-2) and eastern (SAF) branches of the Subantarctic Front are most clearly observed during the warm season of the Southern Hemisphere (Fig. 5, *a*). During this period, SAF-2 separates the warmed shelf waters from the colder waters carried by the WFC and the SAF separates the waters carried by the EFC-1 flow from even colder waters carried by the main branch of the EFC (Fig. 4, *a*). These fronts become most intense in February – March (Figs. 6, *a*; 7, *a*) when the maximum warming of the waters in the southern part of the shelf is observed (SST values > 12.5–13 °C) (Fig. 4, *a*). During these months, the northern boundary of the cold water tongue along the 9–12 °C isotherms is located in the south and only changes its latitudinal

³ Lomakin, P.D. and Skripaleva, E.A., 2008. *The Circulation and Water Structure in the Southwest Atlantic and Antarctic Adjacent Areas*. Sevastopol: EKOSI-Gydropfizika, 116 p. (in Russian).

position slightly (Figs. 8, *a*; 8, *c*). During the cold season (from May to August), the SST values over the southern part of the shelf do not exceed 7–9 °C (Figs. 4, *b*; 4, *c*). Temperature contrasts between the coastal waters and the waters carried by the WFC and EFC decrease noticeably, which leads to SAF-2 and SAF weakening (Fig. 6, *a*). During this period, the EFC-1 flow brings colder waters with temperatures < 6–8 °C from the south (Figs. 4, *b*; 4, *c*). Judging by the rapid shift of the 9–10°C isotherms to the north, it can be noted that the maximum decrease rate of SST values in the cold water tongue is observed in May (Fig. 8, *a*). This leads to an increase in temperature contrasts in the zone of the SAF-1 front central branch, the greatest intensification of which is observed in May – June (Fig. 5, *a*).

North of 45°S, the SAF structure exhibits one branch throughout the year which is the western boundary of the tongue of cold waters transported by the FC separating them from the warmer shelf waters (Figs. 5, *b – d*). Here, the maximum SAF intensification occurs in February – March (Figs. 6, *b, c*; 7, *a*) when the maximum warming of surface waters is observed. During this period, the 9–12 °C isotherms in the tongue of cold waters do not practically change their latitudinal position and are maximally shifted to the south (Figs. 8, *a, c*). The intensification of temperature contrasts supporting the front is due to more intense warming of the shelf waters where the SST values increase in the northerly direction from 16 °C to 21°C during this period, while they change from 12 °C to 17 °C to the east of the front in the tongue of cold waters (Fig. 4, *a*).

So, the main branch of the SAF intensifies in February – March on the entire western periphery of the meander, whereas a longer period of front intensification from November to May in [14] and from December to March in [7] was noted earlier.

At the northern meander apex, in the convergence zone of the Falkland and Brazil currents which, according to [13, 25], intensify in antiphase in the Southern Hemisphere winter and summer, respectively, the SAF intensity also changes with a semi-annual period with maxima in April – May and November (Figs. 6, *d*; 7, *a*). In April – May, the SAF intensification occurs during an intense cooling period when the boundary of the cold water tongue along the 9–12 °C isotherms shifts quickly north (Figs. 8, *a, c*) and the temperature of the shelf waters remains quite high and exceeds 15 °C (Fig. 4, *b*). The second maximum of the SAF intensity (in November) is observed during intense warming period when the 9–12 °C isotherms in the cold water tongue shift quickly to the south (Figs. 8, *a, c*) and the temperature of the coastal shelf waters rises to 17–18 °C (Fig. 4, *d*).

South of the Brazil – Falkland Confluence up to approximately 40°S, where the SAF+BCF front is the boundary between the cold and warm waters carried by these currents, it intensifies in June – July when the 11–12 °C isotherms in the tongue of cold waters are shifted maximally to the north (Figs. 6, *d*; 7, *a*; 8, *a, c*). South of 40°S, where the SAF+BCF serves as the western boundary of the warm water tongue separating them from the colder waters carried by the FRC, it intensifies in August – September (Figs. 6, *b, c*; 7, *b*). During this period, maximum cooling of surface waters is observed and the 15–17 °C isotherms in the tongue of

warm waters are shifted maximally to the north (Figs. 8, *b, c*). Front strengthening is due to the fact that in August – September the temperature of the waters carried by the FRC does not exceed 9–10 °C while the SST values in the tongue of warm waters, despite the general cooling, remain higher and amount to 11–15 °C (Fig. 4, *c*). The Subantarctic Front which is located west of the SAF+BCF and separates the waters carried from the north by the FRC from even colder waters carried from the south by the FC intensifies in March – April (Figs. 6, *b, c*; 7, *b*). During this period, cooling of surface waters begins, especially pronounced in the cold tongue. According to the isotherms of 9–12 °C, its boundary shifts to the north by almost 500 km in April (Figs. 8, *a, c*) while the waters coming from the north with the FRC are still noticeably warmer at this time (SST values > 13–15 °C). Note that the SAF intensifies on the eastern periphery of the meander approximately a month later than on the western one (Fig. 7). According to an earlier work [7], at the eastern boundary of the cyclonic meander south of 42°S, the SAF intensified in May – June, i.e. the delay in the onset of the maximum compared to the western periphery was almost half a year. Analysis of the intra-annual course of the temperature change rate Δ SST (difference between the SST values of the current and previous months) showed that a similar phase delay of one month was observed at the onset of the maximum rate of water cooling west and east of the SAF at the western and eastern peripheries of the meander, respectively (Fig. 8, *d*). The maximum rate of water cooling (Δ SST ~ -2.5 °C) at the western periphery of the meander is observed in April, at the eastern periphery – a month later, in May.

To the south of 48°S, above the northern boundary of the Falkland Plateau, the main extremum of the ZTG in the SAF structure observed throughout the year (Fig. 5, *a*) is maximally intensified in May (Figs. 6, *a*; 7, *b*) during the period of intense cooling of surface waters.

Conclusion

Based on *NOAA OI SST* data, the spatial structure of the Subantarctic Front in the climatic field of sea surface temperature in the Patagonian shelf region has been refined and its relationship with the bottom topography features and geostrophic currents that form a large-scale cyclonic meander in this region has been analyzed.

High spatial resolution of the used data array allowed identifying several branches in the SAF structure in the mean long-term SST climatic field. For the first time, the isobaths in the SST climatic field are shown, over which these SAF branches pass in different parts of the water area. Three branches of the Subantarctic Front were identified on the western periphery of the meander south of 45°S. The main SAF branch (eastern) corresponds to the most intense EFC jet and passes over the 900–1000 m isobaths. The central and western SAF branches correspond to the weaker EFC-1 and WFC jets and pass over the 300–400 m and 130–150 m isobaths, respectively. One branch of the SAF can be observed north of 45°S. It corresponds to the FC which passes above the 150–170 m isobaths. At the top of

the cyclonic meander, closer to the Brazil – Falkland Confluence, the SAF passes above the 50–60 m isobaths.

For the first time it is shown that two FC recirculation zones leading to the formation of two SAF branches on the eastern periphery of the meander are observed as a result of topographic features (the presence of a terrace between the 200 and 1400 m isobaths north of 40°S). One branch (SAF+BCF) is formed as a result of the BC and the FRC convergence, the second one (SAF) is formed south of 40°S and corresponds to one more recirculation of the Falkland Current. These two branches can be traced to approximately 45°S. The SAF+BCF branch passes above the 800–1000 m isobaths up to 40°S, further south – above depths of > 4000 m and weakens gradually in the southern direction. The SAF is observed over the continental slope along the 1000–2500 m isobaths and intensifies gradually in the southern direction.

For the first time, the characteristics of the climatic seasonal cycle of each SAF branch on the western and eastern peripheries of the meander were obtained. It is found that the SAF branches have a stable position under the bottom topography influence, especially on the western periphery of the meander, with their intra-annual shifts not exceeding 1° at longitude. It is revealed that the values of intra-annual changes in the intensity of the SAF branches differ significantly in different parts of the water area. They do not exceed 0.012 °C/km in the south, increase to 0.016–0.02 °C/km north of 45°S, decrease again at the top of the meander and are 0.006 °C/km at 35–36°S. Seasonal changes in the SAF+BCF intensity weaken in the southern direction from 0.04–0.05 °C/km at 35–36°S up to 0.012 °C/km at 44°S.

Differences in the periods of maximum intensification of the SAF branches in different areas of the western and eastern peripheries of a large-scale meander are revealed. It is shown that they are associated with differences in the rates of heating and cooling of the waters separated by these branches. It is found that the SAF branches intensify to the maximum on the western periphery of the meander in February – March when maximum heating of the waters is observed on the shelf. The SAF intensifies on the eastern periphery of the meander south of 40°S approximately a month later, in March – April. The same one-month delay was revealed at the onset of the maximum rate of water cooling on the western and eastern peripheries of the meander. It is found that the SAF intensity changes at the northern meander apex, in the Brazil – Falkland Confluence, with a semi-annual period with the maxima in April – May during intensive cooling of waters and in November during the intensive heating period. The SAF+BCF up to approximately 40°S intensifies on the eastern periphery of the meander, south of the Brazil – Falkland Confluence, in June – July when the maximum rate of surface waters cooling is observed and south of 40°S – in August – September when the minimum SST values are observed. The SAF intensifies to the maximum over the northern boundary of the Falkland Plateau in May, during the period of surface waters intensive cooling.

REFERENCES

1. Zyryanov, V.N. and Severov, D.N., 1979. Water Circulation in the Falkland – Patagonian Region and Its Seasonal Variability. *Oceanology*, 19(5), pp. 782-791.
2. Guretsky, V.V., 1987. Surface Thermal Fronts in the Atlantic Sector of the Southern Ocean. *Meteorologiya i Gidrologiya*, (8), pp. 81-89 (in Russian).
3. Peterson, R. and Whitworth, T., 1989. The Subantarctic and Polar Fronts in Relation to Deep Water Masses through the Southwestern Atlantic. *Journal of Geophysical Research: Oceans*, 94(C8), pp. 10817-10838. <https://doi.org/10.1029/JC094iC08p10817>
4. Peterson, R.G. and Stramma, L., 1991. Upper-Level Circulation in the South Atlantic Ocean. *Progress in Oceanography*, 26(1), pp. 1-73. [https://doi.org/10.1016/0079-6611\(91\)90006-8](https://doi.org/10.1016/0079-6611(91)90006-8)
5. Belkin, I.M., 1993. Frontal Structure of the South Atlantic. In: N. M. Voronina, ed., 1993. *Pelagic Ecosystems of the Southern Ocean*. Moscow: Nauka, pp. 40-53 (in Russian).
6. Orsi, A.H., Whitworth, T.III and Nowlin, W.D.Jr., 1995. On the Meridional Extent and Fronts of the Antarctic Circumpolar Current. *Deep Sea Research Part I: Oceanographic Research Papers*, 42(5), pp. 641-673. [https://doi.org/10.1016/0967-0637\(95\)00021-W](https://doi.org/10.1016/0967-0637(95)00021-W)
7. Artamonov, Yu.V. and Skripaleva, E.A., 2005. [Structure and Seasonal Variability of the Subantarctic Front in the Southwest Atlantic from Satellite Measurements of Ocean Surface Temperature]. *Monitoring Systems of Environment*, (8), pp. 237-239 (in Russian).
8. Sokolov, S. and Rintoul, S.R., 2009. Circumpolar Structure and Distribution of the Antarctic Circumpolar Current Fronts: 1. Mean Circumpolar Paths. *Journal of Geophysical Research: Oceans*, 114(C11), C11018. <https://doi.org/10.1029/2008JC005108>
9. Barré, N., Provost, C., Renault, A. and Sennéchaël, N., 2011. Fronts, Meanders and Eddies in Drake Passage during the ANT-XXIII/3 Cruise in January–February 2006: A Satellite Perspective. *Deep Sea Research Part II: Topical Studies in Oceanography*, 58(25-26), pp. 2533-2554. <https://doi.org/10.1016/j.dsr2.2011.01.003>
10. Graham, R.M., de Boer, A.M., Heywood, K.J. and Chapman, M.R., 2012. Southern Ocean Fronts: Controlled by Wind or Topography? *Journal of Geophysical Research: Oceans*, 117(C8), C08018. <https://doi.org/10.1029/2012JC007887>
11. Artamonov, Yu.V., Skripaleva, E.A. and Nikolsky, N.V., 2022. Climatic Structure of the Dynamic and Temperature Fronts in the Scotia Sea and the Adjacent Water Areas. *Physical Oceanography*, 29(2), pp. 117-138. <https://doi.org/10.22449/1573-160X-2022-2-117-138>
12. Roden, G.I., 1986. Thermohaline Fronts and Baroclinic Flow in the Argentine Basin during the Austral Spring of 1984. *Journal of Geophysical Research: Oceans*, 91(C4), pp. 5075-5093. <https://doi.org/10.1029/JC091iC04p05075>
13. Remeslo, A.V., Chernyshkov, P.P., Morozov, E.G. and Neiman, V.G., 2004. Structure and Variability of the Falkland Current. *Doklady Earth Sciences*, 399(8), pp. 1156-1159.
14. Franco, B.C., Piola, A.R., Rivas, A.L., Baldoni, A. and Pisoni, J.P., 2008. Multiple Thermal Fronts near the Patagonian Shelf Break. *Geophysical Research Letters*, 35(2), L02607. <https://doi.org/10.1029/2007GL032066>
15. Piola, A.R., Franco, B.C., Palma, E.D. and Saraceno, M., 2013. Multiple Jets in the Malvinas Current. *Journal of Geophysical Research: Oceans*, 118(4), pp. 2107-2117. <https://doi.org/10.1002/jgrc.20170>

16. Artana, C.I., Ferrari, R., Koenig, Z., Saraceno, M., Piola, A.R. and Provost, C., 2016. Malvinas Current Variability from Argo Floats and Satellite Altimetry. *Journal of Geophysical Research: Oceans*, 121(7), pp. 4854-4872. <https://doi.org/10.1002/2016JC011889>
17. Artana, C.I., Lellouche, J.M., Park, Y.H., Garric, G., Koenig, Z., Sennéchaël, N., Ferrari, R., Piola, A.R., Saraceno, M. [et al.], 2018. Fronts of the Malvinas Current System: Surface and Subsurface Expressions Revealed by Satellite Altimetry, Argo Floats, and Mercator Operational Model Outputs. *Journal of Geophysical Research: Oceans*, 123(8), pp. 5261-5285. <https://doi.org/10.1029/2018JC013887>
18. Saraceno, M., Provost, C. and Piola, A.R., 2005. On the Relationship between Satellite-Retrieved Surface Temperature Fronts and Chlorophyll a in the Western South Atlantic. *Journal of Geophysical Research: Oceans*, 110(C11), C11016. <https://doi.org/10.1029/2004JC002736>
19. Sokolov, S. and Rintoul, S.R., 2007. On the Relationship between Fronts of the Antarctic Circumpolar Current and Surface Chlorophyll Concentrations in the Southern Ocean. *Journal of Geophysical Research: Oceans*, 112(C7), C07030. <https://doi.org/10.1029/2006JC004072>
20. Chapman, C.C., Lea, M.-A., Meyer, A., Salée, J.-B. and Hindell, M., 2020. Defining Southern Ocean Fronts and Their Influence on Biological and Physical Processes in a Changing Climate. *Nature Climate Change*, 10, pp. 209-219. <https://doi.org/10.1038/s41558-020-0705-4>
21. Morozov, E.G., Tarakanov, R. Yu., Demidova, T.A., Frey, D.I., Makarenko, N.I., Remeslo, A.V. and Gritsenko, A.M., 2016. Velocity and Transport of the Falkland Current at 46°S. *Russian Journal of Earth Sciences*, 16(6), ES6005. <https://doi.org/10.2205/2016ES000588>
22. Frey, D.I., Piola, A.R., Krechik, V.A., Fofanov, D.V., Morozov, E.G., Silvestrova, K.P., Tarakanov, R. Yu. and Gladyshev, S.V., 2021. Direct Measurements of the Malvinas Current Velocity Structure. *Journal of Geophysical Research: Oceans*, 126(4), e2020JC016727. <https://doi.org/10.1029/2020JC016727>
23. Artamonov, Yu.V., 2000. Seasonal Variability of the Position of the Subantarctic Front in the South-West Atlantic Ocean. *Reports of the National Academy of Sciences of Ukraine*, (10), pp. 115-120 (in Russian).
24. Reynolds, R.W., Smith, T.M., Liu, C., Chelton, D.B., Casey, K.S. and Schlax, M.G., 2007. Daily High-Resolution-Blended Analyses for Sea Surface Temperature. *Journal of Climate*, 20(22), pp. 5473-5496. <https://doi.org/10.1175/2007JCLI1824.1>
25. Matano, R.P., Schlax, M.G. and Chelton, D.B., 1993. Seasonal Variability in the Southwestern Atlantic. *Journal of Geophysical Research: Oceans*, 98(C10), pp. 18027-18035. <https://doi.org/10.1029/93JC01602>

Submitted 04.03.2024; approved after review 06.05.2024;
accepted for publication 16.05.2024.

About the authors:

Yuri V. Artamonov, Leading Researcher, Marine Hydrophysical Institute of RAS (2 Kapitanskaya Str., Sevastopol, 299011, Russian Federation), DSc. (Geogr.), **ResearcherID: AAC-6651-2020**, **ORCID ID: 0000-0003-2669-7304**, artam-ant@yandex.ru

Elena A. Skripaleva, Chief Researcher, Marine Hydrophysical Institute of RAS (2 Kapitanskaya Str., Sevastopol, 299011, Russian Federation), CSc. (Geogr.), **ResearcherID: AAC-6648-2020**, **ORCID ID: 0000-0003-1012-515X**, sea-ant@yandex.ru

Nikolay V. Nikolsky, Junior Researcher, Marine Hydrophysical Institute of RAS (2 Kapitanskaya Str., Sevastopol, 299011, Russian Federation), **ResearcherID: AAT-7723-2020**, **ORCID ID: 0000-0002-3368-6745**, nikolsky.geo@gmail.com

Contribution of the authors:

Yuri V. Artamonov – general scientific supervision of the research, setting of study aims and objectives, qualitative analysis of the results and interpretation thereof, discussion of the study results, conclusions formulation

Elena A. Skripaleva – review of the literature on the research problem, qualitative analysis of the results and interpretation thereof, processing and description of the study results, discussion of the study results, conclusions formulation, article text preparation

Nikolay V. Nikolsky – development and debugging of computer programs for data processing and carrying out the necessary calculations, computer implementation of algorithms, graphs and diagrams construction, participation in the discussion of article materials

The authors have read and approved the final manuscript.

The authors declare that they have no conflict of interest.

Dynamics of Accumulative Coast under the Influence of Transverse Hydraulic Structure

Yu. N. Goryachkin, D. I. Lazorenko ✉, V. V. Fomin

Marine Hydrophysical Institute of RAS, Sevastopol, Russian Federation
✉ d.lazorenko.dntmm@gmail.com

Abstract

Purpose. The study is purposed at determining modern dynamics of the Lake Sasyk bay-bar (Crimean Peninsula) and the impact of the local seawater intake upon the coastal zone based on long-term *in situ* observations, satellite data and mathematical modeling. The study was conducted in view of the proposed construction of transverse hydraulic structures.

Methods and Results. Regular (2007–2014) and occasional *in situ* observations of the coastline dynamics at the Lake Sasyk bay-bar were used. The maximum inter-annual oscillations in the coastline locations are shown to be 5.8 m in the sections to the southeast from the transverse structure (seawater intake) and 3.4–7.2 m – in the sections to the northwest. Seasonal variability is significantly higher: the maximum range is 14.6 m in the sections to the southeast, and in those to the northwest – 26.7 m. The wave climate was investigated. The wave reanalysis data for 1979–2022 have shown that the southwestern direction of waves approaching the coast with a frequency exceeding 30% is most probable. The highest waves also come from this direction. The extreme values of wave characteristics which can occur once in n years were obtained. The mean long-term values of storm numbers in the area under study are given depending on their duration. Application of the *GenCade* integrated lithodynamic model permitted to obtain the estimates of changes in the coastline position in this area on the interannual scales.

Conclusions. The model calculations made it possible to reproduce the main features and trends in changes of the beach width in the area of the structure obtained due to *in situ* observations. The mean annual sediment flows in the area under study are directed clockwise (to the southeast) that is conditioned by the coastline orientation and the wave climate features. Difference between the mean annual sediment rates at the area boundaries is negligible – less than 4% of the multi-year average. This fact indicates insignificant impact of the structure upon the sediment total transfer to the southeast.

Keywords: Black Sea, Lake Sasyk, bay-bar, water intake, lithodynamics, mathematical modeling, wave climate, GenCade

Acknowledgments: the study was carried out within the framework of the theme of state assignment of FSBSI FRC MHI FNNN 2024-0016.

For citation: Goryachkin, Yu.N., Lazorenko, D.I. and Fomin, V.V., 2024. Dynamics of Accumulative Coast under the Influence of Transverse Hydraulic Structure. *Physical Oceanography*, 31(4), pp. 486-506.

© 2024, Yu. N. Goryachkin, D. I. Lazorenko, V. V. Fomin

© 2024, Physical Oceanography

Introduction

The largest accumulative formation of the coastal zone in Western Crimea – the Lake Sasyk bay-bar (Fig. 1) – is located between Yevpatoria and Saki. A motorway and a railway as well as other communications are laid along it. A complex of multi-storey hotels was planned to be built on the bay-bar in the early 2000s. The project included the construction of a number of transverse hydraulic structures (yacht marinas, berths, groins), but no detailed project development was



carried out. The completion of Simferopol – Yevpatoria – Mirny highway construction is scheduled for 2024. This project envisages the transfer of the highway from the Lake Sasyk bay-bar to bypass it. The administrative bodies of the Republic of Crimea announced the upcoming implementation of the project for the construction of recreational facilities on the bay-bar. The construction of transverse hydraulic structures is also involved. At the same time, recent negative experience of constructing such facilities during the implementation of embankment construction project on Lake Sakskeye bay-bar led to the need to revise the project, delay its implementation and unjustified financial costs [1]. In this regard, it seems relevant to study the coastal zone reaction to the construction of a transverse hydraulic structure for a specific area.

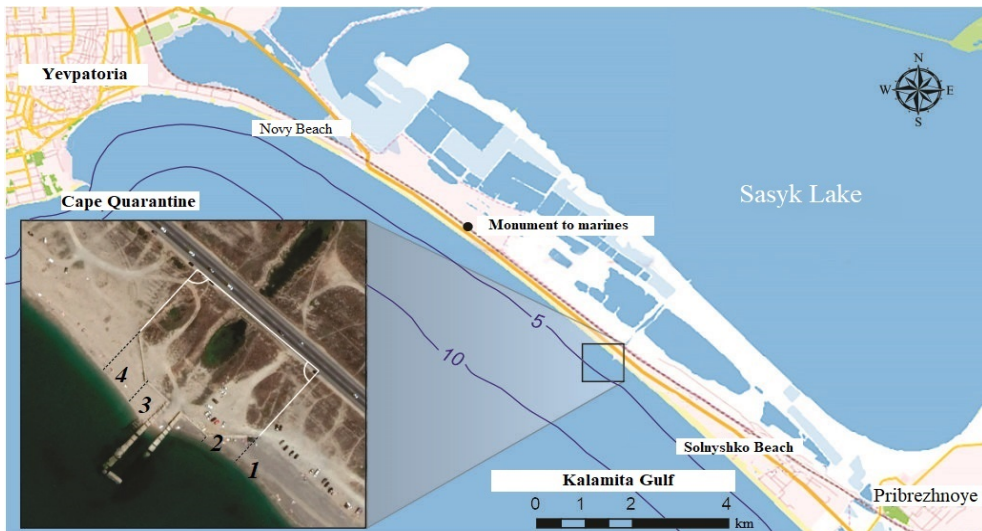


Fig. 1. Schematic map of the Kalamitsky Bay northern part. Inset shows a satellite image of seawater intake on the Lake Sasyk bay-bar, numerals denote section locations and numbers

This work is purposed at determining modern dynamics of the Lake Sasyk bay-bar and the impact of the local sea water intake upon the coastal zone based on long-term *in situ* observations, satellite data and mathematical modeling.

The most detailed studies of the Lake Sasyk bay-bar were carried out in 1930–1934 by an expedition led by Academician N.S. Kurnakov and Professor A.I. Dzens-Litovskiy¹. These studies were carried out in order to provide chemical industry with brine raw materials from the Crimean salt lakes. A bay-bar description based on the results of these works is given in^{1, 2, 3}.

¹ Dzens-Litovskiy, A.I., 1938. “Peresypys” (Bars) and “Limans” (Estuaries) of the Azof-Black Sea Coast and the Steppe Crimea. *Priroda*, (6), pp. 22-36 (in Russian).

² Dzens-Litovskiy, A.I., 1934. [Complex Hydrogeological Study of Salt and Mud Lakes and Estuaries]. In: Central Geological, Hydrogeodetic and Geodetic Department, 1934. [*The Water Resources of the Subsoil of the Earth at the Service of Socialist Construction. Issue 5: Mineral Waters*]. Leningrad, pp. 159-196 (in Russian).

³ Kurnakov, N.S., Kuznetsov, V.G., Dzens-Litovskiy, A.I. and Ravich, M.I., 1936. [*Salt Lakes of Crimea*]. Moscow; Leningrad: Izd-vo AN SSSR, 278 p. (in Russian).

In ⁴, according to the data from the expeditions of the 1940s and 1950s, some considerations about the bay-bar origin are given. In the 1980s and 1990s, occasional observations were carried out by I.I. Mechnikov Odessa National University during summer student practical trainings; the information they obtained is summarized in [2].

Observations of aeolian processes were previously conducted at the bay-bar as well [3, 4]. Individual episodic observations of the bay-bar dynamics were carried out by various organizations in Crimea. However, the results obtained have not been previously published, but it was reported that there were no signs of significant changes in the coastline over the past 70 years as a whole, as indicated by the analysis of aerial and satellite images as well as contact measurement data [5].

Dynamics of the Lake Sasyk bay-bar according to contact and satellite data

The bay-bar stretches from the eastern border of Yevpatoria to the watershed between Lake Saks koye and Lake Sasyk for 13 km. The maximum width is noted in the eastern part of the bay-bar (up to 800 m), the minimum – in the western one (150-200 m). The typical height above sea level is 1.5-2.3 m. The Lake Sasyk bay-bar is composed of sand, shell, gravel and pebbles. Some shell is mixed with sand in the largest fractions. The percentage of gravel and pebble fraction increases at the water edge, as we move south. The bay-bar formation is associated with a sea level rise during the Holocene, its age is, apparently, ~5000 years [6]. The mouths of several gullies and dry rivers formed a sea bay on the site of modern Lake Sasyk as a result of transgression. Subsequently, sediments that were formed southwards of the region under consideration during abrasion and solid runoff from rivers were included in the alongshore transport regime which led to the bay-bar creation.

The Lake Sasyk bay-bar is one of the main discharge points for alongshore sediment flows coming from the south. According to Yu.D. Shuisky, the main amount of sediment falls to the depths due to the relatively steep underwater slope (0.020), some of which, affected by wind, become a part of sandy kuchugurs (hills of aeolian origin), and the shells are worn away by up to 10% per year. He also considers that an average amount of 65 thousand m³/year of sediments enters the discharge area of the Kalamitsky stream over a long-term period. At the same time, the flow capacity is not enough to accumulate them – on the contrary, a coastline retreat is observed [2]. Nonetheless, he shows the Lake Sasyk bay-bar growing by 1 m/year on the map in his work ⁵. However, this contradicts reality, since with such an increase in the coastline during the period he indicates, the beach would have increased by one and a half times, and the pile piers that were on the bay-bar in the 1960s–1980s would have ceased to exist.

⁴ Zenkovich, V.P., 1958. *Morphology and Dynamics of the Soviet Black Sea Coast. Vol. 1.* Moscow: AS USSR Publ., 187 p. (in Russian).

⁵ Shuisky, Yu.D. and Vykhovanets, G.D., 2006. Map of Average Abrasion and Accumulation Rate. 1960-1994. In: L. I. Mitin, ed., 2006. *Atlas of the Black Sea and Sea of Asov Nature Protection.* St. Petersburg: GUNiO MO of the Russian Federation, 44 p. (in Russian).

The longest monthly observations of the coastline position were carried out in the 1980s by the Regime and Operational Station of Yevpatoria. Observations were performed in the western part of the bay-bar (the monument to marines) and in its eastern part (Solnyshko beach). According to these data, the maximum range of interannual fluctuations in the coastline position was up to 6 m, in the western part 2 m on average, in the eastern one – 4 m (Fig. 2). No significant trend is distinguished in the western part, in the eastern it is 0.7 m/year. However, the observation period is too short to consider this trend significant.

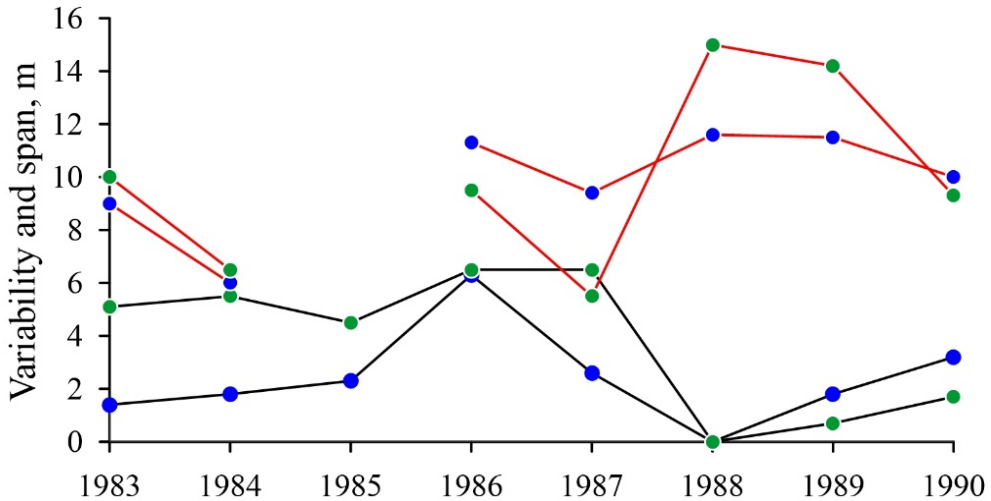


Fig. 2. Interannual variability of the coastline position (black curves) and the range of its seasonal fluctuations (red curves). Blue points show the western part of the Lake Sasyk bay-bar, green ones – its eastern part

The coast retreat by 6 m on both sections in 1986–1988 is noteworthy. It is possible that this is due to the construction of a transverse structure (NITKA facility) in 1983 in the area of Lake Kyzyl-Yar (located 12 km to the southeast) [5].

This object blocked the alongshore sediment flow directed counterclockwise in the Kalamitsky Bay. For this cause, the coastline of the Lake Saksokoye bay-bar located southwestwards retreated abruptly during 1984–1985 by 10 m [1]. Intra-annual fluctuations in the shoreline position are generally significantly greater than inter-annual ones and amount to 6–15 m (Fig. 2). In general, the maximum of the coastline progradation, according to these data, is typical for spring and retreat is typical for autumn.

After a break in the 1990s, observations were resumed in the 2000s.

In the period 2000–2014 (with short breaks), measurements were taken on a monthly basis at three sections in the bay-bar western part (Novy beach and the monument to marines). Additionally, measurements were taken in summer at three more sections of the bay-bar eastern part. Analysis of these data revealed that no significant trends in the coastline position changes were identified during this

period. The amplitudes of seasonal and interannual changes in the coastline position are within the limits characteristic of the period 1983–1990.

The data obtained at four sections in the water intake area in the bay-bar central part (2006–2014) are of the greatest interest. The seawater intake for salt extraction by *Solprom* Enterprise was built in the mid-1960s in the central part of the Lake Sasyk bay-bar. This transverse U-shaped reinforced concrete structure is 68 m long and has a depth of 3 m at the sea edge. It has not been used for its intended purpose since the 1990s and is in a dilapidated state (Fig. 3).



Fig. 3. Sea water intake on the Lake Sasyk bay-bar (view from the north)

The sections were located in pairs on the western and eastern sides of the water intake (Fig. 1, inset). Measurements were usually taken in the middle of each month. Since the distance between sections in a pair was 30 m, it is advisable to consider the coastline position variations as an average for two sections.

No statistically significant trends are distinguished in the interannual variability. The maximum range of interannual fluctuations is 5.8 m at sections 1, 2 and 7.2 m at sections 3, 4. Seasonal variability is significantly higher: thus, their maximum range is 14.6 m at sections 1, 2 and 26.7 m at sections 3, 4. In other words, seasonal variability range is three times greater than interannual variability one which corresponds to the values given above for the coast without hydraulic structures. At the same time, the range of fluctuations is approximately twice as large.

The pronounced antiphase of fluctuations is noteworthy. The coastline progradation westwards of the water intake corresponds to a retreat from the east and vice versa, while the correlation coefficient of the two series is 0.6. Obviously, this is due to variation in the direction of the alongshore sediment flow. This is even better seen in the graph of interannual variability obtained from the analysis of

satellite images from the Google Earth service. We used 19 images obtained during 2006–2022 (Fig. 4).

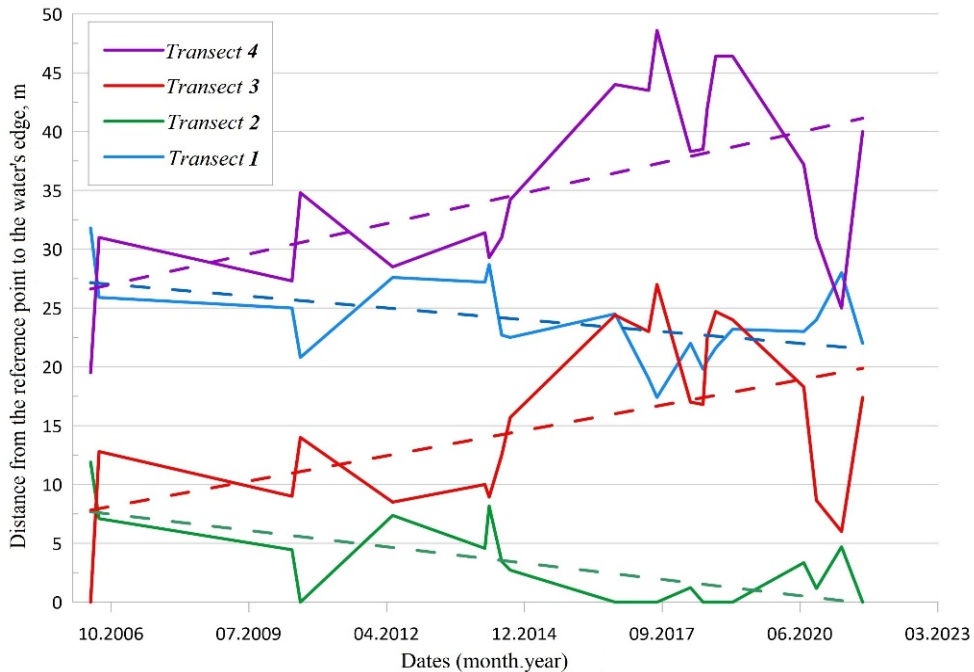


Fig. 4. Interannual variability of distance from the benchmarks to the water’s edge at sections 1–4

In addition to the antiphase of the coastline position fluctuations on both sides of the water intake, a positive trend is also noticeable on the western side and a negative one – on the eastern side.

To determine the coastline variability on the 500 meter long sections adjacent to the water intake on both sides, 50 cross-sections of the beach drawn every 20 m were analyzed. The main calculation algorithms described in the DSAS module ⁶ were applied for the analysis.

Fig. 5 shows the following results. For each section, the distances between the two lines corresponding to the maximum and minimum dates (resulting displacements) and the maximum coastline displacements (positive values of the range, independent of the date) were calculated. Fig. 5 also shows that the coastline advanced on the water intake western side by 8–20 m over a distance of 200–250 m and then insignificantly (1–3 m) over the period 2006–2022. On the eastern side, a coastline retreat is observed in all sections with a typical value of 4 m (maximum up to 8 m). At the same time, the maximum coastline displacements reach 26–28 m on the water intake western side and 12–16 m on the eastern side. Moreover, the greatest values are observed in five sections (100 m) on both sides of the water intake. The range of coastline fluctuations coincides almost completely

⁶ Himmelstoss, E.A., Henderson, R.E., Farris, A.S., Kratzmann, M.G., Bartlett, M.K., Ergul, A., McAndrews, J., Cibaj, R., Zichichi, J.L. and Thieler, E.R., 2024. *Digital Shoreline Analysis System version 6.0: U.S. Geological Survey software release*. <https://doi.org/10.5066/P13WIZ8M>

with the values obtained during measurements at the sections. The comparison of figures can also show that it is necessary to use not the extreme dates of the images, but their entire available array to determine the coastline dynamics. To state the coastline interannual variability, the obtained values of the edge position for each section were averaged within a year and along the entire length of the sections. Undoubtedly, such averaging contains errors associated with the failure to take into account seasonal and spatial variability. Nevertheless, it gives some idea of the interannual variability (Fig. 6). The typical range of interannual fluctuations along the entire length of the sections is 1–7 m, which practically corresponds to the values obtained from measurements at the sections in 1983–1990. It should also be noted that the sediment accumulation predominantly on the western side of the water intake and the greater range of fluctuations compared to the eastern side can indirectly confirm our earlier conclusion about the predominance of a clockwise alongshore sediment flow in this area [7]. This differs from the opinions of other authors who believed that in the area under consideration the counterclockwise flow weakened gradually⁴ [2].

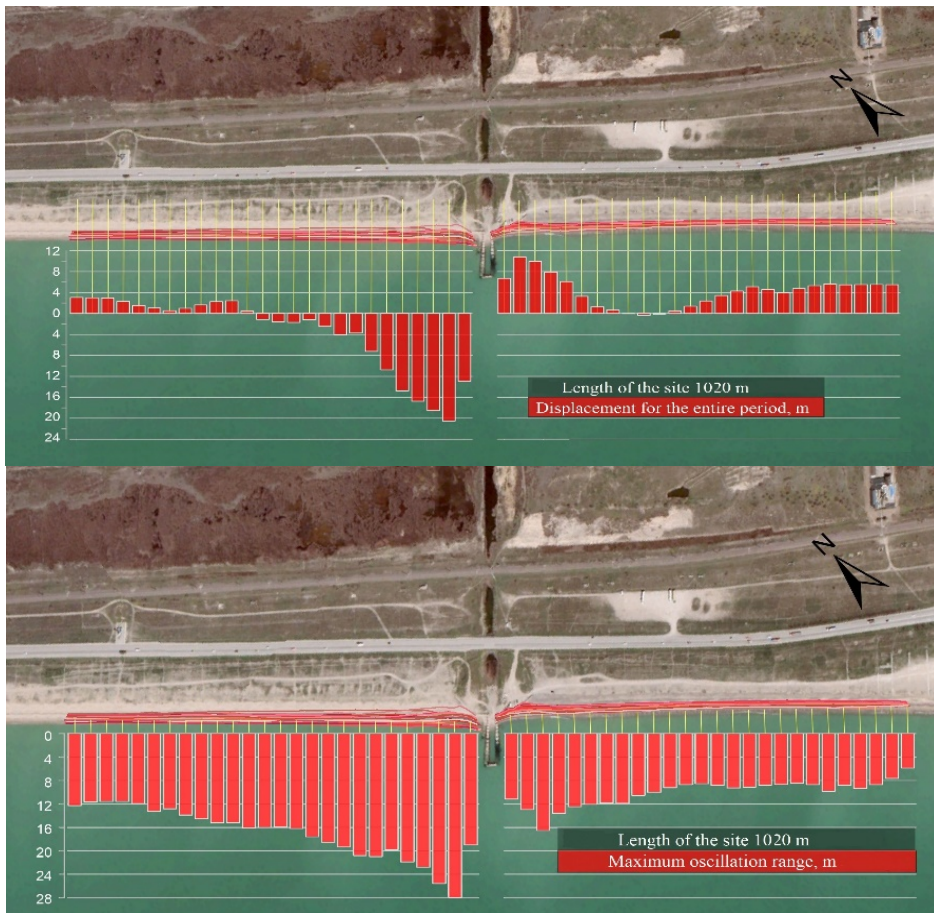


Fig. 5. Resultant (top) and maximum (bottom) coastline displacements in 2006–2022 based on satellite images

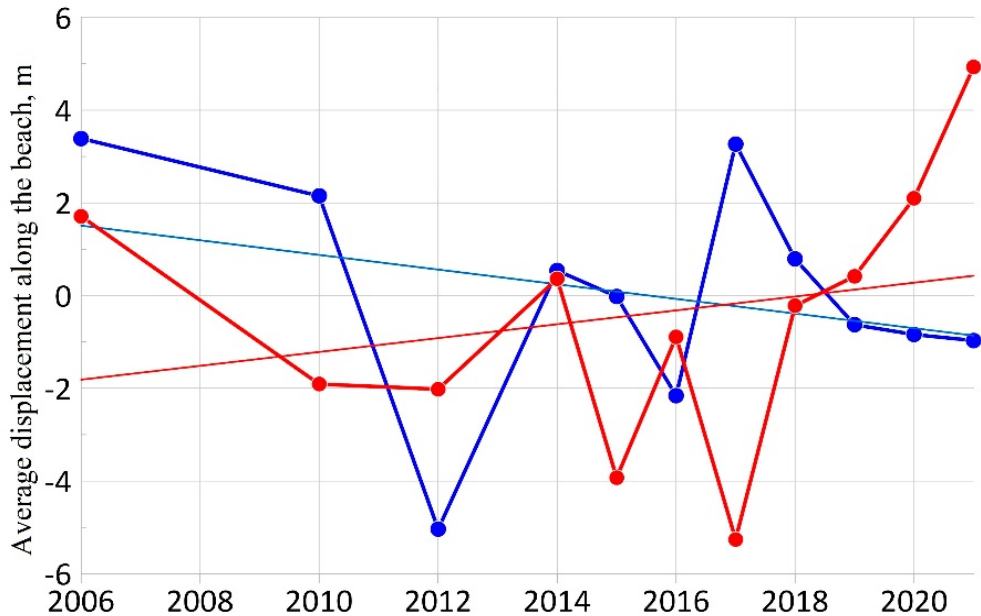


Fig. 6. Average over the section length interannual variability of coastline to the west (red curve) and east (blue curve) from water intake in 2006–2022. Straight lines show trends

Wave climate in the area of the Lake Sasyk bay-bar

The wave climate has a decisive effect on the lithodynamic processes in the area of the Lake Sasyk bay-bar. For its study, the data of wind wave reanalysis in the Black Sea for the period 1979–2022 (hereinafter referred to as the SWAN-ERA array) were applied. The array was obtained using SWAN⁷ model on an unstructured computational mesh with thickening in the coastal zone [8]. ERA-Interim and ERA5 reanalysis data from the apps.ecmwf.int website were used as atmospheric forcing. The computational grid node closest to the technological structure with a depth of ~6.8 m was selected from SWAN-ERA array and long-term series including speed W and direction θ_a of wind, significant wave height h_s , mean wave period $\bar{\tau}$, mean wave direction θ were formed. The discreteness of series was 1 hour.

We are to consider some statistical characteristics of waves obtained from the calculated series. Fig. 7 demonstrates repeatability p of significant wave heights and mean wave periods. As can be seen, waves of 0.25 m height have the maximum repeatability. As the wave height increases, its repeatability decreases monotonically. Values h_s do not exceed 0.5 m in 71% of all cases. At $h_s \geq 1$, the waves have a repeatability of 12%, at $h_s \geq 2.0$ m – less than 1.5%. The highest repeatability of mean wave periods falls on the interval of 2.0–2.5 s which includes 56% of all cases.

⁷ The SWAN Team, 2018. *SWAN User Manual. SWAN Cycle III Version 41.20*. Delft, Netherlands: Delft University of Technology, 121 p.

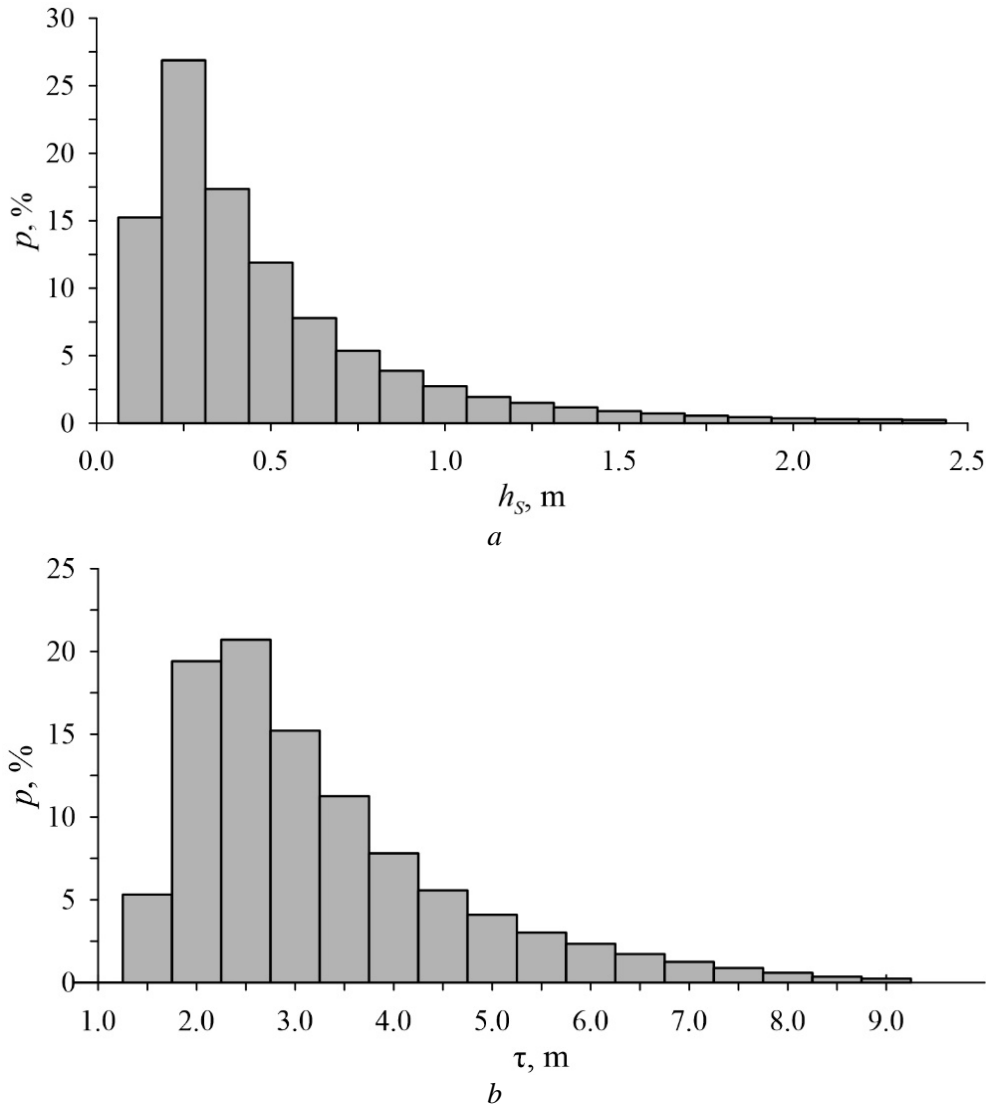


Fig. 7. Repeatability of significant wave heights (*a*) and wave mean periods (*b*)

Fig. 8 shows the wind speed repeatability by direction (wind rose). The northeasterly wind has the maximum repeatability (10%) and maximum speeds. From the sea, the southwesterly wind has the highest repeatability (6%). The most probable direction of wave approach to the shore is southwest with a repeatability of $> 30\%$ (Fig. 9). The highest waves ($h_s > 2.5$ m) also come from this direction. The maximum direction repeatability of waves approaching the shore correspond to the maximum repeatability of wind direction from the open sea. This approach of waves is facilitated by refraction, under the effect of which, as they approach the shore, the wave fronts are oriented parallel to the isobaths.

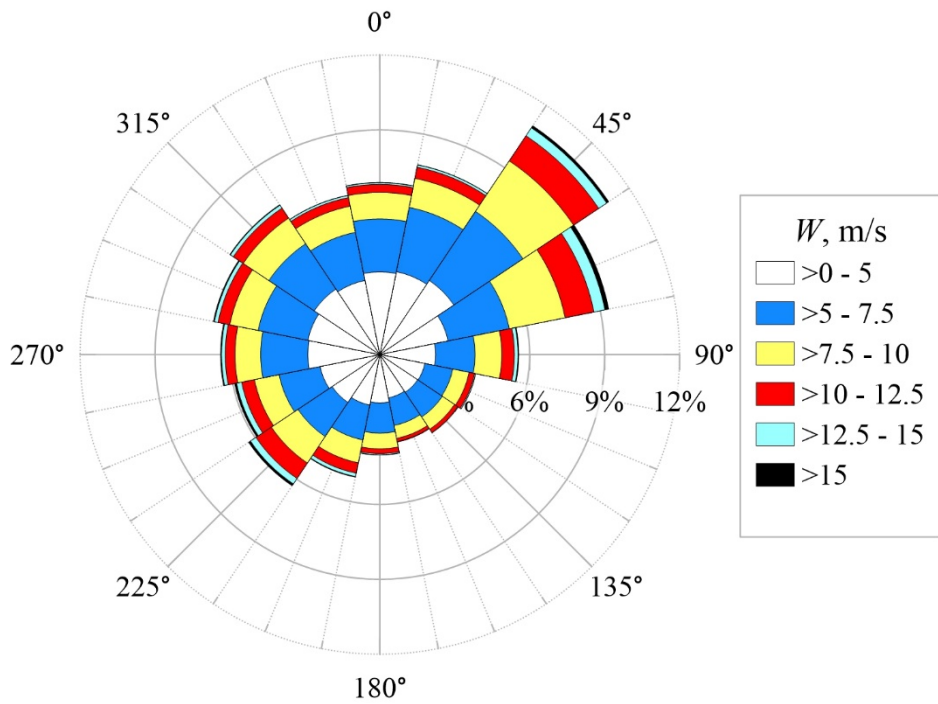


Fig. 8. Wind rose

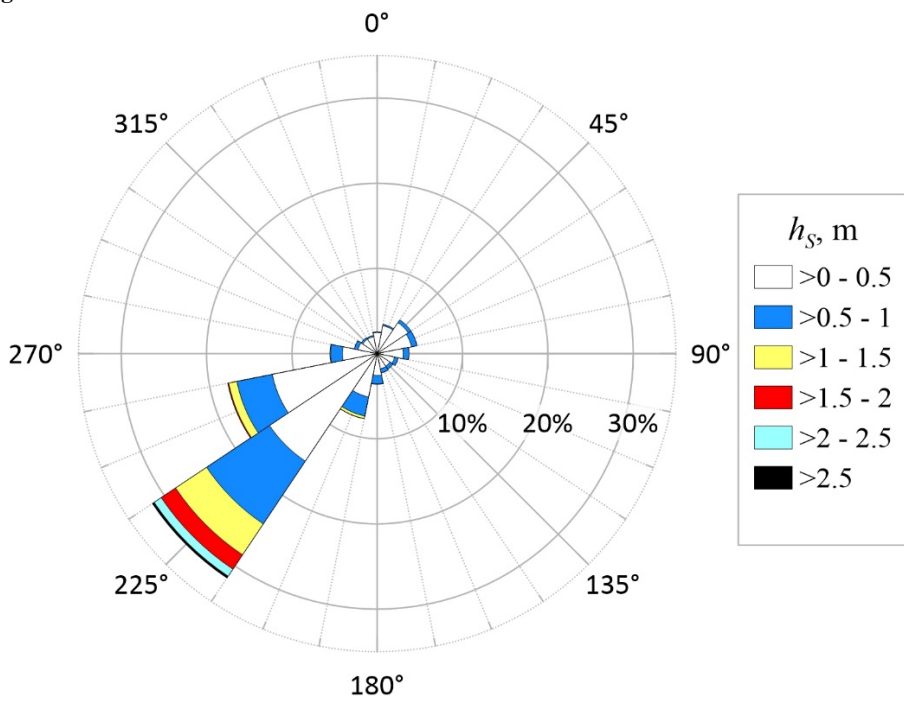


Fig. 9. Wave rose

Based on the available wave series, the duration of storm situations was also estimated. According to [1, 9], we applied the following condition as a criterion for identifying storm events

$$h_s \geq h_p, \quad (1)$$

where $h_p = \bar{h}_s + 2\sigma = 1.372$ m is h_s threshold value; $\bar{h}_s = 0.544$ m is h_s mean long-term value for a given series; $\sigma = 0.414$ m is h_s root-mean-square deviation from \bar{h}_s .

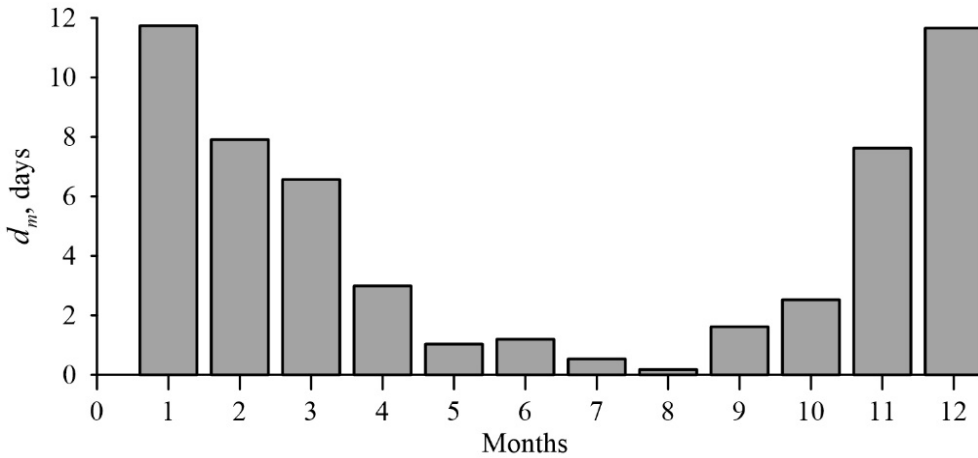


Fig. 10. Distribution of mean long-term duration d_m of storms by months

Fig. 10 demonstrates seasonal variation of mean annual duration d_m of storms. The longest storm situations in the area under study occur in December – January ($d_m > 10$), the minimum duration of storms ($d_m < 1$) is observed in July – August.

Fig. 11 represents the distribution of total duration d of storm situations by year. As can be seen, it varies within 4.9–26.0 days. The mean d value is 15.1 days. A long total duration of storms ($d > 20$ days) is observed in 1981, 1983, 1995, 2001, 2017 and 2021. The storms of 2001 and 2021 have the longest total duration.

Total distribution of storm duration does not provide an idea of their intensity. From this point of view, a more informative characteristic is the storm power index (*SPI*) [1, 9]:

$$SPI = h_d^2 \cdot T_d, \quad (2)$$

where T_d is storm duration (h); h_d is mean h_s (m) value over the storm period. In formula (2), when calculating T_d and h_d , all values of h_s series that satisfy condition (1) are summed up.

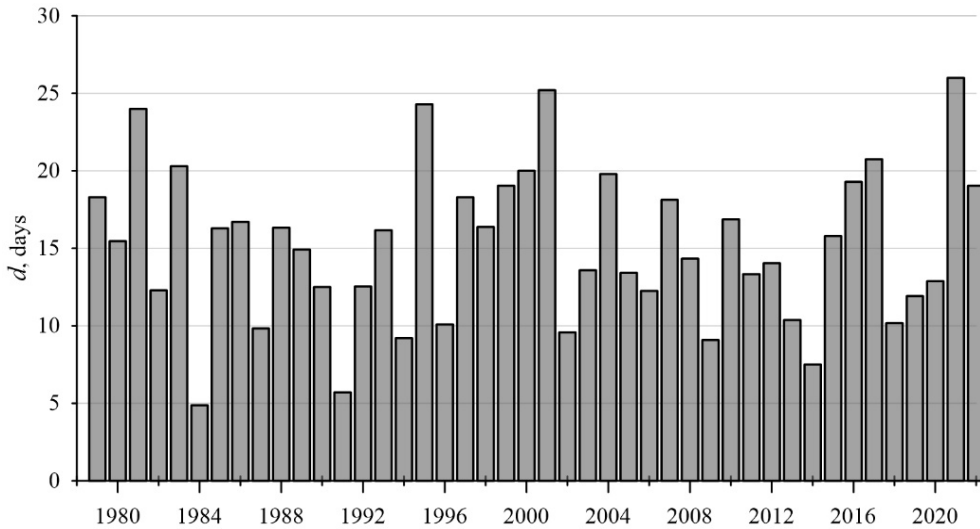


Fig. 11. Distribution of total storm duration d by years

Fig. 12 shows the distribution of total dimensionless storm power index $SPI_1 = SPI/SPI_0$ by year, where $SPI_0 = 0.573 \cdot 10^6 \text{ m}^2 \cdot \text{h}$ is the mean SPI value. 5 years (1994, 1995, 2001, 2009 and 2015) with increased storm activity ($SPI_1 > 1.5$) stand out in the graph. It is noteworthy that this list does not include 2021, which has the maximum total duration of storms (Fig. 11).

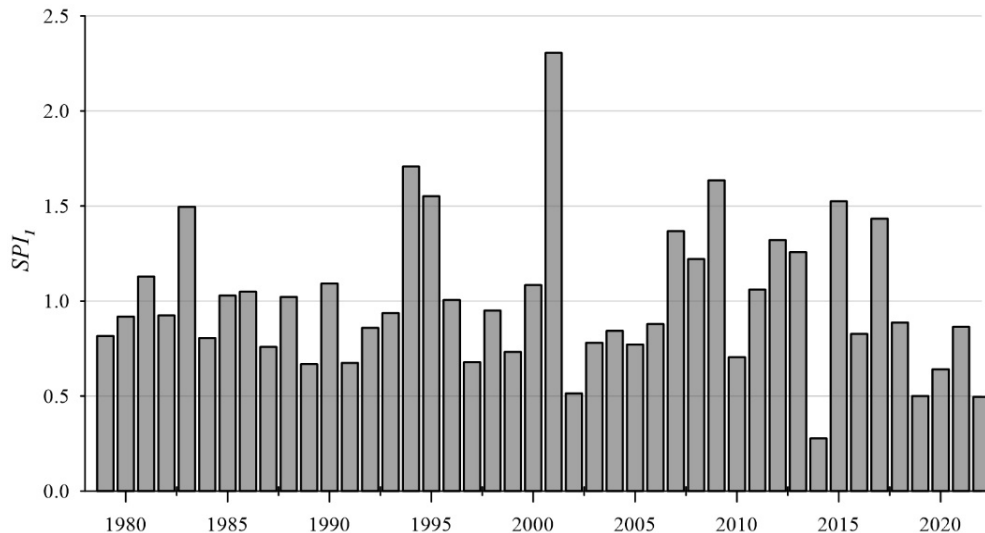


Fig. 12. Distribution of the storm power index SPI_1 by years

Extreme values of wave characteristics possible once per n years were estimated using the standard method described in [1]. Table 1 presents the estimates obtained. As can be seen, the wave heights of different probability and recurrence periods T differ slightly from each other which is due to the shallowness of the area under

study. With T increase from 1 to 100 years, h_s values increase by 19% and $h_{1\%}$ values – by 15%.

Table 1

Significant wave heights h_s , mean wave heights \bar{h} , wave heights of 13%-, 3%- and 1%-probability, mean wave periods $\bar{\tau}$, mean wave length $\bar{\lambda}$ in the system of storms which are possible once per 1, 5, 10, 25, 50 and 100 years

h_s , m	\bar{h} , m	$h_{13\%}$, m	$h_{3\%}$, m	$h_{1\%}$, m	$\bar{\tau}$, s	$\bar{\lambda}$, m
2.6	1.6	2.4	3.0	3.3	9.4	72
2.7	1.7	2.5	3.1	3.4	10.4	81
2.8	1.8	2.6	3.2	3.5	11.0	86
2.9	1.8	2.7	3.3	3.6	11.6	91
3.0	1.9	2.8	3.3	3.7	12.1	95
3.1	1.9	2.8	3.4	3.8	12.6	100

For a calculated storm that is possible once per 25 years, wave parameter values are as follows: $h_s = 2.9$ m, $h_{1\%} = 3.6$ m, $\bar{\tau} = 11.6$ s, $\bar{\lambda} = 91$ m. Note that these wave characteristics are basic when designing coastal protection structures such as groins and breakwaters.

Table 2

Storm situation statistics for different gradations t_s

t_s , h	N_s	\bar{T}_d , h	SPI_m , m ² ·h
≥ 6	724	21	80
≥ 12	548	26	98
≥ 24	231	38	153
≥ 36	96	52	216
≥ 48	51	61	263

Now we are to analyze statistical characteristics of individual storms. For the sake of certainty, we consider storm situations with a duration (t_s) of at least 6 h. Table 2 provides the following for each of the five selected gradations t_s : total number of storms N_s ; mean duration of storms \bar{T}_d ; mean storm power index SPI_m . As the lower threshold of gradations increases, the number of storms decreases. If for gradation $t_s \geq 12$ h there are 548 storm events with mean

duration of 26 h and mean storm power index of 98 $\text{m}^2\cdot\text{h}$, then for gradation $t_s \geq 48$ h only 51 events were identified. Mean duration of these events is 61 h and mean power index is 263 $\text{m}^2\cdot\text{h}$.

Figure 13 shows the distribution of N_s values by years for five storm duration gradations t_s given in Table 2. The histograms shown there detail the information from Fig. 11. For all years except 2021, N_s value for $t_s \geq 6$ h is less than 25. According to $t_s \geq 6$ h gradation, 2021 has the largest storm number ($N_s = 35$). However, this year is inferior to other years in terms of the number of the longest (strongest) storms. For $t_s \geq 48$ h gradation, the number of storms in descending order is as follows: $N_s = 6$ for 1995; $N_s = 5$ for 1981; $N_s = 4$ for 2001; $N_s = 3$ for 1986 and 2007. Next comes a group of eight years with $N_s = 2$ which includes 2021. Another 12 years have $N_s = 1$. Mean long-term values of storm number by gradations of duration are as follows: 16 storms for $t_s \geq 6$ h; 12 storms for $t_s \geq 12$ h; 5 storms for $t_s \geq 24$ h; two storms for $t_s \geq 36$ h; one storm for $t_s \geq 48$ h.

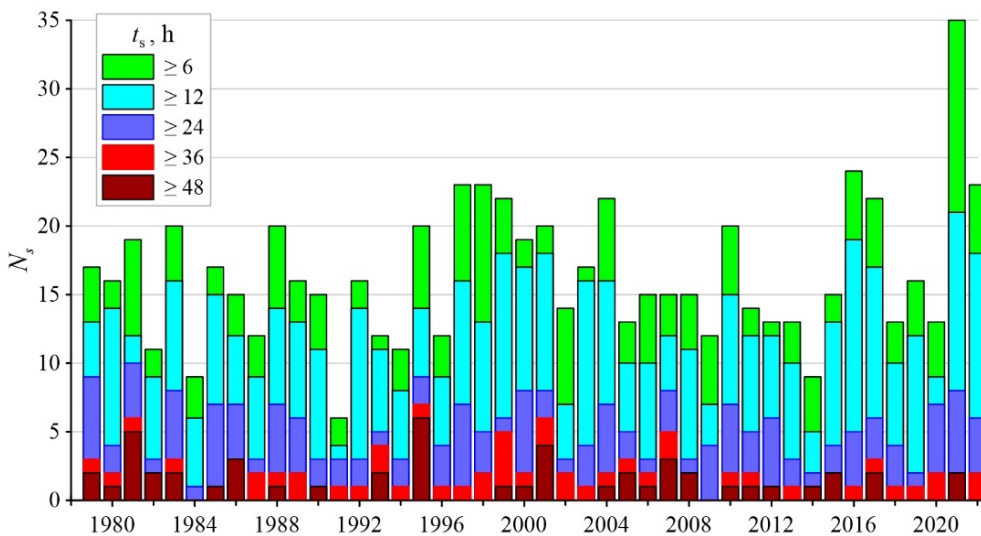


Fig. 13. Distribution of storm number N_s for different gradations t_s by years

Table 3 contains the characteristics of ten most powerful storms in the area under study based on wave reanalysis data for the period 1979–2022. Initial date of storm occurrence is given in the following format: year, month, day, hour. Four storms with SPI power index > 400 $\text{m}^2\cdot\text{h}$ are distinguished. The storms that began on December 25, 2000 and November 22, 2001 are the most powerful ones in the past 44 years.

Characteristics of extreme storms

Initial date	T_d , h	h_d , m	SPI , m ² ·h
2000122506	100	2.19	480
2001112210	118	2.01	476
2008112017	81	2.32	437
2015112009	75	2.37	423
1981120714	74	2.26	376
1995122303	67	2.26	344
2015013022	70	2.21	343
1979121019	65	2.27	334
1993012217	88	1.95	334
2021122409	57	2.39	325

Calculation of lithodynamic characteristics in the area of the Lake Sasyk bay-bar

Integral lithodynamic models ^{8, 9} are applied to assess long-term coastline variations [10, 11]. In this paper, we used *GenCade* ⁹ integral model to calculate the coastline variations in the area of the structure. It is based on the coastline evolution equation of the following form

$$\frac{\partial y}{\partial t} + \frac{1}{(D_B + D_C)} \frac{\partial Q}{\partial x} = 0. \quad (3)$$

Here, $y(x, t)$ is coastline coordinate, D_B is berm height, D_C is closure depth, $Q(x, t)$ is alongshore sediment flow. The x coordinate is defined in the interval $[0, L]$, where L is total length of the coastal zone section under consideration. A detailed description of the model is presented in 9 [11].

After integrating equation (3) over the variable x within the range $0-L$, we obtain an ordinary differential equation

$$\frac{dV}{dt} = Q(0, t) - Q(L, t), \quad (4)$$

$$V = (D_B + D_C) \int_0^L y(x, t) dx, \quad (5)$$

⁸ Hanson, H. and Kraus, N.C., 1989. *GENESIS: Generalized Model for Simulating Shoreline Change. Report 1: Technical Reference*. Washington: U.S. Army Corps of Engineers, 247 p. <https://doi.org/10.5962/bhl.title.48202>

⁹ Frey, A.E., Connell, K.J., Hanson, H., Larson, M., Thomas, R.C., Munger, S. and Zundel, A., 2012. *GenCade Version 1 Model Theory and User's Guide: Final Report*. Vicksburg, MS: U.S. Army Engineer Research and Development Center, 187 p.

where V is total volume of sediments; $Q(0,t)$, $Q(L,t)$ are sediment flows on the left ($x = 0$) and right ($x = L$) computational domain boundaries, respectively. Equation (4) describes temporal variation of the total volume of sediments (formula (5)) at the studied beach area. If the right side of formula (4) is different from zero, then there will be an increase or decrease in the total volume of transported material.

The computational domain was a section of the coast totaling 1000 m selected in such a way that the structure was located in its middle. General direction of the coastline was 129° (the direction of the x -axis is close to northwest). Thus, positive Q values correspond to the movement of sediments from the southeast to the northwest in the adopted coordinate system. The calculation grid step in space was 20 m, the integration step in time was 4 min. According to [12], granulometric composition of bottom sediments at the water intake is characterized by the presence of a sand-gravel mixture, medium-grained and fine-grained sand. Moreover, the sand-gravel mixture is the predominant fraction. On this basis, the mean diameter of bottom sediment particles d_{50} was taken to be 0.8 mm.

To calculate the sediment flux Q in equation (3), a composite array of wave parameters (h_s , $\bar{\tau}$ and θ) obtained from *SWAN-ERA* data was applied. The array included only waves directed toward the shore, i.e. those waves for which the inequality $|\theta - \theta_N| < 90^\circ$ is true, where $\theta_N = 219^\circ$ is the direction of the normal to the general coastline direction of the area under consideration.

Based on preliminary calculations, the following values of model 9 parameters were selected: normalization constants in the formula for calculating the sediment flow $K_1 = K_2 = 0.77$; berm height $D_B = 2$ m; permeability coefficient of the structure $p = 0.2$. In all cases, closure depth in equation (3) $D_C = 5.5$ m. To estimate D_C , an empirical dependence of type 9 was applied:

$$D_C = 2.28 \cdot h_E - 68.5 \frac{h_E^2}{g \tau_E^2},$$

where h_E , τ_E are mean values of annual maxima h_s and $\bar{\tau}$, respectively, obtained from *SWAN-ERA* wave reanalysis data.

Calculations of the coastline variation in the technological structure area were carried out from March 12, 2014 to July 23, 2022, since, based on the analysis of Google Earth service satellite images, the greatest variability in the coastline position was observed during this period and the quality of images made it possible to digitize the coastline position. Numerical experiments revealed that the calculated coastline position corresponding to July 23, 2022 and its position in satellite images coincide in the best possible way with the selected values of model parameters. At the same time, a characteristic detail is traced: an accumulation of beach material takes place on the northwestern side of the structure, and coast erosion occurs on the southeastern side (Fig. 14).

In addition to coastline position variation, its increments were also calculated for each of four sections by formula $\Delta y^i(x) = y_s^i(x) - y_f^i(x)$, where $y_s^i(x)$ and $y_f^i(x)$ are coastline position at section i at the initial and final moments of time, respectively.

Positive Δy^i values correspond to the coastline progradation, negative values – to its retreat.

For each section 1–4, the minimum values of calculated increments Δy_{\min}^i were found and graphs of calculated relative increments $y_r^i(x) = \Delta y^i - \Delta y_{\min}^i$ were constructed for the simulated time period of March 12, 2014 – July 23, 2022 (Fig. 15). The trends (dashed lines of the same color) corresponding to relative increments for each section are also given in the figure.

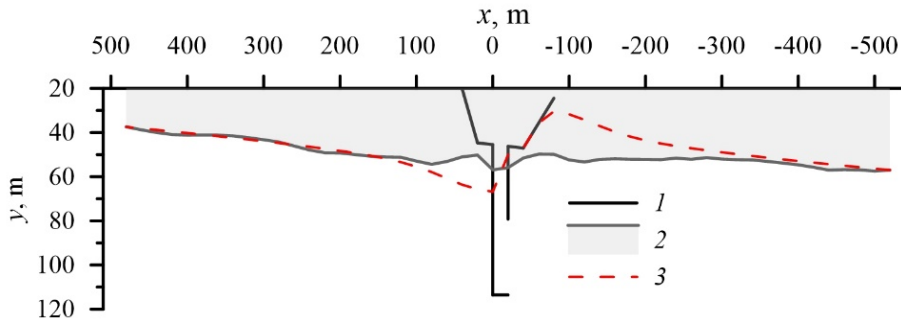


Fig. 14. Results of calculating the changes in coastline position: 1 – water intake construction; 2 – initial coastline position on March 12, 2014; 3 – calculated coastline position on July 23, 2022

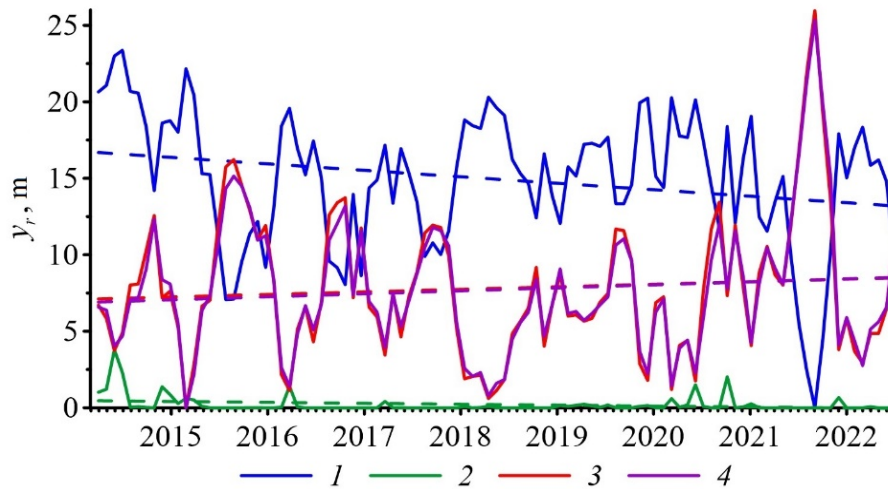
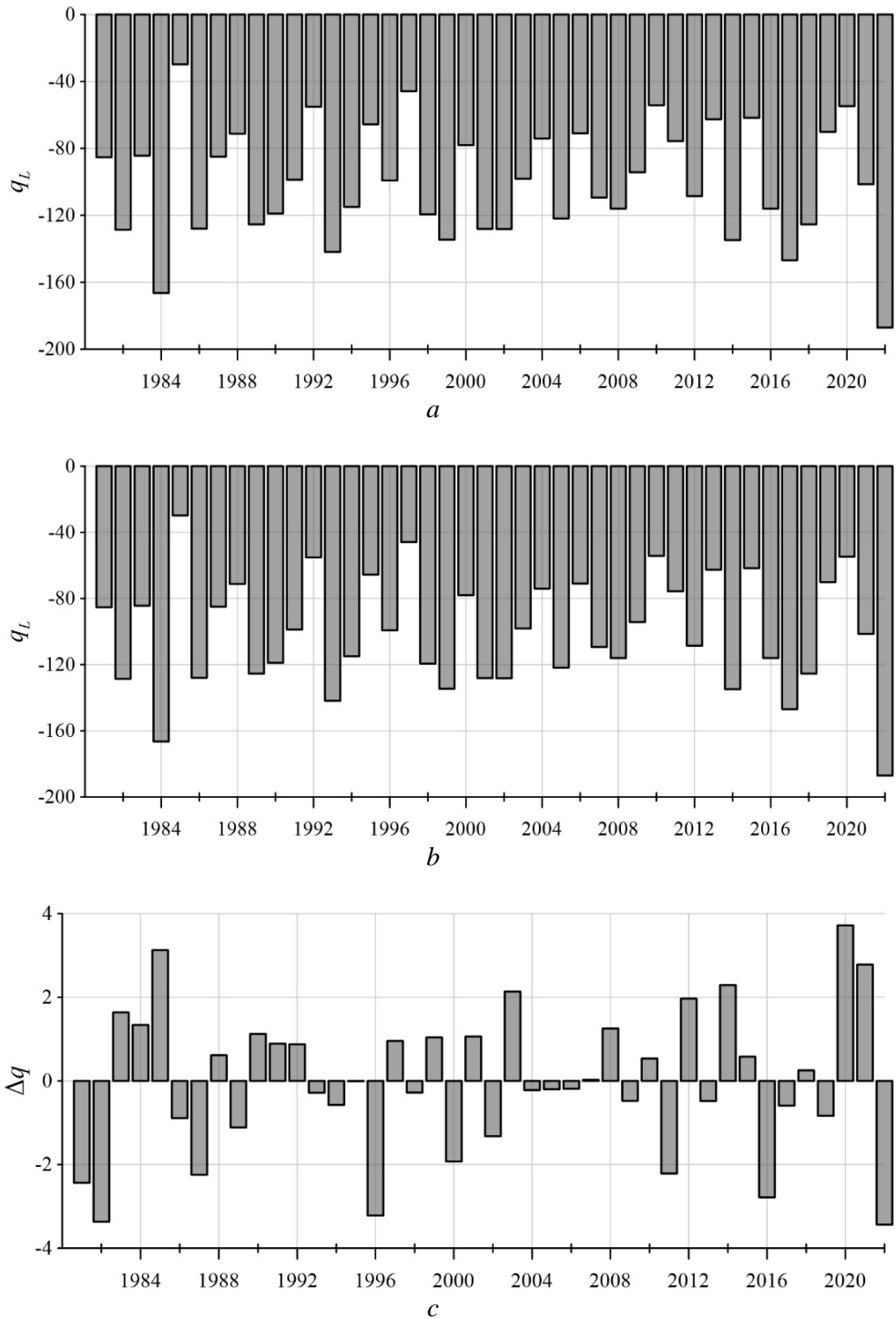


Fig. 15. Calculated relative increments of the coastline position y_r at sections 1–4 from 12.03.2014 to 23.07.2022. Dashed lines show trends

The calculation results revealed that there was a coastline retreat with mean long-term rate of ~ 0.42 and 0.06 m/year, respectively, at sections 1 and 2 and a beach width increase with a mean long-term rate of approximately 0.17 and 0.19 m/year took place at sections 3 and 4. Thus, the model calculation results reproduce the effects of beach material accumulation northwestwards of the structure and coast erosion southeastwards of it, described above based on *in situ* data.



F i g. 16. Mean annual values of sediment rates: a – at the southeastern boundary ($x = 0$); b – at the northwestern boundary ($x = L$); c – difference between the sediment rates at the southeastern and northwestern boundaries

Mean annual values of sediment rates on the left (q_0) and right (q_L) computational domain boundaries, as well as their difference Δq , presented in dimensionless form are given in Fig. 16 for the period 1979–2022. They were calculated using formulas

$$q_0 = 10^2 \cdot \bar{Q}_0 / q_m, \quad q_L = 10^2 \cdot \bar{Q}_L / q_m, \quad \Delta q = q_0 - q_L,$$

where \bar{Q}_0 and \bar{Q}_L are mean annual sediment flows on the left and right boundaries, respectively; $q_m = 75900 \text{ m}^3/\text{g}$ is normalization constant representing mean long-term value of sediment flows at the left and right boundaries for 1979–2022 period.

As can be seen from the analysis of the presented diagrams, the mean annual values of q_0 and q_L are negative for the entire long-term time interval, i.e. the sediment flows are directed southeastwards. Their maximum absolute values reach $1.9 \cdot q_m$ and the standard deviation is $\pm 35\%$ of q_m . Unidirectionality of the flows is due to the coastline orientation and wave climate characteristics. In the area under study, the prevailing direction for the waves approaching the coast is sector $225^\circ \leq \theta \leq 235^\circ$ (Fig. 9), and the normal to the coastline general direction is oriented at an angle of $\theta_N = 219^\circ$. It is with this ratio of the angles between the waves approaching the coast and the normal to the coastline that the sediment flows of the southeastern direction will prevail.

The difference in flows at the Δq area boundaries changes sign from year to year (Fig. 16, c). According to equation (4), at $\Delta q > 0$, material accumulates in the area under study, at $\Delta q < 0$ material is consumed. As can be seen, the difference in flows between the left and right boundaries of the computational area is insignificant (less than $\pm 4\%$ of q_m). This indicates that the studied area is mainly transit of material. At the same time, local changes in the sediment flow near the technological structure do not have a significant effect on the total transport of bottom material in the southeastern direction.

Conclusion

A comprehensive study of lithodynamic processes was carried out on a section of the Crimean coast adjacent to Lake Sasyk and including a transverse hydraulic structure.

Based on the analysis of the coastline position *in situ* measurements in the area of the structure for 2006–2014, it was found that the maximum range of interannual fluctuations was 5.8 m at the sections to the southeast of the structure and 3.4–7.2 m at the sections to the northwest. Seasonal variability is significantly higher: for example, their maximum range is 14.6 m at the sections southeastwards of the structure and 26.7 m at the sections to the northwest. Analysis of the coastline position satellite images in the structure area revealed that the range of coastline fluctuations is in very good agreement with the estimates obtained from *in situ* measurements.

The study of wave climate in the technological structure area was carried using the reanalysis data for 1979–2022. It indicated that the most probable direction of

wave approaching the coast is southwestern one with a frequency of $> 30\%$. The highest waves also come from this direction. The extreme values of wave characteristics which can occur once in n years were obtained. The mean long-term values of storm numbers in the area under study are given depending on their duration.

Application of the *GenCade* integrated lithodynamic model permitted to obtain the estimates of changes in the coastline position in this area on the interannual scales. The model calculations made it possible to reproduce the main features and trends in changes of the beach width in the area of the structure obtained due to *in situ* observations. The mean annual sediment flows in the area under study are directed clockwise (to the southeast) that is conditioned by the coastline orientation and the wave climate features. Difference between the mean annual sediment rates at the area boundaries is negligible ($< 4\%$ of the multi-year average). This fact indicates insignificant impact of the structure upon the sediment total transfer to the southeast.

Under modern conditions, sediment flows in the area under study are balanced, and the coastline position is relatively stable. At the same time, cyclic changes in the coastline position directly at the water intake are typical. They are associated with changes in the directions of storm waves approaching the coast and, accordingly, the alongshore sediment flow. Any lithodynamic system consisting of both underwater (coastal slope) and above-water (beach) parts is extremely sensitive to the volumes and scales of external impacts. The construction of hydrodynamic structures in the coastal zone should be based on careful preliminary studies, including *in situ* observations, as well as physical and numerical modeling.

REFERENCES

1. Fomin, V.V. and Goryachkin, Yu.N., 2022. Accounting for the Local Wave and Morphodynamic Processes in Coastal Hydraulic Engineering. *Physical Oceanography*, 29(3), pp. 271-290. <https://doi.org/10.22449/1573-160X-2022-3-271-290>
2. Shuisky, Yu.D., 2005. Basic Peculiarities of Morphology and Dynamic of the Western Crimea Peninsula Coast. In: MHI, 2005. *Ecological Safety of Coastal and Shelf Zones and Comprehensive Use of Shelf Resources*. Sevastopol: ECOSI-Gidrofizika. Iss. 13, pp. 62-72 (in Russian).
3. Shuyskiy, Yu.D. and Karasyev, L.M., 1983. Eol Processes on Coastal Accumulative Forms in the West Crimea. *Izvestiya VGO*, 115(6), pp. 503-508 (in Russian).
4. Vykhovanets, G.V., 2003. [*Aeolian Process on the Sea Shore*]. Odessa: Astroprint, 368 p. (in Russian).
5. Goryachkin, Yu.N. and Dolotov, V.V., 2019. *Sea Coasts of Crimea*. Sevastopol: Kolorit Co. Ltd., 256 p. (in Russian).
6. Subetto, D.A., Sapelko, T.V., Stolba, V.F., Kuznetsov, D.D., Ludikova, A.V. and Neustrueva, I.Yu., 2023. Paleolimnology of Lakes of Western Crimea. *Doklady Earth Sciences*, 510(1), pp. 329-334. <https://doi.org/10.1134/S1028334X23600184>
7. Udovik, V.F. and Goryachkin, Yu.N., 2013. Interannual Variability of Alongshore Sediment Flux in the Coastal Zone of Western Crimea. In: MHI, 2013. *Ecological Safety of Coastal and Shelf Zones and Comprehensive Use of Shelf Resources*. Sevastopol: MHI. Iss. 27, pp. 363-368 (in Russian).
8. Divinsky, B.V., Fomin, V.V., Kosyan, R.D. and Ratner, Yu.D., 2020. Extreme Wind Waves in the Black Sea. *Oceanologia*, 62(1), pp. 23-30. <https://doi.org/10.1016/j.oceano.2019.06.003>
9. Amarouche, K. and Akpınar, A., 2021. Increasing Trend on Storm Wave Intensity in the Western Mediterranean. *Climate*, 9(1), 11. <https://doi.org/10.3390/cli9010011>

10. Leont'yev, I.O. and Akivis, T.M., 2020. The Effect of a Groin Field on a Sandy Beach. *Oceanology*, 60(3), pp. 412-420. <https://doi.org/10.1134/S0001437020030042>
11. Lazorenko, D.I., Kharitonova, L.V. and Fomin, V.V., 2016. Calculation of Changes Beach Shoreline Yevpatoriya Coast under the Influence Wind Waves. *Ecological Safety of Coastal and Shelf Zones of Sea*, (1), pp. 31-38 (in Russian).
12. Gurov, K.I., Udovik, V.F. and Fomin, V.V., 2019. Modeling of the Coastal Zone Relief and Granulometric Composition Changes of Sediments in the Region of the Bogaily Lake Bay-Bar (the Western Crimea) during Storm. *Physical Oceanography*, 26(2), pp. 170-180. <https://doi.org/10.22449/1573-160X-2019-2-170-180>

Submitted 12.12.2023; approved after review 06.05.2024;
accepted for publication 16.05.2024.

About the authors:

Yuri N. Goryachkin, Chief Research Associate, Marine Hydrophysical Institute of RAS (2 Kapitanskaya Str., Sevastopol, 299011, Russian Federation), DSc. (Geogr.), **ORCID ID: 0000-0002-2807-201X**, **ResearcherID: I-3062-2015**, yngor@mhi-ras.ru

Dmitry I. Lazorenko, Research Associate, Department of Computational Technologies and Mathematical Modeling, Marine Hydrophysical Institute of RAS (2 Kapitanskaya Str., Sevastopol, 299011, Russian Federation), CSc. (Tech.), **ORCID ID: 0000-0001-7524-565X**, **ResearcherID: J-1925-2015**, d.lazorenko.dntmm@gmail.com

Vladimir V. Fomin, Head of Department of Computational Technologies and Mathematical Modeling, Marine Hydrophysical Institute of RAS (2 Kapitanskaya Str., Sevastopol, 299011, Russian Federation), DSc. (Phys.-Math.), **ORCID ID: 0000-0002-9070-4460**, **ResearcherID: H-8185-2015**, v.fomin@mhi-ras.ru

Contribution of the co-authors:

Yuri N. Goryachkin – research initiation; formulation of the study goals and objectives; qualitative analysis of the results and their interpretation; discussion of the work results; formulation of conclusions; literature review on the research problem; search and critical analysis of materials in domestic and foreign sources; preparation of the paper text; editing and revision of the text; data visualization / presentation in the text

Dmitry I. Lazorenko – mathematical modeling of lithodynamic processes; analysis of modeling results; preparation of paper text; construction of tables, graphs, diagrams; discussion of paper materials; revision of paper text

Vladimir V. Fomin – mathematical modeling of wave regime; analysis of modeling results; preparation of paper text; construction of graphs, diagrams; discussion of the paper materials; revision of the paper text

The authors have read and approved the final manuscript.

The authors declare that they have no conflict of interest.

Comparison of Bio-Optical Properties of Optically Complex Waters with Different Trophic Status

T. Ya. Churilova^{1,✉}, T. V. Efimova¹, N. A. Moiseeva¹,
E. Yu. Skorokhod¹, D. V. Kalmykova¹, I. A. Sutorikhin²,
V. V. Kirillov²

¹ *A. O. Kovalevsky Institute of Biology of the Southern Seas of RAS,
Sevastopol, Russian Federation*

² *Institute for Water and Environmental Problems of SB of RAS,
Barnaul, Russian Federation*

✉ tanya.churilova@ibss-ras.ru

Abstract

Purpose. Development of regional satellite algorithms requires the information on bio-optical properties of a particular water area. The present study is aimed at comparative analysis of bio-optical properties of optically complex waters differing in their trophic status.

Methods and Results. The study combined the results of measuring the spectral bio-optical properties in the waters of the Black, Azov, Barents and Norwegian seas, the Arctic and Southern oceans (Atlantic sector) and Baikal and Teletskoye lakes. Spectral coefficients of light absorption by phytoplankton, non-algal particles and colored dissolved organic matter were measured in accordance with the *International Ocean Colour Coordinating Group* Protocols. The study areas included the waters with trophic levels from the oligotrophic to the eutrophic ones (the chlorophyll *a* concentrations in the surface layers varied from 0.066 to 24 mg·m⁻³) and with high heterogeneity in their bio-optical properties: the total non-water light absorption at the wavelength of 438 nm varied from 0.021 to 0.97 m⁻¹.

Conclusions. In all the regions, a high (within an order of magnitude or higher) spatial variability in the values of light absorption coefficients by all the optically active components and their ratios was noted. This fact indicates the optical complexity of waters in each of the regions under study. The regional specificity of parameterization coefficients for light absorption by phytoplankton, non-algal particles and colored dissolved organic matter was shown. The revealed parameterization coefficients for light absorption by the optically active environment components can be used to develop regional satellite algorithms for assessing water quality and productivity indicators. Based on the empirically revealed dependencies, the following additional indicators of water quality were proposed: the euphotic zone depth and the spectral characteristics of downwelling irradiance which can be retrieved based on remote sensing data.

Keywords: chlorophyll *a*, light absorption, phytoplankton, non-algal particles, colored dissolved organic matter, Black Sea, Sea of Azov, Barents Sea, Norwegian Sea, Arctic Ocean, Southern Ocean, Lake Baikal, Lake Teletskoye

Acknowledgements: The study was carried out within the framework of the state assignment theme No. 124030100106-2 “Study of regional features of bio-optical properties of water bodies as a basis for decoding remote sensing data to assess multi-scale variability of primary production characteristics of pelagic ecosystems”. The authors are grateful to the reviewers for their useful recommendations and comments.

For citation: Churilova, T. Ya., Efimova, T. V., Moiseeva, N. A., Skorokhod, E. Yu., Kalmykova, D. V., Sutorikhin, I. A. and Kirillov, V. V., 2024. Comparison of Bio-Optical Properties of Optically Complex Waters with Different Trophic Status. *Physical Oceanography*, 31(4), pp. 507-526.

© 2024, T. Ya. Churilova, T. V. Efimova, N. A. Moiseeva, E. Yu. Skorokhod, D. V. Kalmykova, I. A. Sutorikhin, V. V. Kirillov

© 2024, Physical Oceanography



Introduction

In the context of a changing climate [1] and an increasing negative impact of human activity on nature, the issues of operational monitoring of the aquatic ecosystem state and forecasting its changes under the influence of natural and anthropogenic factors are becoming increasingly relevant [2, 3]. Remote sensing approach provides an unique opportunity for multiscale recording of aquatic environment parameters and monitoring of the marine areas [4, 5]. However, to date, the complete realization of the unique potential of remote sensing approach has been limited by the capabilities of bio-optical algorithms. Their standard solutions do not provide correct assessments of water quality and productivity indicators on a global scale [6], which is associated with high heterogeneity of the World Ocean in terms of bio-optical water properties [7–9].

Case 2 waters [7], which are typically characterized by a high content of non-algal particles (NAP) and colored dissolved organic matter (CDOM), as well as the lack of correlation between the content of chlorophyll a (a marker of phytoplankton biomass – the third optically active component), are the most difficult to solve the problem of transforming a satellite signal into inherent optical properties of waters (IOPs) [8, 9]. A three-band *Chl*-CDM algorithm [10] has been developed for the Black Sea (Case 2 waters [11]). It ensures accurate retrieval of the IOPs of the Black Sea waters [12]. This algorithm can be adapted for other water bodies of the Russian Federation as well as for the polar regions of the World Ocean, which are of political and economic interest to our country. Empirically revealed dependences of variability of bio-optical properties of waters are required to adapt the *Chl*-CDM algorithm to other water areas, in particular, parameterization of light absorption by all optically active components (phytoplankton, NAP and CDOM), assessment of each component contribution to the total non-water light absorption at different wavelengths.

The bio-optical studies carried out at the modern methodological and technological level in different areas of the World Ocean (the Azov-Black Sea basin, the Arctic, Antarctica, Baikal and Teletskoye lakes) [13–19] make it possible to combine the results obtained in waters with different trophic levels (trophic status) and with different optical complexity. The trophic status of waters is determined based on productivity indicators: chlorophyll a concentration and primary production. The Sea of Azov is a highly trophic region with a high phytoplankton content, high chlorophyll a concentrations and high primary production [20]. The open Black Sea waters are classified as mesotrophic waters [21]. The coastal Black Sea waters are affected by coastal and river runoff and are therefore characterized by high heterogeneity in productivity indicators [22], which is accompanied by a change in the trophic level from mesotrophic to eutrophic. In the Atlantic sector of the Southern Ocean a unique situation was revealed – a high content of nutrients, but a low concentration of chlorophyll a [23], which allows to conclude that the waters in this area are oligotrophic. The waters of the European

sector of the Arctic (the Norwegian and Barents seas, the Arctic Ocean) are mostly (namely the Arctic Ocean waters) oligotrophic [24, 25]. The waters of Lake Baikal have a unique transparency – they are oligotrophic. The highly trophic waters of Lake Teletskoye are subject to intense coastal and river runoff, which determines the ecological state of the waters and their optical properties [26].

The present research is aimed at generalizing the results obtained and at comparative analyzing of bio-optical properties of waters with different trophic status.

Methods

The data obtained in different areas of the World Ocean (Fig. 1) were summarized:

1) the Norwegian Sea, Barents Sea and Arctic Ocean – cruise No. 80 of R/V *Akademik Mstislav Keldysh* (August 2020);

2) the Atlantic sector of the Southern Ocean – cruise No. 79 of R/V *Akademik Mstislav Keldysh* (January – February 2020);

3) the Black Sea, coastal waters of Crimea – cruises No. 106 (April – May 2019) and No. 113 (June 2020) of R/V *Professor Vodyanitsky*, regular weekly bio-optical monitoring on the small R/V *Victoria* (2009 – 2022);

4) the Black Sea, deep-water region – cruise No. 122 of R/V *Professor Vodyanitsky* (June 2022);

5) the Sea of Azov – scientific expeditions on R/V *Professor Vodyanitsky* carried out in different seasons (2016 – 2020);

6) Lake Baikal – expeditions on R/V *G. Yu. Vereshchagin* (July 2018) and on R/V *G. Titov* (September 2019);

7) Lake Teletskoye – expedition on IVEP SB RAS R/V No. 209 (*Yaroslavets* type) (August 2022).

The water samples were collected using a cassette of *GO-Flo* bottles or single bottle. The chlorophyll a concentration in total with phaeopigments (*TChl-a*) was determined spectrophotometrically [27, 28]. The water samples were filtered through glass fiber filters (*Whatman GF/F*) under a vacuum (< 0.2 atm). The filters with the particles were folded, wrapped in foil and stored in dewar with liquid nitrogen until measurement in the laboratory. The pigments were extracted with a 90% acetone solution (5 ml) using a two-stage approach and a vibratory homogenizer for completeness of extraction. The tubes with acetone extracts of the pigments were stored in a refrigerator (+8 °C) for 18 h. The pigment extracts were clarified by sedimentation of the particles by centrifugation for 5 minutes (at a centrifugal acceleration of 5000 g). The optical density (OD) of the acetone extracts of pigments was measured with a *Lambda 35* dual-beam spectrophotometer (*PerkinElmer*).

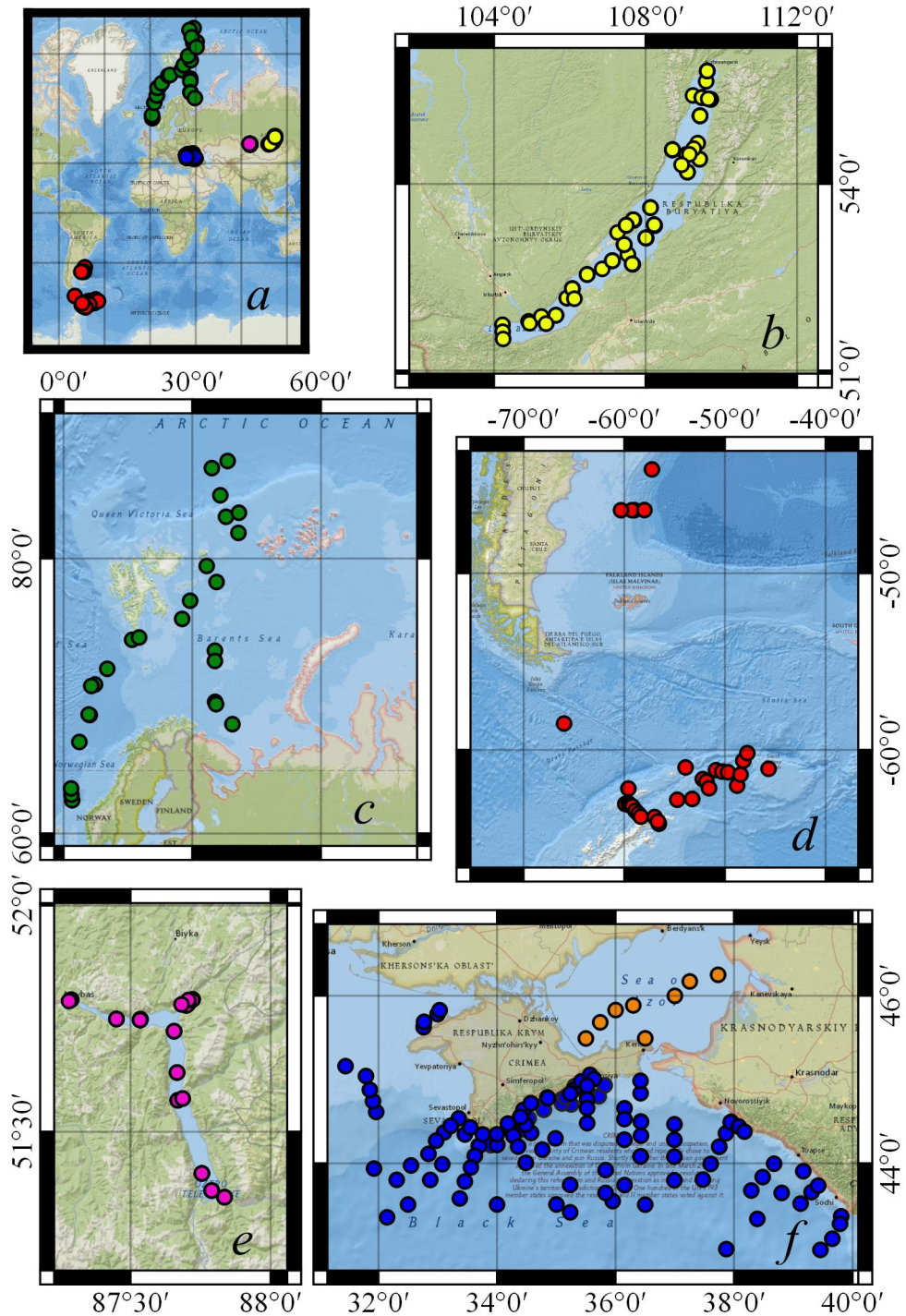


Fig. 1. Location of stations (marked with colored circles) in the study areas of the World Ocean (a); enlarged image of the study areas: *b* – Lake Baikal (yellow), *c* – Barents and Norwegian seas, and Arctic Ocean (green), *d* – Atlantic sector of the Southern Ocean (red), *e* – Lake Teletskoye (purple), *f* – Black (blue) and Azov (brown) seas

The spectral light absorption coefficients by in-water optically active components (OAC): phytoplankton ($a_{\text{ph}}(\lambda)$), non-algal particles ($a_{\text{NAP}}(\lambda)$) and colored dissolved organic matter ($a_{\text{CDOM}}(\lambda)$) were measured in accordance with modern protocols [29, 30] using a *Lambda* 35 dual-beam spectrophotometer (*PerkinElmer*) equipped with an integrating sphere. The methodology for $a_{\text{p}}(\lambda)$, $a_{\text{ph}}(\lambda)$, $a_{\text{NAP}}(\lambda)$ and $a_{\text{CDOM}}(\lambda)$ determination is described in detail in the article [17].

The parameterization of light absorption by in-water optically active components was carried out in accordance with modern approaches [31, 32]. The parameterization of phytoplankton light absorption is aimed at obtaining the relationship between $a_{\text{ph}}(\lambda)$ and *TChl-a*. Chlorophyll *a* is the main photosynthetically active pigment, which determines its ecological significance and explains its use in the analysis of the $a_{\text{ph}}(\lambda)$ variability, despite the fact that light absorption by phytoplankton is associated not only with chlorophyll *a*, but with the complex of pigments that differ in their function [33, 34]. To describe the relationship between $a_{\text{ph}}(\lambda)$ and *TChl-a*, a power function was used [31]:

$$a_{\text{ph}}(\lambda) = A(\lambda) \cdot TChl-a^{(B(\lambda))}. \quad (1)$$

The coefficients $A(\lambda)$ and $B(\lambda)$ were determined by the method of least squares using the logarithmic form of equation (1).

The spectra of the NAP and CDOM light absorption coefficients have an exponential form [35]. The NAP and CDOM light absorption parameterization are aimed at determining the parameters of the equation that describes the shapes of the $a_{\text{NAP}}(\lambda)$ and $a_{\text{CDOM}}(\lambda)$ spectra [32]:

$$a_i(\lambda) = a_i(\lambda_r) \cdot e^{(-S_i \cdot (\lambda - \lambda_r))}, \quad (2)$$

where i denotes NAP and CDOM; wavelength λ_r is the reference wavelength (in our studies we used 438 nm); S_i denotes the spectral slope S_{NAP} and S_{CDOM} .

The S_{NAP} was determined in the 400–700 nm wavelength range. The S_{CDOM} value varies depending on the selected wavelength range [36]. The S_{CDOM} was determined in the 350–500 nm wavelength range, which is used in most studies [32, 37] and allows for a comparative assessment of the obtained values using literature data.

The contribution of phytoplankton, NAP and CDOM to the total non-water light absorption by suspended and dissolved organic matter ($a_{\text{tot-w}}$), was estimated at particular wavelengths selected based on their significance: 1) at 438 nm, which is physiologically significant for phytoplankton due to the fact that at this wavelength the phytoplankton light absorption is maximum within the visible light spectrum (400–700 nm); 2) at 490 nm, which corresponds to the spectral band of optical scanners (*SeaWiFS*, *MERIS*, *MODIS*, *VIIRS*, *OLCI*) and is used in the developed

three-band *Chl-CDM* algorithm for assessing chlorophyll a concentration based on remote sensing data [10].

The downwelling irradiance spectra $E_d(\lambda)$ were measured with the 1 m step within the euphotic zone using a *RAMSES* submersible spectroradiometer (*TrioOS*, Germany) or were modeled [38] using the measured spectral bio-optical properties as input parameters [38]. The values of photosynthetically available radiation (PAR) were obtained by integrating $E_d(\lambda)$ within the visible light spectrum (400–700 nm). The euphotic zone (Z_{eu}) was estimated by the penetration depth of 1% of the PAR value incident on the sea surface. The first optical depth (1_{opt}) was determined in accordance with the formula [35]:

$$1_{opt} = Z_{eu}/4.6.$$

The wavelength of maximum of the $E_d(\lambda)$ spectrum (λ_{max}) was used as a feature of spectral properties of the downwelling irradiance.

Results and discussion

The $a_{ph}(\lambda)$, $a_{NAP}(\lambda)$ and $a_{CDOM}(\lambda)$ measured in the 1_{opt} layer are shown in Figs. 2–4. High (within an order of magnitude) variability of all the parameters studied was noted in the Sea of Azov. The chlorophyll a concentration (*TChl-a*) in the surface layer varied during the year in the range from 1.7 to 22 mg·m⁻³. A relationship between the $a_{ph}(\lambda)$ and *TChl-a* was revealed at particular wavelengths (Table 1), described by a power function (equation (1)). Seasonal differences between the $A(\lambda)$ coefficient values (equation (1)) have been revealed, most pronounced in the blue range of the spectrum (almost two-fold differences) [19]. It is explained by a change in the degree of pigment packing [39] due to phytoplankton adaptation to the intra-annual variability in environmental conditions, which leads to a change in the intracellular composition and concentration of pigments [40].

The analysis of variability of the light absorption coefficient NAP ($a_{NAP}(\lambda)$) and CDOM ($a_{CDOM}(\lambda)$) showed high (within an order of magnitude) variability $a_{NAP}(438)$ (0.036–0.58 m⁻¹) and $a_{CDOM}(438)$ (0.083–0.54 m⁻¹). It was found that the light absorption of CDOM did not correlate with *TChl-a*. The S_{NAP} and S_{CDOM} varied in the 0.0080 – 0.014 nm⁻¹ (0.010 ± 0.0015 nm⁻¹) and 0.014 – 0.024 nm⁻¹ (0.018 ± 0.0024 nm⁻¹) ranges (Table 2), respectively. The relation between S_{CDOM} and $a_{CDOM}(\lambda)$, described by the equation (Table 3), was revealed. A similar dependence was obtained for the total light absorption coefficient of NAP and CDOM ($a_{CDM}(\lambda)$) (Table 3). The value of $a_{tot-w}(438)$ varied from 0.31 to 0.68 and averaged 0.61 ± 0.45 m⁻¹ (Table 2). The relative contribution of phytoplankton to $a_{tot-w}(438)$ varied from 7% in spring and autumn to 51% in winter (January) and reached 70% in summer (July). The contribution of CDOM and NAP to $a_{tot-w}(438)$ varied from 13 to 76% and from 10 to 52%, respectively.

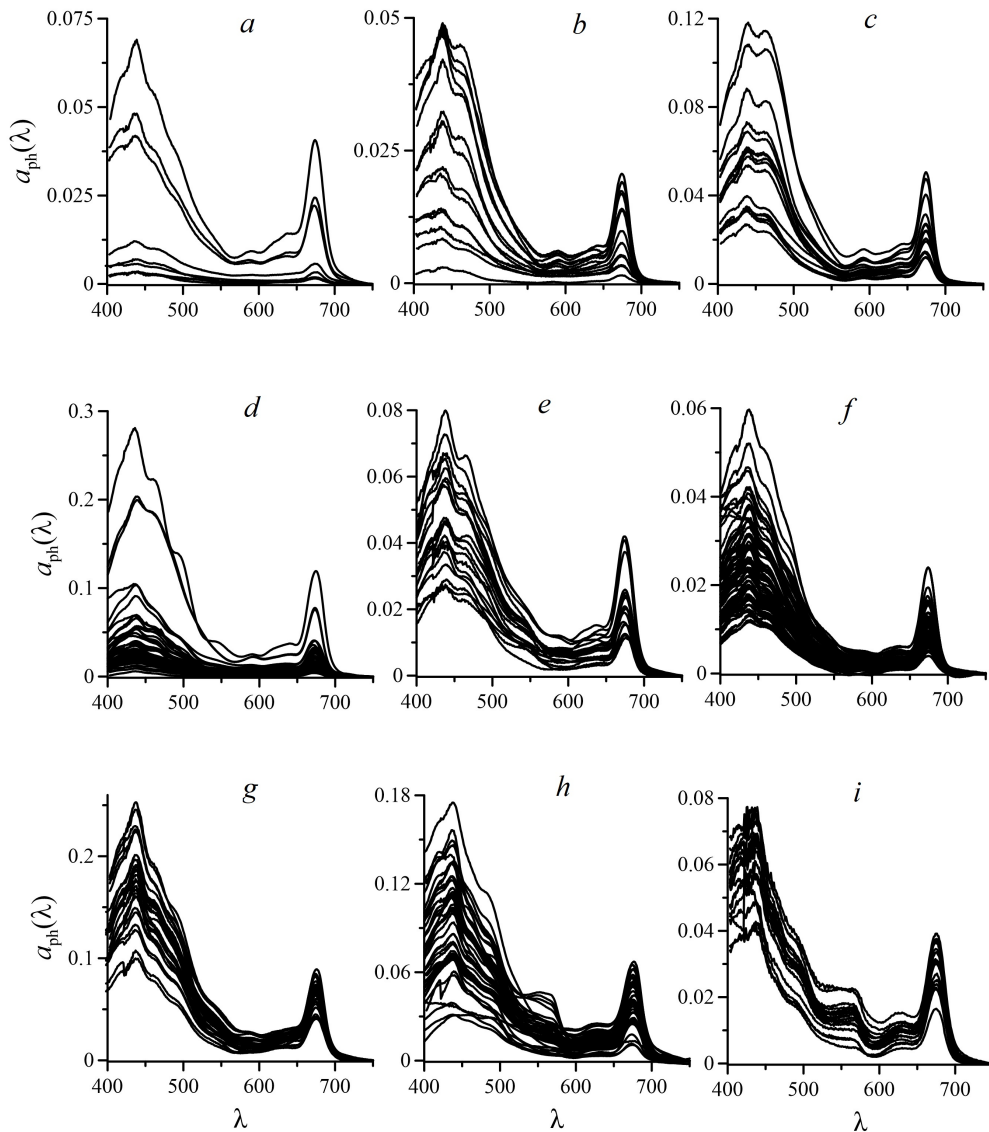


Fig. 2. Spectra of light absorption coefficients of phytoplankton ($a_{ph}(\lambda)$) in the surface layers of the Arctic Ocean (*a*), the Barents (*b*) and Norwegian (*c*) seas, Atlantic sector of the Southern Ocean (*d*), the Black Sea in winter (*e*) and summer (*f*), the Sea of Azov (*g*), and the Baikal (*h*) and Teletskoye (*i*) lakes

The coastal waters in Sevastopol Bay differed in trophic status. A high range of *TChl-a* variability (from 0.19 to 5.6 mg m⁻³) was noted in the surface layer (l_{opt}). The $a_{ph}(\lambda)$ and $a_{NAP}(\lambda)$ values also varied by an order of magnitude. Unlike suspended matter, CDOM showed lower variability of light absorption coefficients (Table 2). No relationship was observed between $a_{CDOM}(\lambda)$ and *TChl-a*. It was

found that the relationship between $TChl-a$ and $a_{ph}(\lambda)$ reflects the common dependence in a wide range of water trophicity, namely the $A(\lambda)$ and $B(\lambda)$ coefficients in equation (1) are the same [13]. At the same time, seasonal differences were revealed between the values of coefficient A in equation (1) for $a_{ph}(\lambda)$ at particular wavelengths (Table 1), which emphasizes the prevailing influence of environmental conditions (primarily radiance) on the values of the $TChl-a$ specific light absorption coefficients of phytoplankton.

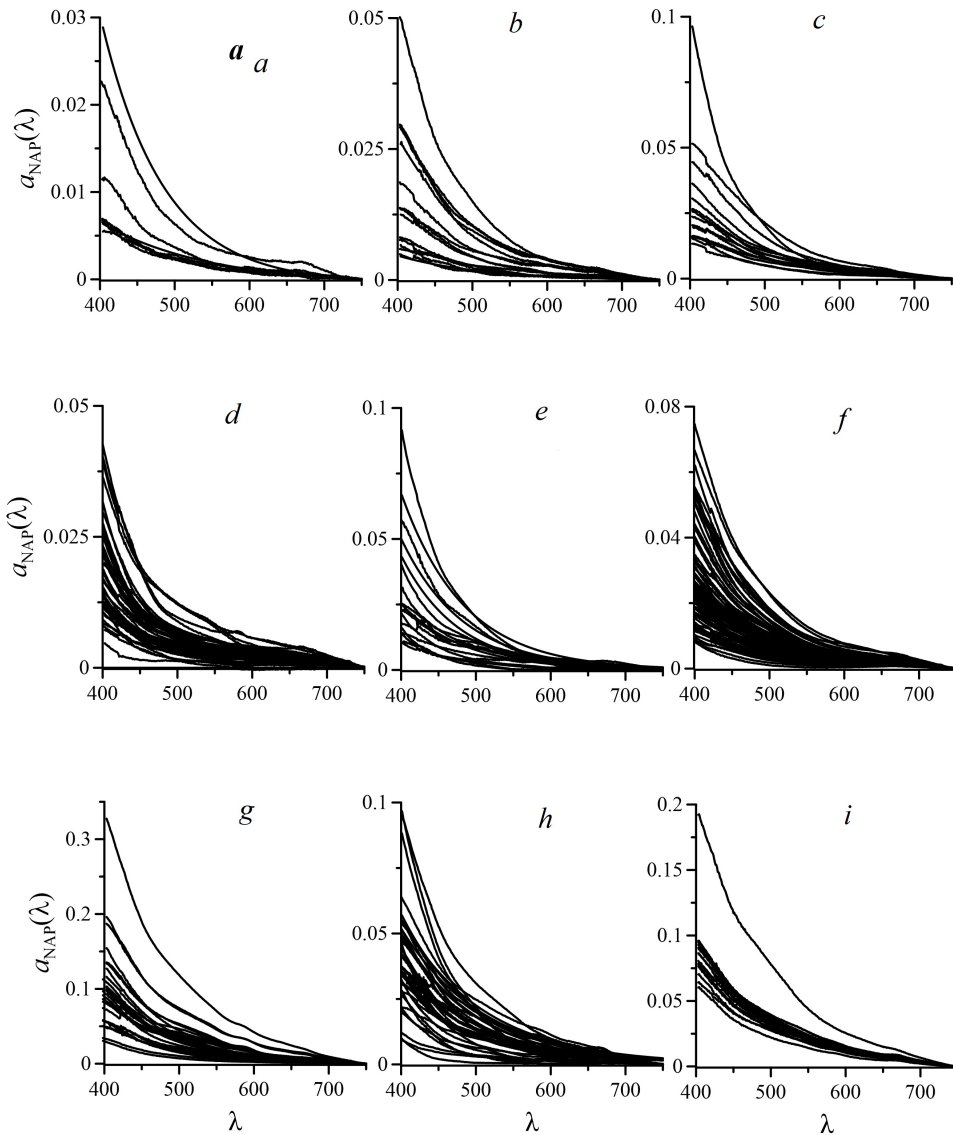


Fig. 3. Spectra of light absorption coefficients of non-algal particles ($a_{NAP}(\lambda)$) in the surface layers of the Arctic Ocean (*a*), the Barents (*b*) and Norwegian (*c*) seas, Atlantic sector of the Southern Ocean (*d*), the Black Sea in winter (*e*) and summer (*f*), the Sea of Azov (*g*), and the Baikal (*h*) and Teletskoye (*i*) lakes

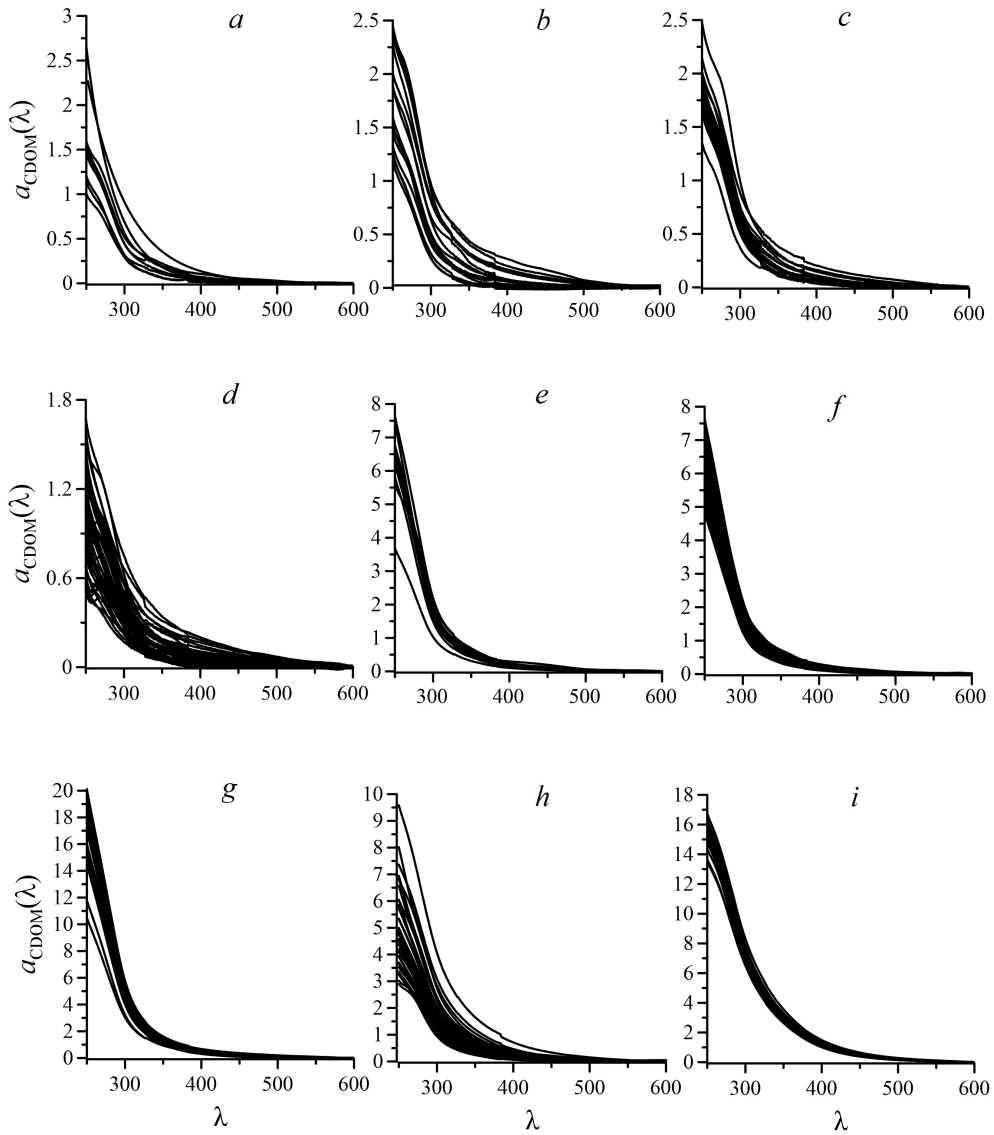


Fig. 4. Spectra of light absorption coefficients of colored dissolved organic matter ($a_{\text{CDOM}}(\lambda)$) in the surface layers of the Arctic Ocean (*a*), the Barents (*b*) and Norwegian (*c*) seas, the Atlantic sector of the Southern Ocean (*d*), the Black Sea in winter (*e*) and summer (*f*), the Sea of Azov (*g*), and Baikal (*h*) and Teletskoye (*i*) lakes

The S_{NAP} value averaged $0.011 \pm 0.002 \text{ nm}^{-1}$ (Table 2), which is consistent with the results obtained in other areas of the World Ocean [32, 37]. The S_{CDOM} decreased from 0.019 to 0.015 nm^{-1} when water trophicity increased, which reflected a change in the chemical composition of CDOM, namely an increase in the proportion of high-molecular weight compounds [36] that was probably due to the influence of river runoff (the Chernaya River runoff) as well as a lower degree of CDOM

photodegradation in turbid trophic waters [35]. A relationship between S_{CDOM} (S_{CDOM}) and $a_{CDOM}(\lambda)$ ($a_{CDOM}(\lambda)$) was revealed (Table 3). The $a_{tot-w}(438)$ value varied in winter from 0.11 to 0.82 m^{-1} (on average $0.27 \pm 0.12 m^{-1}$) and in summer from 0.069 to 0.90 m^{-1} (on average $0.30 \pm 0.16 m^{-1}$) (Table 2). Due to the lack of co-variability of the CDOM absorption and $TChl-a$, the assessment of the light absorption budget at the 438 nm wavelength showed significant variability in the CDOM contribution and the dominance of phytoplankton in the most trophic waters.

Table 1

**Coefficients of the power-law dependence $a_{ph}(490) = A(490) \cdot TChl-a^{(B(490))}$
of the light absorption coefficient by phytoplankton at 490 nm ($a_{ph}(490)$, m^{-1})
upon the chlorophyll a concentration in total with phaeopigments ($TChl-a$, $mg \cdot m^{-3}$)**

Region	$A(490)$, $m^2 \cdot mg^{-1}$	$B(490)$	r^2	n
Southern Ocean	0.021	0.93	0.83	126
Norwegian Sea				
Barents Sea	0.033	0.99	0.97	41
Arctic Ocean				
Black Sea *	0.031	0.79	0.78	79
Black Sea **	0.048	0.78	0.66	39
Sea of Azov **	0.050	0.59	0.74	39
Sea of Azov *	0.016	0.95	0.53	7
Lake Baikal	0.039	0.62	0.83	58
Lake Teletskoye	0.018	0.74	0.54	39

* Measurements were taken during a winter season.

** Measurements were taken during a summer season.

Note: r^2 is the determination coefficient; n is a number of measurements.

Studies in the surface layer of the Norwegian and Barents seas as well as the Arctic Ocean [14] showed high variability of $TChl-a$ (from 0.058 to 1.5 $mg \cdot m^{-3}$) and light absorption coefficients by all in-water optically active components: $a_{ph}(438)$ (0.0014 – 0.12 m^{-1}), $a_{NAP}(438)$ (0.00031 – 0.068 m^{-1}) and $a_{CDOM}(438)$ (0.0074 – 0.20 m^{-1}) (Table 2). Light absorption by NAP correlated with light absorption by phytoplankton and with $TChl-a$. The NAP contribution to the particulate light absorption at the 438 nm wavelength in the Norwegian and Barents seas and the Arctic Ocean averaged 27, 34 and 39%, respectively (Table 2). No correlation between the light absorption by CDOM and $TChl-a$ was observed.

Table 2

Mean value of bio-optical water properties \pm standard deviation

Region	$TC/hl-a$	$a_{NAP}(490)$	$\frac{a_{NAP}(438)}{\sigma_p(438)}$	S_{NAP}	$a_{CDOM}(490)$	S_{CDOM}	$a_{CDM}(490)$	S_{CDM}	$a_{det-w}(438)$
Southern Ocean	0.97 ± 0.47	0.0071 ± 0.0042	0.24 ± 0.12	0.011 ± 0.004	0.027 ± 0.023	0.014 ± 0.008	0.034 ± 0.023	0.012 ± 0.006	0.11 ± 0.076
Norwegian Sea	1.0 ± 0.44	0.011 ± 0.005	0.27 ± 0.13	0.011 ± 0.003	0.028 ± 0.022	0.017 ± 0.005	0.039 ± 0.024	0.016 ± 0.004	0.12 ± 0.079
Barents Sea	0.41 ± 0.26	0.0073 ± 0.0046	0.34 ± 0.12	0.011 ± 0.003	0.030 ± 0.032	0.017 ± 0.005	0.037 ± 0.035	0.016 ± 0.004	0.12 ± 0.10
Arctic Ocean	0.43 ± 0.54	0.0037 ± 0.0019	0.39 ± 0.17	0.011 ± 0.003	0.011 ± 0.010	0.017 ± 0.005	0.015 ± 0.010	0.016 ± 0.004	0.063 ± 0.039
Black Sea, coastal region*	1.2 ± 0.7	0.019 ± 0.018	0.33 ± 0.15	0.011 ± 0.002	0.038 ± 0.018	0.019 ± 0.003	0.054 ± 0.022	0.017 ± 0.002	0.27 ± 0.12
Black Sea, coastal region**	0.50 ± 0.20	0.017 ± 0.017	0.34 ± 0.11	0.011 ± 0.002	0.035 ± 0.019	0.019 ± 0.003	0.049 ± 0.025	0.017 ± 0.002	0.30 ± 0.16
Sea of Azov	6.0 ± 2.3	0.094 ± 0.079	0.41 ± 0.20	0.011 ± 0.0014	0.097 ± 0.031	0.019 ± 0.0024	0.19 ± 0.15	0.015 ± 0.0026	0.61 ± 0.45
Lake Baikal	2.2 ± 1.2	0.023 ± 0.021	0.23 ± 0.11	0.01 ± 0.0017	0.059 ± 0.038	0.018 ± 0.0028	0.081 ± 0.056	0.016 ± 0.0019	0.28 ± 0.19
Lake Teletskoye	1.7 ± 0.37	0.038 ± 0.012	0.54 ± 0.10	0.009 ± 0.0006	0.24 ± 0.034	0.018 ± 0.0007	0.28 ± 0.044	0.017 ± 0.0008	0.72 ± 0.09

* Measurements were taken during a winter season

** Measurements were taken during a summer season.

Note: $TC/hl-a$ is the chlorophyll a concentration in total with pheopigments, $mg \cdot m^{-3}$; $a_{NAP}(490)$ is the light absorption coefficient by non-algal particles (m^{-1}), $a_{CDOM}(490)$ is the light absorption coefficient by colored dissolved organic matter (m^{-1}), and $a_{CDM}(490)$ is the light absorption coefficient by colored detrital matter (m^{-1}) at the wavelength 490 nm; $a_{det-w}(438)$ is the total non-water light absorption at 438 nm (m^{-1}); $a_{NAP}(438)/a_p(438)$ is the ratio of $a_{NAP}(438)$ to the particulate absorption coefficient at the wavelength 438 nm ($a_p(438)$); S_{NAP} is the spectral slope of light absorption by non-algal particles (nm^{-1}); S_{CDOM} is the spectral slope of light absorption by colored detrital matter (nm^{-1}), and S_{CDM} is the spectral slope of light absorption by colored detrital matter (nm^{-1}) for the upper mixed layer.

Table 3

Coefficients of power-law dependence $S = A \cdot a(490)^B$

Region	A_{CDOM}	B_{CDOM}	r^2	n	A_{CDM}	B_{CDM}	r^2	n
Southern Ocean	0.0045	-0.27	0.60	126	0.0034	-0.380	0.52	126
Norwegian Sea *	0.0056	-0.28	0.81	80	0.0052	-0.320	0.73	80
Barents Sea *								
Arctic Ocean *								
Black Sea **	0.0065	-0.29	0.77	138	0.009	-0.200	0.63	138
Sea of Azov **	0.012	-0.19	0.41	118	0.013	-0.060	0.32	118
Lake Baikal	0.011	-0.15	0.39	82	0.012	-0.091	0.31	82

*Common dependencies for the Norwegian and Barents seas, and the Arctic Ocean.

** Common dependencies for all the seasons.

Note: 1. For Lake Teletskoye no dependence was found.

2. A_{CDOM} and B_{CDOM} are the coefficients of power-law dependence of the spectral slope of light absorption by colored dissolved organic matter (S_{CDOM} , nm^{-1}) upon the light absorption coefficient by colored dissolved organic matter ($a_{CDOM}(490)$, m^{-1}); A_{CDM} and B_{CDM} are the coefficients of power-law dependence of the spectral slope of light absorption by colored detrital matter (S_{CDM} , nm^{-1}) upon the light absorption coefficient ($a_{CDM}(490)$, m^{-1}); r^2 is the determination coefficient; n is a number of measurements.

For the Norwegian and Barents seas, as well as for the Arctic Ocean, a relationship between $a_{ph}(\lambda)$ and $TChl-a$ was revealed, which was described by unified equations for particular wavelengths (Table 1) without statistically significant differences between water areas [14]. As a result of parameterization (equation (2)) the S_{NAP} and S_{CDOM} values were obtained. The values of these parameters were on average 0.011 ± 0.003 and $0.017 \pm 0.004 \text{ nm}^{-1}$, respectively (Table 2). The S_{CDOM} values ($0.010\text{--}0.025 \text{ nm}^{-1}$) increased with decreasing $a_{CDOM}(\lambda)$, which was described by a power equation with the same coefficients for the Norwegian and Barents seas and the Arctic Ocean (Table 3). A similar relationship was established for S_{CDM} и $a_{CDM}(\lambda)$ (Table 3). The $a_{tot-w}(438)$ value in the surface layer of the Norwegian and Barents seas and the Arctic Ocean varied from 0.067 to 0.25 m^{-1} ($0.12 \pm 0.079 \text{ m}^{-1}$), from 0.025 to 0.24 m^{-1} ($0.12 \pm 0.10 \text{ m}^{-1}$) and from 0.021 to 0.15 m^{-1} ($0.063 \pm 0.039 \text{ m}^{-1}$) (Table 2), respectively. An absorption budget assessment at the 438 and 490 nm wavelengths showed that CDOM dominated in the light absorption over most of the studied water area. The share of CDOM in the total non-water light absorption at the 438 nm wavelength varied from 80 to 20%. Such a wide range of relative light absorption by CDOM is associated with increase in CDOM share in absorption due to the river runoff [41–43]. Phytoplankton biomass increase, if $TChl-a$ is considered as a marker of phytoplankton biomass, led to the dominance (65%) of phytoplankton in light

absorption, and, consequently, to a decrease in the CDOM share in the total non-water light absorption.

The research in the Southern Ocean showed that bio-optical properties of the surface waters (1_{opt} layer) changed by an order of magnitude or more: $TChl-a - 0.20-4.4 \text{ mg}\cdot\text{m}^{-3}$, $a_{\text{ph}}(438) - 0.0051-0.29 \text{ m}^{-1}$, $a_{\text{NAP}}(438) - 0.0038-0.022 \text{ m}^{-1}$, $a_{\text{CDOM}}(438) - 0.0054-0.19 \text{ m}^{-1}$. There was a relationship between $a_{\text{ph}}(\lambda)$ and $TChl-a$ (Table 1). A correlation between $a_{\text{NAP}}(438)$ and $TChl-a$ and no connection between $a_{\text{CDOM}}(438)$ and $TChl-a$ was noted. As a result of parameterization of light absorption by non-algal optical components, spectral slopes were obtained for $a_{\text{NAP}}(\lambda)$ and $a_{\text{CDOM}}(\lambda)$. Their mean values were $S_{\text{NAP}} = 0.010 \pm 0.0021 \text{ nm}^{-1}$ and $S_{\text{CDOM}} = 0.013 \pm 0.0059 \text{ nm}^{-1}$ (Table 2). A negative (inverse) correlation between $a_{\text{CDOM}}(\lambda)$ ($a_{\text{CDM}}(\lambda)$) and S_{CDOM} (S_{CDM}), which is described by a power law (Table 3), was revealed. The $a_{\text{tot-w}}(438)$ value in the surface layer of the Southern Ocean varied from 0.039 to 0.37 m^{-1} ($0.11 \pm 0.076 \text{ m}^{-1}$) (Table 2). An assessment of the light absorption budget at the 438 nm wavelength showed that under conditions of high variability of CDOM light absorption uncorrelated with $TChl-a$, a shift in the dominating component occurs: CDOM dominates (about 60%) in light absorption in waters with low $TChl-a$ values, phytoplankton dominates (about 80%) in waters with high $TChl-a$ values. The waters of the Atlantic sector of the Southern Ocean are optically contrasting in the content of both phytoplankton and CDOM [17].

Research on Lake Baikal has shown high (within an order of magnitude or more) variability of all bio-optical properties studied [16, 18]. $TChl-a$ in the surface layer (1_{opt} layer) varied within 0.58–5.3 $\text{mg}\cdot\text{m}^{-3}$. A connection between $a_{\text{ph}}(\lambda)$ and $TChl-a$ at separate wavelengths, which is described by a power law (Table 1), was revealed. The $a_{\text{NAP}}(\lambda)$ and $a_{\text{CDOM}}(\lambda)$ values at the 438 nm wavelength varied within 0.0024–0.099 m^{-1} and 0.035–0.31 m^{-1} . A correlation between $a_{\text{NAP}}(438)$ and $TChl-a$ was found. No connection between CDOM light absorption and $TChl-a$ was observed. The S_{NAP} parameter was $0.010 \pm 0.0017 \text{ nm}^{-1}$ in average (Table 2). The S_{CDOM} values varied from 0.011 to 0.026 nm^{-1} . A negative correlation between $a_{\text{CDOM}}(\lambda)$ ($a_{\text{CDM}}(\lambda)$) and S_{CDOM} (S_{CDM}), which was described by a power equation (Table 3), was revealed. The $a_{\text{tot-w}}(438)$ values in the surface layer varied within 0.12–0.57 m^{-1} and were $0.28 \pm 0.19 \text{ m}^{-1}$ in average (Table 2). Due to the high variability of all bio-optical parameters and the absence of correlation between CDOM light absorption coefficient and $TChl-a$, a change in the component dominating in light absorption was noted. In some areas of the lake, CDOM dominated in the light field formation, its contribution to the total non-water light absorption reached ~ 85%. In the lake areas where a high $TChl-a$ content (over 1.5 $\text{mg}\cdot\text{m}^{-3}$) was noted, phytoplankton dominated and its contribution to the total non-water light absorption reached ~ 80%.

The bio-optical studies on Lake Teletskoye revealed high contents of phytoplankton, NAP and CDOM. $TChl-a$ values during the study period varied from 1.1 to 2.3 $\text{mg}\cdot\text{m}^{-3}$. Relationship between the $a_{\text{ph}}(\lambda)$ and $TChl-a$ were revealed at

particular wavelengths (Table 1). The $a_{\text{NAP}}(438)$ and $a_{\text{CDOM}}(438)$ coefficients varied from 0.029 to 0.14 m^{-1} and from 0.46 to 0.76 m^{-1} . The mean values of light absorption coefficients of NAP and CDOM at the 490 nm wavelength are given in Table 2. The $a_{\text{tot-w}}(438)$ varied from 0.56 to 0.97 m^{-1} , averaging $0.72 \pm 0.02 \text{ m}^{-1}$ (Table 2). For light absorption CDOM and CDM, relationships between the spectral slope (S_{CDOM} and S_{CDM}) and the light absorption coefficients at the 490 nm wavelength (Table 3) were revealed. On average, in the Lake Teletskoye waters, the $a_{\text{NAP}}(438)/a_{\text{p}}(438)$ ratio was 0.54 ± 0.10 , which significantly exceeded the values of this ratio obtained in other water areas under consideration (Table 2).

Based on the combined dataset, a comparative analysis and systematization of the areas under consideration was carried out for *TChl-a* and $a_{\text{tot-w}}(438)$ in the l_{opt} layer (Table 2). It was found that the *TChl-a* values varied by several orders of magnitude (0.066–24 $\text{mg}\cdot\text{m}^{-3}$), while the $a_{\text{tot-w}}(438)$ values varied by more than an order of magnitude (0.021–0.97 m^{-1}). The average *TChl-a* values varied by an order of magnitude from $0.41 \pm 0.26 \text{ mg}\cdot\text{m}^{-3}$ to $6.0 \pm 2.3 \text{ mg}\cdot\text{m}^{-3}$ in the Barents Sea – the Arctic Ocean – the Crimean coastal waters – the Southern Ocean – the Norwegian Sea – Lake Teletskoye – Lake Baikal – the Sea of Azov series. The $a_{\text{tot-w}}(438)$ coefficient on average also changed by an order of magnitude from $0.063 \pm 0.039 \text{ m}^{-1}$ to $0.90 \pm 0.21 \text{ m}^{-1}$ in the Arctic Ocean – the Southern Ocean – the Barents Sea – the Norwegian Sea – the Crimean coastal waters – Lake Baikal – the Sea of Azov – Lake Teletskoye series (Table 2). Based on the average *TChl-a* values (Table 2), it can be concluded that the most trophic region among those studied is the Sea of Azov. In all regions, the CDM (= NAP + CDOM) prevailed in light absorption. At the same time, in Lake Teletskoye, CDM dominated in the total light absorption to a greater extent than was observed in the most trophic waters – in the Sea of Azov. As a result, the maximum $a_{\text{tot-w}}(438)$ values were noted in Lake Teletskoye. In fact, this is due to the distinctive feature of this water body, which consists in the predominance of NAP in the particulate light absorption ($a_{\text{NAP}}(438) > a_{\text{ph}}(438)$), which is due to the influence of abundant coastal runoff on the bio-optical properties of the lake. This feature of Lake Teletskoye distinguishes it from other studied water areas, where phytoplankton dominates in the particulate light absorption.

For all the studied water areas, the absence of co-variability of the $a_{\text{ph}}(\lambda)$ and $a_{\text{CDOM}}(\lambda)$ was revealed, and, consequently, the absence of co-variability of *TChl-a* and $a_{\text{tot-w}}(\lambda)$.

The generalized results obtained in waters (deep-water and coastal areas of the Black Sea, the Sea of Azov and Lake Teletskoye) with values of $a_{\text{tot-w}}(\lambda)$ varying by more than an order of magnitude were used to obtain relationships:

1) between Z_{eu} and $a_{\text{tot-w}}(\lambda)$ in the surface layer of the sea. Since Z_{eu} is associated with the diffuse attenuation coefficient of photosynthetically available radiation K_{d} ($K_{\text{d}} = 4.6/Z_{\text{eu}}$) [35], K_{d} can be estimated by $a_{\text{tot-w}}(\lambda)$;

2) between λ_{max} near the bottom of the euphotic zone and $a_{\text{tot-w}}(\lambda)$ in the surface layer of the sea [44]:

$$\lambda_{\max} = 579 \cdot a_{\text{tot-w}}(438)^{0.057}, r^2 = 0.99;$$

$$Z_{\text{eu}} = 7.96 \cdot a_{\text{tot-w}}(438)^{-0.727}, r^2 = 0.96.$$

Taking into account that $a_{\text{tot-w}}(\lambda)$ represents the sum of the coefficients $a_{\text{ph}}(\lambda) + a_{\text{CDM}}(\lambda)$, which are retrieved using the regional *Chl*-CDM algorithm, the revealed relationships allow increasing the number of parameters (by adding Z_{eu} , K_d and λ_{\max}), retrieved based on satellite data using the regional *Chl*-CDM algorithm.

The revealed regionally specific coefficients of light absorption parameterization by all in water optically active components (Tables 1–3) enable to modify the regional three-band *Chl*-CDM algorithm [10] and expand this algorithm application geography. The obtained regional coefficients of the relationship between *TChl-a* and $a_{\text{ph}}(\lambda)$ at the 490 nm wavelength (Table 1) will allow to correct *TChl-a* determination based on the modelled $a_{\text{ph}}(490)$. The regionally revealed coefficients of the relationship between *TChl-a* and $a_{\text{ph}}(490)$ are different due to the packing effect, i.e. the influence of the packing of pigments in cells on the ability of these cells to absorb light. Consequently, the relationship between *TChl-a* and $a_{\text{ph}}(\lambda)$ takes into account (indirectly) the adaptive changes in phytoplankton at the cell and community levels in response to changes in environmental factors of a particular water area. The revealed regional relationships between $a_{\text{CDM}}(490)$ and the S_{CDM} (Table 3) will allow correct retrieval of $a_{\text{CDM}}(490)$. The regionally specific coefficients of this relationship will enable (indirectly) to take into account the relationship between NAP and CDOM, as well as the chemical structure of CDOM [36], which determines the spectral slope of $a_{\text{CDOM}}(\lambda)$ in a particular water area. The regionally specific coefficients of light absorption parameterization by in-water optically active components (Tables 1–3) will permit to adapt *Chl*-CDM algorithm [11] to the water areas under consideration.

Conclusions

Regional relationships between $a_{\text{ph}}(\lambda)$ and *TChl-a* will make it possible to determine *TChl-a* correctly based on the value of $a_{\text{ph}}(\lambda)$, retrieved using regional algorithms (including the three-channel *Chl*-CDM algorithm), since the parameterization of the relationship between $a_{\text{ph}}(\lambda)$ and *TChl-a* takes into account (indirectly) the influence of environmental conditions on the intracellular pigment composition and concentration, as well as on the size-species structure of phytoplankton. The revealed regionally specific relationships between $a_{\text{CDM}}(490)$ ($a_{\text{CDM}}(490) = a_{\text{NAP}}(490) + a_{\text{CDOM}}(490)$) and S_{CDM} are used to retrieve the $a_{\text{CDM}}(490)$ parameter. The regionally specific parameterization coefficients of NAP and CDOM light absorption make it possible (indirectly) to take into account the relationship between NAP and CDOM, as well as the chemical structure of CDOM, which determines the spectral slope of CDOM light absorption in a particular region.

Based on empirically revealed dependencies, additional indicators of the water quality (the euphotic zone and the spectral properties of light in the sea), which can be assessed using satellite data, were proposed.

The development of regional algorithms based on empirically revealed dependencies opens up the perspective of operational monitoring of the pelagic ecosystem state based on a set of water quality and productivity indicators. This will allow to track the spread of organic dissolved matter and suspended matter in coastal waters affected by industrial wastewater and sewage and also to assess the wastewater impact on water transparency which is crucial for the functioning of the primary producers and, therefore, for pelagic ecosystem.

REFERENCES

1. Doney, S.C., Ruckelshaus, M., Duffy, E.J., Barry, J.P., Chan, F., English, C.A., Galindo, H.M., Grebmeier, J.M., Hollowed, A.B. [et al.], 2012. Climate Change Impacts on Marine Ecosystems. *Annual Review of Marine Science*, 4, pp. 11-37. <https://doi.org/10.1146/annurev-marine-041911-111611>
2. Groom, S., Sathyendranath, S., Ban, Y., Bernard, S., Brewin, R., Brotas, V., Brockmann, C., Chauhan, P., Choi, J.-K. [et al.], 2019. Satellite Ocean Colour: Current Status and Future Perspective. *Frontiers in Marine Science*, 6, 485. <https://doi.org/10.3389/fmars.2019.00485>
3. Sathyendranath, S., Brewin, R.J.W., Brockmann, C., Brotas, V., Calton, B., Chuprin, A., Cipollini, P., Couto, A.B., Dingle, J. [et al.], 2019. An Ocean-Colour Time Series for Use in Climate Studies: The Experience of the Ocean-Colour Climate Change Initiative (OC-CCI). *Sensors*, 19(19), 4285. <https://doi.org/10.3390/s19194285>
4. Adjovu, G.E., Stephen, H., James, D. and Ahmad, S., 2023. Overview of the Application of Remote Sensing in Effective Monitoring of Water Quality Parameters. *Remote Sensing*, 15(7), 1938. <https://doi.org/10.3390/rs15071938>
5. Mobley, C.D., ed., 2022. *The Oceanic Optics Book*. Dartmouth: International Ocean Colour Coordinating Group (IOCCG), 924 p. <https://doi.org/10.25607/OBP-1710>
6. Mélin, F., ed., 2019. *Uncertainties in Ocean Colour Remote Sensing*. IOCCG Report Series; No. 18. Dartmouth: International Ocean-Colour Coordinating Group (IOCCG), 170 p.
7. Morel, A. and Prieur, L., 1977. Analysis of Variations in Ocean Color. *Limnology and Oceanography*, 22(4), pp. 709-722. <https://doi.org/10.4319/lo.1977.22.4.0709>
8. Mobley, C.D., Stramski, D., Bissett, W.P. and Boss, E., 2004. Optical Modeling of Ocean Waters: Is the Case 1 - Case 2 Classification Still Useful? *Oceanography*, 17(2), pp. 60-68. <https://doi.org/10.5670/oceanog.2004.48>
9. Mélin, F. and Vantrepotte, V., 2015. How Optically Diverse Is the Coastal Ocean? *Remote Sensing of Environment*, 160, pp. 235-251. <https://doi.org/10.1016/j.rse.2015.01.023>
10. Suslin, V. and Churilova, T., 2016. A Regional Algorithm for Separating Light Absorption by Chlorophyll-a and Coloured Detrital Matter in the Black Sea, Using 480–560 nm Bands from Ocean Colour Scanners. *International Journal of Remote Sensing*, 37(18), pp. 4380-4400. <https://doi.org/10.1080/01431161.2016.1211350>
11. Kopelevich, O.V., Burenkov, V.I., Ershova, S.V., Sheberstov, S.V. and Evdoshenko, M.A., 2004. Application of SeaWiFS Data for Studying Variability of Bio-Optical Characteristics in the Barents, Black and Caspian Seas. *Deep Sea Research Part II: Topical Studies in Oceanography*, 51(10-11), pp. 1063-1091. [https://doi.org/10.1016/s0967-0645\(04\)00101-8](https://doi.org/10.1016/s0967-0645(04)00101-8)

12. Suslin, V.V., Churilova, T.Ya., Lee, M., Moncheva, S. and Finenko, Z.Z., 2018. Comparison of the Black Sea Chlorophyll-*A* Algorithms for SeaWiFS and MODIS Instruments. *Fundamental and Applied Hydrophysics*, 11(3), pp. 64-72. <https://doi.org/10.7868/S2073667318030085> (in Russian).
13. Efimova, T., Churilova, T., Moiseeva, N., Zemlianskaia, E., Krivenko, O. and Sakhon, E., 2018. Dynamics in Pigment Concentration and Light Absorption by Phytoplankton, Non-Algal Particles and Colored Dissolved Organic Matter in the Black Sea Coastal Waters (Near Sevastopol). In: SPIE, 2018. *Proceedings of SPIE. 24th International Symposium on Atmospheric and Ocean Optics: Atmospheric Physics*. Tomsk: SPIE. Vol. 10833, 108336C. <https://doi.org/10.1117/12.2504657>
14. Efimova, T., Churilova, T., Skorokhod, E., Suslin, V., Buchelnikov, A., Glukhovets, D., Khrapko, A. and Moiseeva, N., 2023. Light Absorption by Optically Active Components in the Arctic Region (August 2020) and the Possibility of Application to Satellite Products for Water Quality Assessment. *Remote Sensing*, 15(17), 4346. <https://doi.org/10.3390/rs15174346>
15. Moiseeva, N.A., Churilova, T.Ya., Efimova, T.V., Sutorikhin, I.A., Kirillov, V.V. and Skorokhod, E.Yu., 2023. Spectral Bio-Optical Properties of Lake Teletskoye in Summer. In: SPIE, 2023. *Proceedings of SPIE. 29th International Symposium on Atmospheric and Ocean Optics: Atmospheric Physics*. Moscow: SPIE. Vol. 12780, 1278049. <https://doi.org/10.1117/12.2690958>
16. Churilova, T.Ya., Moiseeva, N.A., Latushkin, A.A., Suslin, V.V., Usoltseva, M.V., Zakharova, Yu.R., Titova, L.A., Gnatovsky, R.Yu. and Blinov, V.V., 2018. Preliminary Results of Bio-Optical Investigations at Lake Baikal. *Limnology and Freshwater Biology*, (1), pp. 58-61. <https://doi.org/10.31951/2658-3518-2018-a-1-58>
17. Churilova, T., Moiseeva, N., Skorokhod, E., Efimova, T., Buchelnikov, A., Artemiev, V. and Salyuk, P., 2023. Parameterization of Light Absorption of Phytoplankton, Non-Algal Particles and Coloured Dissolved Organic Matter in the Atlantic Region of the Southern Ocean (Austral Summer of 2020). *Remote Sensing*, 15(3), 634. <https://doi.org/10.3390/rs15030634>
18. Churilova, T., Moiseeva, N., Efimova, T., Skorokhod, E., Sorokovikova, E., Belykh, O., Usoltseva, M., Blinov, V., Makarov, M. [et al.], 2020. Study of Absorption Characteristics of Phytoplankton, Particles and Colored Dissolved Organic Matter in Lake Baikal (July 2018 and September 2019). *Limnology and Freshwater Biology*, (2), pp. 387-390. <https://doi.org/10.31951/2658-3518-2020-A-2-387>
19. Churilova, T.Ya., Efimova, T.V., Moiseeva, N.A. and Skorokhod, E.Yu., 2022. Spectral Light Absorption Coefficient of Particles and Colored Dissolved Organic Matter in the Sea of Azov. *Fundamental and Applied Hydrophysics*, 15(3), pp. 73-83. <https://doi.org/10.59887/fpg/ex1p-9vtp-phu8> (in Russian).
20. Matishov, G.G., Povazhnyi, V.V., Berdnikov, S.V., Moses, W.J. and Gitelson, A.A., 2010. Satellite Estimation of Chlorophyll-*a* Concentration and Phytoplankton Primary Production in the Sea of Azov. *Doklady Biological Sciences*, 432(1), pp. 216-219. <https://doi.org/10.1134/S0012496610030142>
21. Yunev, O.A., Vedernikov, V.I., Basturk, O., Yilmaz, A., Kideys, A.E., Moncheva, S. and Kononov, S.K., 2002. Long-Term Variations of Surface Chlorophyll *a* and Primary Production in the Open Black Sea. *Marine Ecology Progress Series*, 230, pp. 11-28. <https://doi.org/10.3354/meps230011>
22. Stelmakh, L.V., 1992. Intensity of Photosynthesis in Two Size Fractions of Phytoplankton in Eutrophic Waters of the Sevastopol Bay. *Hydrobiological Journal*, 28(3), pp. 14-20 (in Russian).
23. Pitchford, J.W. and Brindley, J., 1999. Iron Limitation, Grazing Pressure and Oceanic High Nutrient-Low Chlorophyll (HNLC) Regions. *Journal of Plankton Research*, 21(3), pp. 525-547. <https://doi.org/10.1093/plankt/21.3.525>

24. Le Fouest, V., Zakardjian, B., Xie, H., Raimbault, P., Joux, F. and Babin, M., 2013. Modeling Plankton Ecosystem Functioning and Nitrogen Fluxes in the Oligotrophic Waters of the Beaufort Sea, Arctic Ocean: A Focus on Light-Driven Processes. *Biogeosciences*, 10(7), pp. 4785-4800. <https://doi.org/10.5194/bg-10-4785-2013>
25. Ardyna, M., Babin, M., Gosselin, M., Devred, E., Bélanger, S., Matsuoka, A. and Tremblay, J.-É., 2013. Parameterization of Vertical Chlorophyll a in the Arctic Ocean: Impact of the Subsurface Chlorophyll Maximum on Regional, Seasonal, and Annual Primary Production Estimates. *Biogeosciences*, 10(6), pp. 4383-4404. <https://doi.org/10.5194/bg-10-4383-2013>
26. Kuderina, T., Suslova, S., Grabenko, E., Kuhta, A. and Medvedev, A., 2019. The Ecological Situation of Teletskoe Lake to Environmental Changes. *Field Studies in the Altai Biosphere Reserve*, (1), pp. 86-91 (in Russian).
27. Jeffrey, S.W. and Humphrey, G.F., 1975. New Spectrophotometric Equations for Determining Chlorophylls a, b, c₁ and c₂ in Higher Plants, Algae and Natural Phytoplankton. *Biochimie und Physiologie der Pflanzen*, 167(2), pp. 191-194. [https://doi.org/10.1016/S0015-3796\(17\)30778-3](https://doi.org/10.1016/S0015-3796(17)30778-3)
28. Lorenzen, C.J., 1967. Determination of Chlorophyll and Pheo-Pigments: Spectrophotometric Equations. *Limnology and Oceanography*, 12(2), pp. 343-346. <https://doi.org/10.4319/lo.1967.12.2.0343>
29. Neeley, A.R. and Mannino, A., eds., 2018. *Inherent Optical Property Measurements and Protocols: Absorption Coefficient*. Dartmouth, NS, Canada, 83 p. (IOCCG Protocol Series Ocean Optics & Biogeochemistry Protocols for Satellite Ocean Colour Sensor Validation; vol. 1). <https://doi.org/10.25607/OBP-119>
30. Mannino, A., Novak, M.G., Nelson, N.B., Belz, M., Berthon, J.-F., Blough, N.V., Boss, E., Bricaud, A., Chaves, J. [et al.], 2019. *Measurement Protocol of Absorption by Chromophoric Dissolved Organic Matter (CDOM) and Other Dissolved Materials*. Dartmouth, Canada: IOCCG, 77 p. (Inherent Optical Property Measurements and Protocols: Absorption Coefficient). Available at: https://ioccg.org/wp-content/uploads/2019/10/cdom_abs_protocol_public_draft-19oct-2019-sm.pdf [Accessed: 30 July 2024].
31. Bricaud, A., Babin, M., Morel, A. and Claustre, H., 1995. Variability in the Chlorophyll-Specific Absorption Coefficients of Natural Phytoplankton: Analysis and Parameterization. *Journal of Geophysical Research*, 100(C7), pp. 13321-13332. <https://doi.org/10.1029/95jc00463>
32. Babin, M., Stramski, D., Ferrari, Gm., Claustre, H., Bricaud, A., Obolensky, G. and Hoepffner, N., 2003. Variations in the Light Absorption Coefficients of Phytoplankton, Nonalgal Particles, and Dissolved Organic Matter in Coastal Waters around Europe. *Journal of Geophysical Research: Oceans*, 108(C7), 3211. <https://doi.org/10.1029/2001jc000882>
33. Jeffrey, S.W., Mantoura, R.F.C. and Wright, S.W., 1997. *Phytoplankton Pigments in Oceanography: Guidelines to Modern Method*. Paris: UNESCO Publishing, 661 p.
34. Churilova, T.Ya., Finenko, Z.Z. and Akimov, A. I., 2008. Microalgal Pigments. In: Yu. N. Tokarev, Z. Z. Finenko and N. V. Shadrin, eds., 2008. *The Black Sea Microalgae: Problems of Biodiversity Preservation and Biotechnological Usage*. Sevastopol: ECOSI-Gidrofizika, pp. 301-319 (in Russian).
35. Kirk, J.T.O., 2011. *Light and Photosynthesis in Aquatic Ecosystems*. Cambridge: Cambridge University Press, 3rd ed., 665 p.
36. Helms, J.R., Stubbins, A., Ritchie, J.D., Minor, E.C., Kieber, D.J. and Mopper, K., 2008. Absorption Spectral Slopes and Slope Ratios as Indicators of Molecular Weight, Source, and Photobleaching of Chromophoric Dissolved Organic Matter. *Limnology and Oceanography*, 53(3), pp. 955-969. <https://doi.org/10.4319/lo.2008.53.3.0955>
37. Nelson, N.B. and Siegel, D.A., 2013. The Global Distribution and Dynamics of Chromophoric Dissolved Organic Matter. *Annual Review of Marine Science*, 5, pp. 447-476. <https://doi.org/10.1146/annurev-marine-120710-100751>

38. Churilova, T.Ya., Suslin, V.V., Efimova, T.V., Moiseeva, N.A. and Skorokhod, E.Yu., 2020. Effect of Dissolved and Suspended Matter on Light in the Sea and Phytoplankton Light Absorbance Capacity in Coastal Waters of the Black Sea. *Fundamental and Applied Hydrophysics*, 13(2), pp. 43-50. <https://doi.org/10.7868/S2073667320020057> (in Russian).
39. Morel, A. and Bricaud, A., 1981. Theoretical Results Concerning Light Absorption in a Discrete Medium, and Application to Specific Absorption of Phytoplankton. *Deep Sea Research Part A. Oceanographic Research Papers*, 28(11), pp. 1375-1393. [https://doi.org/10.1016/0198-0149\(81\)90039-X](https://doi.org/10.1016/0198-0149(81)90039-X)
40. Finenko, Z., Hoepffner, N., Williams, R. and Piontkovskij, S., 2003. Phytoplankton Carbon to Chlorophyll a Ratio. Response to Light, Temperature and Nutrient Limitation. *Marine Ecology Journal*, 2(2), p. 40-64.
41. Fichot, C.G., Kaiser, K., Hooker, S.B., Amon, R.M.W., Babin, M., Bélanger, S., Walker, S.A. and Benner, R., 2013. Pan-Arctic Distributions of Continental Runoff in the Arctic Ocean. *Scientific Reports*, 3(1), 1053. <https://doi.org/10.1038/srep01053>
42. Sánchez-García, L., Alling, V., Pugach, S., Vonk, J., van Dongen, B., Humborg, C., Dudarev, O., Semiletov, I. and Gustafsson, Ö., 2011. Inventories and Behavior of Particulate Organic Carbon in the Laptev and East Siberian Seas. *Global Biogeochemical Cycles*, 25(2), GB2007. <https://doi.org/10.1029/2010gb003862>
43. Zatsepin, A.G., Zavialov, P.O., Kremenetskiy, V.V., Poyarkov, S.G. and Soloviev, D.M., 2010. The Upper Desalinated Layer in the Kara Sea. *Oceanology*, 50(5), pp. 657-667. <https://doi.org/10.1134/s0001437010050036>
44. Churilova, T.Ya., Moiseeva, N.A., Efimova, T.V., Skorokhod, E.Yu., Vazyulya, S.V., Buchelnikova, V.A., Zemlianskaia, E.A., Kalmykova, D.V., Sutorikhin I.A. [et al.], 2023. Water Transparency and Spectral Downwelling Irradiance in the Black and Azov Seas and in Lake Teletskoye. In: SPIE, 2023. *Proceedings of SPIE. 29th International Symposium on Atmospheric and Ocean Optics: Atmospheric Physics*. Moscow: SPIE. Vol. 12780, 1278047. <https://doi.org/10.1117/12.2690845>

About the authors:

Tatyana Ya. Churilova, Leading Researcher, Head of the Laboratory of Photosynthesis and Marine Biooptics, A.O. Kovalevsky Institute of Biology of the Southern Seas of RAS (2 Nakhimov Ave., Sevastopol, 299011, Russian Federation), CSc. (Biology), **ORCID ID: 0000-0002-0045-7284**, **Scopus Author ID: 6603622802**, **ResearcherID: O-8437-2016**, tanya.churilova@ibss-ras.ru

Tatyana V. Efimova, Senior Researcher the Laboratory of Photosynthesis and Marine Biooptics, A.O. Kovalevsky Institute of Biology of the Southern Seas of RAS (2 Nakhimov Ave., Sevastopol, 299011, Russian Federation), CSc. (Biology), **ORCID ID: 0000-0003-3908-4160**, **Scopus Author ID: 57194423783**, **WoS ResearcherID: X-1355-2019**, tefimova@ibss-ras.ru

Natalya A. Moiseeva, Researcher the Laboratory of Photosynthesis and Marine Biooptics, A.O. Kovalevsky Institute of Biology of the Southern Seas of RAS (2 Nakhimov Ave., Sevastopol, 299011, Russian Federation), **ORCID ID: 0000-0003-1356-7981**, **Scopus Author ID: 57194431032**, **WoS ResearcherID: AAH-2819-2019**, moiseeva@ibss-ras.ru

Elena Yu. Skorokhod, Researcher the Laboratory of Photosynthesis and Marine Biooptics, A.O. Kovalevsky Institute of Biology of the Southern Seas of RAS (2 Nakhimov Ave., Sevastopol, 299011, Russian Federation), **ORCID ID: 0000-0002-3057-3964**, **Scopus Author ID: 57215009764**, **WoS ResearcherID: A-6831-2019**, elenaskorokhod@ibss-ras.ru

Darya V. Kalmykova, Junior Researcher the Laboratory of Photosynthesis and Marine Biooptics, A.O. Kovalevsky Institute of Biology of the Southern Seas of RAS (2 Nakhimov Ave., Sevastopol, 299011, Russian Federation), **Scopus Author ID: 58688288100**, daria-k.kalmykova@ibss-ras.ru

Igor A. Sutorikhin, Chief Researcher of Hydrology and Geoinformatics Laboratory, Institute for Water and Environmental Problems of SB of RAS (1 Molodezhnaya Str., Barnaul, 656038, Russian Federation), DSc. (Phys.-Math.), Professor, **ORCID ID: 0000-0002-7037-4812**, sia@iwep.ru

Vladimir V. Kirillov, Head of Aquatic Ecology Laboratory, Institute for Water and Environmental Problems of SB of RAS (1 Molodezhnaya Str., Barnaul, 656038, Russian Federation), CSc. (Biology), Assistant Professor, **ORCID ID: 0000-0003-1080-737X**, vkirillov@iwep.ru

Contribution of the co-authors:

Tatyana Ya. Churilova – scientific idea, analysis of the data and writing of the article text

Tatyana V. Efimova – collection of the data during the scientific cruise (the Black and the Azov seas, Baykal and Teletskoe lakes), analysis of the data and preparation of graphic materials

Natalya A. Moiseeva – collection of the data during the scientific cruise (the Southern Ocean, Baykal and Teletskoe lakes), optical measurements, primary analysis of the data and preparation of graphic materials

Elena Yu. Skorokhod – collection of the data during the scientific cruise (the Southern and the Arctic oceans, the Black and the Azov seas), optical measurements and data processing

Darya V. Kalmykova – collection of the data during the scientific cruise (the Black Sea), optical measurements

Igor A. Sutorikhin – collection of the data during the scientific cruise (Teletskoe Lake), measurement of hydrological data, primary analysis of the data

Vladimir V. Kirillov – collection of the data during the scientific cruise (Teletskoe Lake), measurement of hydrological data, primary analysis of the data


The authors have read and approved the final manuscript.

The authors declare that they have no conflict of interest.

Original article

Investigation of the Wind Wave Breaking Shape Using the Sea Surface Video Records

V. V. Malinovsky , A. E. Korinenko

Marine Hydrophysical Institute of RAS, Sevastopol, Russian Federation
 vladimir.malinovsky@mhi-ras.ru

Abstract

Purpose. The work is aimed at studying the statistics of width-to-length ratio of a breaking crest for an active phase of wind wave breakings and at assessing the possibility of approximating the geometric shape of a breaking with an ellipse.

Methods and Results. The experimental data including the video records of sea surface and the wind speed measurements were obtained at the stationary oceanographic platform in the Black Sea Hydrophysical Subsatellite Polygon of Marine Hydrophysical Institute (near the village of Katsiveli, the Southern Coast of Crimea) in 2015–2019. Processing the *in situ* data made it possible to form the arrays both of lengths and areas of the breakings and the synchronous measurements of wind speed.

Conclusions. The distributions of random variables proportional to the minor-to-major axes ratios of breakings are obtained. It is shown that these distributions are coincident for the whitecaps of different scales. This fact testifies to the similarity of breaking geometric shapes. The average value of breaking axis ratio obtained from all the data is 0.41. It is concluded that the average geometric shape of the breaking boundaries is satisfactorily described by an ellipse with eccentricity 0.91. The ratio of the speed of a breaking centroid to that of its anterior front is estimated to be 0.9.

Keywords: wind wave breakings, *in situ* studies, distribution of wave breaking lengths, self-similarity of wave breaking geometric form

Acknowledgments: The study was carried out with financial support of the Russian Science Foundation grant No. 24-27-20105, and under the Agreement with the Department of Education and Science of Sevastopol No. 85 dated June 19, 2024.

For citation: Malinovsky, V.V. and Korinenko, A.E., 2024. Investigation of the Wind Wave Breaking Shape Using the Sea Surface Video Records. *Physical Oceanography*, 31(4), pp. 527-538.

© 2024, V. V. Malinovsky, A. E. Korinenko

© 2024, Physical Oceanography

Introduction

Many works have been devoted to the results of studies of the statistical characteristics of wind wave breakings. For example, the distributions of the lengths of whitecap ridges obtained as a result of aircraft surveys [1] over the Black Sea were approximated by a gamma distribution. In [2], distributions of whitecap lengths and their speeds were obtained at wind speeds of 5–15 m/s based on the results of four experiments carried out on the FLIP research platform 150 km west of California. Study [3] presents the probability densities of whitecap lengths L , which are well described by the power function $p(L) \sim L^{-2.3}$, and the distribution of the direction of movement of the breakings approximated by the function $A \sim \cos^q$, where q varies from 5 to 4 with an increase in wind speed in the range of 10–16 m/s. The time evolution of the whitecap was studied in [4]. It shows that the wave breaking length and width grow at constant rates proportional to the whitecap speed with coefficients of 0.56 and 0.19, respectively. The relationship between the wave breaking length



and the length of the breaking wave λ is considered in [5], with obtained average ratio $\langle L/\lambda \rangle = 0.1$.

In [1, 6, 7], the sea surface foam area was approximated by ellipses and subsequently the sizes and speeds of whitecap movement were determined. Unfortunately, no justification for such an approximation of wave breaking by an ellipse is given in the abovementioned works. In [8], foam structures were identified using the threshold method. Coordinates of the outer boundary of the selected foam shape were determined to define the breaking area and morphology. Study [8] provides a detailed comparison of the shape method and the ellipse method and shows that both of them give similar results in determining the geometric dimensions and velocities of breakings.

Nevertheless, the question of the type of wave breaking shape approximation remains open to this day. The observed wave breakings during their breaking shape development in the active phase have different shapes – from close to elliptical to “crescent-shaped”, when parts of the crest of the breaking wave (mostly short) move at different angles relative to its propagation direction (see Figs. 1 and 2 in [4]). Additional studies of the geometric dimensions of the whitecaps are required to determine the function describing the wave breaking shape.

Note that the width-to-length ratio of the breaking remains insufficiently studied despite the large number of studies on the statistics of the lengths of wing wave breakings and their areas. Such a relationship, if it is constant, will mean that the geometric shape of the whitecap boundaries is self-similar.

Studying the geometric shape of breakings can be important when analyzing data from radar stations installed, for example, on coastal structures or sea vessels. In this case, measurements are carried out at small grazing angles, at which the received signal level is determined by non-Bragg scattering component σ_{nb} formed by breaking wind waves (see [9] and references cited therein). Thus, the study of the whitecap shape and the relationships between their linear sizes will make it possible to develop models of the non-Bragg component of radar scattering.

The work is aimed at studying the width-to-length ratio of a breaking crest for an active phase of wind wave breakings and at assessing the possibility of approximating the geometric shape of a whitecap with an ellipse.

Experimental work area and equipment used

The present study used a database of archival data obtained in the autumn periods of 2015, 2018 and 2019 during full-scale experiments on a stationary oceanographic platform of the Black Sea Hydrophysical Subsatellite Polygon of Marine Hydrophysical Institute (near the village of Katsiveli, Southern Coast of Crimea). The platform is installed approximately 480 m from the shore, the sea depth is ~ 30 m.

Work [5] describes the process of wind wave breaking recording using a video camera. The video camera with a lens providing horizontal viewing angles of 54° and vertical ones of 32° recorded at shooting frequency f_r equal to 25 frames per second, with the 1920×1080 -pixel resolution. The camera was installed on the platform deck at an altitude of 11.4 m above sea level with a viewing direction of 30 – 40° to the horizon and 50 – 60° to the “upwind” direction. The observation geometry ensured no sun glare in the frame.

Wind speed and direction measurements were carried out by the Davis 6152EU complex, which includes a wind speed and direction meter, an air temperature sensor and a water temperature sensor installed at a depth of 3 m. At an altitude of 23 m above sea level, an anemometer was located on the oceanographic platform mast, data from which were recalculated into effective neutrally stratified wind speed U at the 10 m height according to method [10].

In situ data were obtained with neutral atmospheric stratification and wind speeds of 5.3–20 m/s.

Data processing method

This work is based on the analysis of a database of archival video sea surface recordings. Pre-processing of *in situ* data was carried out using the algorithm proposed in [11]. The methodology for subsequent calculation of various characteristics of wind wave breaking is described in detail in [3, 5, 12, 13]. Main processing stages required in this work are listed below.

A sign of the whitecap presence in a video frame was a change in the shape of brightness distribution $p(I')$ relative to background distribution $p(I)$ obtained in the absence of foam structures. The surface area where the radiance exceeded a given threshold value was recorded as a breaking. The analysis of time evolution of geometric whitecap foam area characteristics is given in [4, 5, 13], where an algorithm for dividing the breaking process into the active phase and spread foam is considered.

At the final stage of data processing, each pixel of the video frame was tied to coordinates on the horizontal plane taking into account the observation geometry. The intersection point of the optical axis of the lens with the selected plane was taken as the origin of coordinates.

Crest length L , occupied area S , geometric center coordinates (x_c, y_c) were determined for each whitecap. The temporal evolution of a whitecap moving at a very specific speed is characterized by an increase in S and L . The maximum values of its area S_m and length L_m are achieved at a time equal to τ , which was considered the breaking lifetime.

Velocity vector components C_c^x and C_c^y were calculated from values $x_c(t), y_c(t)$ for each breaking. The centroid velocity modulus was defined as

$$C_c = \sqrt{(C_c^x)^2 + (C_c^y)^2}. C_c \text{ is taken as breaking velocity } C_{wb} \text{ in this study.}$$

In total, 451,724 breakings were identified when processing video recordings, for each of which the values of S_m, L_m, C_{wb} and τ were recorded in a file.

Estimate of geometric shape of breakings

To consider the breaking shape, we introduce variable η defined as the ratio of minimum axis l_m of the whitecap to length L_m , i.e. $\eta = l_m/L_m$. Axis l_m passes through the breaking centroid perpendicular to L_m . Variable η gives a general idea of the whitecap “elongation”. Note that size l_m is only several pixels for small breakings, which will lead to errors in determining l_m . Due to the problems with determining the actual lengths of the minor axis of the whitecap, values l_m were not defined in the present work.

Assume that the breaking area is proportional to the product of its axes: $S_m = \beta L_m l_m$, where β is coefficient depending on the figure approximating the breaking (for example, $\beta = 1$ for a rectangle, $\beta = \pi/4$ for an ellipse or circle). Dividing both sides of the indicated expression by L_m^2 , we find $S_m/L_m^2 = \beta\eta$. Variables S_m and L_m are random values obtained as a result of *in situ* measurements for each breaking. Consequently, it is not difficult to calculate the statistical characteristics of random variable S_m/L_m^2 coinciding with $\beta\eta$. Note that random variable here is η , while coefficient β is some constant, which can take different values for different breakings in the general case. At the same time, both β and η are considered at this stage as unknown variables.

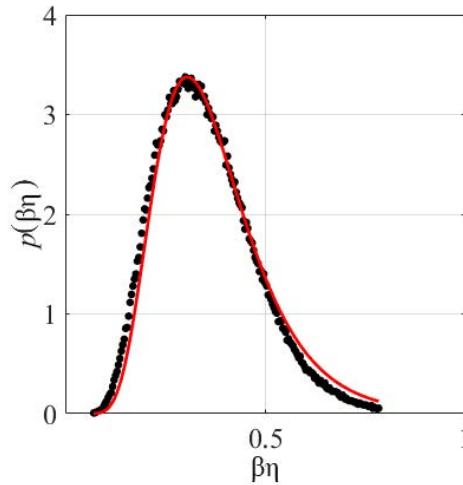


Fig. 1. Probability density of all the measured values of $\beta\eta$. Solid red line is calculated by function (1)

Consider probability density $p(\beta\eta)$. Figure 1 shows its distribution obtained for all measured values S_m/L_m^2 by black dots. The probability density is satisfactorily described by the function shown in Fig. 1 by red line:

$$p(\beta\eta) = b \exp \left[-a \ln^2 \left(d \frac{\beta\eta}{\eta_0} \right) \right], \quad (1)$$

where $a = 0.69$, $b = 3.39$, $d = 0.87$. These coefficients were obtained using the least squares method. Coefficient $\eta_0 = 0.35$ was defined as the average of all found values S_m/L_m^2 . Note that the deviation of the average value $\langle \beta\eta \rangle = \int_0^m (\beta\eta) p(\beta\eta) d(\beta\eta)$ equal to 0.365, does not exceed 4% from η_0 (m is the maximum value of $\beta\eta$).

Note that type of distribution (1) was not chosen randomly, but due to the fact that the probability density is close to a parabola on a double logarithmic scale

$$\ln[p(\beta\eta)] = B - a[\ln(\beta\eta) - \ln(\eta_0/d)]^2.$$

Since coefficient β , as mentioned above, can take different values for different scales of breaking, behavior of $p(\beta\eta)$ for different C_{wb} and τ is to be estimated.

Really, as shown in [5], the distribution of ratio L_m to breaking wave length λ is quite “narrow” and $\langle L_m \rangle = 0.1\lambda$. Assuming that whitecap speed is equal to breaking wave speed, we obtain $\langle L_m \rangle \sim C_{wb}^2$. Thus, the maximum breaking length depends on C_{wb} . However, the relationship between S_m/L_m^2 and C_{wb} is not obvious.

Let us determine the distributions of $p(\beta\eta)$ at various observed whitecap speeds. The range of all measured C_{wb} (1–8 m/s) is divided into three intervals with a step $\Delta C_{wb} = 2.5$ m/s. In Fig. 2, *a*, symbols show the distributions of $p(\beta\eta)$ in selected intervals of breaking rates (numbers in the legend). All probability densities $p(\beta\eta)$ coincide practically and the entire set of points is satisfactorily described by function (1) shown by the red line.

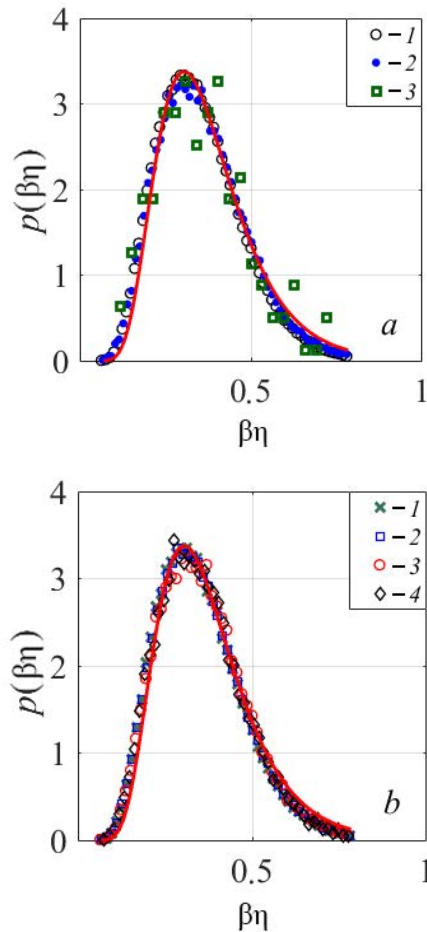


Fig. 2. Probability densities of the measured variables of $\beta\eta$: *a* – in the intervals of wave breaking velocities, m/s ($1 - 1 \leq C_{wb} \leq 3.5$; $2 - 3.5 \leq C_{wb} \leq 6$; $3 - 6 \leq C_{wb} \leq 8$); *b* – in the intervals of whitecaps lifetime, s ($1 - 0.16 \leq \tau \leq 0.56$; $2 - 0.56 \leq \tau \leq 0.96$; $3 - 0.96 \leq \tau \leq 1.36$; $4 - 1, 36 \leq \tau \leq 1.76$)

Of interest are distributions $p(\beta\eta)$ calculated for different breaking lifetime. As shown in [4], the values of the maximum whitecap lengths grow linearly in time at a rate of $C_L = 0.56C_{wb}$ and reach their maximum at $t = \tau$. Thus, the breaking lifetime determines value L_m . Let us divide the range of all measured τ (0.16–1.8 s) into four intervals with a step of $\Delta\tau = 0.4$ s. In Fig. 2, *b*, symbols show the distributions of $p(\beta\eta)$ in selected intervals τ (numbers in the legend). Here, as in Fig. 2, *a*, all probability densities $p(\beta\eta)$ coincide and are well described by function (1) shown by the red line.

Average characteristics of distribution $p(\beta\eta)$ are considered below. In Fig. 3, *a*, squares show the values of $\langle\beta\eta\rangle$ in the studied intervals, the solid line corresponds to the average value of η_0 equal to 0.35.

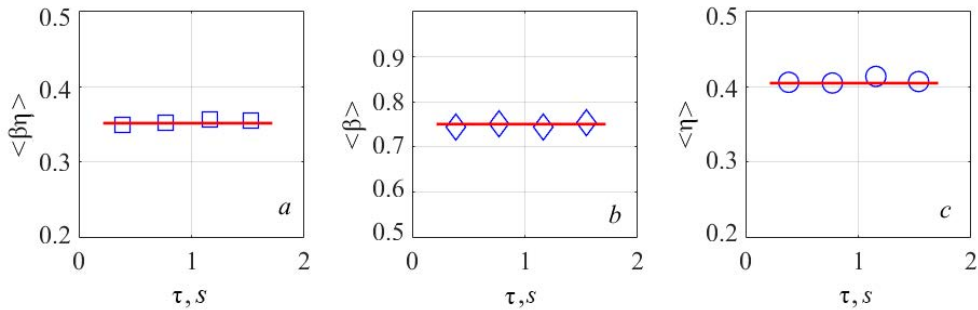


Fig. 3. Dependencies of mean characteristics of probability distribution $p(\beta\eta)$ on wave breaking lifetime: first moment (*a*); coefficient β (*b*); wave breaking axis ratio (*c*)

Standard deviation of population $\langle\beta\eta\rangle$ from η_0 is 0.003, which confirms the coincidence of distributions $p(\beta\eta)$ for different scales of breakings.

To estimate coefficient β , distribution normalization condition (1) is used:

$$\int_0^m p(\beta\eta)d(\beta\eta) = 1. \quad (2)$$

It will be assumed that η theoretically varies within $0 \leq \eta \leq 1$ and takes a value equal to zero when only the leading front breaks without foam generation behind it, and equal to one in the case when the major and minor whitecap axes coincide (for example, for a circle). Since in our assumption coefficient β is constant and can take different values for different scales of breakings, expression (2) is written in the following form:

$$\beta \int_0^1 p(\beta\eta)d\eta = 1.$$

Then, integrating over η , we obtain

$$\frac{1}{2} \sqrt{\frac{\pi b \eta_0}{a d}} \exp\left(\frac{1}{4a}\right) \left[1 + \operatorname{erf}\left(\frac{2a \ln\left(d \frac{\beta}{\eta_0}\right) - 1}{2\sqrt{a}}\right) \right] = 1. \quad (3)$$

Coefficient β can be estimated using the obtained formula. Setting its initial value equal to β_0 , we calculate the difference modulus between the left side, which we denote as f , and the right side in the specified formula. Next, using the iteration

method, taking into account the sign of difference $f - 1$, increment $\Delta\beta_j$ and $\beta_{j+1} = \beta_j + \Delta\beta_j$ is determined until value $f - 1$ will be established up to given $|f - 1| \leq \epsilon$. In the present calculations, $\epsilon = 10^{-5}$ was specified.

In Fig. 3, *b*, diamonds show estimates of β calculated using formula (3) for distributions in considered intervals τ . Values β have a small spread and cluster around a mean $\langle\beta\rangle$ of 0.75 (solid line). The behavior of $\langle\eta\rangle$ in different $\beta\eta$ intervals requires separate consideration.

Taking into account that $\beta \approx \text{const}$ and using found value $\beta\langle\eta\rangle$ presented in Fig. 3, *a*, it is not difficult to determine the average value of the ratio of the breaking axes. In Fig. 3, *c*, $\langle\eta\rangle$ in the above τ intervals is shown by circles, the solid line corresponds to expression $\langle\eta\rangle = 0.41$; values $\langle\eta\rangle$ are grouped around straight line $\langle\eta\rangle$ with a standard deviation of 0.006.

The above results show that the average ratio of the breaking axes is the same regardless of its scale when analyzing the entire data set obtained. In this case, we can talk about the self-similarity of the breaking geometric shape.

Until now, the analysis was based on the array of measured random values S_m and L_m and their ratios $S_m/L_m^2 = \beta\eta$. If we use the values of the semi-axes instead of L_m and l_m , the expression for the breaking area will be written as follows

$$S_m = 4\beta(L_m/2)^2\eta. \quad (4)$$

Taking into account the results obtained above, 4β is equal to 3, which is only 4.7% less than value π . Thus, formula (4) describes the ellipse area quite satisfactorily.

Discussion of results

Aforementioned probability densities $p(\beta\eta)$ shown in Figs. 1 and 2 and values η_0 should be considered as average dependencies obtained for the characteristics of all breakings during their lifetime.

In the present work, a specific geometric shape of a whitecap was not initially determined when studying the statistical characteristics of breakings. The only assumption was that the breaking area was proportional to the product of its major and minor axes. This proportionality coefficient value makes it possible to evaluate the possibility of whitecap approximating with a specific geometric figure.

In our opinion, the value of proportionality coefficient $\beta \approx \pi/4$ obtained in this work in formula (4) is significant. It can be said then that the breaking boundaries are described by an ellipse.

It is of interest to compare the results obtained in this work and earlier. In [4], the growth rates of breaking axes during their lifetime are considered, and these rates are almost constant: $C_l = 0.19C_{wb}$ for the minor axis of a whitecap, $C_L = 0.56C_{wb}$ for the major axis. In this work, the maximum values of breaking axes are defined as $l_m = C_l\tau$ and $L_m = C_L\tau$, then ratio l_m/L_m is 0.34, which is 20% different from $\langle\eta\rangle$ obtained in this work equal to 0.41. It should be noted here that ratio $\langle\eta\rangle$ does not depend on the scale of whitecaps according to the results of this work and work [4].

As shown above, since the boundaries of breakings are satisfactorily described by an ellipse, η can be determined by formula $\eta = \sqrt{1 - \epsilon^2}$, where ϵ is average

eccentricity of breakings. Few works present dependence $\langle \varepsilon \rangle$ on wind speed. To compare our data with the results of other authors, the range of wind speeds is divided into 6 intervals with a step $\Delta U = 2.5$ m/s and average wind speed values $\langle U \rangle$ in them.

In Fig. 4, squares show the wind dependence of our calculated ε , the solid line shows the average value $\langle \varepsilon \rangle$ equal to 0.91; light circles correspond to the data of [1], dark circles – to the data of [14].

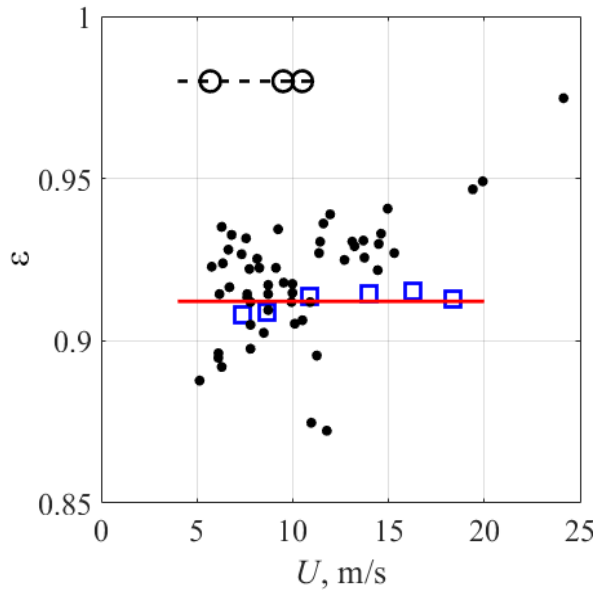


Fig. 4. Dependence of eccentricity on wind speed when approximating the wave breaking with an ellipse

The obtained eccentricity estimate is consistent with average value $\langle \varepsilon \rangle$ equal to 0.9 and calculated for an array of whitecaps generated by winds with a speed of 5–24 m/s [14]. According to the results of aircraft measurements of breakings [1], $\langle \varepsilon \rangle = 0.98 \pm 0.007$ at $U = 5.7\text{--}10.5$ m/s, which is significantly greater than results obtained in this research. A possible reason for the increased eccentricity value in [1] can be inaccuracy in determining the minor breaking axis, which varies in the range of 0.39–0.56 m (see Table 1 and Fig. 3, a in [1]) with spatial resolution of measurements 0.2 m.

In [1, 14], the eccentricity value was determined by approximating the breaking by an ellipse, whereas in the present case, estimate $\langle \varepsilon \rangle$ was obtained without initially determining the whitecap shape. Note that, as in the aforementioned works, value $\langle \varepsilon \rangle$ does not change under different observation conditions.

The results obtained in this work indicate that the breakings geometric shape is self-similar. This conclusion can be useful for the development of models describing the non-Bragg radar signal component. Indeed, σ_{nb} is determined by sea surface fraction Q covered by breakings in [15]. If $L = \int \Lambda(\mathbf{k}) d\mathbf{k}$ is total length of breaking crests on a sea surface unit, then Q will be proportional to $k^{-1} \Lambda(\mathbf{k}) d\mathbf{k}$ under

the condition of a self-similar form of breakings. The proportionality coefficient was determined by comparing model σ_{nb} with radar measurement data in [15]. The results of this work will further make it possible to estimate the proportionality coefficient relating σ_{nb} to the wind wave breaking size.

When determining the velocities of different whitecap sections, the above values η and the elliptical shape of the breakings are important. Of interest is the ratio of C_{wb} to phase velocity of the breaking wave.

In [5, 12], it is assumed that the centroid speed is equal to phase velocity of the breaking wave, $C_c = c$, while in [2] $C_c = 0.9c$. During laboratory studies, the whitecap crest speed was measured and it was found that $C_c = (0.8-0.9) c$ [16].

At the same time, the author understood the breaking movement speed as the movement speed of its front C_f in [17]. If the front is understood as the breaking boundary leading in the direction of movement, then its speed and the speed of the centroid will differ, since coordinates (x_c, y_c) are determined in the entire foam structure area.

As the whitecap area increases, the length of its minor axis in the direction of movement also increases and, therefore, leading front speed C_f must exceed C_c .

Let us estimate breaking ratio C_c to its front speed C_f . Here, C_f is understood as the movement speed of the intersection point of the minor axis of the ellipse with the breaking leading front. Let us choose a coordinate system in which axis x coincides with the breaking movement direction. At time t , coordinate x_f is defined as $x_f(t) = x_c(t) + l(t)/2$, and the distance covered by the whitecap front during time Δt will be as follows

$$x_f(t + \Delta t) - x_f(t) = x_c(t + \Delta t) - x_c(t) + [l(t + \Delta t) - l(t)]/2. \quad (5)$$

Dividing the left and right sides of this equation by Δt , the following expression including C_c and C_f is obtained:

$$C_f = C_c + 0.5C_l, \quad (6)$$

where C_l is increase rate l in the interval $(t, t + \Delta t)$. Given the definition of η , it can be written that $C_l = \eta C_L$. Then, using expression $C_L = 0.56C_c$ from [4] and dividing the left and right sides of equation (6) by C_c , we obtain

$$C_c = C_f/[1 + 0.28\eta]. \quad (7)$$

Thus, if it is assumed that the phase velocity of the breaking wave coincides with C_f [17], then, as follows from formula (7), the whitecap centroid velocity is less than the leading front velocity. When using value $\langle \eta \rangle = 0.41$ obtained above, the speed ratio is $C_c/C_f \cong 0.9$. This can be significant, for example, when calculating dissipation of wave energy $E_D \sim \int_0^\infty c^5 \Lambda dc$ associated with breakings. If the dissipation energy is written as $E_D^f \sim \int_0^\infty C_f^5 \Lambda dC_f$ for the speed of the breaking leading front and $E_D^c \sim \int_0^\infty C_c^5 \Lambda dC_c$ for the centroid speed, then $E_D^f = 1.88E_D^c$.

Conclusion

This work examines the statistical characteristics of the ratio of the minor-to-major axes of wind wave breaking. The analysis was carried out using an experimental data set including 451,724 identified breakings, which were obtained by processing video recordings of the sea surface. The studies were carried out at wind speeds of 5.3–20 m/s. Its lifetime, the speed of centroid movement, as well as the maximum area and maximum length along the breaking wave crest were determined for each individual whitecap.

In general, breakings have a complex geometric shape. Initially, we did not make any assumptions about the geometric shape of its boundaries, for example, in the form of an ellipse. The only hypothesis was that the whitecap area was proportional to product $\beta\eta$, where β is certain coefficient, η is random variable representing the ratio of the breaking axes (minimum to maximum).

It is shown that the probability densities of random variable $\beta\eta$ coincide practically in all observed intervals of τ and breaking rates. Thus, distribution $\beta\eta$ is universal for breakings of various scales and $\langle\beta\eta\rangle$ is equal to 0.35, where β and η are unknown variables.

Using distribution normalization condition $p(\beta\eta)$, required parameters β and $\langle\eta\rangle$, equal to 0.75 and 0.41, respectively, were determined using the iterative method. Almost constant value $\langle\eta\rangle$ obtained for different sizes of whitecaps gives grounds to speak about the self-similarity of the breaking geometric shape.

The results obtained show that value 4β coincides with π with an accuracy of $\sim 4\%$ and, therefore, the breaking geometric shape is quite satisfactorily described by an ellipse. It was found that the average eccentricity value is 0.91 and does not change under different observation conditions.

The work provides an estimate of the whitecap leading front speed. It is shown that it is 10% higher than the speed of the breaking centroid.

REFERENCES

1. Bondur, V.G. and Sharkov, E.A., 1986. Statistical Characteristics of Linear Elements of Foam Formations on the Sea Surface as Derived from Optical Sounding Data. *Issledovanie Zemli iz Kosmosa*, (4), pp. 21-31 (in Russian).
2. Gemmrich, J.R., Banner, M.L. and Garrett, C., 2008. Spectrally Resolved Energy Dissipation Rate and Momentum Flux of Breaking Waves. *Journal of Physical Oceanography*, 38(6), pp. 1296-1312. <https://doi.org/10.1175/2007JPO3762.1>
3. Korinenko, A.E., Malinovsky, V.V. and Kudryavtsev, V.N., 2018. Experimental Research of Statistical Characteristics of Wind Wave Breaking. *Physical Oceanography*, 25(6), pp. 489-500. <https://doi.org/10.22449/1573-160X-2018-6-489-500>
4. Korinenko, A.E. and Malinovsky, V.V., 2023. Field Investigations of the Geometric Features of Wind Wave Breaking. *Physical Oceanography*, 30(6), pp. 776-791.
5. Korinenko, A.E., Malinovsky, V.V., Kudryavtsev, V.N. and Dulov, V.A., 2020. Statistical Characteristics of Wave Breakings and Their Relation with the Wind Waves' Energy Dissipation Based on the Field Measurements. *Physical Oceanography*, 27(5), pp. 472-488. <https://doi.org/10.22449/1573-160X-2020-5-472-488>

6. Sharkov, E.A., 2007. *Breaking Ocean Waves: Geometry, Structure, and Remote Sensing*. Berlin, Heidelberg: Springer, 278 p. <https://doi.org/10.1007/978-3-540-29828-1>
7. Schwendeman, M.S. and Thomson, J., 2017. Sharp-Crested Breaking Surface Waves Observed from a Ship-Based Stereo Video System. *Journal of Physical Oceanography*, 47(4), pp. 775-792. <https://doi.org/10.1175/JPO-D-16-0187.1>
8. Kleiss, J.M. and Melville, W.K., 2011. The Analysis of Sea Surface Imagery for Whitecap Kinematics. *Journal of Atmospheric and Oceanic Technology*, 28(2), pp. 219-243. <https://doi.org/10.1175/2010JTECHO744.1>
9. Malinovsky, V.V., Korinenko, A.E. and Kudryvtsev V.N., 2018. Empirical Model of Radar Scattering in the 3-cm Wavelength Range on the Sea at Wide Incidence Angles. *Radiophysics and Quantum Electronics*, 61(2), pp.98-108. <https://doi.org/10.1007/s11141-018-9874-7>
10. Fairall, C.W., Bradley, E.F., Hare, J.E., Grachev, A.A. and Edson, J.B., 2003. Bulk Parameterization of Air-Sea Fluxes: Updates and Verification for the COARE Algorithm. *Journal of Climate*, 16, pp. 571-591. [https://doi.org/10.1175/1520-0442\(2003\)016<0571:BPOASF>2.0.CO;2](https://doi.org/10.1175/1520-0442(2003)016<0571:BPOASF>2.0.CO;2)
11. Mironov, A.S. and Dulov, V.A., 2008. Detection of Wave Breaking Using Sea Surface Video Records. *Measurement Science and Technology*, 19(1), 015405. <https://doi.org/10.1088/0957-0233/19/1/015405>
12. Dulov, V.A., Korinenko, A.E., Kudryvtsev, V.N. and Malinovsky, V.V., 2021. Modulation of Wind-Wave Breaking by Long Surface Waves. *Remote Sensing*, 13(14), 2825. <https://doi.org/10.3390/rs13142825>
13. Pivaev, P.D., Kudryvtsev, V.N., Korinenko, A.E. and Malinovsky, V.V., 2021. Field Observations of Breaking of Dominant Surface Waves. *Remote Sensing*, 13(16), 3321. <https://doi.org/10.3390/rs13163321>
14. Mironov, A.S. and Dulov, V.A., 2008 Statistical Properties of Individual Events and Energy Dissipation of Breaking Waves. *Ecological Safety of Coastal and Shelf Zones and Comprehensive Use of Shelf Resources*, (16), pp. 97-115 (in Russian).
15. Kudryvtsev, V.N., Hauser, D., Caudal, G. and Chapron, B., 2003. A Semiempirical Model of the Normalized Radar Cross-Section of the Sea Surface 1. Background Model. *Journal of Geophysical Research: Oceans*, 108(C3), 8054. <https://doi.org/10.1029/2001JC001003>
16. Banner, M.L. and Peirson, W.L., 2007. Wave Breaking Onset and Strength for Two-Dimensional Deep-Water Wave Groups. *Journal of Fluid Mechanics*, 585, pp. 93-115. <https://doi.org/10.1017/S0022112007006568>
17. Phillips, O.M., 1985. Spectral and Statistical Properties of the Equilibrium Range in Wind-Generated Gravity Waves. *Journal of Fluid Mechanics*, 156, pp. 505-531. <https://doi.org/10.1017/S0022112085002221>

Submitted 22.04.2024; approved after review 02.05.2024;
accepted for publication 16.05.2024

About the authors:

Vladimir V. Malinovsky, Senior Researcher, Marine Hydrophysical Institute of RAS (2 Kapitanskaya Str., Sevastopol, 299011, Russian Federation), CSc. (Phys.-Math.), **ORCID ID: 0000-0002-5799-454X**, **ResearchID: F-8709-2014**, **Scopus Author ID: 23012976200**, vladimir.malinovsky@mhi-ras.ru

Aleksandr E. Korinenko, Senior Researcher, Marine Hydrophysical Institute of RAS (2 Kapitanskaya Str., Sevastopol, 299011, Russian Federation), CSc. (Phys.-Math.), **Scopus Author ID: 23492523000**, **ORCID ID: 0000-0001-7452-8703**, korinenko.alex@mhi-ras.ru

Contribution of the co-authors:

Vladimir V. Malinovsky – development of experimental research method, analysis and synthesis of research results, preparation of the paper text

Aleksandr E. Korinenko – development of techniques and carrying out the experimental studies, participation in the discussion of the article materials, analysis and synthesis of the research results

The authors have read and approved the final manuscript.

The authors declare that they have no conflict of interest.

An Advanced Electric Power Generator for Offshore Autonomous Stations

D. G. Gryazin^{1,2,✉}, K. A. Gleb³

¹“Concern “SCRI “Elektropribor”, JSC, Saint Petersburg, Russian Federation

²FSAEI HE “National Research University ITMO”, Saint Petersburg, Russian Federation

³PJSC «Gazprom», Saint Petersburg, Russian Federation

✉ volnagd@yandex.ru

Abstract

Purpose. The research is purposed at substantiation of the design of floating marine stations with a wave energy generator. The proposed construction is of higher efficiency as compared to the known designs due to the application of roll oscillations and resonance operating mode.

Methods and Results. The resonance method of converting wave energy into electrical energy, as well as the design of an autonomous station based on the resonance conversion of the station hull roll oscillations into the electrical energy are described. The method implies adjusting the frequency of natural angular oscillations of the floating station hull to the significant wave frequency. It has been theoretically proved that the conversion of roll oscillations energy is more effective than the conversion of vertical oscillations. This is due to the fact that the amount of damping during vertical vibrations of a cylindrical body in water exceeds the amount of damping during angular oscillations of such a body. Besides, the proposed method is shown to be effective for applications in the development of measurement systems and storage devices. The design of a floating station is proposed for implementing the resonance method for converting wave energy. It is shown that adjusting the frequency of natural onboard oscillations of the station hull to the significant wave frequency can be done using the additional filled tanks. The algorithm for adjusting the hull roll oscillations to the resonance with significant wave frequency is described. The kinematic scheme for a mechanical converter of roll energy into electrical one is proposed.

Conclusions. The results of theoretical studies were validated experimentally using the device test model in a wave experimental basin. They show that the hydrodynamic efficiency of the proposed wave converter increases as the wave heights decrease.

Keywords: energy, waves, conversion, mechanical, electrical energy, floating stations, roll oscillations

Acknowledgements: The authors are grateful to Sergei G. Zhivitsa, PhD, a specialist of FSUE Krylov State Research Center, for his valuable assistance in conducting the studies and preparing the materials for the paper.

For citation: Gryazin, D.G. and Gleb, K.A., 2024. An Advanced Electric Power Generator for Offshore Autonomous Stations. *Physical Oceanography*, 31(4), pp. 539-561.

© 2024, D. G. Gryazin, K. A. Gleb

© 2024, Physical Oceanography

Introduction

As a result of rapid development of marine engineering, a category of offshore autonomous stations has appeared. They are used for collecting hydrophysical information on the shelves of the seas and the World Ocean for real-time oceanological studies and for charging the batteries of underwater unmanned autonomous vehicles (UAVs). These stations are floating vessel-like structures up to



10 m long, with the displacement up to 50 tons; they are equipped with hydrophysical^{1, 2} [1, p. 151–152] or other target equipment as well as power sources, the capacity of which determines the endurance of their operation. These stations are developed and manufactured mainly in the US where these works as well as other defense projects are funded by DARPA and the Department of Energy. The stations are equipped with renewable energy sources such as solar panels and wind-powered generators to recharge the batteries and increase the endurance of equipment operation (Fig. 1).

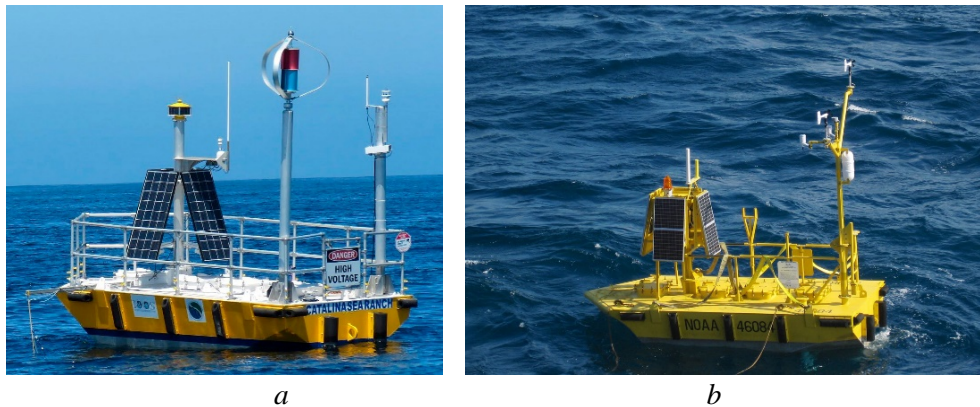


Fig. 1. Offshore floating stations for real-time ocean monitoring owned by the *Catalina Sea Ranch* Company (a) and the US Coast Guard (b)

It should be noted that in recent years UAVs have been actively developing for defense missions, sea bed mapping, underwater surveillance³ [2] and geological exploration⁴. They support distributed monitoring of the hydrological parameters of aquatic environment⁵. UAV batteries are recharged at special offshore autonomous stations. The British company *AVS Global* holds the leadership in the development of such systems; the results of their research [3] were used for creating a number of surface vehicles and their functional systems. The Russian designers follow the same

¹ Defense Visual Information Distribution Service, 2013. *Coast Guard, NOAA Return Weather Buoy to Service in Southeast Alaska*. [online] Available at: <https://www.dvidshub.net/image/1000279/coast-guard-noaa-return-weather-buoy-service-southeast-alaska> [Accessed: 21 April 2024].

² AXYS Technologies Inc., 2024. *Ocean Sentinel NOMAD™ MetOcean Buoy*. [online] Available at: <https://axys.com/ocean-sentinel-nomad-metoccean-buoy> [Accessed: 21 April 2024].

³ NauticExpo.ru., 2024. *Hydrographic Survey Marine Drones*. [online] Available at: <https://www.nauticexpo.ru/proizvoditel-sudno/morskoj-besplotnik-gidrograficeskih-issledovaniy-42947.html> [Accessed: 21 April 2024].

⁴ Korabel.ru., 2018. *[The Use of Underwater Gliders for Exploration]*. [online] Available at: https://www.korabel.ru/news/comments/primenenie_podvodnyh_glayderov_dlya_geologorazvedki.html [Accessed: 31 January 2024] (in Russian).

⁵ Boyko, A., 2021. *[Catalog of Underwater Robots]*. [online] Available at: <http://robotrends.ru/robopedia/katalog-podvodnyh-robotov> [Accessed: 21 April 2024] (in Russian).

way ⁶, however, the use of wave energy as a renewable power source is no less efficient. Since the hull of the floating station is directly involved in the power generation process, it becomes a wave-activated power generator (WPG) also known as a wave absorber. Such a generator has been implemented in the *SeaRAY* system designed by *Columbia Power Technologies* ⁷ (Fig. 2, 3).

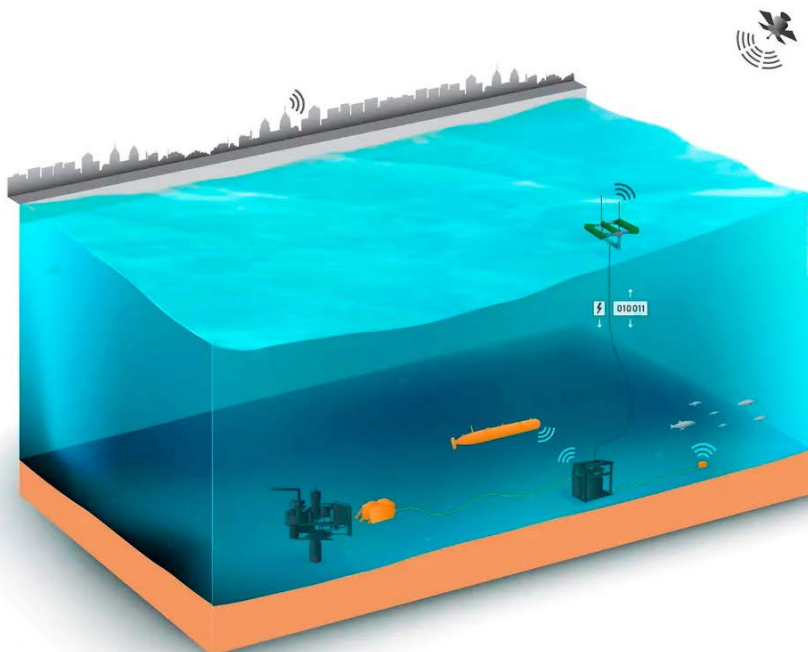


Fig. 2. UAV battery recharge station *SeaRAY* designed by the *Columbia Power Technologies* company

It is much more difficult to collect the wave energy in the open sea than in the coastal zone. The reason is that in the former case it is necessary to ensure high reliability of the WPG operation under a wide range of disturbing effects without any additional maintenance which requires proven engineering solutions to be applied. Their design should be simple and maintainable. There are well-known structures of a buoy with WPG employing the vertical oscillations of the buoy designed by *Ocean Power Technologies* ⁸, however, the efficiency of wave energy

⁶ Boyko, A., 2022. [*Catalog of Solar-Powered Surface Robots*]. [online] Available at: <http://robotrends.ru/robopedia/katalog-nadvodnyh-robotov-na-solnechnyh-batareyah> [Accessed: 31 January 2024] (in Russian).

⁷ Garanovic, A., 2020. *SeaRAY Autonomous Offshore Power System Set for Sea Trials*. Available at: <https://www.offshore-energy.biz/searay-autonomous-offshore-power-system-set-for-sea-trials> [Accessed: 21 April 2024].

⁸ Ocean Power Technologies, 2011. *Company Presentation*, 36 p. [online] Available at: <https://oceanpowertechnologies.gcs-web.com/static-files/212d7a27-1fee-40cc-92e2-ca600045c8a0> [Accessed: 03 August 2024].

collection in these converters depends strongly on the amplitude and frequency response of their vertical oscillations.

It should be noted that the amplification factor of the response characteristics for the oscillations of floating objects is affected by damping forces considerably. Since the values of these forces are smaller during the roll oscillations than during the vertical ones, it is the rolling of marine stations that is advisable to use for collecting the wave energy. This feature is explained by the fact that during vertical oscillations of a floating object, the damping forces depend mainly on the intensity of waves propagating from the oscillating object and are proportional to the area of its waterline. All other components, such as vortex damping and skin friction damping which depend on the shape and roughness of the underwater part, are usually much smaller. When a vessel-like object without protruding parts is rolling the level of damping depends primarily on the vortex component while the wave and friction damping play a secondary role. Improving the WPG energy efficiency is obviously an urgent task. To ensure the maximum efficiency, a station with WPG should apparently work in the controlled resonance mode, i.e. adjust the frequency of its own oscillations to the frequency of sea waves.

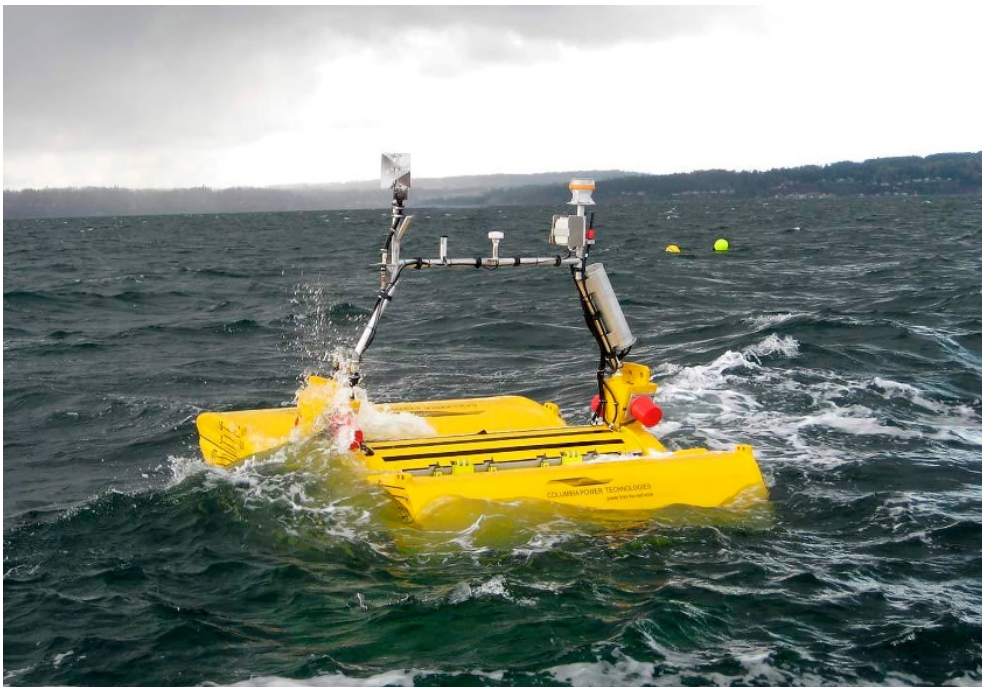


Fig. 3. Wave absorber within the *SeaRAY* system

The objective of the proposed research is to provide rationale for the design of a station with WPG operated in the open sea, the efficiency of which is higher than in the existing designs due to the use of roll oscillations and resonance operation mode.

Resonance-based method for wave energy conversion by floating stations

The wave energy can be converted into the electric power required for recharging the batteries of a floating station by converting the energy of oscillations of the station with WPG into electric power by means of onboard generators. Buoy oscillation on a wave is used for energy conversion by such WPGs as *SEAREV*⁷ [4, 5] and *PeWEC* [6]. For example, *Searay* consists structurally of a block that includes several cylindrical floats installed parallel to each other and having separate rotation axes relative to the load frame (Fig. 3). A pendulum body is installed inside each cylindrical float. The rotation of the pendulum with the angular deflection of each float generates mechanical energy when the cylindrical body performs angular oscillations under the influence of waves. The highest operating efficiency of such converters is achieved when they operate in a controlled resonance mode. That is why it is necessary to control the system for converting mechanical energy into electrical energy [7]. Research into operation of onboard resonance-based converters of buoy oscillation energy into electric power has led to the registration of patents^{9, 10}.

To create a station with WPG which uses controlled resonance is a challenging task since the frequency of the spectral maximum of wave elevations depends significantly on the wave intensity. Moreover, depending on the time of wind activity, the waves can be developing, fully-developed or decaying. The developing waves are typically shorter, i.e., having a smaller period, while the decaying waves are longer, with a larger period. In addition, waves of small intensity may have a bimodal spectrum. Considering these specific features, the characteristics of the station with WPG should be restructured for operating in resonance mode with the waves having different average periods.

One of the examples of such systems is *AquaHarmonics* [8] comprising an anchored floating buoy, power generator of which is installed in the anchor. The rotor of the electric machine is connected to the buoy via the anchor rope and has a spring mechanism. The buoy performs orbital oscillations on the front and back slopes of the waves and the rope is slack enough to separate the buoy and the anchor. Horizontal components of these oscillations are used for power generation. When the buoy approaches the anchor the rope slack is compensated by winding it onto a pulley by means of the spring mechanism and when the buoy moves in the opposite direction the pulley spins the rotor of the electric machine. The eigen frequency of the system of the generator, rope and buoy is controlled by damping the multidirectional rotation of the rotor. This system can operate only in shallow water and is not designed for oceanographic instruments installation. There

⁹ Gryazin, D.G. and Velichko, O.O., 2016. *Installation for Recovery of Energy of Sea Buoys*. Russian Federation Patent No. RU2577924C1. Concern “SCRI “Elektropribor”, JSC (in Russian).

¹⁰ Gryazin, D.G. and Epifanov, O.K., 2018. *Installation for Battery Energy Replenishment of Small Marine Autonomous Equipment and Buoys*. Russian Federation Patent No. RU2658713C1. Concern “SCRI “Elektropribor”, JSC (in Russian).

are also other known designs of buoys with WPG working in the controlled resonance mode and collecting the energy of the buoy vertical oscillations ¹¹.

The maximum use of the wave front energy for converting it into the energy of oscillations should be made by combining the period of the station free roll oscillations with the dominant period of the waves. The reason is that the damping forces determined by the resistance coefficients are much smaller during the angular oscillations of floating bodies than those during their vertical oscillations. The resistance coefficients are not constant; they are velocity functions and have a nonlinear dependence. They are determined experimentally for the weight and size of the floating bodies. For example, the expression for the resistance coefficient in the case of its linear approximation for the vertical oscillations of a floating body can be found from formula ¹²

$$W_{\text{vert}} = \frac{4}{3\pi} \rho C_Q S r \omega_V, \quad (1)$$

where ρ is density of water, C_Q is quadratic coefficient of resistance determined experimentally; r is wave amplitude, S is area of the waterline and ω_V is frequency of its vertical oscillations. This expression is convenient for practical calculation of the resistance coefficient (function) which evidently depends on the variables $r\omega$, i.e., on the velocity.

resistance coefficient can be obtained for the angular oscillations of a floating body according to the method proposed in ¹³ from expression

$$W_{\text{ang}} = 0.85 \omega_F r_A K_W, \quad (2)$$

where ω_F is frequency of free angular oscillations of the floating body, r_A is amplitude of angular oscillations, $K_W = C_W (J_{\text{AIR}} - J_{\text{ADD}})$, C_W is quadratic coefficient of resistance depending on the velocity, J_{AIR} is body moment of inertia in the air, and J_{ADD} is added mass moment of inertia of water.

The analysis of expressions (1) and (2) shows that in the case of vertical oscillations of a floating body, the resistance coefficient depends on the area of the floating body waterline while in the case of angular oscillations it depends only on its moment of inertia and added mass moment of inertia of water. Thus, we observe less resistance during roll oscillations than during vertical ones. This is most clearly manifested on spherical or cylindrical floating objects which have the lowest resistance to roll oscillations.

¹¹ Korobkov, V.A., 1986. *Ocean Energy Conversion*. Leningrad: Shipbuilding, 280 p. (in Russian).

¹² Berto, G.O., 1979. *Oceanographic Buoys*. Leningrad: Shipbuilding, 215 p. (in Russian).

¹³ Blagoveshchenskiy, S.N. and Kholodilin, A.N., 1976. [*Reference Book on Statics and Dynamic Behaviour of Ships. V. 2. Dynamics (Rolling) of the Ship*]. Leningrad: Shipbuilding, 176 p. (in Russian).

To adjust the rolling mode of the station with WPG to the resonance mode in which the amplitudes of its rolling oscillations will be maximal, the eigen frequency of rolling should correspond to the frequency of the maximum spectral density of incident waves. At the same time, variation in the eigen frequency of rolling ω_R of the station with WPG is achieved by varying correspondingly transverse metacentric height h , i.e., its stability margin in accordance with known formula ¹⁴

$$T = 2\pi\sqrt{\frac{I}{Dh}}, \quad (3)$$

where T is period of free oscillations of the station during rolling; I is moment of inertia of the station mass (relative to the longitudinal axis passing through the center of gravity) calculated with the added mass moment of inertia taken into account; D is station draught; h is transverse metacentric height, i.e. the transverse metacenter elevation above the center of gravity.

It is known that in the absence of developed stern or bow superstructures, a free-drifting vessel turns into a position when its side is almost parallel to the wave and experiences mainly vertical and roll oscillations. This makes it possible to use the rolling conversion and in this case the cylindrical shape of the WPG hull will be most efficient to practically remove the wave and vortex components of damping and to ensure the minimum resistance to roll oscillations, thus reaching the significant amplitudes at resonance that are much greater than the amplitude of the wave slope angle. As a result, the employment of roll energy is expected to considerably increase the efficiency of wave energy harvesting even when the station with WPG has a small draught. In practical implementation, certainly, it is necessary to take relevant design measures against the deck flooding and the WPG overturn during resonance rolling on storm waves.

To convert the roll energy into electric power, it is advisable to use the mechanical energy storage units that would ensure the rotation of the generator rotor of the electric machine at a uniform angular rate similarly to the solution described in ¹⁵. At the same time, the rotation of the electric machine rotor should be unidirectional rather than alternating, during which significant reactive power is generated [9]. It is this sequence of technological solutions that should be implemented in the design of a station with WPG.

It should be mentioned that the maximum use of the roll energy is achieved by combining the period of free oscillations of the generator moving proof mass with the WPG rolling period (Fig. 4). In this case, as soon as the resonance is achieved, the pendulum will decline from the vertical in the opposite direction, i.e., with

¹⁴ Nogid, L.M., 1967. [*Design of Marine Vessels. Part 2. Vessel Stability and Behavior in Rough Seas*]. Leningrad: Shipbuilding, 72 p. (in Russian).

¹⁵ Temeev, A.A., 1995. *Float Wave Power Station*. Russian Federation Patent No. RU2037642C1. (in Russian).

a phase shift by 90° relative to the roll oscillations. Among the advantages of the proposed method is the fact that such a generator will collect the wave energy in a wide range of wave periods.

Design of advanced floating station

A station with WPG (Fig. 4) consists of hull 1 with positive buoyancy, energy conversion mechanism 2, ballast tanks 3, pendulum with moving proof mass 4 and computer. The station hull should be close to cylindrical shape because it has the least resistance to roll oscillations. The pendulum can change the length of suspension by varying length l of extendable rod 5 by means of extendable rod drive 6. Ballast tanks 3 should be equipped with level gauges and the water should be supplied into and discharged from the tanks using a pump and drain valves which are not shown in Fig. 4.

The energy conversion mechanism (Fig. 5) consists of two parts: a roll energy converter (REC) and an accumulator — mechanical energy converter (AMEC). The computer (Fig. 4) comprises a microprocessor unit generating control commands, a memory with a recorded control algorithm, analog-to-digital and digital-to-analog converters as well as amplifiers of analog signals for controlling the pump and the valves of the ballast tanks as well as extendable rod drive 17 (Fig. 5). The computer processes the measurement data received from sensor 3 of input shaft 1 twist angle (Fig. 5), the level gauge of ballast tanks 3 (Fig. 4) and multi-turn angle sensor 24 (Fig. 5).

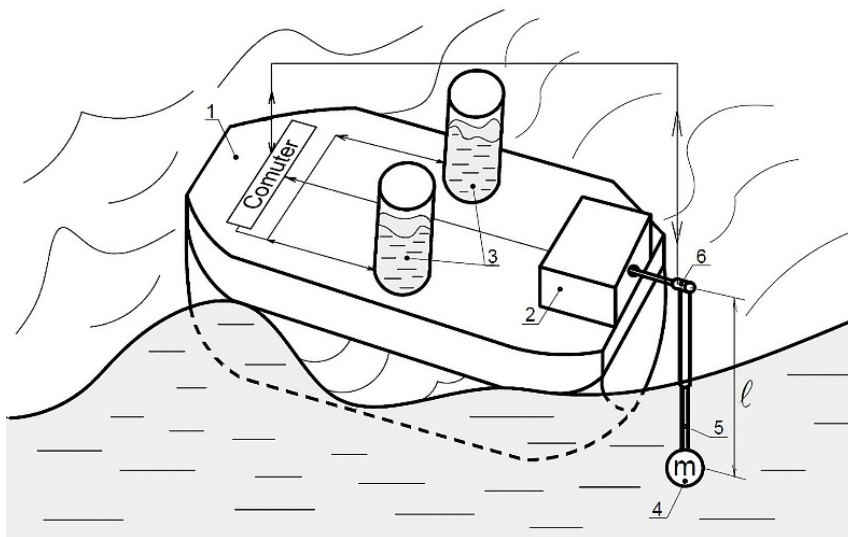


Fig. 4. Design of the station hull with WPG: 1 – floating hull; 2 – energy conversion mechanism; 3 – ballast tanks; 4 – pendulum moving proof mass; 5 – extendable rod; 6 – extendable rod drive

The station with WPG operates as follows. Floating hull 1 of the station (Fig. 4) performs wave-induced roll oscillations relative to the position of pendulum 4 which is close to vertical. The pendulum is damped by water and has mass m commensurate with the buoy draught. In order to use the wave front energy to the maximum extent in terms of its conversion into the kinetic energy of rolling by combining the period of free roll oscillations of the floating buoy with the prevailing period of waves, the period of free roll oscillations of the station floating buoy is changed using expression (3) by changing the metacentric height of the buoy. It is changed by filling or draining ballast tanks 3 (Fig. 4). The amplitude and period of roll oscillations are measured by sensor 3 twist angle (Fig. 5) and the computer (Fig. 4) calculates forced oscillations of the station hull.

The algorithm for tuning the hull roll oscillations in resonance with the prevailing frequency of the waves after arbitrary filling of the ballast tanks includes:

- 1) record of oscillations over the 900 s interval during which the rolling process is considered stationary;
- 2) determining maximum range of oscillations θ_{max} ;
- 3) determining the region of secondary oscillations θ_H making 20% of the maximum range;
- 4) determining the ranges of oscillations caused by prevailing waves $\theta_{Pi} > \theta_H$,

their number N and average value
$$\bar{\theta}_p = \frac{\sum_{i=1}^N \theta_{Pi}}{N};$$

- 5) calculation of the period of prevailing waves $T_{Pi} = 900/2N$;
- 6) filling the ballast tanks to 10% of the volume;
- 7) repeating the sequence of operations 1 to 5;
- 8) analysis of values $\bar{\theta}_H$ obtained before and after filling the ballast tanks;
- 9) if value $\bar{\theta}_p$ obtained after filling is larger than the value before filling the ballast tanks, the latter should be filled according to point 6, and if it is less, it is necessary to start reducing the water level in the tanks by 20% for the first time and then by 10%;
- 10) as soon as next obtained value $\bar{\theta}_p$ is less than the previous one, it is necessary to restore the water level in the ballast tanks as it was with the previous value.

The ballast tanks are adjusted in accordance with the algorithm depending on whether the waves are decaying, developing or stationary. This adjustment is done programmatically, in the time intervals from 1 to 12 hours. All values of oscillations are calculated by the algorithm in the computer (Fig. 4).

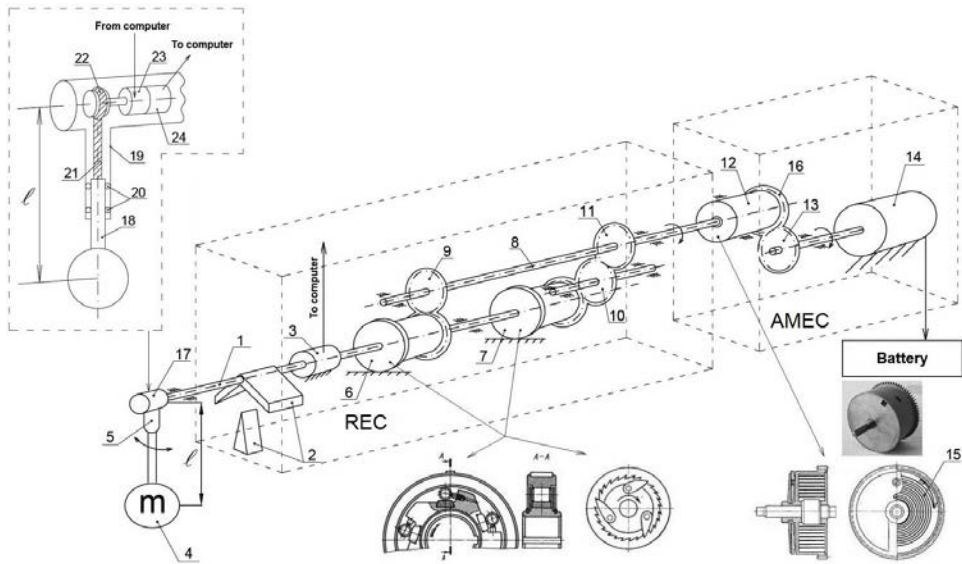


Fig. 5. Mechanism for converting roll energy into electric power: 1 – input shaft; 2 – twist stop; 3 – angle sensor; 4 – pendulum; 5 – extendable rod; 6 and 7 – unidirectional rotation freewheel couplings, e.g., ratchet or freewheel clutches, with tooth rims; 8 – output shaft; 9, 10 and 11 – gear wheels; 12 – spring drum; 13 – gear wheel of electric machine; 14 – electric machine; 15 – flat spiral spring; 16 – tooth rim; 17 – extendable rod mechanism; 18 – extendable rod; 19 – drive housing pipe; 20 – extendable rod bearings; 21 – rope; 22 – pulley; 23 – motor with gearbox; 24 – multi-turn angle sensor

The period of oscillations of the pendulum installed in the lower part of the station with WPG and water-damped will be less than Schuler period equal to 84.4 minutes, therefore, it will be perturbed by the oscillations during rolling; in addition, its perturbation will also depend on the orbital displacement of the buoy hull oscillating on the waves. Thus, the pendulum will perform some forced oscillations relative to the vertical position with a frequency of this perturbing force. To convert the kinetic energy of roll oscillations into electric power efficiently, the period of free oscillations of the moving proof mass is matched with the period of the buoy rolling. To do so, length l of pendulum 4 is selected and set using the extendable rod 5 (Fig. 5). The resonance frequency of the pendulum oscillations is determined from expression ¹⁶

$$\omega_p = \sqrt{\omega_0^2 - 2K_D^2},$$

where $\omega_0^2 = \frac{mgl}{J}$ is eigen frequency of the pendulum oscillations; $K_D = \frac{Wl_l}{J}$ is damping coefficient. Here, m is mass of the pendulum; l is length of its suspension;

¹⁶ Kuchling, H., 1985. *Paperback of Physics*. Moscow: Mir, 520 p. (in Russian).

J is moment of inertia of the system; l_I is arm of the integral force of resistance including the resistance of both moving proof mass and its suspension rod; W is quadratic coefficient of resistance to the motion of pendulum and its suspension in water depending on the pendulum motion velocity and the cross-section of the pendulum and suspension rod determined experimentally. The period of oscillations is found by known formula $T_p = \frac{2\pi}{\omega_p}$. Length l is calculated in the computer (Fig. 4).

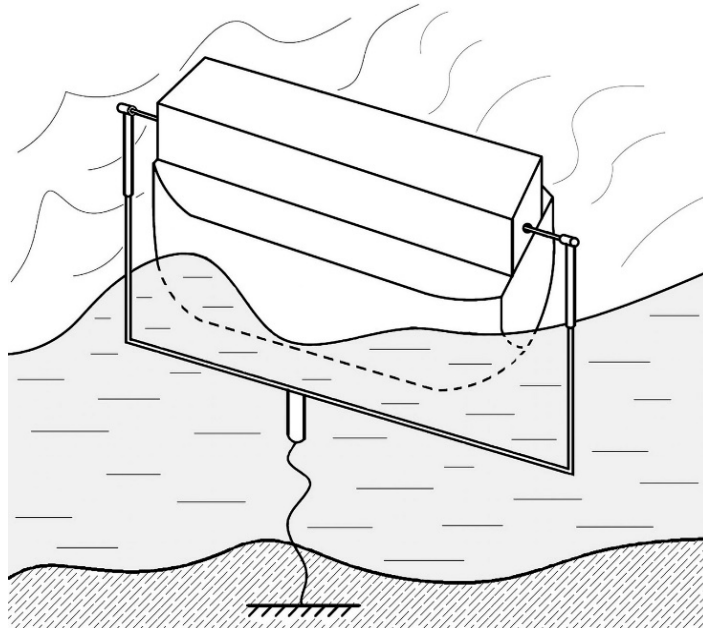


Fig. 6. Design of a station with WPG for installation at an anchor

It should be noted that due to the changed phase of oscillations in the resonance region when the periods of the station hull rolling are close to the periods of its free oscillations the pendulum will decline at a small angle to the side opposite the angle of the buoy hull inclination and twist shaft l of the energy converter (Fig. 5) at an additional angle. In order to prevent the hull overturn in the case of stability loss caused by the resonance phenomena, this input shaft of the energy converter is equipped with twist stop 2 (Fig. 5) which will limit the angle of twist and prevent the buoy overturn. The design of the mechanism has been patented ¹⁷.

The energy conversion mechanism (Fig. 5) works as follows. During rolling, the station hull turns relative to the vertical position of pendulum 4 with extendable

¹⁷ Gryazin, D.G., Mashoshin, A.I. and Pashkevich, I.V., 2022. *Mobile Distributed Underwater Surveillance System*. Russian Federation Patent No. RU2767384C1 (in Russian).
PHYSICAL OCEANOGRAPHY VOL. 31 ISS. 4 (2024)

rod 5, and input shaft 1 twists at the same time. The shaft twist is converted into the output signal of angle sensor 3 which is transmitted to the computer.

When the station hull turns counter-clockwise relative to moving proof mass 4 with rod 5, the moment is transferred from shaft 1 by unidirectional rotation freewheel coupling 6 which can be of various designs such as ratchet or freewheel clutch as described in Fig. 5 (coupling hereinafter) and when the hull turns clockwise, this is done by coupling 7. Coupling 6 converts the twist of shaft 1 into the counter-clockwise turn of the coupled gear wheel while coupling 7 does the same in clockwise direction; these couplings are connected opposite each other. Owing to gear wheel 9, intermediate shaft 8 turns clockwise. Owing to the pair of gear wheels 10 and 11, the coupled gear wheel of coupling 7 also turns shaft 8 clockwise. The gear ratio of the gear wheels connected to couplings 6 and 7 is increasing and equal in relation to shaft 8. Thus, the REC converts the alternating turn of the station hull relative to the pendulum into the clockwise turn of shaft 8. Rotation of shaft 8 involves the flat spiral spring of the AMEC located in drum 12. The torque of the spring is less than the moment of restoring forces during the station hull rolling which maintains its stability. Tooth rim 16 of drum 12 turns wheel 13 when the flat spiral spring is untwisting. Wheel 13 transfers the torque to the rotor of electric machine 14 functioning as a DC generator. The spiral spring has a normal characteristic and almost constant torque when untwisting which ensures small variation in the number of the electric machine rotor revolutions¹⁸. The current is supplied from generator 14 to recharge the battery. To set the mechanical part of the generator in resonance with the frequency of the station hull free oscillations, pendulum suspension length l is changed by extending rod 18 with load 4 from pipe 19. Rod 18 is put into a required position by moving it vertically, for which purpose the rope fixed in the upper part of the rod and wined on pulley 22 is driven by motor 23. To bring the rod into a specified position, multi-turn angle sensor 24 connected to the computer is calibrated in accordance with the turn of pulley 22 and the length of rope 22 wound on it. The pendulum length is changed on command from the computer in accordance with the functional dependence of the pendulum length on the eigen frequency of the station hull rolling. This dependence is determined experimentally, based on the recorded free oscillations of the station with the tanks filled to different levels and with the pendulums of different lengths against the criterion of the largest range of free oscillations achieved by the station hull. The functional dependence mentioned above is determined experimentally at tranquil sea in the absence of external perturbing forces.

¹⁸ Ponomarev, S.D. and Andreeva, L.E., 1980. [*Design of Elastic Elements in Machines and Devices*]. Moscow: Mechanical Engineering, pp. 64-66 (in Russian).

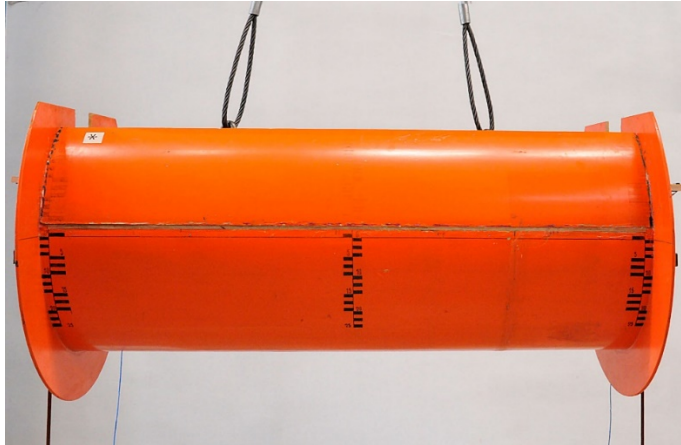


Fig. 7. Model tested in a wave experimental basin

It should be noted that the achievements of modern mechanics make it possible to design the energy conversion mechanism based on other elements; however, their purpose will be the same.

In the case of an anchored station with WPG, a structure shown in Fig. 6 can be used. In this structure, it is proposed to install two energy converters (Fig. 5), connect the extendable rods to each other with an additional horizontal rod and connect an anchor system in the center of the latter. In this case, the position of rod 5 (Fig. 5) will be controlled by the anchor and may be different from vertical; nevertheless, this will not affect the power generated by electric machine 14. Due to this structure, the station with WPG will be able to turn its side towards the direction of the waves.

Validation of the proposed method

The proposed method was validated by the experimental study of a schematized model of a station with WPG (Fig. 7) in the wave basin at Krylov State Research Center.

The cylindrical model was 1650 mm long, its hull diameter was 640 mm and the mass was 172 kg. The sides of the model were made high in order to keep the waterline area unchanged at large inclination angles. Two pendular systems (Fig. 8) were installed using ball bearings on both side plates of the model hull, at the level of the model center of gravity. The pendular systems comprised rods 1 with a length of 0.9 m fixed on rotation shafts 2 on the axis of the center of mass on the side faces of the model; the position of the axis of the center of mass was identified during the model preparation. The pendular systems were made in the form of rods; there was load 3 on each suspension which could be moved along the rod, thus changing the length of the pendulum. The loads were fixed on the rod using a screw stop.

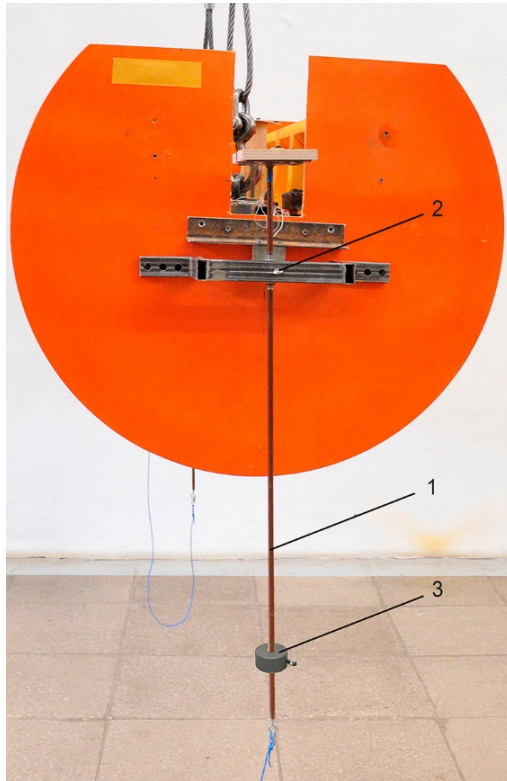


Fig. 8. One of two pendular systems fixed on the model sides: 1 – rod; 2 – rod rotation shaft fixed on the axis of the model center of mass; 3 – load with a screw stop moving along the rod

The model was tested in a wave basin (Fig. 9) 90 m long, 20 m wide and 4 m deep. The waves were formed by wave generator located at the end of the tank; it could generate regular (harmonic) waves with a length ranging from 0.6 to 12 m and a height from 20 to 240 mm or waves within a specified frequency band.

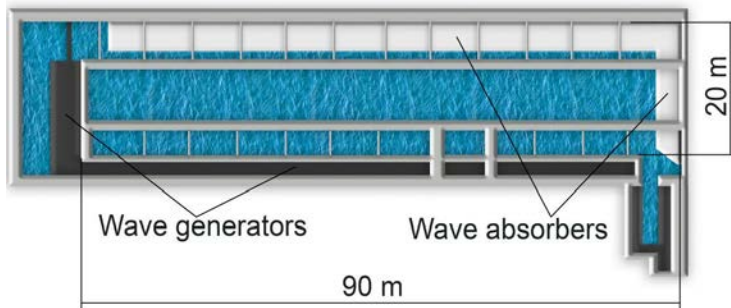


Fig. 9. Scheme of the wave experimental basin in Krylov State Research Center

Angular positions of the model and rods of the pendular system were captured by an optical tracker *Optotrak Certus HD*¹⁹; side inclinations of the model hull and rods were measured independently. To do this, triangular frames with three LEDs were installed on the model and on the platforms attached to the rods for the optical system to measure roll angles relative to the horizontal plane. Wave elevations were recorded by an electrolytic wave-recorder. In the course of the experiment, the measured processes were registered with a sampling interval of 0.01 s.

During the experiment, the model was positioned across the basin to model the position when the side faces the incident waves. The model heading was maintained by means of a retention system (Fig. 10) of two thin nylon ropes with elastic elements, one end of which was fixed to the model side at the height of its center of gravity and the other end — to basin structures. The rigidity of the elastic elements in the model retention system was to meet the requirement for the period of free sway oscillations of the retained model to differ enough from both the period of free roll oscillations and the average period of incident waves. This approach minimized the influence of the retention system on the model rolling.

Before the experimental study, the period of the model free roll oscillations and the moment of inertia with the added mass moment of inertia were identified, which were 1.89 s and 10.7 kg·m², respectively. Regular waves and bands of irregular waves were selected in accordance with the identified period.

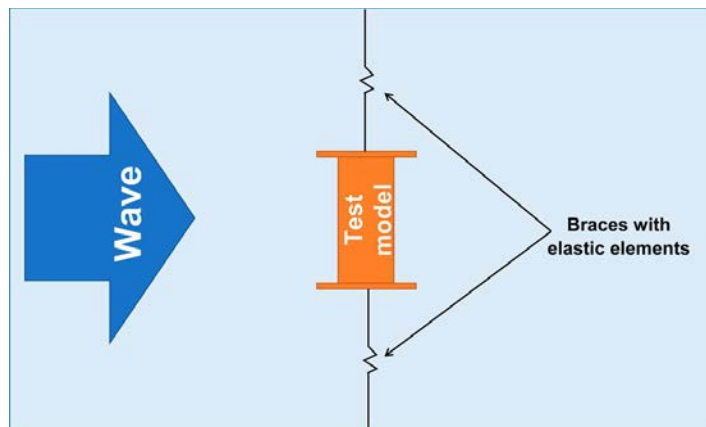


Fig. 10. Scheme of the system for model retention at the wave selection point in the experimental basin

The regular waves were selected before installing the vessel model in the wave basin; they had a period of 1.89 s, a height of 60 mm and a wave slope angle of 1.9°. Under these wave conditions, the angle of the model rolling was about 35°. Fig. 11

¹⁹ NDI, 2022. *Legacy Products: NDI's 40-Year History and Transition*. [online] Available at: <https://www.ndigital.com/products/legacy-products> [Accessed: 21 April 2024].

shows a fragment of the video of the model rolling and Fig. 12 presents the realization of roll oscillations measured by the optical system.



Fig. 11. Model during wave tests in the experimental wave basin

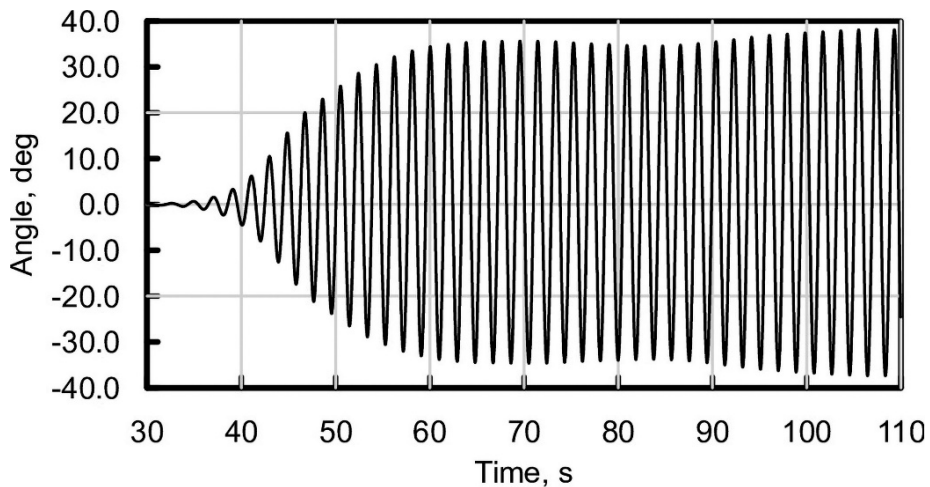


Fig. 12. Fragment of recorded realization of model rolling oscillations on regular waves of 0.06 m high with the period 1.89 s in real time

The record of the model roll in Fig. 12 shows the growing resonance effect which consists in increasing amplitude of oscillations when the wave frequencies coincide with the frequency of the model free oscillations. In this case, the model had performed about 15 oscillations before the amplitude became more than 30°. The maximum amplitude of the model steady-state oscillations was 38° while the wave slope angle was just 1.9° which is 20 times less. Obviously, when the wave

height changes, its period remains the same, i.e., when the wave steepness changes, the maximum amplitude of rolling and the time of achieving significant amplitudes of oscillations will change as well. The greater wave steepness is, the larger rolling amplitude is and the faster significant amplitudes are achieved. This is due to the fact that energy of wave E_w depends on its amplitude ²⁰:

$$E_w = \frac{1}{2} \rho g a^2,$$

where ρ is density of water; g is gravity acceleration; and a is wave amplitude.

At the next stage of the experimental study, the angular oscillations of the pendular system were measured. For this purpose, a load and its position on the rod were selected so that the difference of phases was 135° . Based on the obtained results, the hydrodynamic efficiency of this object was calculated. The hydrodynamic efficiency is the percentage ratio of the power of model angular oscillations to the power of wave [10]. According to ²¹, average power N_w of a regular wave crest per the crest length corresponding to the length of the object under study (the model) can be calculated by the formula:

$$N_w = \frac{\rho g^2 h^2 \tau l}{32\pi},$$

where h is wave height; τ is wave period; and l is wave crest length equal to the length of the model.

For the wave generated in the wave basin and experimentally selected to have parameters $h = 0.06$ m, $\tau = 1.89$ s, $l = 1.65$ m, the average corrected power over one period per one meter of the wave crest length was 6.26 W/m.

The power of model angular oscillations N_m can be found from the kinetic energy of angular motion, acquired by the model during angular oscillations. The power of angular motion is equal to amount of work performed by the model

over a time unit $\frac{J}{s} = W$:

$$N_m = \frac{A_m}{\Delta t}, \tag{5}$$

where A_m is work performed by the model, and Δt is sampling rate.

Work A_m (J) performed by the model over time unit Δt is equal to the variation in the model kinetic energy over this time unit Δt :

²⁰ Lugovskii, V.V., 1976. *Sea Dynamics*. Leningrad: Shipbuilding, 200 p. (in Russian).

²¹ Kochin, N.E., Kibel, I.A. and Roze, N.V., 1964. *Theoretical Hydromechanics*. New York – London – Sydney: Interscience Publishers, 577 p.

$$A_m = \frac{\Delta E_{km}}{\Delta t},$$

where E_{km} is kinetic energy of the model angular motion, its J is equal to

$$E_{km} = \frac{1}{2}(J + \Delta J)\dot{\theta}^2,$$

where J is moment of inertia of the model; ΔJ is added mass moment of inertia, $\dot{\theta}$ is angular velocity of the model roll oscillations.

Then, knowing the kinetic energy of the model at each time point, we find power of the model angular oscillations N_m (W):

$$N_m = \frac{\Delta E_{km}}{\Delta t}.$$

The power of angular oscillations can be found from the torque generated by the model angular oscillations, which is equal to the product of the moment of inertia and the added mass moment of inertia by the angular acceleration:

$$M = (J + \Delta J)\ddot{\theta},$$

where M is moment, $\frac{kg \cdot m}{s^2} m = Nm$; $\ddot{\theta}$ is angular acceleration.

We find the work from expression:

$$A_m = M \Delta \alpha,$$

where A_m is work, $Nm = \frac{kg \cdot m}{s^2} m = \frac{kg \cdot m^2}{s^2} = J$; $\Delta \alpha$ is variation in the model angular position in radians over sampling interval dt .

Then the power of oscillations is determined by equation (5).

Using the proposed method and the recorded realizations of the model roll with a sampling rate of 0.01 s, the average power of the model rolling over one period was calculated; it was equal to 54.98 W. The power value per one meter of the model length was 33.32 W/m. Taking into account the normalized power of the selected wave equal to 6.26 W/m, the hydrodynamic efficiency calculated in accordance with the definition proposed in [10] was 532%. Such a large value can be explained by several factors. First, the model roll amplitude is 20 times larger than the amplitude of the wave slope angle. Second, the power of the model roll energy is considered in

the steady-state mode of resonance oscillations. Thus, the calculations do not take into account the quantity of energy consumed for building up the model oscillations to the maximum roll angles. Moreover, if we consider only the first oscillations of the model, the angular deviation of which does not exceed the wave slope angle, then the normalized power developed by the model under these conditions will be just 0.08 W/m and the hydrodynamic efficiency will be just 1.33%.

Besides the studies on regular waves, the hydrodynamic efficiency was also studied on irregular waves. For this purpose, two Pearson – Moskowitz spectra were selected with the same periods of the spectral maximum τ_p equal to 1.89 s and significant heights of waves h_s equal to 87.71 mm and 44.69 mm. Figs. 13 and 14 show the records of the model rolling realization in time in the selected spectra of irregular waves at the sampling rate of 0.01 s.

Since the wave spectrum contains a number of harmonics, calculation of power by formula (4) appears to be difficult because this expression has been derived for one harmonic. Therefore, to assess the hydrodynamic efficiency of the model under the conditions of irregular wave spectrum, the power of waves was calculated as average spectral power of waves N_{sp} (W/m) per length unit of the wave profile by formula [11]:

$$N_{sp} = 490\tau_E h_s^2,$$

where τ_E is energy period of waves equal to $0.9\tau_p$ for *JONSWAP* spectrum and $0.86\tau_p$ for Pierson – Moskowitz spectrum.

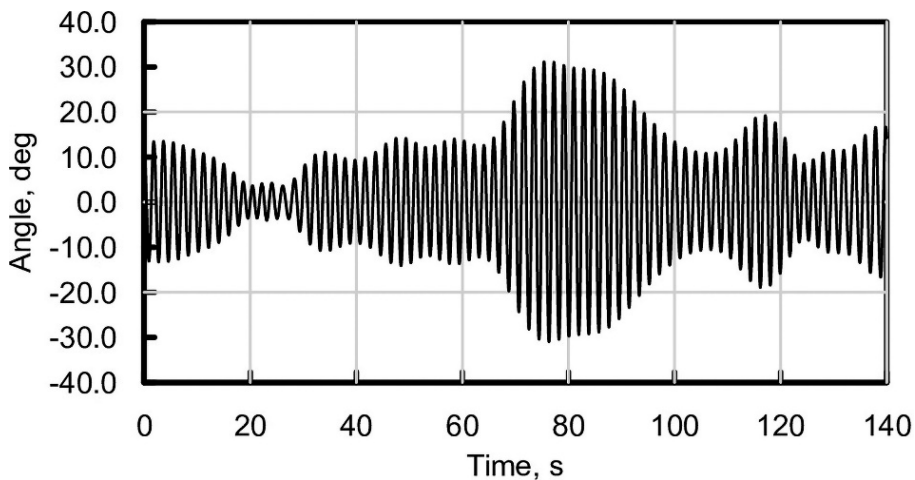


Fig. 13. Fragment of recorded realization of the model rolling in real time on irregular waves generated in the wave basin with spectrum No. 1 ($\tau_p = 1.89$ s, $h_s = 87.71$ mm)

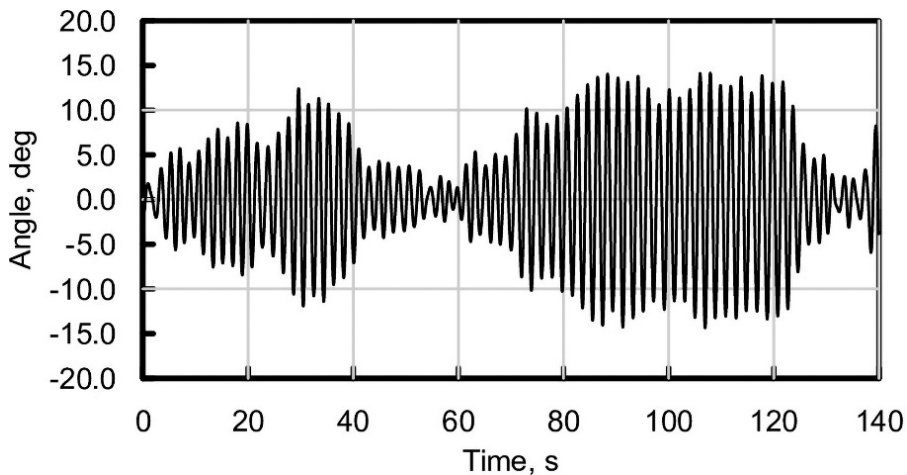


Fig. 14. Fragment of recorded realization of the model rolling in real time on irregular waves generated in the wave basin with spectrum No. 2 ($\tau_p = 1.89$ s, $h_s = 44.69$ mm)

In accordance with the realizations shown in Figs. 13 and 14, the power per a unit of wave crest length was 4.90 and 1.30 W/m for spectra Nos. 1 and 2 of irregular waves, respectively. The normalized power of the model angular oscillations was 5.81 W/m for spectrum No. 1 and 1.91 W/m for spectrum No. 2. The hydrodynamic efficiency was 119% and 148%, respectively. Based on these results, it can be concluded that the hydrodynamic efficiency increases with reducing heights of the waves and invariant period of the spectral maximum peak.

The obtained values of hydrodynamic efficiency for irregular waves proved expectedly to be lower than the values obtained for the regular waves, but still amounted to more than 100%. This can be explained by the fact that the period of the spectral maximum of both spectra of selected waves corresponded to the period of free oscillations of the model. This means that the spectra included a large number of waves, the periods of which were close to or coincided with the period of the model free oscillations. These waves caused strong roll oscillations due to the resonance effect which can be clearly seen in Fig. 13 at the 80th second, when the angle of roll oscillations reached 30° .

It should be noted that the hydrodynamic efficiency of resonance-based WPG will reduce even more in the case of irregular waves with the periods of the spectral maximum differing from the period of the model free oscillations since the resonance effect will be minimal or missing at all. The model rolling will reduce considerably because the model will tend to perform angular oscillations in conformity with the angles of the incident wave slopes. Hydrodynamic efficiency on the waves with the periods differing from the period of the model free oscillations will depend on the quality of the model oscillations, i.e., on the peak height and the resonance bandwidth.

Based on the experimental hydrodynamic efficiency results, it is possible to compare a resonance-based WPG to the well-known Salter's duck [10] which is believed to be one of the most efficient designs of a wave energy converter. The advantage of the Salter's duck is that it is of cylindrical shape with a protruding part with a large damping coefficient, due to which it can perform angular oscillations under the effect of waves and create a large torque between its sections to transfer it to the generator. At the same time, the cylindrical part has the minimal resistance in water and does not hinder the wave-induced angular rotation of the duck, so it can collect the maximum energy of the incident waves. However, this design is also a disadvantage since the duck follows the wave slope angle and the resonance effect hardly manifests itself in this structure. Therefore, its efficiency determined by the method applied in [10] cannot exceed 100% while the efficiency of a resonance-based WPG can be higher.

Conclusions

As can be seen from the above discussion, the energy of waves, even low-intensity ones, is quite significant. It depends largely on the wavelength and low-frequency waves make the main contribution in the total energy of the waves. Since the hull of a station with WPG is the primary converter of the wave energy, its linear dimensions will determine the power of the collected energy which depends on the wave profile length. Oscillations of the station with WPG are converted into electric power and it is advisable to use resonance-based energy converters in order to increase the efficiency of such conversion.

Under the conditions of resonance oscillations, it is more efficient to use roll oscillations of the wave buoys and floating stations rather than their vertical oscillations because the angular oscillations can be much greater in resonance than the slope angles of the incident waves. The principle of controlled resonance used in the wave absorbers improves significantly their performance efficiency. Hydrodynamic efficiency of the proposed device increases with reducing heights and periods of waves which is extremely important for collecting energy in low-wave conditions.

Increased efficiency of power generation by stations with WPG will inevitably lead to the need for increasing the strength of its hull since the load of incident waves will grow. The increase in strength will, in turn, result in greater mass of the station. In addition, when determining the WPG efficiency, it is necessary to take into account the electric generator loads which may introduce significant damping and reduce the intensity of roll oscillations.

Thus, to ensure the maximum efficiency of power generation, it is essential to select the parameters of stations with WPG for each area of operation considering the average parameters of the waves. On the other hand, adjustment of the frequency of the station free oscillations will increase the range of efficiency coefficients for the wave energy conversion.

REFERENCES

1. Pachauri, R.K., Pandey, J.K., Sharmu, A., Nautiyal, O.P. and Ram, M., eds., 2021. *Applied Soft Computing and Embedded System Applications in Solar Energy*. Boca Raton, USA: CRC Press, 254 p.
2. Mikhaylov, D.N., Senin, R.N., Dubrovin, F.S., Boreyko, A.A., Strykul, R.I. and Khramov, O.A., 2017. Autonomous Underwater Vehicle Application for Hydrographic Research in the Sea of Okhotsk. *Underwater Investigations and Robotics*, 2(24), pp. 4-13 (in Russian).
3. Storey, J.P., Hammond, J.L., G-H-Cater, J.E., Metcalfe, B.W. and Wilson, P.R., 2016. Modelling Dynamic Photovoltaic Arrays for Marine Applications. In: IEEE, 2016. *2016 IEEE 17th Workshop on Control and Modeling for Power Electronics (COMPEL)*. Trondheim, Norway, pp. 1-8. <https://doi.org/10.1109/COMPEL.2016.7556720>
4. Ruellan, M., BenAhmed, H., Multon, B., Josset, C., Babarit, A. and Clement, A., 2010. Design Methodology for a SEAREV Wave Energy Converter. *IEEE Transactions on Energy Conversion*, 25(3), pp. 760-767. <https://doi.org/10.1109/TEC.2010.2046808>
5. Rhinefrank, K., Schacher, A., Prudell, J., Hammagren, E., von Jouanne, A. and Brekken, T., 2015. Scaled Development of a Novel Wave Energy Converter through Wave Tank to Utility-Scale Laboratory Testing. In: IEEE, 2015. *2015 IEEE Power & Energy Society General Meeting*. Denver, CO, USA, pp. 1-5. <https://doi.org/10.1109/PESGM.2015.7286008>
6. Pozzi, N., Bracco, G., Passione, B., Sirigu, S., Vissio, G., Mattiazzo, G. and Sannino, G., 2017. Wave Tank Testing of a Pendulum Wave Energy Converter 1:12 Scale Model. *International Journal of Applied Mechanics*, 9(2), 1750024. <https://doi.org/10.1142/S1758825117500247>
7. Clément, A.H. and Babarit A., 2012. Discrete Control of Resonant Wave Energy Devices. *Philosophical Transactions of the Royal Society A. Mathematical, Physical, and Engineering Sciences*, 370(1959), pp. 288-314. <https://doi.org/10.1098/rsta.2011.0132>
8. Saeidtehrani, S., Lomónaco, P., Hagmüller, A. and Levites-Ginsburg, M., 2017. Application of a Simulation Model for a Heave Type Wave Energy Converter. In: EWTEC, 2017. *Proceedings of the 12th European Wave and Tidal Energy Conference, 27th Aug – 1st Sept 2017*. Cork, Ireland, 948.
9. Bal, V.B., Gecha, V.Ya., Goncharov, V.I., Ezhov, E.V., Chirkin, V.G., Shirinsky, S.V. and Petrichenko, D.A., 2015. Linear Electrical Reciprocating Machines – Types and Design of Electrical Machines. *Electromechanical Matters. VNIEM Studies*, 148(5), pp. 3-13 (in Russian).
10. Salter, S., 2016. Wave Energy: Nostalgic Ramblings, Future Hopes and Heretical Suggestions. *Journal of Ocean Engineering and Marine Energy*, 2(4), pp. 399-428. <https://doi.org/10.1007/s40722-016-0057-3>
11. Pastor, J., Dou, Y.-Q. and Liu, Y., 2014. Wave Energy Resource Analysis for Use in Wave Energy Conversion. In: IETC, 2014. *Proceedings of the 36th Industrial Energy Technology Conference (IETC 2014)*. New Orleans, USA.

Submitted 29.02.2024; approved after review 11.04.2024;
accepted for publication 16.05.2024.

About the authors:

Dmitry G. Gryazin, Chief Metrologist of “Concern “SCRI “Elektroprigor”, JSC, (30 Malaya Posadskaya Str., Saint-Petersburg, 197046, Russian Federation), Professor of the Faculty of Control Systems and Robotics, FSAEI HE “National Research University ITMO” (49, Lit. A, Kronverksky Prospekt, Saint-Petersburg, 197101, Russian Federation), DSc. (Tech.), **SPIN-code: 3914-7387**, **ORCID ID: 0000-0003-3562-6815**, **Scopus Author ID: 25638150600**, volnagdg@yandex.ru

Konstantin A. Gleb, Chief Technologist of PJSC “Gazprom” (2, Block 3, Building 1, Lakhtinsky Prospekt, Saint-Petersburg, 197229, Russian Federation), CSc. (Tech.), **SPIN-code: 5681-0690**, **ORCID ID: 0000-0003-4914-3603**, **Scopus Author ID: 57214354068**

Contribution of the co-authors:

Dmitry G. Gryazin – experimental studies, development of the proposed method, preparation of the article for publication

Konstantin A. Gleb – experimental studies, development of the proposed method, preparation of the article for publication

The authors have read and approved the final manuscript.


The authors declare that they have no conflict of interest.

Original article

Geoinformation System for *Argo* Floats Drift Assessment: The Black Sea Case

E. V. Zhuk , N. V. Markova

Marine Hydrophysical Institute of RAS, Sevastopol, Russian Federation

 elena.zhuk @mhi-ras.ru

Abstract

Purpose. The work is aimed at developing and implementing a geographic information system (GIS) that provides an opportunity for online work with the *Argo* floats data in the Black Sea and for its application to assess the float drift velocities in different sea layers.

Methods and Results. The geoinformation system is developed based on a client-server architecture using *PostgreSQL* DBMS to store the *Argo* float data, the *jQuery*, *Plotly* and *mapbox gl* libraries and, therefore, to implement a user interface and a cartographic service. The floats drift velocities are calculated and analyzed using the information provided by the *Argo* project in the public domain. The information is received from the autonomous drifting profiling floats and includes data on their satellite positioning, drift depths and profiling. The velocities at the float drift horizon are calculated using the data on its trajectory, meanwhile GIS assumes the possibility to recalculate velocities swiftly when new observation data are received, adjust calculation methodology, expand the range of statistical characteristics as well as to add a number of additional options. The *Argo* data array (early 2005 – mid 2022) was included in the system current version to calculate and analyze velocities. Application of GIS made it possible to estimate floats drift velocities in the Black Sea, specify mean velocity values as compared to the previous studies and show its seasonal variability in different layers of the sea.

Conclusions. The online services of the *Argo* project are complemented by the developed GIS that simplifies processing and scientific analysis of the Black Sea oceanographic data significantly with no need to use additional scripts, data downloads and external visualization systems. The examples of applying the system for the assessment of floats drift velocities at different depths and in certain parts of the sea are shown. In the future, GIS can be supplemented with new modules, such as automatic downloading of *Argo* data, operating with similar data arrays obtained, for example, from drifters or ADCP current profilers. Besides, it can be applied to any other regions.

Keywords: geoinformation system, GIS, *Argo* floats, drift velocity, currents, Black Sea, database, DB

Acknowledgements: the work on development and implementation of GIS was carried out within the framework of the themes of state assignment of FSBSI FRC MHI FNNN-2024-0012 and FNNN-2024-0014. The velocity field features were studied within the framework of theme of state assignment FNNN-2024-0001. The authors are grateful to DSc. (Geogr.) V.N. Belokopytov for useful consultations while developing and testing the system, as well as to the reviewers for their attention to the work and its appreciation.

For citation: Zhuk, E.V. and Markova, N.V., 2024. Geoinformation System for *Argo* Floats Drift Assessment: The Black Sea Case. *Physical Oceanography*, 31(4), pp. 562-579.

© 2024, E. V. Zhuk, N. V. Markova

© 2024, Physical Oceanography

Introduction

Argo autonomous profiling floats ¹ have become a source of regular data on the profiles of the main hydrological, hydrochemical and other characteristics of

¹ ARGO. *ARGO Data Management*. 2024. [online] Available at: <http://www.ARGOfloats.org/> [Accessed: 18 March 2024].



the marine environment over the past two decades. Both data obtained by them and complete information about the main stages of the World Ocean observation system development using *Argo* floats including their design and operational features are publicly available. Profiling floats can be equipped with various sensors appropriate to the assigned tasks to carry out observations of marine environment parameters, while the basic observed parameters are temperature and salinity [1]. At the same time, they are unable to measure directly one of the most important oceanographic characteristics – current velocity. Calculation of velocity based on floats trajectories when the floats are used as Lagrangian tracers makes it possible to estimate direction and amplitudes of currents, structure and variability of the velocity field.

A fairly complete critical review of information obtained from *Argo* floats is presented in [2] which also refers to the methodology for calculating the velocity of floats movement under water based on their satellite positioning on the surface. At the same time, among the first works on calculating velocities in the ocean, study ² is noteworthy, which provides the basics of methodology for calculating the velocities of *Argo* floats at their drift depths (parking levels) as well as assessing errors of such calculations due to vertical velocity shear. Calculations of average float velocities in the World Ocean were also carried out in a number of works, for example, in [3, 4] and in [5–8] when assessing currents in the Black Sea. Archives of calculated velocities obtained by various research groups are now freely available (Fig. 1), but a simple and convenient online system for scientific analysis of these data has not yet been created.

A procedure for calculating Lagrangian velocities for arbitrarily selected data and region is absent in the *Argo* project online services, although arrays with estimates of floats velocities based on their trajectories for the entire World Ocean are periodically added for public access, in particular in *Copernicus Marine Service* (Fig. 1). Although the data files are in the netCDF format, the lack of ability to select data (by float ID, region, date, parking level, etc.) makes these arrays not entirely convenient for analyzing dynamic processes.

At the same time, all other quality-controlled information received from *Argo* floats is currently available and is regularly updated. Therefore, taking into account continuous obtaining of new *Argo* observational data, it is necessary to create a flexible system for sampling, processing and primary analysis of float velocities in the selected basin, which is capable to produce the latest data processing results swiftly and visualize them. GIS implementation for calculating and processing Lagrangian velocities in the Black Sea basin at this stage is completely justified and useful as a rational addition to existing services. Its application will make it possible to obtain information on drift velocities for various samples (by layer, time, region) as well as determine quickly statistical characteristics and recalculate results in case of velocity calculation methodology improvement.

² Lebedev, K.V., Yoshinari, H., Maximenko, N.A. and Hacker, P.W., 2007. *YoMaHa'07: Velocity Data Assessed from Trajectories of Argo Floats at Parking Level and at the Sea Surface*. Asia-Pacific Data-Research Center, 16 p. (IPRC Technical Note No. 4(2)). doi:10.13140/RG.2.2.12820.71041

Velocity products				
Global Velocity Products				
Institution	Documentation & Access	description	Temporal coverage	Update frequency
Univ. Brest, IFREMER, CNRS (SNO Argo France/LOPS)	10.1175/JTECH-D-12-00073.1 data access	ANDRO: a global Argo based deep displacement dataset	2001 – 2020	yearly, but partially
Copernicus Marine Service	quality information pdf data access	Global trajectory product based on v3.1 and higher trajectory files	1997 – present	daily
CSIO	data access	Global trajectory product based on v3.1 and higher trajectory files	2001-2022	twice a year
IFREMER	pdf data access	ANDRO in Argo Trajectory V3 NetCDF files	2001 – 2009	rarely
IPRC	pdf data access	YoMaHa'07: velocity data assessed from trajectories of Argo floats at parking level and at the sea surface	1997 –	monthly
JAMSTEC	10.1007/s10872-010-0046-4 data access	Global gridded ASCII and NetCDF of YoMaHa'07 QC'ed Argo drift trajectories	Average since 2001-01-01	rarely
Scripps Institution of Oceanography	data access	Scripps Argo trajectory-based velocity product	2001 – 2022	twice a year
University of Washington	10.1175/JPO-D-12-0206.1 data access	Absolute Geostrophic Velocities from Argo (AGVA)	2004 – 2010	rarely

Fig. 1. Data arrays on the floats drift velocities presented on the website <https://argo.ucsd.edu/data/argo-data-products/velocity-products/>

Thus, this work is purposed at developing and implementing a GIS that allows working online with *Argo* profiling floats data in the Black Sea and also, as an application example, to use it to assess the floats drift velocities in different sea layers for 2005–2022.

Data and methods

Observational data. The main data sources for calculating velocities are publicly available archives of *Argo* project¹ which contain information obtained by both active and already inactive profiling floats. It includes metadata for each float (with technical characteristics and settings) as well as observational oceanographic parameters and satellite positioning data. The drift depth of a profiling float is specified, but it is not necessarily a constant parameter for the entire operating time of the float. In addition, this depth may not be achieved in real conditions when the float moves (due to the characteristics of the bottom topography). The floats drift depths can be reconstructed from the built-in pressure sensor data, while at the same time their accuracy at certain moments of movement depends primarily on the specified discreteness of data recording. Thus, there are data arrays where pressure information was recorded only at the initial and final moments of the stages of float operating cycle (Fig. 2), which did not guarantee its drift at the same parking level (for example, in the presence of a bottom rise or access to shallow water). This

point had to be taken into account when implementing the velocity calculation algorithm.

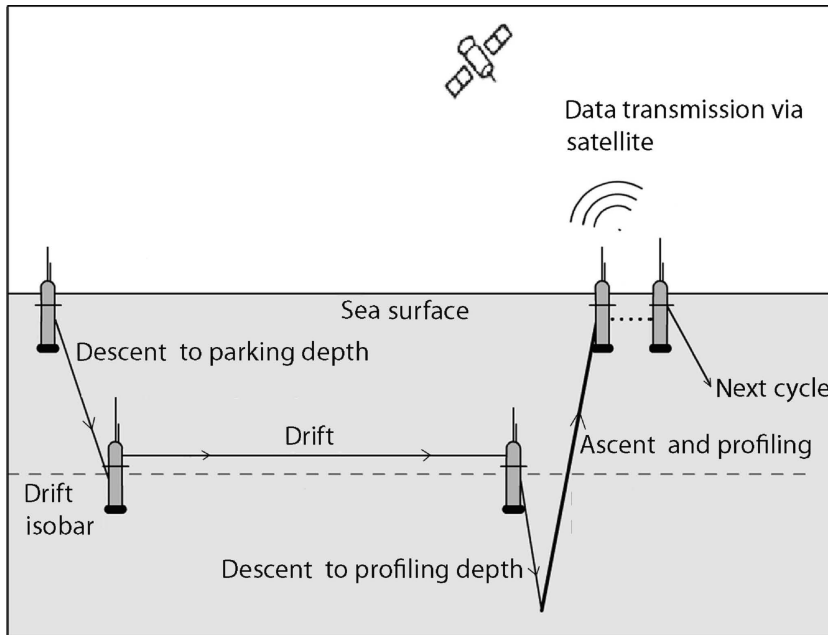


Fig. 2. *Argo* float cycle

In the Black Sea, the most typical float cycle has a period of 120 hours (5 days), the parking levels are between 200–1500 m, and profiling depths reach up to 2000 m. The presented study analyzes velocities calculated using *Argo* dataset including information for 2005–2022 from all profiling floats which exceeds in volume the data on the Black Sea applied in previous similar publications [5–8]. Most of the recently deployed floats are positioned by the *Iridium* satellite system, which makes it possible to improve the accuracy of determining float coordinates when surfacing compared to the previously more common *Argos*³ communication system [2] and, accordingly, to calculate drift velocity more accurately.

Algorithm for drift velocity calculation. Mean drift velocities were calculated according to profiling float satellite positioning data as ratio of the distance of float covered underwater by the corresponding time interval between the float surfacing and its previous descent to the parking level: $\mathbf{v} = d\mathbf{r}/dt$, where $d\mathbf{r}$ is the distance between positioning points in cycles i and $i-1$; dt is time interval between float positioning in i and $i-1$ cycles.

As already noted, a similar technique for calculating the Lagrangian velocity for the Black Sea basin was first applied in [5] and later in [6–8]. It is clear that

³ Xeos Technologies Inc. *A Comparison of Iridium vs Argos Technology in Xeos Location Beacons*. 2019. [online] Available at: <https://xeostech.com/comparison-iridium-vs-argos-technology-xeos-location-beacons> [Accessed: 18 March 2024].

the previously mentioned formula assumes an error in determining velocity at any parking horizon, since the time interval includes not only periods of float drift at the parking level, but also periods of float drift on the sea surface (between the moments of its actual surfacing/descent and the closest positioning via satellite) and periods of float movement in vertical sections (during its ascent to the surface and its backward descent) (Fig. 2). Methods to eliminate errors were proposed for the World Ocean, for example, in works ² and [3]. It is quite difficult to calculate accurately the float movement in the vertical sections of its trajectory in the Black Sea because the main assumptions for such correction are not only the constancy of ascent/descent velocity of the float (≈ 10 cm/s), but also the constancy of vertical velocity shear during the float cycle ². This condition is often violated due to strong density stratification of the Black Sea waters (presence of a permanent pycnocline) and spatiotemporal variability of currents in the basin [9, 10]. Therefore, a methodology similar to research [5–8] is used in this work, and the resulting refinement of velocity assessment is primarily due to an increase in the total amount of accumulated float data as well as faster positioning of most recently deployed floats by the *Iridium* system on the sea surface compared to previously used *Argos*. The database (DB) seeding with new float data implies further improvement of their velocity assessment.

This work uses data from 42 *Argo* floats drifting in the Black Sea at 200–1500 m depths from early 2005 to mid 2022. Velocity vectors were calculated with regard to all available data and monitoring whether the float reached the programmed depths. The drift depth metadata applied for each profiling float cycle are more accurate than in [8] when the parking level specified in the metadata for the entire float trajectory was considered. In addition, their percentage increases with the deployment of new floats positioned by the *Iridium* satellite system using GPS [2, p. 5]. *Iridium* telecommunications system provides faster and more accurate determination of float coordinates and the ascent/descent surface timing. When processing the *Argo* ¹ data, it was discovered that although they were quality-controlled before being made available for users to download, they still contained errors in positioning of some stations. As a result, these stations were rejected and data quality flags were stored in the GIS database.

Geographic information system. Drift velocities of *Argo* floats were assessed by an analysis of the calculation of their mean velocity using GIS available at: <http://www.bod-mhi.ru/ff/> ⁴. The data sources for GIS were *Argo* float data files in netCDF and csv formats containing information about the float ID, its location, profile time, measured parameters as well as separate metadata files that provide information about the drift depth before the start of profiling. Actual drift depth during the cycle is known for all floats except ID 7900465, 7900466, 4900540, 4900541, 4900542, 4900489. For these floats, the same check method as in [8] was used. In this case, the data from the float description section (profiling cycles, measurement depth and drift depth) on the website ¹ was applied; the indicated drift

⁴ MHI of RAS. *Oceanographic Data Bank of the Marine Hydrophysical Institute of RAS*. [online] Available at: <http://www.bod-mhi.ru/ff/> [Accessed: 27 March 2024].

depth was checked for compliance with actual observations (profiling start depth and site depth must be no less than declared drift depth). Similar checks were carried out in [3, p. 769].

Based on the analysis of floats data structure, the authors developed the structure of a relational database as well as software modules for source data parsing and inputting information to the database tables. *PostgreSQL* is used as a DBMS ⁵. The database consists of a table containing metadata (*argo_trajectories*) and measurement data table (*argo_profiles*) corresponded to each other by key fields. The database initial structure was presented in [11]. In this work, *argo_trajectories* table was supplemented with drift velocity values; the updated structure of the tables is given below (Tables 1 and 2). The tables were filled in automatically using a developed software module in Python.

Table 1

Metadata (*argo_trajectories*)

Field name	Data type	Description
<i>id</i>	serial	Index
<i>argo_platform_id</i>	int	<i>Argo</i> identifier
<i>cycle</i>	int	Profiling cycle number
<i>date_time</i>	timestamp	Date and time of profiling
<i>latitude</i>	float	Latitude
<i>longitude</i>	float	Longitude
<i>drift_depth</i>	float	Drift depth
<i>velocity</i>	float	Drift velocity absolute
<i>direction</i>	int	Drift direction
<i>qc</i>	int	Quality flag

Table 2

Profiling data (*argo_profiles*)

Field name	Data type	Description
<i>id</i>	serial	Index
<i>argo_platform_id</i>	int	<i>Argo</i> identifier
<i>cycle</i>	int	Profiling cycle number
<i>pressure</i>	float	Pressure
<i>temperature</i>	float	Temperature
<i>salinity</i>	float	Salinity
<i>doxy</i>	float	Oxygen concentration
<i>chlorophyll</i>	float	Chlorophyll concentration

Note: Key fields in the tables are highlighted in bold.

A user web interface that provides all the necessary functionality was developed for convenience in database access, carrying out statistical calculations, selecting and visualization of profiling and drift data. The structure of data storage and retrieval system is shown in Fig. 3.

⁵ *PostgreSQL: The World's Most Advanced Open Source Relational Database*. 2024. [online] Available at: <https://www.postgresql.org/> [Accessed: 27 March 2024].

- The developed GIS provides the ability to work in two main modes:
- with **one** profiling float selected by identifier,
 - with **all** the floats.

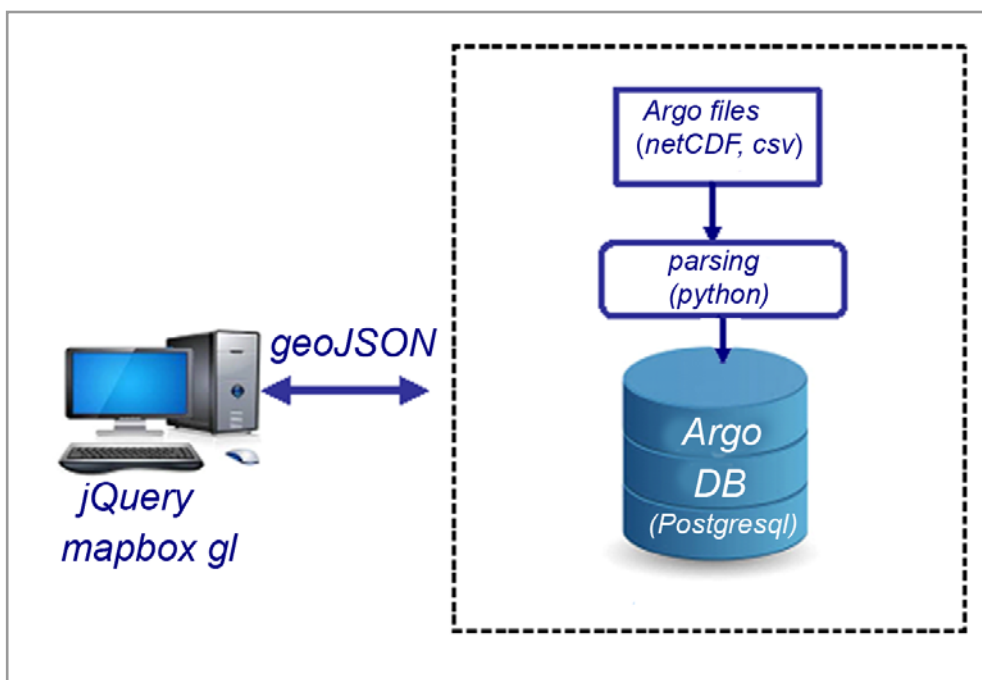
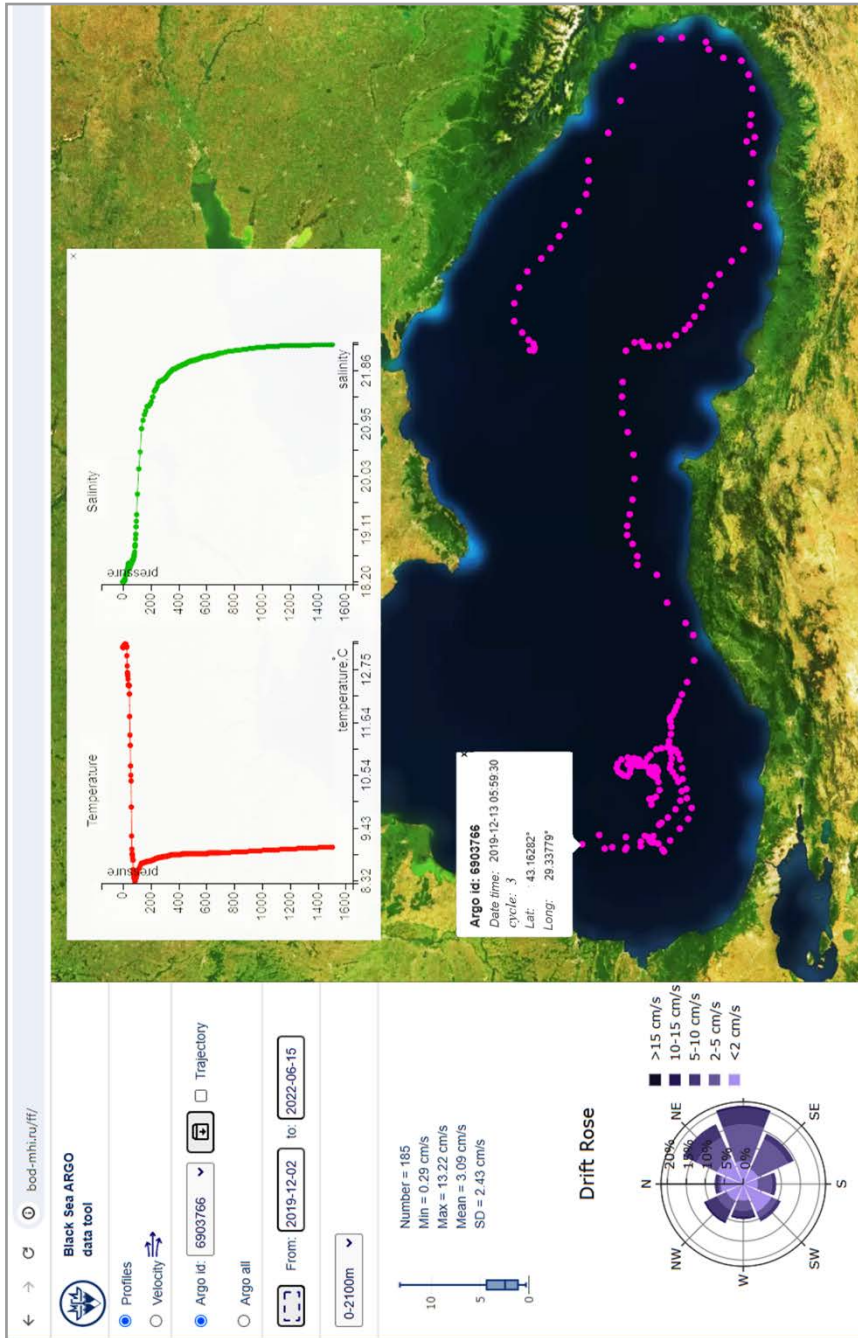


Fig. 3. Structure scheme of the *Argo* data access system for the Black Sea

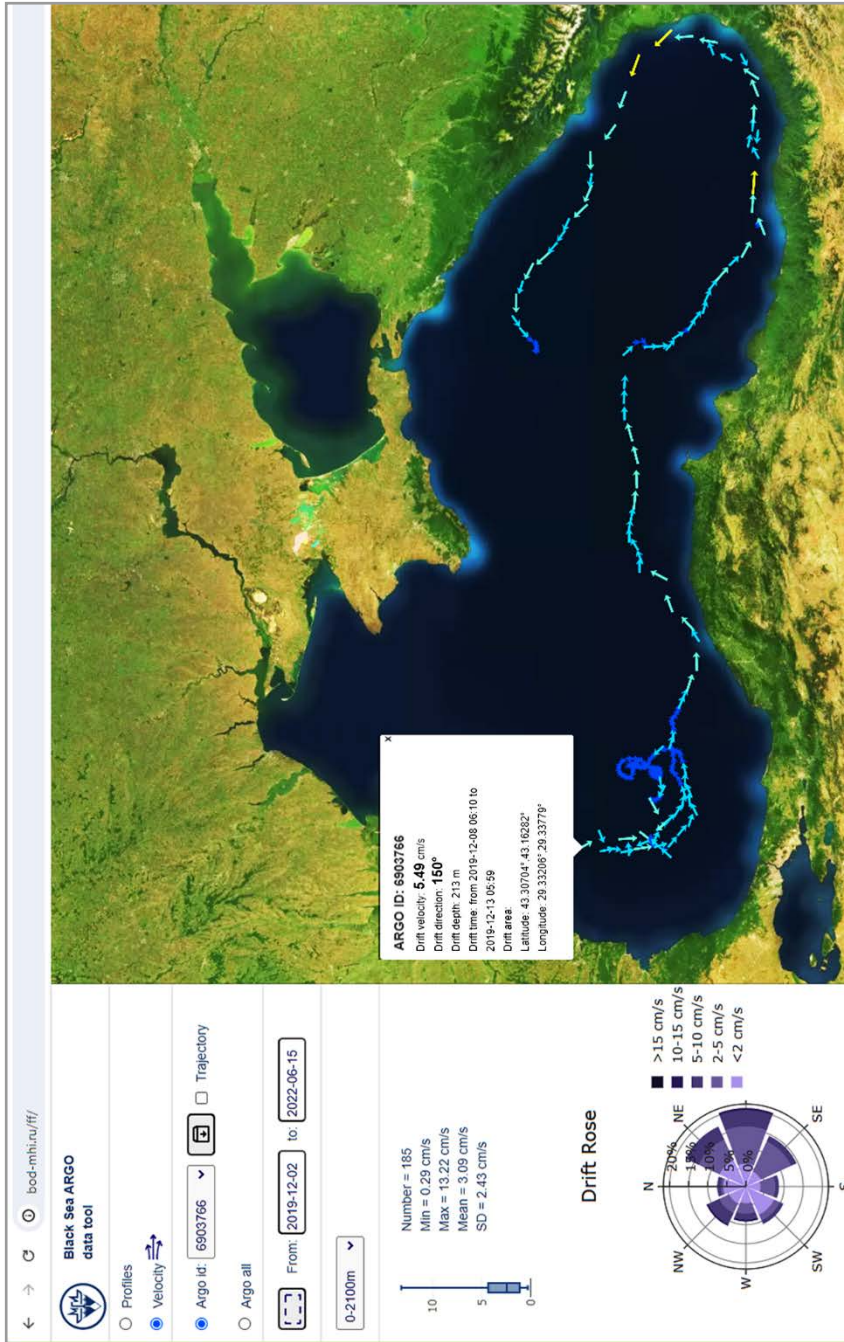
Switching between the modes occurs with a special user interface option. In each of the modes, it is possible to display the float (floats) position as points (if Profiles option is selected) or as drift velocity vectors (if Velocities option is selected). When a User clicks on the displayed point or vector, a pop-up window appears with information about the float ID, coordinates, station; profiles of parameters measured during this sounding are constructed (if Profiles option is selected) or information about the float drift velocity and direction is displayed (if Velocity option is selected). For both modes, it is possible to retrieve data over a rectangular area specified on the map and over a specified time interval.

Selection by layers corresponding to the floats drift depths is also available in the mode when all floats are selected (All option). For each new selected dataset, the main statistical characteristics of drift velocities are calculated (minimum and maximum velocities, mean value, standard deviation), a current rose and a box and whisker diagram are constructed.

Data downloading by float ID in netCDF format is available. Figs. 4–6 demonstrate examples of data selecting and visualization. In the figures next to the maps, there are diagrams (roses) of currents demonstrating direction and value of calculated velocities in the selected area.



a



b

Fig. 4. An example of using the web interface to display: a – trajectory of the *Argo* float ID 6903766 and vertical profiles of temperature and salinity, and *b* – float drift velocities

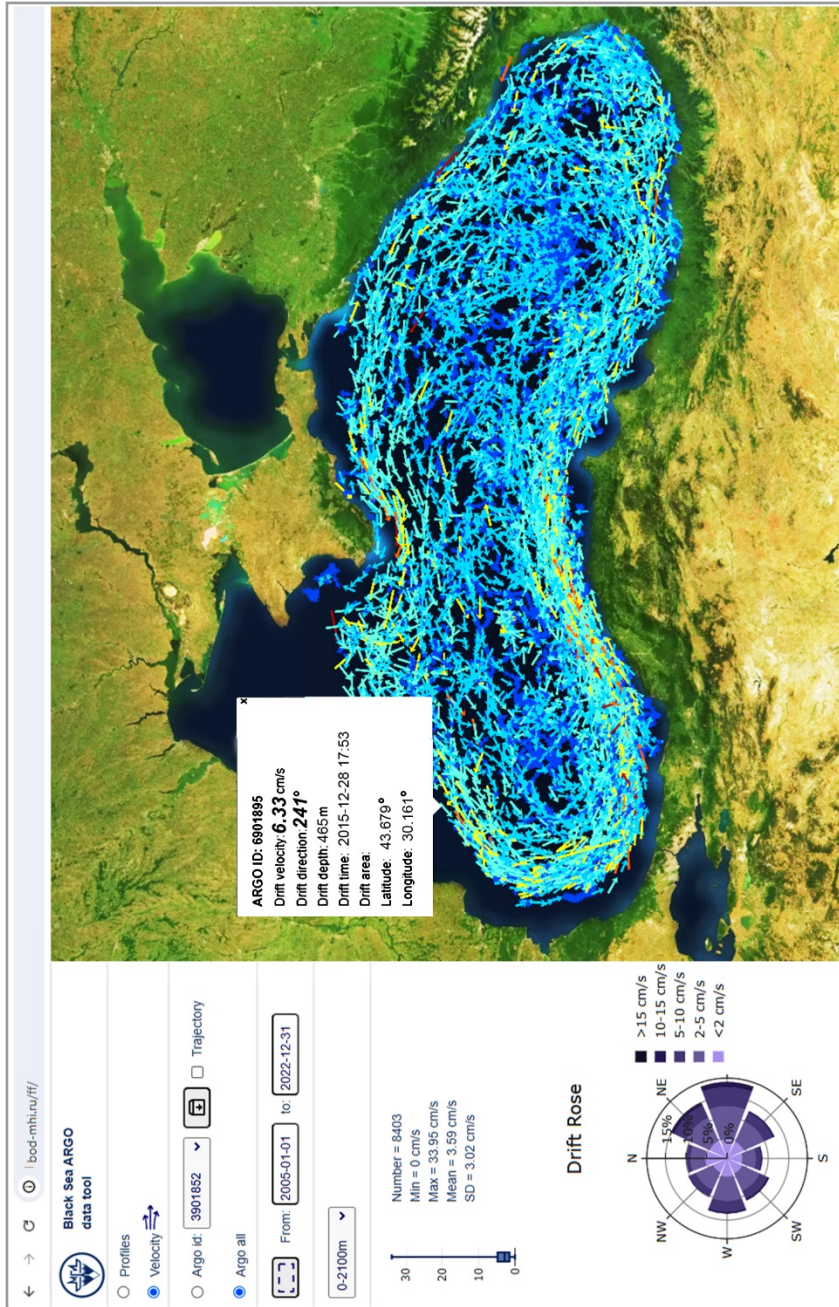


Fig. 5. An example of using the web interface to display velocities of all the *Argo* floats drifting in the 150–350 m layer

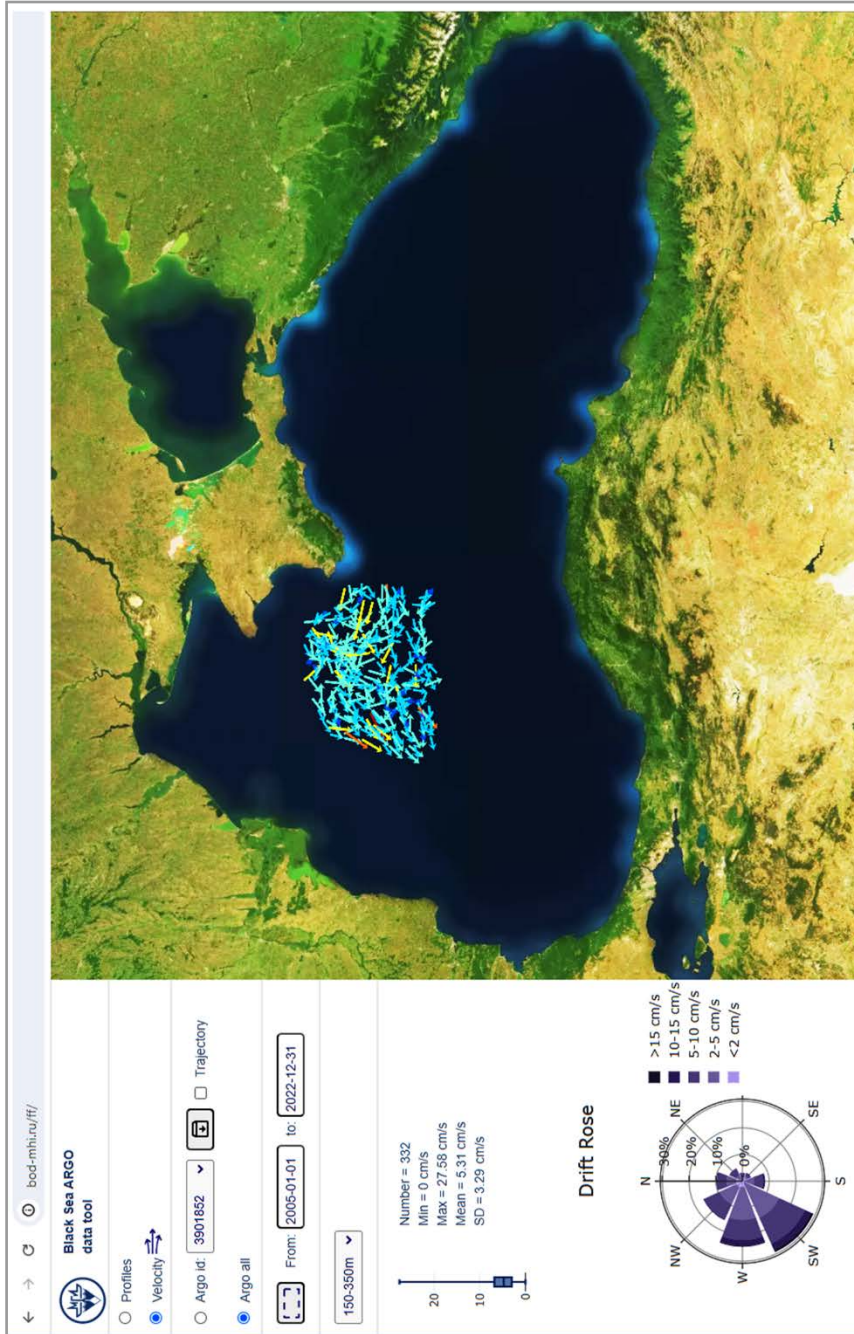


Fig. 6. An example of using the web interface to display velocities of all the *Argo* floats drifting in the 150–350 m layer within the selected rectangular area

Results analysis

Using the developed GIS, the Black Sea velocities calculated from *Argo* floats data were analyzed in comparison with the most comprehensive published results on this topic. In [5], data from only three profiling floats were considered: mean velocity of the float at 200 m horizon was estimated at 7 cm/s, at 750 m horizon – at ~4 cm/s, at 1550 m horizon – within the range of 1–5 cm/s. In [6], based on the data from 7 floats that operated in 2002–2009, it is shown that their mean velocities at 750–1550 m depths were 2.2–2.7 cm/s, at 500 m horizon – 4 cm/s. In [7], after examining the data from floats with parking levels of 200–1000 m for the period 2005–2010, it was shown that current velocities decrease with depth, and in summer they are weaker than in other seasons. The calculated velocities at 750 m depth were up to 10 cm/s and at 1000 m depth they were within the range of 1–5 cm/s. In [8], a 10-year array of *Argo* measurements (2005–2015) was applied to estimate the velocities, which made it possible to examine the dynamics of the Black Sea deepwater currents in more detail, but the velocities in the upper layer were not assessed. In this case, the authors determined the following velocity values: 3.6 ± 0.4 cm/s at 350–600 m depths, 4.0 ± 0.2 cm/s in 600–800 m layer, 5.7 ± 0.6 cm/s in 800–1200 m layer and 3.5 ± 0.2 cm/s in 1200–1600 m layer (the lower of the considered ones) [8, p. 32]. Compared to this work, the number of deep-water *Argo* observations by mid 2022 increased significantly: at least 1.3 times in the layer below 1200 m and more than 5 times in 800–1200 m layer. For 200 m horizon, the number of observations increased by more than three times compared to the number used in the work with the most relevant data [7]: from approximately 1500 stations in 2015 to 4774 ones in 2022. Table 3 shows the calculation results of *Argo* floats drift velocities in different layers of the Black Sea. The number of calculated velocity vectors turned out to be less than the number of performed stations because in some cases the condition for the float to be located in the same layer between neighboring stations was not met. This situation is possible, in particular, when a float enters a zone with depths less than its parking level during one cycle and then the resulting velocity vector cannot be attributed to any of the layers.

Table 3

Statistics of calculated velocity vectors by layers

Layers by depth, m	Number of stations	Number of vectors	Mean velocity, cm/s	95% confidence interval, cm/s
150–250	4774	4695	4.2	± 0.1
350–600	409	345	2.3	± 0.2
600–850	1419	1348	2.9	± 0.1
850–1200	820	772	3.4	± 0.3
1200–1600	636	614	2.9	± 0.2

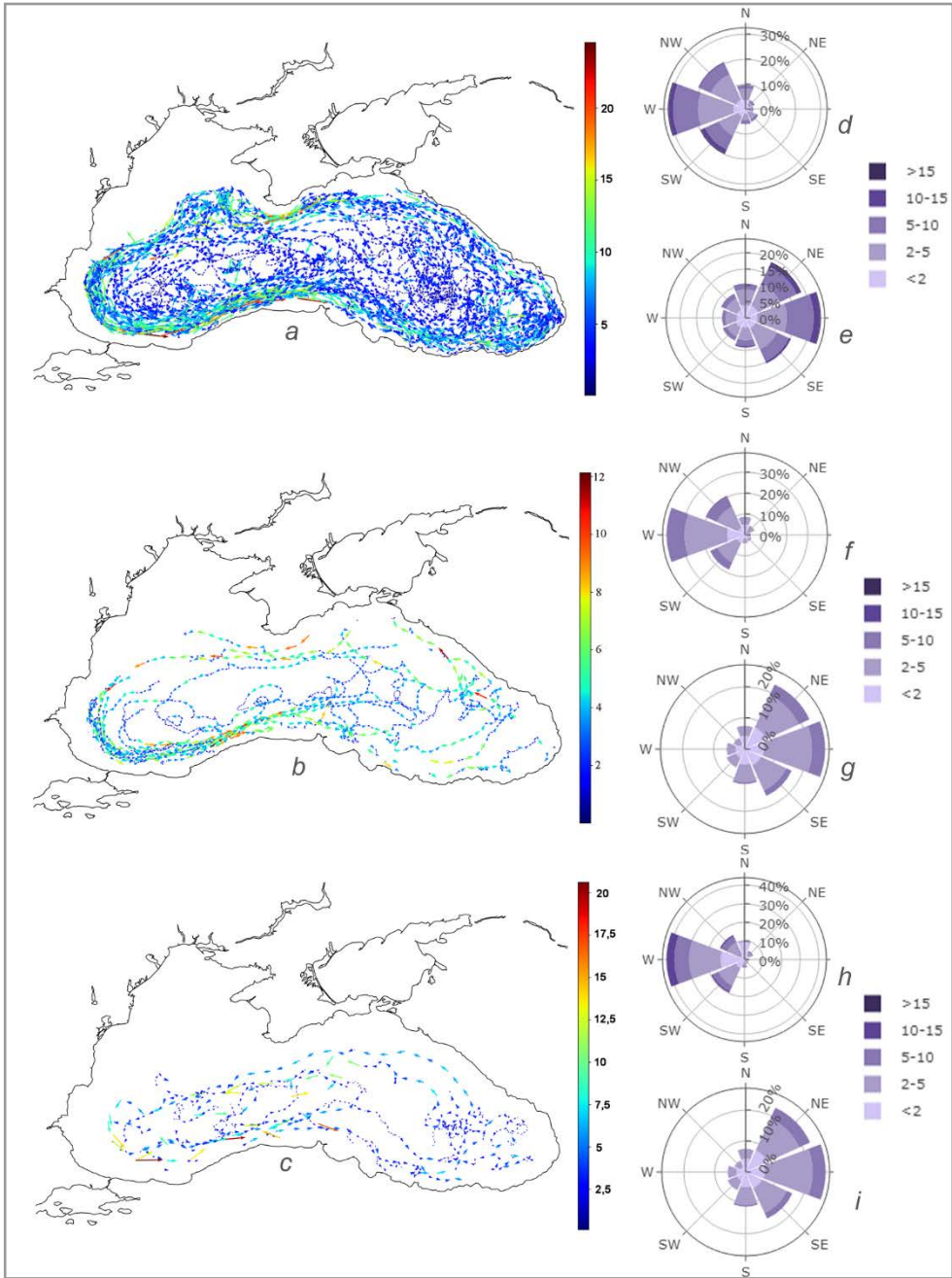


Fig. 7. Calculated vectors of the *Argo* floats velocities (cm/s) and corresponding current roses in the 150–250 m (a), 600–850 m (b) and 1200–1600 m (c) layers in the northern (d, f, h) and southern (e, g, i) parts of the sea

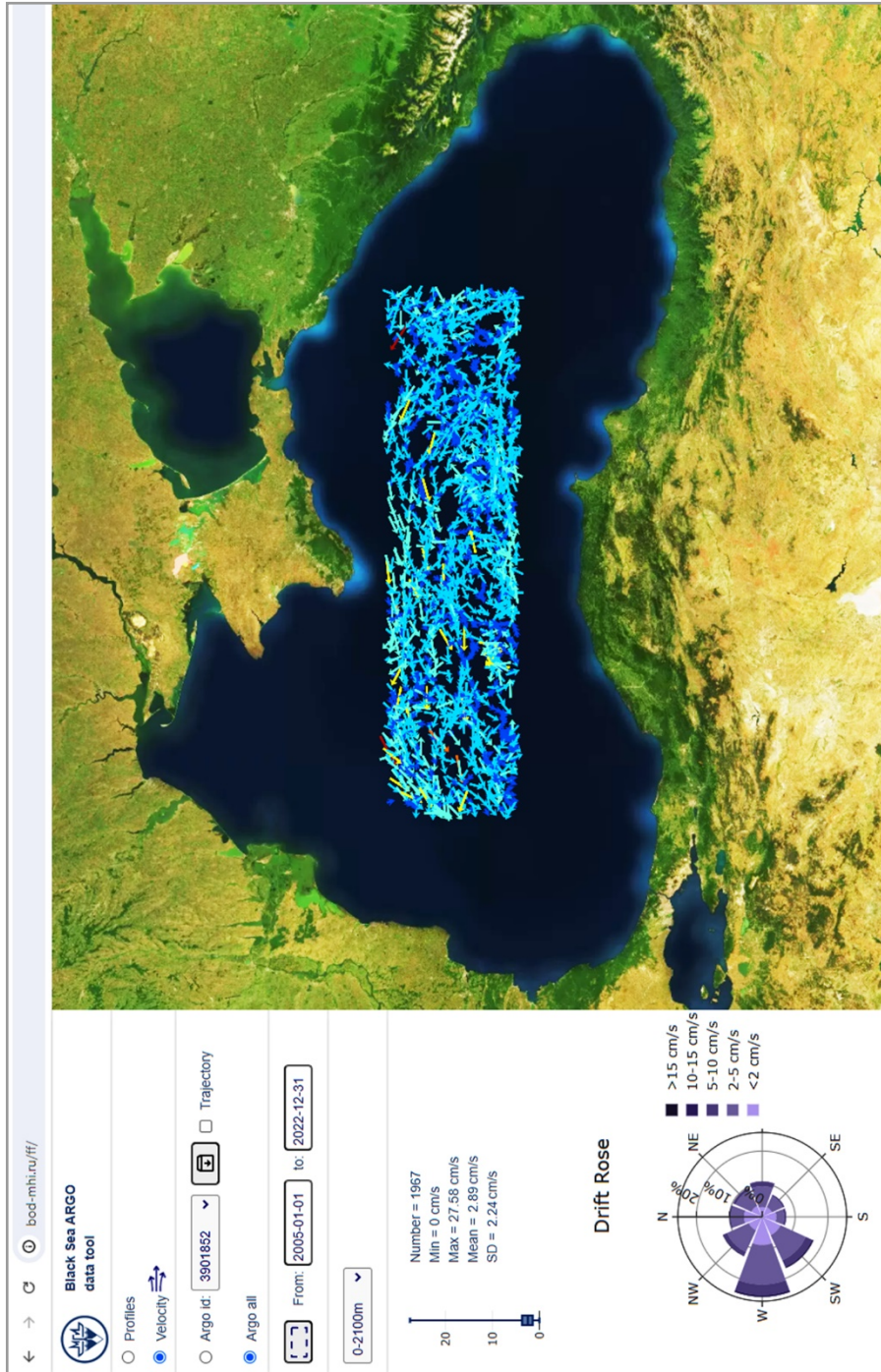


Fig. 8. Calculated vectors of the *Argo* floats velocities in all the layers of the sea central part and corresponding current rose

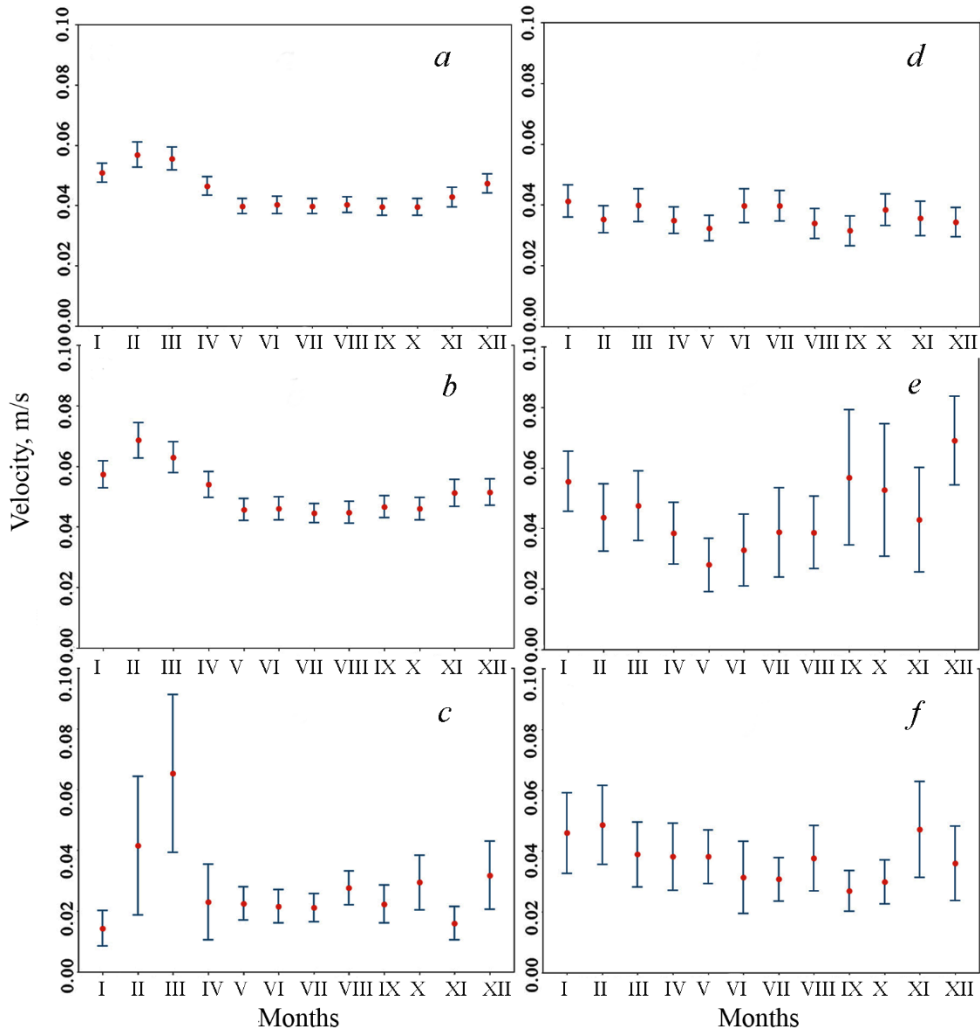


Fig. 9. Seasonal variation of the *Argo* floats drift velocities in the Black Sea (red dots) with the corresponding confidence intervals (vertical segments): *a* – in the whole volume of the basin; *b* – in the 150–250 m layer; *c* – in the 350–600 m layer; *d* – in the 600–850 m layer; *e* – in the 850–1200 m layer and *f* – in the 1200–1600 m layer

It can be seen from Table 3 that the largest number of drift velocity vectors was calculated for 200 ± 50 m layer, the mean value with a 95% probability falls in the range of 4.2 ± 0.1 cm/s. In the next layer of 350–600 m, the number of calculated vectors is an order of magnitude smaller and mean velocity was 2.3 cm/s which is lower than the value of 4 cm/s indicated in [5, 6] and the values 3.6 ± 0.2 cm/s from [8]. In three deeper layers, mean velocities were slightly higher (2.9, 3.4 and 2.9 cm/s, respectively). Thus, in 850–1200 m layer, we reveal a slight increase in the mean velocity previously obtained in [8] and confirmed in this work using a significantly larger dataset. Moreover, taking into account the confidence interval, the mean velocity values in deep-water layers are quite close and amount to ~ 3 cm/s.

Fig. 7 shows the maps of calculated drift velocities of *Argo* profiling floats in some sea layers. According to the constructed diagrams, the prevailing direction of currents is western in the northern part of the sea in all layers, and in the southern part – eastern which is consistent with the concept of general cyclonic circulation in the basin. In addition to the main direction, the western, northwestern and southwestern directions of drift velocities are also clearly defined in the lowest layer. Velocity values in this layer are predominantly 2–4 cm/s, but they can reach 10–12 cm/s. In the central part of the basin, westerly drift predominates (Fig. 8) with 5–10 cm/s velocities and a maximum of 15 cm/s in 150–250 m layer (based on data on 1091 calculated velocity vectors), with 2–5 cm/s velocities in 350–600 m layer (93 calculated vectors) and 2–5 cm/s in 600–800 m layer (354 velocity vectors). In general, calculated characteristics of floats drift indicate a complicated structure of the current field in all layers, in particular, the presence of vortex formations of different scales and vorticity sign.

Figure 9 is plotted using monthly mean velocity found for the entire period under consideration; it shows that float drift velocities are higher in winter at almost all horizons than in summer. This is the result of a seasonal increase in winds over the sea in winter [9, p. 26]. Indicative in this regard are the diagrams for two upper layers (Fig. 9, *b, c*) which make the greatest contribution to the overall increase in velocity-(Fig. 9, *a*). At the same time, the maximum of mean velocities in the upper layer is observed in February (7 cm/s), in the second layer (at 350–600 m depths) – in March (6.5 cm/s). In summer, velocities decrease to 2.5–4 cm/s in two upper layers. In 600–850 m layer (Fig. 9, *d*), seasonal variation in the mean velocities is not distinguished and mean velocities over the entire period are about 2.9 cm/s. In the deeper layers, at > 850 m depths, summer velocities (3–4 cm/s) are less than in other seasons (up to 6 cm/s).

Conclusion

Using the developed geographic information system, the drift velocity of *Argo* profiling floats which obtained oceanographic data in the Black Sea in 2005–2022 was assessed. Velocity analysis was performed on a more complete *Argo* dataset compared to previously published works. Mean velocity was clarified and drift features in some sea layers were shown. It is found that the winter increase in float velocities in the Black Sea associated with a seasonal increase in wind occurs not only in the upper, but also in the deeper sea layers. It is determined that in winter, at depths of more than 850 m, mean velocities increase up to 1.5–2 times relative to summer ones, and mean velocities in 350–600 m layer can increase up to 2–2.5 times with a clearly defined maximum in February–March. The dominant western direction of floats movement in the northern part of the sea at all horizons and dominant eastern one in the southern part indicate the cyclonic circulation pattern in the basin. The predominance of westerly directed drift velocities is determined in the central deep-water part of the sea. Analysis of vectors of other directions indicates the velocity field inhomogeneity, non-stationariness of currents and presence of vortex formations of different scales in all the layers under consideration.

GIS application for analyzing *Argo* data simplifies the work with oceanographic data for the Black Sea region and their scientific analysis greatly. At the same time, GIS implies the possibility of quick velocities recalculation when new observational data occur, to include a number of additional options into the system as well as to improve a methodology for calculating velocities at a parking level with regard to various estimates of float movement during its ascent/descent cycle phase.

Further system development implies adding functionality to visualize data from drifters and ADCP current profilers for the Black Sea, and enabling an automatic seeding of the database with new observational data from *Argo* floats. It is also possible to adapt the developed GIS for other areas of the World Ocean.

REFERENCES

1. Riser, S.C., Freeland, H.J., Roemmich, D., Wijffels, S., Troisi, A., Belbéoch, M., Gilbert, D., Xu, J., Pouliquen, S. [et al.], 2016. Fifteen Years of Ocean Observations with the Global Argo Array. *Nature Climate Change*, 6(2), pp. 145-153. <https://doi.org/10.1038/nclimate2872>
2. Wong, A.P.S., Wijffels, S.E., Riser, S.C., Pouliquen, S., Hosoda, S., Roemmich, D., Gilson, J., Johnson, G.C., Martini, K. [et al.], 2020. Argo Data 1999–2019: Two Million Temperature-Salinity Profiles and Subsurface Velocity Observations from a Global Array of Profiling Floats. *Frontiers in Marine Science*, 7, 700. <https://doi.org/10.3389/fmars.2020.00700>
3. Ollitrault, M. and Rannou, J.-P., 2013. ANDRO: An Argo-Based Deep Displacement Dataset. *Journal of Atmospheric and Oceanic Technology*, 30(4), pp. 759-788. <https://doi.org/10.1175/JTECH-D-12-00073.1>
4. Park, J.J., Kim, K., King, B.A. and Riser, S.C., 2005. An Advanced Method to Estimate Deep Currents from Profiling Floats. *Journal of Atmospheric and Oceanic Technology*, 22(8), pp. 1294-1304. <https://doi.org/10.1175/JTECH1748.1>
5. Korotaev, G., Oguz, T. and Riser, S., 2006. Intermediate and Deep Currents of the Black Sea Obtained from Autonomous Profiling Floats. *Deep Sea Research Part II: Topical Studies in Oceanography*, 53(17-19), pp. 1901-1910. <https://doi.org/10.1016/j.dsr2.2006.04.017>
6. Gerasimova, S.V. and Lemeshko, E.E., 2011. Estimation of Deep-Water Current Velocities Based on ARGO Data. *Environmental Control Systems*, 15, pp. 187-196 (in Russian).
7. Milanova, M. and Peneva, E., 2016. Deep Black Sea Circulation Described by Argo Profiling Floats. In: Sofia University “St. Kliment Ohridski”, 2016. *Annual of Sofia University “St. Kliment Ohridski”, Faculty of Physics*. Sofia: St. Kliment Ohridski University Press. Vol. 109, 12 p. Available at: https://www.phys.uni-sofia.bg/annual/archive/109/full/GSU-Fizika-109_02.pdf [Accessed: 07 July 2024].
8. Markova, N.V. and Bagaev, A.V., 2016. The Black Sea Deep Current Velocities Estimated from the Data of ARGO Profiling Floats. *Physical Oceanography*, (3), pp. 23-35. <https://doi.org/10.22449/1573-160X-2016-3-23-35>
9. Ivanov, V.A. and Belokopytov, V.N., 2013. *Oceanography of the Black Sea*. Sevastopol: MHI, 210 p.
10. Demyshev, S.G., Dymova, O.A., Markova, N.V., Korshenko, E.A., Senderov, M.V., Turko, N.A., and Ushakov, K.V., 2021. Undercurrents in the Northeastern Black Sea Detected on the Basis of Multi-Model Experiments and Observations. *Journal of Marine Science and Engineering*, 9(9), 933. <https://doi.org/10.3390/jmse9090933>
11. Zhuk, E., 2023. ARGO Black Sea Database: Storage and Visualization. In: K. Themistocleous, D. G. Hadjimitsis, S. Michaelides and G. Papadavid, eds., 2023. *Proceedings of SPIE*. SPIE. Volume 12786: Ninth International Conference on Remote Sensing and Geoinformation of the Environment (RSCy2023), 127861Q. <https://doi.org/10.1117/12.2681583>

Submitted 02.04.2023; approved after review 02.05.2024;
accepted for publication 16.05.2024.

About the authors:

Elena V. Zhuk, Junior Research Associate, Marine Hydrophysical Institute of RAS (2 Kapitanskaya Str., Sevastopol, 299011, Russian Federation), **ORCID ID: 0000-0002-4263-7734**, **ResearcherID: JCD-8660-2023**, **Scopus Author ID: 57191412660**, elena.zhuk@mhi-ras.ru

Natalia V. Markova, Senior Research Associate, Marine Hydrophysical Institute of RAS (2 Kapitanskaya Str., Sevastopol, 299011, Russian Federation), Ph.D. (Phys.-Math.), **ORCID ID: 0000-0002-7123-6657**, **ResearcherID: Q-2638-2017**, **Scopus Author ID: 57198013260**, n.v.markova@mhi-ras.ru

Contribution of the co-authors:

Elena V. Zhuk – source data analysis and processing, database development, GIS development and implementation, software code writing, carrying out calculations of velocity and statistical characteristics, results visualization, paper preparation and editing

Natalia V. Markova – statement of the research problem, analysis of input data and results of their processing, participation in GIS testing, processing calculation results, analysis, interpretation and discussion of results, formulation of conclusions, paper preparation and editing

The authors have read and approved the final manuscript.

The authors declare that they have no conflict of interest.

Evaluating and Adjusting ERA5 Wind Speed for Extratropical Cyclones and Polar Lows Using AMSR-2 Observations

V. Cheshm Siyahi¹, ✉, E. V. Zabolotskikh¹,
V. N. Kudryavtsev^{1, 2}

¹ *Russian State Hydrometeorological University, Saint Petersburg, Russian Federation*
✉ vahid@rshu.ru

² *Marine Hydrophysical Institute of RAS, Sevastopol, Russian Federation*

Abstract

Purpose. Wind speed accuracy in diverse storm systems is crucial for weather prediction, climate studies and marine applications. This study aims to evaluate the performance of the European Centre for Medium-Range Weather Forecasts (ECMWF) fifth-generation atmospheric reanalysis (ERA5) for wind speeds in extratropical cyclones (ETCs), polar lows (PLs) and tropical cyclones (TCs), as well as to propose a correction function for potential biases.

Methods and Results. We compared the ERA5 wind speeds with the data from the Advanced Microwave Scanning Radiometer-2 (AMSR-2) satellite for various storm events. Statistical metrics, including bias, root mean squared error (RMSE) and correlation coefficient (R), were calculated to quantify discrepancies between the two datasets. Based on the observed biases, a simple exponential correction function was proposed to adjust the ERA5 wind speeds. The effectiveness of the correction function was evaluated through visual comparisons and quantitative analyses. The analysis revealed that the ERA5 systematically underestimated wind speeds across large areas within ETCs, PLs and TCs compared to the AMSR-2 observations. The proposed correction function successfully improved the agreement between ERA5 and AMSR-2 wind speeds in ETCs and PLs. However, applying the same function to TCs revealed significant structural discrepancies between the ERA5 and the AMSR-2 wind fields within these systems.

Conclusions. This study demonstrates effectiveness of the proposed correction function in enhancing wind speed accuracy for ETCs and PLs, bringing them closer to AMSR-2 observations. However, further research is necessary to develop approaches for addressing wind speed biases in TCs, considering the unique characteristics and limitations of existing reanalysis data. This research contributes to improving our understanding and representation of wind speeds in diverse storm systems, ultimately aiding in more accurate weather forecasting and climate monitoring.

Keywords: extratropical cyclones, polar lows, tropical cyclones, reanalysis, wind speed adjustment, ERA5, AMSR-2, remote sensing

Acknowledgements: The work under this project was supported by the Ministry of Science and Higher Education of Russia, State Assignment 0763-2020-0005.

For citation: Cheshm Siyahi, V., Zabolotskikh, E.V. and Kudryavtsev, V.N., 2024. Evaluating and Adjusting ERA5 Wind Speed for Extratropical Cyclones and Polar Lows Using AMSR-2 Observations. *Physical Oceanography*, 31(4), pp. 580-591.

© 2024, V. Cheshm Siyahi, E. V. Zabolotskikh, V. N. Kudryavtsev

© 2024, Physical Oceanography



1. Introduction

Marine applications heavily rely on accurate wind speed data for various purposes, including navigation, offshore operations, and monitoring environmental phenomena. The accurate representation of wind speed is particularly crucial in the context of tropical, extratropical, and polar cyclones, where even slight inaccuracies can lead to serious consequences such as shipwrecks, damage to offshore structures, and coastal flooding. Therefore, ensuring the precision of wind speed data is paramount to advancing our understanding and prediction capabilities in marine meteorology.

The European Centre for Medium-Range Weather Forecasts (ECMWF) provides valuable global reanalysis datasets, such as ERA5 and ERA-Interim, which serve as resources for researchers and operational meteorologists. While these datasets have significantly contributed to the understanding of atmospheric conditions, it is imperative to evaluate and improve their accuracy, especially in terms of wind speed representation.

Several studies, such as [1–11], have scrutinized the accuracy of wind speed data in ERA5 and ERA-Interim, revealing discrepancies that may impact the reliability of these datasets in marine applications. The ERA5's ability to predict low wind speed events compared to *in situ* wind speed measurements around the UK was evaluated; and the results show that ERA5 has biases in mean wind speed of 0.166 m/s and -0.136 m/s for onshore and offshore domains, respectively [1]. In [4], it is shown that while reanalysis data like ERA5 offer improved representation of wind speeds compared to earlier versions, discrepancies can still exist in specific regions, particularly for wind gusts in complex terrain.

The study [2] underscores the significance of reliable tropical cyclone information for storm surge forecasts and discusses the limitations of the ERA5 reanalysis data, particularly in high wind conditions. The authors found that the ERA5 reanalysis data underestimate maximum wind speeds during tropical cyclones in comparison to the IBTrACS (International Best Track Archive for Climate Stewardship) data. Thus, they suggested a wind reconstruction method to enhance the accuracy of the ERA5 representation, which aligns well with the data obtained from the SFMR (stepped frequency microwave radiometer) and SMAP (soil moisture active passive) L-band radiometer measurements.

The paper [3] evaluated the surface winds of ECMWF ERA5 reanalysis in the Atlantic Ocean, and found that the reanalysis provided high-quality winds for non-extreme conditions with some site-dependent errors. They also compared two bias-correction models and concluded that the quantile mapping method offered significant improvement for strong winds, achieving a 10% reduction in root mean square error (RMSE) and a 50% reduction in bias compared to the original reanalysis.

The recent launch of spaceborne L-band radiometers operating at 1.4 GHz, such as soil moisture and ocean salinity [12, 13] radiometer and SMAP radiometer, has brought new capabilities for measuring sea surface wind speeds under rainy conditions [13]. However, for wind speeds below 30 kt/15 m/s, the performance of L-band radiometers in measuring wind speeds has been limited, with larger radiometer noise and lower sensitivity compared to higher frequency radiometers, i.e., Advanced Microwave Scanning Radiometer-2 (AMSR-2) [13].

radiometers, such as the radiometers of the AMSR series having combinations of C-band and X-band channels, are also able to determine wind speeds under rainy conditions [14–17].

This study aims to contribute to the ongoing efforts to enhance the accuracy of wind speed data by validating and correcting ERA5 wind speed data using a straightforward yet effective correction function based on the AMSR-2 wind speed retrievals. Through this validation and correction approach, we aspire to advance the reliability of wind speed data, fostering improvements in marine meteorology and bolstering our ability to mitigate the risks associated with cyclonic events.

2. Materials and methods

2.1. Methodology

To evaluate the accuracy of ERA5 wind speeds in various storm systems, we employed a multi-step approach. Firstly, we selected case studies encompassing diverse cyclone types: extratropical cyclones (ETCs), polar lows (PLs), and tropical cyclones (TCs). Next, we acquired wind speed data from both sources for each selected case. ERA5 data provided hourly wind speeds at a 10-meter height (U_{10}), while the AMSR-2 data consisted of swath measurements at specific times (several swaths per day dependently on the observation latitude). The AMSR-2 brightness temperature measurements were processed with an algorithm developed earlier [17] to obtain wind speed fields. This algorithm employs all six AMSR-2 C and X-band channel measurements to effectively separate the influence of rain from the wind signal. Subsequently, the corrected measurements at 6.9 GHz and 10.65 GHz are used to retrieve the sea surface wind speed (for more details see [17]).

Following visual comparisons of wind fields from both sources, we constructed the scatter plots to quantitatively assess the relationship between the ERA5 and AMSR-2 wind speeds. To quantify discrepancies, we calculated statistical metrics including bias (1), RMSE (2), and correlation coefficient (3). These metrics provided insights into the overall agreement and specific deviations between the two datasets.

$$\text{Bias} = \frac{1}{n} \sum_{i=1}^n (X_i - Y_i), \quad (1)$$

$$\text{RMSE} = \sqrt{\frac{1}{n} \sum_{i=1}^n (X_i - Y_i)^2}, \quad (2)$$

$$R = \frac{\sum_{i=1}^n (X_i - \bar{X})(Y_i - \bar{Y})}{\sqrt{\sum_{i=1}^n (X_i - \bar{X})^2 \sum_{i=1}^n (Y_i - \bar{Y})^2}}. \quad (3)$$

Finally, based on the observed patterns and the identified discrepancies, we proposed a simple and straightforward exponential function to adjust the ERA5 wind speeds. This function aimed to improve the agreement with the AMSR-2 observations while maintaining the spatial and temporal characteristics of the ERA5 data. The proposed function offered a practical solution for correcting potential biases in ERA5 wind speeds for the analyzed cyclone types.

2.2. Datasets

2.2.1. ERA5. This study utilizes the fifth-generation atmospheric reanalysis data from the Copernicus Climate Change Service (C3S). The data, known as ERA5 reanalysis, has a temporal resolution of 1 hour and a spatial resolution of $0.25^\circ \times 0.25^\circ$. To enhance the precision, historical wind field observation datasets are assimilated in the ERA5, incorporating data from such instruments as the AMSR-E, AMSR-2, GMI, SSM/I, MVIRI, SEVIRI, GOES, GMS, MTSAT, AHI, AVHRR, MODIS and SeaWinds, and *in situ* sources like weather stations, buoys, ship surveys, and airborne measurements. The gridded ERA5 reanalysis data effectively address the uneven temporal and spatial distribution of satellite and *in situ* data. These reanalysis data play a crucial role in establishing remote sensing satellite retrieval models and providing forcing fields for ocean models [18].

2.2.2. AMSR-2. The AMSR-2 onboard the GCOM-W satellite is a passive microwave radiometer measuring microwave radiation of the atmosphere-ocean system. The AMSR-2 measures the brightness temperatures (BT) of microwave radiation in 14 channels at the frequencies from 6.9 to 89 GHz at both polarizations over a 1450 km swath. Though the ability of satellite passive microwave radiometers to measure sea surface wind speeds has been proven many times over, the addition of new set of C-band channels in the AMSR-2 allowed efficiently separating the rain contribution in BT and retrieve high accuracy wind speeds even under rainy conditions [17].

2.3. Case studies

2.3.1. ETCs. Extratropical cyclones, large-scale weather systems in middle latitudes play a major role in shaping weather and climate across the North Atlantic (NA) and North Pacific (NP) oceans. These powerful storms, frequently crossing these vast regions, are associated with winter low pressures and can generate dangerously high sea states with significant wave height up to 20 m [19–23].

Based on the ERA5 hourly wind (U_{10}) and mean sea level pressure (MSLP) fields and the database of Ocean Prediction Center (OPC) Hurricane Force Low Climatology (<https://ocean.weather.gov/>), seven ETCs over NA and NP were selected (see Table 1). The maximum wind speed and the minimum pressure, representing the cyclone's peak intensity, were extracted from both AMSR-2 and OPC data. Visual comparisons of the wind fields from the AMSR-2 and ERA5 are presented in Fig. 1 (left and middle columns, respectively).

Table 1

Selected ETC cases

Start date	End date	Region	Min MSLP, hPa	Max U_{10} , m/s
11 February 2020	13 February 2020	NA	970	32
12 February 2020	15 February 2020	NA	929	48
03 January 2022	07 January 2022	NA	930	41
22 February 2022	24 February 2022	NA	957	45
12 February 2022	13 February 2022	NP	944	35
15 September 2022	17 September 2022	NP	940	35
09 November 2022	10 November 2022	NP	966	33

* Data are taken from the OPC database.

** Data are taken from the AMSR-2 database.

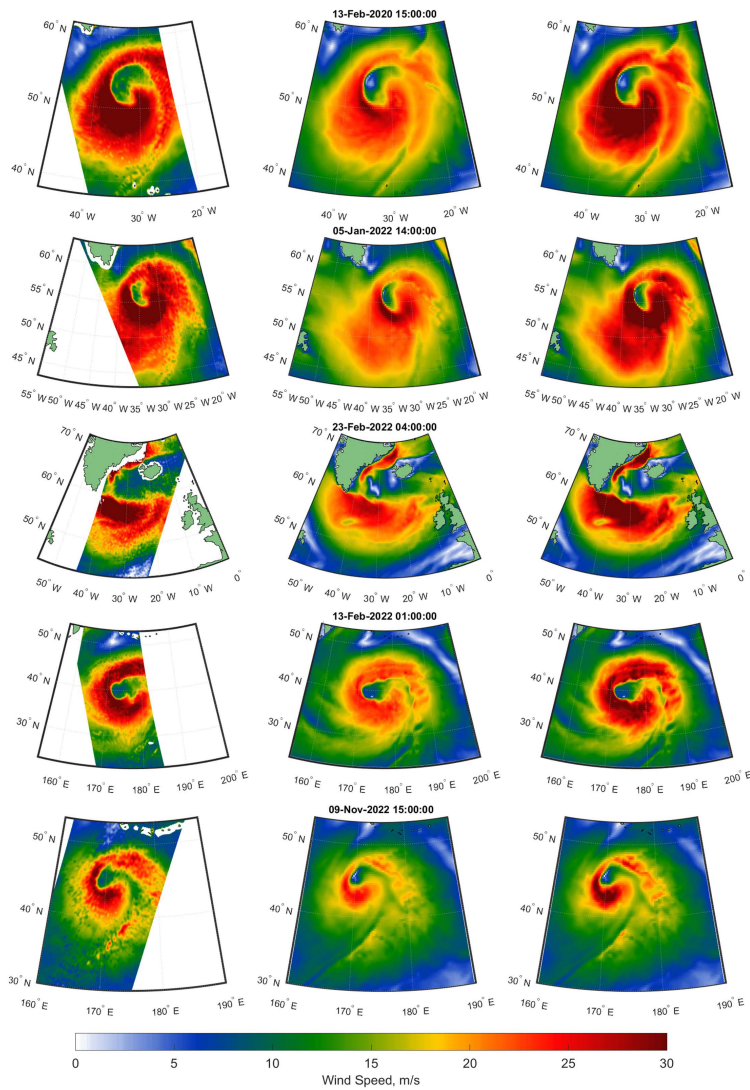


Fig. 1. Surface wind speed fields in considered ETCs. Left column: wind speeds estimated by the AMSR-2; middle column: the ERA5 wind speed estimations; right column: wind speeds adjusted using Eq. (4)

2.3.2. PLs. PLs present powerful cyclones of small scale, forming over warm open ocean near colder land or ice. These storms significantly impact high-latitude ocean waves, generating wave heights of 8–12 meters [24]. Unlike long-lasting tropical cyclones, PLs are short-time living (6–36 hours) and fast-moving (4–10 m/s), often changing direction unpredictably [25, 26].

To validate wind speeds in the ERA5 reanalysis, this study focuses on the four powerful PLs with wind speeds exceeding 30 m/s with their center located far from land and ice (Table 2). Figure 2 shows the wind fields from the AMSR-2 (left column) and ERA5 (middle column) in the selected PLs.

Selected PL cases

Start date	End date	Region	Min MSLP*, hPa	Max U_{10} **, m/s
18 January 2017	21 January 2017	WA	960	31
03 January 2022	03 January 2022	WA	950	45
21 March 2022	23 March 2022	WA	970	37
24 March 2022	25 March 2022	WA	995	32

* Data are taken from the ERA5 database.

** Data are taken from the AMSR-2 database.

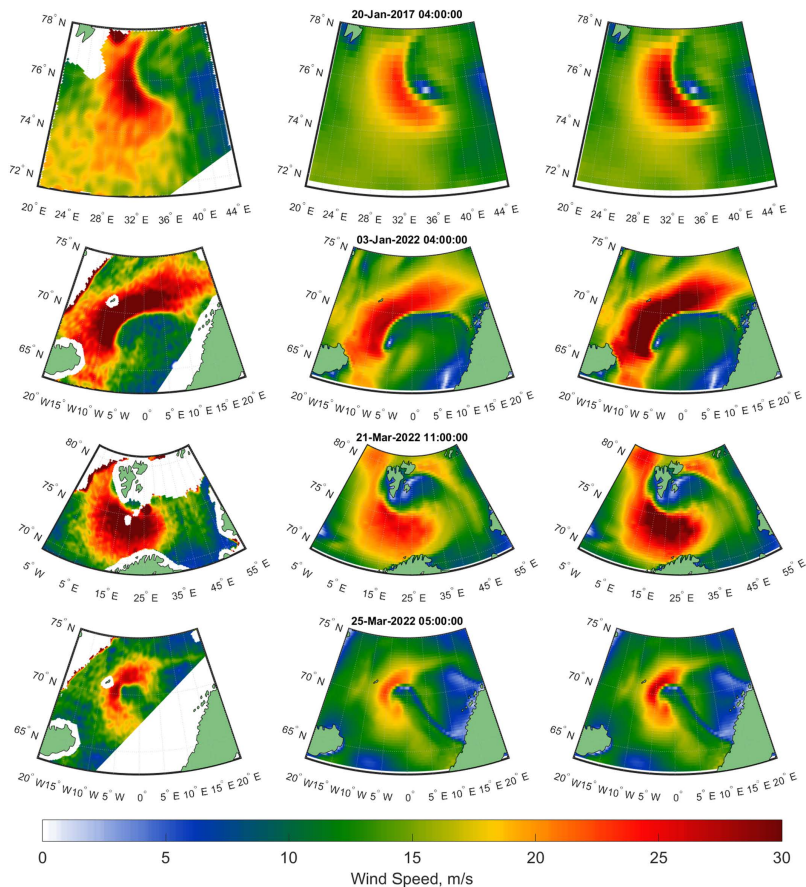


Fig. 2. Surface wind speed fields in considered PLs. Left column: wind speeds estimated by the AMSR-2; middle column: the ERA5 wind speed estimations; right column: wind speeds adjusted using Eq. (4)

2.3.3. TCs. While wind speeds in ETC and PL systems do not exceed 50 m/s, we also explored higher wind speeds by analyzing TCs (typhoons and hurricanes) listed in Table 3, taken from the IBTrACS database. Figure 3 shows the wind speed fields from the AMSR-2 (left) and the ERA5 (center) in the selected TCs. Figure 3

reveals not only ERA5 lower wind speeds as compared to the AMSR-2 wind speeds but also significant in the overall radial wind pattern. These discrepancies make meaningless the direct pixel-by-pixel comparisons of wind speeds. Due to the observed discrepancies between the ERA5 and AMSR-2 wind fields in TCs, this study presents a modification function for the ERA5 wind speeds based on the data from ETCs and PLs, not including TCs.

Table 3

Selected TC cases

Tropical cyclone	Start date	End date	Min MSLP*, hPa (date)	Max U_{10} *, m/s (date)
Super Typhoon MERANT	08 September 2016	14 September 2016	890 (Sep 13 06Z)	87.45 (Sep 13 12Z)
Super Typhoon HAGIBIS	04 October 2019	12 October 2019	890 (Oct 7 12Z)	82 (Oct 7 10Z)
Super Typhoon SURIGAE	11 April 2021	30 April 2021	882 (Apr 17 12Z)	87.45 (Apr 17 12Z)
Major Hurricane LEE	01 September 2023	17 September 2023	926 (Sep 8 06Z)	74.5 (Sep 8 06Z)

* Data are taken from the IBTrACS database.

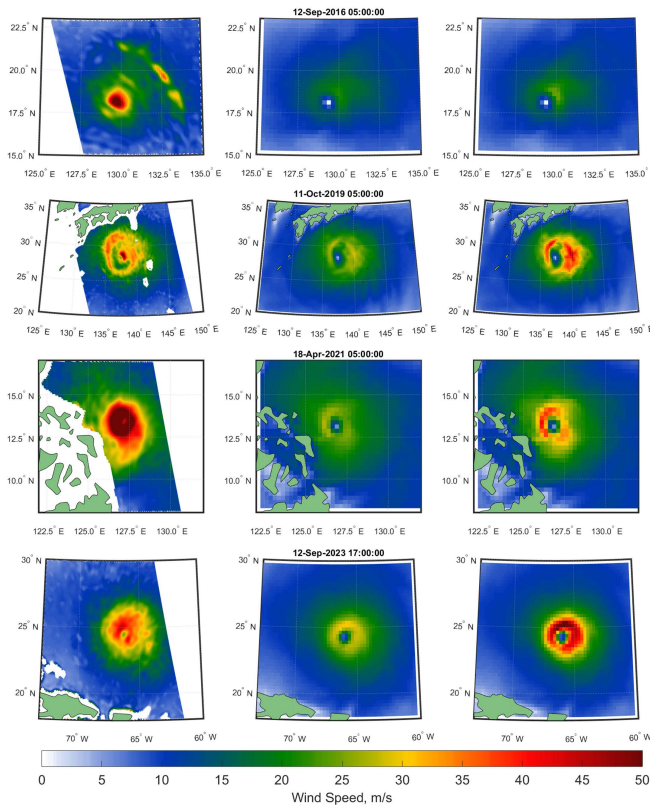


Fig. 3. Surface wind speed fields in considered TCs. Left column: wind speeds estimated by the AMSR-2; middle column: the ERA5 wind speed estimations; right column: wind speeds adjusted using Eq. (4)

3. Results

Visual analysis of Figs. 1–3 reveals that the ERA5 underestimates wind speeds across large areas of the storms as compared to the AMSR-2 wind speeds (left vs. middle columns). These discrepancies are further emphasized in Fig. 4, which shows a scatter plot of wind speeds. While the ERA5 estimations never exceed 35 m/s, the AMSR-2 wind speeds reach significantly higher values (up to 50 m/s). The clear deviation from the 1:1 line in the scatter plot, especially for wind speeds above 10 m/s, confirms the underestimation of wind intensity by the ERA5 as compared to the AMSR-2 wind speeds. Table 4 (first row) summarizes the statistical metrics calculated using Eqs. (1–3) for the full range of wind speeds depicted in Fig. 4.

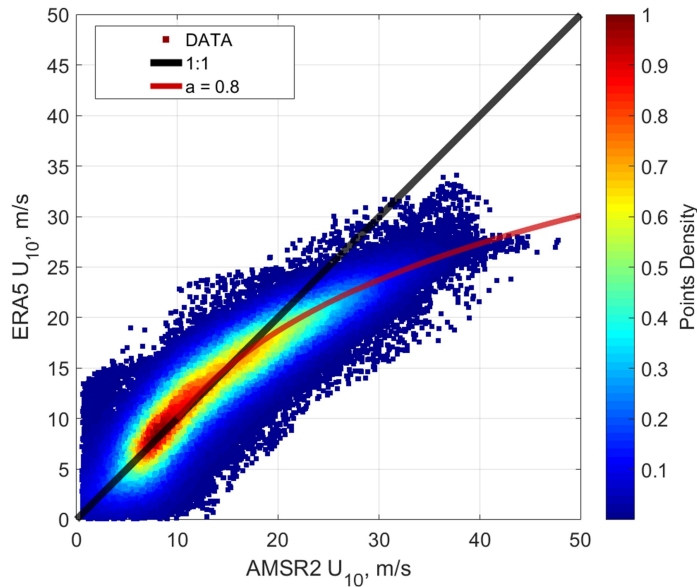


Fig. 4. Scatter plot of wind speeds between AMSR-2 and ERA5 for PLs and ETCs. The color scale shows points density

Building on the methodology, presented in section 2.1, we propose a simple and efficient exponential function to adjust the ERA5 wind speeds to the AMSR-2 wind speeds:

$$U_{10c} = \begin{cases} U_{10} & , U_{10} \leq 10, \\ U_{10p} \exp \left[a \left(\frac{U_{10}}{U_{10p}} - 1 \right) \right] & , U_{10} > 10, \end{cases} \quad (4)$$

where a is a constant and $U_{10p} = 10$ m/s.

Determining the ideal coefficient a for this function can be challenging. Therefore, we use the statistical metrics calculated in Eqs. (1–3) (as presented in Table 4). This analysis reveals that a value of $a = 0.8$ yields the best results. Due to the bias RMSE and R in Table 4, the adjustment function, where $a = 0.8$,

significantly reduces the underestimation of wind speeds by ERA5, bringing them to closer agreement with the observations.

Visual comparisons of the corrected wind fields (illustrated in the right column of Figs. 1–3) with the AMSR-2 data reveal good agreement in both ETCs and PLs. However, discrepancies in radial distribution of wind speeds and the shape of TCs between the ERA5 and the AMSR-2 (see Fig. 3) raise concerns about applying Eq. (4) directly to these atmospheric systems. As shown in the scatterplot of Fig. 5, the adjustment function (4) can be applied only to the wind speeds of ERA5 up to 40 m/s, yet the wind speed within the TCs reaches to about 70 m/s. Therefore, we conclude that the proposed correction function is beneficial for improving wind speeds of ERA5 in ETCs and PLs, but its application to TCs requires further investigation.

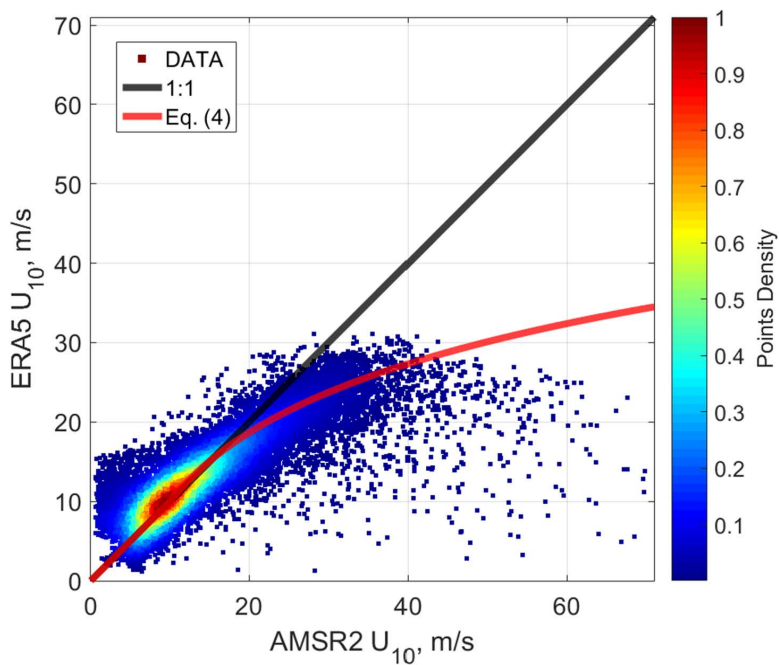


Fig. 5. Scatter plot of wind speeds between AMSR-2 and ERA5 for TCs. The color scale shows points density

Table 4

Statistical metrics for full range of wind speeds in PLs and ETCs shown in Fig. 4

a	Bias	RMSE	R
Original Data	-0.79	2.88	0.92
0.70	-0.89	2.66	0.93
0.75	-0.47	2.46	0.94
0.80	-0.03	2.45	0.94
0.85	+0.43	2.66	0.94

Conclusion

This study is aimed to evaluate the accuracy of the ERA5 wind speeds in diverse storm systems and propose a correction function to address potential biases. Our analysis focused on ETCs, PLs, and TCs.

The findings demonstrate that the ERA5 systematically underestimates wind speeds across large areas within ETCs and PLs as compared to the AMSR-2 retrieved surface wind speeds. We developed a simple exponential correction function based on statistical metrics to improve the agreement between the ERA5 and the AMSR-2 wind speeds. Visual comparisons and quantitative analyses confirmed the effectiveness of this correction function in both ETCs and PLs, successfully reconstructing the observed wind field patterns and maximum wind speeds.

However, applying the same correction function to TCs requires caution. Fundamental discrepancies exist between the ERA5 and the AMSR-2 winds in representing the overall wind field structure within TCs. This suggests that applying the function to TCs directly might not fully capture the complexity of their wind fields.

Therefore, we conclude that the proposed correction function offers a valuable tool for enhancing wind speed accuracy in ETCs and PLs bringing them closer to the AMSR-2 sea surface wind speeds. Further investigations are necessary to develop tailored approaches for addressing wind speed biases in TCs considering the unique characteristics and limitations of existing reanalysis data.

This research contributes to improving our understanding and representation of wind speeds in diverse storm systems, ultimately aiding in more accurate weather forecasting, climate monitoring and marine applications.

REFERENCES

1. Potisomporn, P., Adcock, T.A.A. and Vogel, C.R., 2023. Evaluating ERA5 Reanalysis Predictions of Low Wind Speed Events around the UK. *Energy Reports*, 10, pp. 4781-4790. <https://doi.org/10.1016/j.egy.2023.11.035>
2. Li, X., Yang, J., Han, G., Ren, L., Zheng, G., Chen, P. and Zhang, H., 2022. Tropical Cyclone Wind Field Reconstruction and Validation Using Measurements from SFMR and SMAP Radiometer. *Remote Sensing*, 14(16), 3929. <https://doi.org/10.3390/rs14163929>
3. Campos, R.M., Gramscianinov, C.B., de Camargo, R. and da Silva Dias, P.L., 2022. Assessment and Calibration of ERA5 Severe Winds in the Atlantic Ocean Using Satellite Data. *Remote Sensing*, 14(19), 4918. <https://doi.org/10.3390/rs14194918>
4. Minola, L., Zhang, F., Azorin-Molina, C., Safaei Pirooz, A.A., Flay, R.G.J., Hersbach, H. and Chen, D., 2020. Near-Surface Mean and Gust Wind Speeds in ERA5 across Sweden: Towards an Improved Gust Parametrization. *Climate Dynamics*, 55(3-4), pp. 887-907. <https://doi.org/10.1007/s00382-020-05302-6>
5. Stopa, J.E. and Cheung, K.F., 2014. Intercomparison of Wind and Wave Data from the ECMWF Reanalysis Interim and the NCEP Climate Forecast System Reanalysis. *Ocean Modelling*, 75, pp. 65-83. <https://doi.org/10.1016/j.ocemod.2013.12.006>
6. Caires, S., Sterl, A., Bidlot, J.-R., Graham, N. and Swail, V., 2004. Intercomparison of Different Wind-Wave Reanalyses. *Journal of Climate*, 17(10), pp. 1893-1913. [https://doi.org/10.1175/1520-0442\(2004\)017<1893:IODWR>2.0.CO;2](https://doi.org/10.1175/1520-0442(2004)017<1893:IODWR>2.0.CO;2)

7. Campos, R.M. and Guedes Soares, C., 2017. Assessment of Three Wind Reanalyses in the North Atlantic Ocean. *Journal of Operational Oceanography*, 10(1), pp. 30-44. <https://doi.org/10.1080/1755876X.2016.1253328>
8. Campos, R.M., Guedes Soares, C., Alves, J.H.G.M., Parente, C.E. and Guimaraes, L.G., 2019. Regional Long-Term Extreme Wave Analysis Using Hindcast Data from the South Atlantic Ocean. *Ocean Engineering*, 179, pp. 202-212. <https://doi.org/10.1016/j.oceaneng.2019.03.023>
9. Zabolotskikh, E.V. and Chapron, B., 2020. Analyzing the Accuracy of ERA-Interim Data on Total Atmospheric Water Vapor in the Arctic Estimated from AMSR2 Data. *Russian Meteorology and Hydrology*, 45(3), pp. 179-184. <https://doi.org/10.3103/S106837392003005X>
10. Kerr, Y.H., Waldteufel, P., Wigneron, J.-P., Delwart, S., Cabot, F., Boutin, J., Escorihuela, M.-J., Font, J., Reul, N. [et al.], 2010. The SMOS Mission: New Tool for Monitoring Key Elements of the Global Water Cycle. *Proceedings of the IEEE*, 98(5), pp. 666-687. <https://doi.org/10.1109/JPROC.2010.2043032>
11. Lodise, J., Merrifield, S., Collins, C., Behrens, J. and Terrill, E., 2024. Performance of ERA5 Wind Speed and Significant Wave Height within Extratropical Cyclones Using Collocated Satellite Radar Altimeter Measurements. *Coastal Engineering Journal*, 66(1), pp. 89-114. <https://doi.org/10.1080/21664250.2023.2301181>
12. Reul, N., Tenerelli, J., Chapron, B., Vandemark, D., Quilfen, Y. and Kerr, Y., 2012. SMOS Satellite L-Band Radiometer: A New Capability for Ocean Surface Remote Sensing in Hurricanes. *Journal of Geophysical Research*, 117(C2), C02006. <https://doi.org/10.1029/2011JC007474>
13. Hauser, D., Abdalla, S., Arduin, F., Bidlot, J.-R., Bourassa, M., Cotton, D., Gommenginger, C., Evers-King, H., Johnsen, H. [et al.], 2023. Satellite Remote Sensing of Surface Winds, Waves, and Currents: Where are We Now? *Surveys in Geophysics*, 44(5), pp. 1357-1446. <https://doi.org/10.1007/s10712-023-09771-2>
14. Meissner, T. and Wentz, F.J., 2009. Wind-Vector Retrievals under Rain with Passive Satellite Microwave Radiometers. *IEEE Transactions on Geoscience and Remote Sensing*, 47(9), pp. 3065-3083. <https://doi.org/10.1109/TGRS.2009.2027012>
15. Meissner, T. and Wentz, F.J., 2012. The Emissivity of the Ocean Surface between 6 and 90 GHz over a Large Range of Wind Speeds and Earth Incidence Angles. *IEEE Transactions on Geoscience and Remote Sensing*, 50(8), pp. 3004-3026. <https://doi.org/10.1109/TGRS.2011.2179662>
16. Zabolotskikh, E.V., Reul, N. and Chapron, B., 2016. Geophysical Model Function for the AMSR2 C-Band Wind Excess Emissivity at High Winds. *IEEE Geoscience and Remote Sensing Letters*, 13(1), pp. 78-81. <https://doi.org/10.1109/LGRS.2015.2497463>
17. Zabolotskikh, E., Mitnik, L., Reul, N. and Chapron, B., 2015. New Possibilities for Geophysical Parameter Retrievals Opened by GCOM-W1 AMSR2. *IEEE Journal of Selected Topics in Applied Earth Observations and Remote Sensing*, 8(9), pp. 4248-4261. <https://doi.org/10.1109/JSTARS.2015.2416514>
18. Hersbach, H., Bell, B., Berrisford, P., Hirahara, S., Horányi, A., Muñoz-Sabater, J., Nicolas, J., Peubey, C., Radu, R. [et al.], 2020. The ERA5 Global Reanalysis. *Quarterly Journal of the Royal Meteorological Society*, 146(730), pp. 1999-2049. <https://doi.org/10.1002/qj.3803>
19. Shimura, T., Mori, N. and Mase, H., 2013. Ocean Waves and Teleconnection Patterns in the Northern Hemisphere. *Journal of Climate*, 26(21), pp. 8654-8670. <https://doi.org/10.1175/jcli-d-12-00397.1>
20. Ponce de León, S. and Guedes Soares, C., 2014. Hindcast of Extreme Sea States in North Atlantic Extratropical Storms. *Ocean Dynamics*, 65(2), pp. 241-254. <https://doi.org/10.1007/s10236-014-0794-6>
21. Allen, J.T., Pezza, A.B. and Black, M.T., 2010. Explosive Cyclogenesis: A Global Climatology Comparing Multiple Reanalyses. *Journal of Climate*, 23(24), pp. 6468-6484. <https://doi.org/10.1175/2010JCLI3437.1>

22. Cheshm Siyahi, V., Kudryavtsev, V., Yurovskaya, M., Collard, F. and Chapron, B., 2023. On Surface Waves Generated by Extra-Tropical Cyclones – Part I: Multi-Satellite Measurements. *Remote Sensing*, 15(7), 1940. <https://doi.org/10.3390/rs15071940>
23. Cheshm Siyahi, V., Kudryavtsev, V., Yurovskaya, M., Collard, F. and Chapron, B., 2023. On Surface Waves Generated by Extra-Tropical Cyclones – Part II: Simulations. *Remote Sensing*, 15(9), 2377. <https://doi.org/10.3390/rs15092377>
24. Kudryavtsev, V., Cheshm Siyahi, V., Yurovskaya, M. and Chapron, B., 2023. On Surface Waves in Arctic Seas. *Boundary-Layer Meteorology*, 187, pp. 267-294. <https://doi.org/10.1007/s10546-022-00768-9>
25. Smirnova, J.E., Golubkin, P.A., Bobylev, L.P., Zabolotskikh, E.V. and Chapron, B., 2015. Polar Low Climatology over the Nordic and Barents Seas Based on Satellite Passive Microwave Data. *Geophysical Research Letters*, 42(13), pp. 5603-5609. <https://doi.org/10.1002/2015GL063865>
26. Landgren, O.A., Batrak, Y., Haugen, J.E., Støylen, E. and Iversen, T., 2019. Polar Low Variability and Future Projections for the Nordic and Barents Seas. *Quarterly Journal of the Royal Meteorological Society*, 145(724), pp. 3116-3128. <https://doi.org/10.1002/qj.3608>

Submitted 04.03.2023; approved after review 01.04.2024;

accepted for publication 16.05.2024.

About the authors:

V. Cheshm Siyahi, Researcher, Satellite Oceanography Laboratory, Russian State Hydrometeorological University (98 Malookhtinskiy Ave., Saint Petersburg, 195196, Russian Federation), CSc. (Phys.-Math.), **SPIN-code: 8687-5164**, **ORCID ID: 0000-0002-8770-6182**, **ResearcherID: HJY-7901-2023**, **Scopus Author ID: 57489024100**, vahid@rshu.ru

E.V. Zabolotskikh, Leading Researcher, Satellite Oceanography Laboratory, Russian State Hydrometeorological University (98 Malookhtinskiy Ave., Saint Petersburg, 195196, Russian Federation), DSc. (Phys.-Math.), **SPIN-code: 4328-9035**, **ORCID ID: 0000-0003-4500-776X**, **ResearcherID: R-2221-2016**, **Scopus Author ID: 6506482460**, liza@rshu.ru

V.N. Kudryavtsev, Head of the Laboratory, Satellite Oceanography Laboratory, Russian State Hydrometeorological University (98 Malookhtinskiy Ave., Saint Petersburg, 195196, Russian Federation), Leading Researcher, Remote Sensing Department, Applied Marine Physics Department, Marine Hydrophysical Institute of RAS (2 Kapitanskaya Str., Sevastopol, 299011, Russian Federation), DSc. (Phys.-Math.), **SPIN-code: 2717-5436**, **ORCID ID: 0000-0002-8545-1761**, **ResearcherID: G-1502-2014**, **Scopus Author ID: 7102703183**, kudr@rshu.ru

Contribution of the co-authors:

V. Cheshm Siyahi – analysis and problem statement, algorithm development, visualization, data processing, preparation of the paper text

E. V. Zabolotskikh – formal analysis, data structure development, providing research data, editing the paper text

V. N. Kudryavtsev – conceptualization, supervision

The authors have read and approved the final manuscript.

The authors declare that they have no conflict of interest.